Edith Cowan University

Research Online

Theses: Doctorates and Masters

Theses

2016

An experimental and numerical study of surface interactions in turbulent swirling jets

Zahir Uddin Ahmed
Edith Cowan University

Follow this and additional works at: https://ro.ecu.edu.au/theses

 Part of the Engineering Commons

Recommended Citation

Ahmed, Z. U. (2016). *An experimental and numerical study of surface interactions in turbulent swirling jets*. https://ro.ecu.edu.au/theses/1790

This Thesis is posted at Research Online.
https://ro.ecu.edu.au/theses/1790

Edith Cowan University
Research Online

Theses: Doctorates and Masters | Theses

2016

An experimental and numerical study of surface interactions in turbulent swirling jets

Zahir Uddin Ahmed
Edith Cowan University

Recommended Citation

Ahmed, Z. U. (2016). *An experimental and numerical study of surface interactions in turbulent swirling jets*. Retrieved from http://ro.ecu.edu.au/theses/1790

This Thesis is posted at Research Online.
http://ro.ecu.edu.au/theses/1790

Edith Cowan University

Copyright Warning

You may print or download ONE copy of this document for the purpose of your own research or study.

The University does not authorize you to copy, communicate or otherwise make available electronically to any other person any copyright material contained on this site.

You are reminded of the following:

- Copyright owners are entitled to take legal action against persons who infringe their copyright.

- A reproduction of material that is protected by copyright may be a copyright infringement. Where the reproduction of such material is done without attribution of authorship, with false attribution of authorship or the authorship is treated in a derogatory manner, this may be a breach of the author's moral rights contained in Part IX of the Copyright Act 1968 (Cth).

- Courts have the power to impose a wide range of civil and criminal sanctions for infringement of copyright, infringement of moral rights and other offences under the Copyright Act 1968 (Cth). Higher penalties may apply, and higher damages may be awarded, for offences and infringements involving the conversion of material into digital or electronic form.

An Experimental and Numerical Study of Surface Interactions in Turbulent Swirling Jets

This thesis is presented for the degree of

Doctor of Philosophy

Zahir Uddin Ahmed

Edith Cowan University

School of Engineering

2016

USE OF THESIS

The Use of Thesis statement is not included in this version of the thesis.

Abstract

Convective heat transfer and drying processes are found in industrial applications from gas turbine blade cooling to drying of food products and paper. In many instances, these processes rely on either a single or an array of fluid jets which impinge onto a surface. Traditionally, non-swirling impinging jets have been used, but interest surrounds possible advantages from imposing swirl into these jets to further promote heat and mass transfer at the surface. The challenge of resolving this question is that including swirl further complicates fluid-surface interactions. Studies are faced with the complexity of flow behaviour, the need for intricate measurement techniques and jets which seamlessly transition from non-swirling to swirling with well-defined boundary conditions. To better understand the nature of turbulent jet impingement with, and without, swirl requires carefully designed experiments covering parameters believed to affect the magnitude and uniformity of heat transfer.

This research investigated, experimentally and numerically, incompressible turbulent impinging air jets using aerodynamically derived swirl. The aim was to elucidate the effects of different parameters on fluid flow and surface heat transfer characteristics. Measurements of mean velocity and turbulence, surface pressure and temperatures were done using Constant Temperature Anemometry, integrating micro-manometer (pressure) tappings and steady-state heated thin foil technique via infrared thermography. Imaging for flow visualisations was also done. Numerical simulations were performed using ANSYS Fluent (version 14.5). Test conditions investigated encompassed a range of Reynolds numbers (Re = 11,600 – 35,000), swirl numbers (S = 0 – 1.05) and nozzle-to-plate distances (H = 1D – 6D).

Results show that the use of low-to-medium swirl numbers (S = 0.27 – 0.45) is found to improve heat transfer (Nu) in the impingement region compared to non-swirling (S = 0) jets over $H \leq 4D$, with little improvement in spatial Nu uniformity. When S further increases, significant enhancement in Nu occurs only at near-field impingement ($H \leq 2D$), regardless of the impingement area (footprint). At $H \geq 4D$, a significantly low but more uniform radial profile of Nu is obtained. Results conclude the effect of swirl on the heat transfer characteristics is a complex relationship, which depends on the Reynolds number and nozzle-to-plate distance. Whilst high swirl can lead to significant improvements in heat transfer, this is not necessarily always the case. It appears that there exist a threshold impingement distance and a transitional swirl number (dependent on Re) over which the effect of swirl on

heat transfer improvement varies. Numerical results also predict dramatic behaviours of flow field and turbulence at different swirl numbers and nozzle-to-plate distances, with flow recirculation in near-field impingement ($H = 2D$) and non-swirl like at far-field ($H = 6D$). The occurrence of peak heat transfers at different swirl numbers is largely correlated with swirl induced turbulence characteristics near the impingement surface. Increase in Reynolds number augments the magnitude of *Cp* and heat transfer. For a given *S*, flow field and heat transfer distributions are found to be largely independent of *Re*.

Keywords: Swirl, Impinging jets, Pressure, Velocity field, Turbulence, Heat transfer, CTA, Infrared thermography, CFD, RANS, Nusselt number.

The declaration page
is not included in this version of the thesis

Acknowledgements

I express my deepest gratitude to a number of people, without whom it would have not been possible for me to undertake this program during my four years at Edith Cowan University.

I sincerely thank my principal supervisor, Dr. Yasir Al-Abdeli, and associate supervisors, Dr. Ferdinando Guzzomi and Dr. Miccal Matthews for their invaluable time, continuous moral support, insightful guidance and constructive criticism since the start of the program. The anonymous reviewers of different internationally recognized journals and the thesis are also thanked for their precious time and scholarly comments which were helpful.

I am thankful to the technical and admin staff of the School of Engineering at ECU for their cooperations with regard to manufacturing processes and purchasing raw materials for different experimental setups used in this work. Mr. Brett Thomas is also thanked for the early stage CAD rendering of the swirl nozzle.

Benjamin Leclaire, ONERA, Department of Fundamental and Experimental Aerodynamics, Meudon, France is thankfully acknowledged for clarifying some fundamentals of X-wire probe application.

I am also profoundly indebted to my wife, Kamrun Nahar Deepa and my daughter Zunaira Ahmed Arisha for their endless love, support and tremendous patience throughout the difficult phases of my life. Arisha is also warmly thanked for helping her dad to prepare a component of pressure visualisations setup till late midnight.

The Department of Education and Training of government of Australia and Scope global Ltd. are also acknowledged for granting the Endeavour Postgraduate Scholarship and continuous supports for four years in relation to the scholarship activity to pursue the program in Australia.

List of Journal Publications from This Candidature

For publishers' permission letters for use the published journal articles below in the thesis, please refer to Appendix A. Additionally refer to Appendix B for statement of the contribution of co-authors.

i. Ahmed, Z. U., Al-Abdeli, Y. M. and Matthews, M. T., *The effect of inflow conditions on the development of non-swirling versus swirling impinging turbulent jets,* Computers & Fluids, **118**, p. 255-273, 2015.

ii. Ahmed, Z. U., Al-Abdeli, Y. M. and Guzzomi, F. G., *Impingement pressure characteristics of swirling and non-swirling turbulent jets,* Experimental Thermal and Fluid Science, **68**, p. 722-732, 2015.

iii. Ahmed, Z. U., Al-Abdeli, Y. M. and Guzzomi, F. G., *Corrections of dual-wire CTA data in turbulent swirling and non-swirling jets,* Experimental Thermal and Fluid Science, **70**, p. 166-175, 2016.

iv. Ahmed, Z. U., Al-Abdeli, Y. M. and Guzzomi, F. G., *Heat transfer characteristics of swirling and non-swirling impinging turbulent jets,* International Journal of Heat and Mass Transfer (In review).

v. Ahmed, Z. U., Al-Abdeli, Y. M. and Guzzomi, F. G., *An experimental and numerical study of impingement characteristics in turbulent swirling and non-swirling jets*, International Journal of Thermal Science (In review).

Table of Contents

List of Tables

List of Figures

List of Symbols, Nomenclature

A	Area of the jet exit plane or on the impingement surface (m^2)
C	Specific heat of jet (air) (1.007 kJ/kg.K, at 20^o C and 1 atm pressure)
C_μ	k-ε turbulence model constant
$C_{1\varepsilon}$	k-ε turbulence model constant
$C_{2\varepsilon}$	k-ε turbulence model constant
D	Nozzle diameter at the exit plane (40 mm)
E	CTA raw data signal (voltage)
G	Rate of turbulent energy production ($kg/m.s^3$)
G_x	Axial momentum flux (kg.m/s)
G_θ	Tangential momentum flux (kg.m/s)
h	Heat transfer coefficient ($W/m^2.^oK$)
H	Nozzle-to-plate distance (mm)
k	Turbulent kinetic energy (m^2/s^2)
k_t	Eddy thermal conductivity (W/m.K)
k_w	Thermal conductivity of impingement surface (15 W/m.^{o}K)
L_t	Entry length for the turbulent flow (mm)
Nu	Local Nusselt number (dimensionless)
$\overline{Nu}$	Spatially averaged Nusselt number (dimensionless)
$P(r)$	Local radial pressure (N/m^2)
P_∞	Ambient pressure (N/m^2)
q	Joule heating (W/m^2)
Q	Volumetric flow rate (m^3/s)
q_c	Heat loss due to conduction (W/m^2)
q_{loss}	Total heat loss (W/m^2)
q_r	Heat loss due to radiation (W/m^2)

r	Radial coordinate (mm)
Re	Reynolds number (dimensionless)
S	Swirl number (dimensionless)
T_{aw}	Adiabatic wall temperature (^{o}K)
T_{∞} or T_{amb}	Ambient room temperature (^{o}K)
T_{ref}	Reference temperature (^{o}K)
T_{w}	Heated wall temperature (^{o}K)
U_{b}	Bulk axial velocity at the nozzle exit plane (m/s)
U_{f}	Average jet velocity at the exit plane (m/s) determined from total mass flow rate
$\langle u \rangle$	Time mean axial velocity component (m/s)
u'	Average fluctuating velocity component in axial direction (m/s)
$\langle v \rangle$	Time mean radial velocity component (m/s)
v'	Average fluctuating velocity component in radial direction (m/s)
$\langle w \rangle$	Time mean azimuthal velocity component (m/s)
$\langle w' \rangle$	Average fluctuating velocity component in azimuthal direction (m/s)
x	Axial co-ordinate (mm)
y	Abscissa of the impingement plane (mm)
z	Ordinate of the impingement plane (mm)
δ_{ij}	Kronecker delta
ρ	Density of jet (air) (1.204 kg/m^3 at 20^{o}C)
λ	Thermal conductivity of the bulk fluid (air) (0.0264 W/m.K)
μ	Dynamic viscosity of jet (air) (18.25×10^{-6} kg/m.s, at 20^{o} C)
μ_t	Turbulent eddy viscosity (kg/m.s)
υ	Kinematic viscosity of jet (air) (15.16×10^{-6} m^2/s, at 20^{o} C)
ε	Emissivity coefficient
ε_r	Random error

ε_s	Systematic error
ε	Viscous dissipation rate (m^2/s^3)
σ_k	*k*-*ε* turbulence model constant
σ_ε	*k*-*ε* turbulence model constant

List of Abbreviations and Acronyms

CTA	Constant Temperature Anemometry
FF	Free jet corresponds to the geometry of Fairweather et al. (2006)
FI	Impinging jet correspond to the geometry of Fairweather et al. (2006)
IR	Infrared
LIF	Laser induced fluorescence
PIV	Particle Image Velocimetry
PP	Parabolic tangential velocity profile
RNG	Re-Normalisation Group
RSM	Reynolds Stress Model
SB	Solid-body-rotation type tangential velocity profile
SST	Shear Stress Transport
TF	Free jet corresponds to the geometry of Tummers et al. (2011)
TI	Impinging jet correspond to the geometry of Tummers et al. (2011)
UP	Uniform (top-hat) tangential velocity profile

Chapter 1

1 General Introduction

1.1. Introduction

Jets, which are defined as fluid streams that depart a nozzle or orifice into a surrounding medium, have been extensively studied due to their frequent occurrence in a wide range of practical applications. Impinging jets, where a jet strikes a surface either normally or obliquely, have also undergone many theoretical and experimental investigations due to their unique and complex flow characteristics as well as their ability to transfer heat and mass effectively. Non-swirling jets (flow purely in the stream-wise direction with no rotational component) can have various shapes, which depends on the nozzle and surface configurations, where such shapes include: round jets, slotted jets, oblique jets and confined jets. Each type of jet has a different flow dynamic between the jet and the impingement surface and hence an associated momentum and energy transfer behaviour. When a swirl (or rotational) component is generated upstream of the nozzle exit plane by any means, a swirling jet is developed. Swirling jets typically display complex fluid flow with distinguishable features associated with the swirl, such as flow recirculation and stability. These unique flow characteristics may have significant impact on the jet heat and mass transfer for impinging jet applications.

This chapter presents a general introduction to the research topic, along with a discussion of different engineering (industrial) applications in relation to swirling and impinging jets. Then a brief literature review provides motivation for this project by identifying the current research gap, and is followed by the research questions to be addressed in this thesis. More detailed literature reviews on particular topics are discussed within each chapter. Research methodologies used to pursue the research questions are briefly discussed, and finally the overall thesis outline is presented.

1.1.1. Applications of swirling and impinging jets

Swirl is a common feature within fluid flows, where swirling jets are used in many practical applications as a means of improving mixing in industrial processes and controlling

flames in combustion chambers. Industrial applications include gas turbine combustors, cyclone separators, pneumatic conveyers, internal combustion engines and heat exchangers [1-6]. The use of swirl with streamwise (axial) flows in various applications typically provides some beneficial effects, such as stronger mass and energy transfers, flame stability and preventing pipeline blockages. All of these effects offer lower power usage and ultimately lower running costs.

Impinging jets are widely used in various industrial heat transfer applications, such as cooling of turbine blades and high-power electronics, due to their effective mass and heat transfer capacity between fluid media and the associated impingement surface. The fluid-surface interaction for an impinging jet generally occurs in two forms: cool jets impinging on hot surfaces, or hot jets impinging on cool surfaces. Cool jets have been used extensively in rapid quenching of heated surfaces in different practical applications, such as gas turbine airfoils [7], fuel rods in nuclear reactors [8] and grinding processes [9], in order to avoid thermal damage and cracks. In contrast, applications for hot jets (onto cool surfaces) include direct flame impingement heating [10, 11], where these jets offer fast and efficient heating that is commonly used for melting of scrap metal, shaping glassware and heating metal billets prior to forging.

Although non-swirling impinging jets are beneficial in the above industrial applications, they also present challenges due to their inhomogeneous heat flux distribution on impingement surfaces [12, 13]. This non-uniform or localised heating creates high temperature gradients within the impingement surface that may lead to material damage and/or excessive thermal stresses. As a result, swirling impinging jets have sometimes been applied [2, 14, 15] to improve both heat transfer rates and spatial uniformity. However, experimental and numerical studies report a wide variability of outcomes in the relationship between swirl and surface heat transfer [16-19]. The disparity observed in the results is not well understood, and may be largely due to differences in (upstream) flow conditions of the nozzle.

Impinging jets are also used in mass transfer applications; such as drying of paper, wood and food [20-22]. The advantage of using impinging jets over other methods, (namely conventional and microwave drying) is a significant reduction in drying time and uniformity in drying. These factors reduce thermal stress development in the specimen and also lower electrical energy usage and running costs.

1.1.2. Structure of free jets

A free (non-impinging) axisymmetric non-swirling jet exits the jet nozzle typically into a quiescent environment, where this is the case for this research project. The jet flow entrains surrounding fluid and diverges radially as it advances downstream of the nozzle. This flow characteristic continues until the initial fluid momentum or energy vanishes due to viscous losses. Figure 1.1a shows the fundamental regions of an axisymmetric free jet. When a jet exits the nozzle, it is characterised by a conical potential core surrounded by a mixing region, where an interaction between the jet and the ambient fluid occurs. The length of the potential core is defined by the distance (from the nozzle exit) where the jet mixing region spreads sufficiently inward that it reaches the jet centreline, which causes turbulence development. The length of the potential core typically depends on the type of nozzle and the nozzle exit conditions; usually it is $x = 2.5D$ - $8D$ [23, 24], where D is defined as the nozzle exit diameter. Beyond the potential core, the mixing region continues to spread as the velocity decays at a rate required for the axial momentum conservation and the mean velocity profile approaches the self-similar shape of the fully developed jet. The aforementioned jet flow characteristics are dependent on the inlet conditions, where the inlet conditions can vary the flow development in the near-and far-field of a free jet. For example, an axisymmetric jet from a pipe possesses a thicker initial shear layer and higher turbulence intensity than a contraction jet. Many studies (addressed in a recent review by Ball et al. [23]) have investigated the flow developments, structures and turbulence characteristics of incompressible non-swirling free jets.

When a swirl or rotational component is introduced to an axisymmetric free jet, a swirling free jet exits the nozzle (Figure 1.1b). In a swirling free jet, the presence of a rotational (tangential) flow component may generate both radial and axial pressure gradients, unlike a non-swirling free jet where pressure plays a minor role. The flow loses its strength in both axial and tangential directions as it progresses downstream from the nozzle exit. The swirl effect eventually diminishes at about $10D$, where the flow then resembles a non-swirling free jet [25]. Therefore the most notable flow features appear in the near-field, where swirl is strongest. For a small change in swirl, the flow behaviour in the jet near-field and mixing region may change dramatically [26]. When the tangential momentum exceeds a certain threshold (relative to the axial momentum) a unique feature, known as vortex breakdown, appears in the flow. Vortex breakdown is characterised by a transition from a jet-like axial

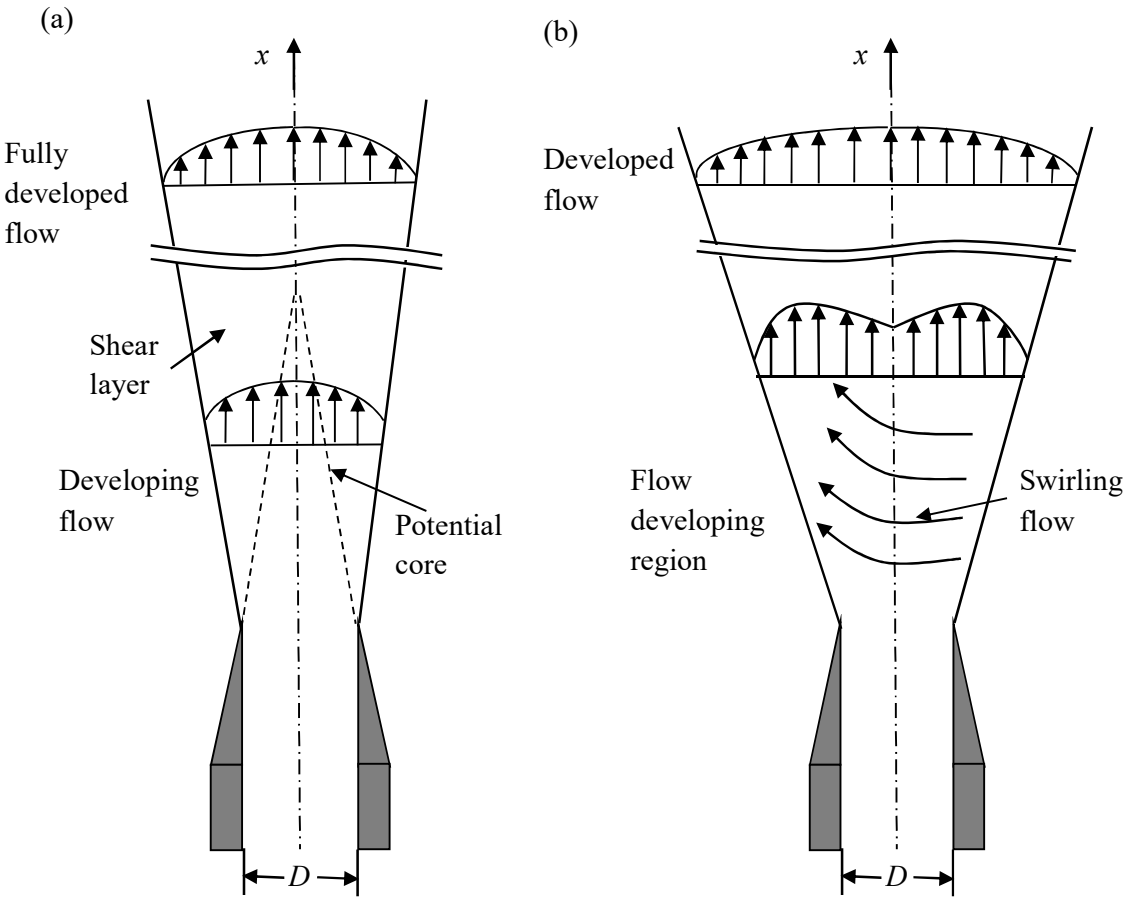

Figure 1.1 Flow structures of free jets: (a) non-swirling; (b) swirling.

velocity profile to a wake-like velocity profile and a local velocity minimum on the jet centreline axis [27]. The local velocity minimum is due to the adverse pressure gradient on the jet centreline generated by the swirling flow [27]. This leads to a stagnation point that is followed by a highly turbulent region of reverse flow further downstream. The detail of flow features and theoretical background on turbulent swirling free jets is widely available in textbooks [28, 29].

1.1.3. Structure of impinging jets

When the jet impinges onto a surface, the flow-field is affected by the complex jet-surface interactions that develop on or near the impingement surface. The flow structure produced by an impinging jet consists of three regions: the free jet region, the stagnation or impingement region and the wall jet region, which are depicted in Figure 1.2a. The free jet region forms as the jet exits the nozzle, where the jet consists of a potential core and a developing region that

entrains surrounding fluid into the jet. The impingement region forms when the jet impacts a surface and the strong interaction between the jet and surface causes the flow to change direction (or deflect). In this region, a rapid decrease in axial velocity and a corresponding rise in static pressure occur. There is disparity in the literature on the axial position where an impingement region starts, which typically extends up to 1*D* - 2*D* from the impingement surface [30]. The wall jet region forms near the impingement surface upon deceleration of the flow, where there is development of radial flow along the impingement surface. The local radial velocity rises rapidly to a maximum near the impingement surface and then reduces with increasing distance from the wall. In this region, the fluid flow experiences significant interaction with the ambient fluid through entrainment of the surrounding air. Although these three regimes can be considered separately, they are not independent. Extensive experimental and numerical studies can be found on the flow characteristics of turbulent impinging jets (for instance, Carlomagno et al. [31]).

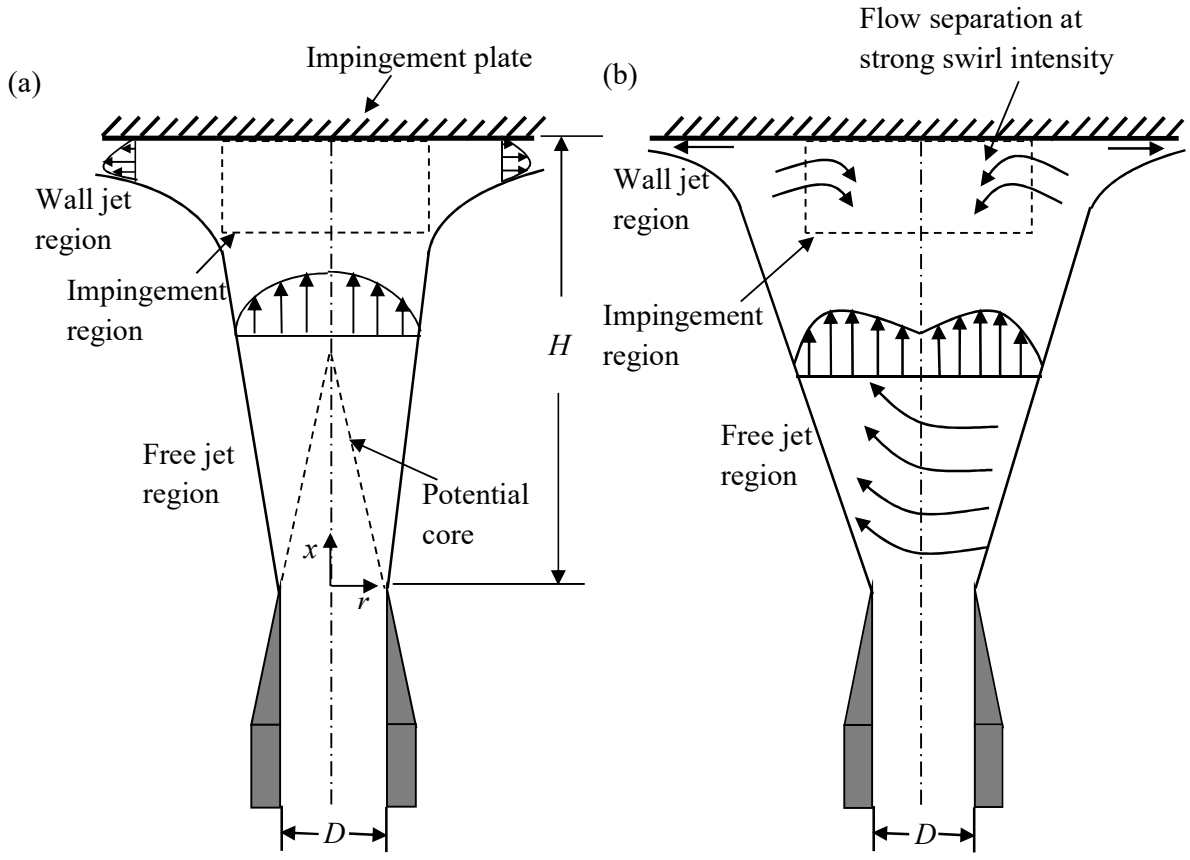

Figure 1.2 Flow structures of impinging jets: (a) non-swirling; (b) swirling.

When swirl flow impinges on a flat surface, an increased complexity in the flow compared to non-swirling impingement may occur due to the phenomena mentioned above that the swirl induces (Figure 1.2b). As a result, there are significantly different flow dynamics, compared to both non-impinging swirl and non-swirling impinging flows, may develop in the near-field and far-field flow and shear layer interactions. The anisotropic nature of turbulence and interaction between the swirling flow and impingement surface via possible recirculating region may make it difficult to resolve both the mean and fluctuating components. These effects potentially affect the wall characteristics such as pressure distributions, wall shear stress and heat transfer distributions on the impingement surface as well as jet spread. The recirculation region not only depends on the swirl intensity of the flow, but also on the mass flow rate and nozzle-to-plate distance.

1.1.4. Swirl generation and intensity

A variety of methods are used to generate swirl or the tangential flow component. These methods can be largely divided into three main groups: geometric, aerodynamic and mechanical [6]. Figure 1.3 illustrates the typical mechanisms used in previous studies associated with the three methods. Geometrically generated swirl is commonly obtained by feeding a streamwise flow through geometric means of some kind, such as twisted tape inserts mounted inside the nozzle [32, 33], radial or guide vanes positioned upstream of the nozzle exit plane [15, 34], and movable block swirl generator [35]. Limitation of these geometric designs restricts the swirl intensities that can be investigated. The variability of the geometric swirl generators inside the nozzle adds further complication, which impedes the comparison between studies in relation to flow behaviour and heat transfer characteristics.

Aerodynamically generated swirl does not use any geometric feature inside the nozzle; rather the axial and tangential flows enter the nozzle separately via a number of ports or slots located around the periphery of the nozzle or pipe wall [36, 37]. The resulting flow then directly mixes in the nozzle and leads to an axial-plus-tangential flow that emanates from the nozzle exit. The relative proportion of the total mass flow rates from axial and tangential ports are responsible for the degree of swirl. A non-swirling jet is generated when no air enters the nozzle tangentially and maximum swirl is attained when the axial inflow is zero.

The swirl flow can also be generated mechanically by rotating the axial flow as it passes through a revolving honeycomb, perforated tube combination or a spinning pipe. The rotation

is usually achieved by an electric motor and the revolutions per second of the motor control the swirl intensity.

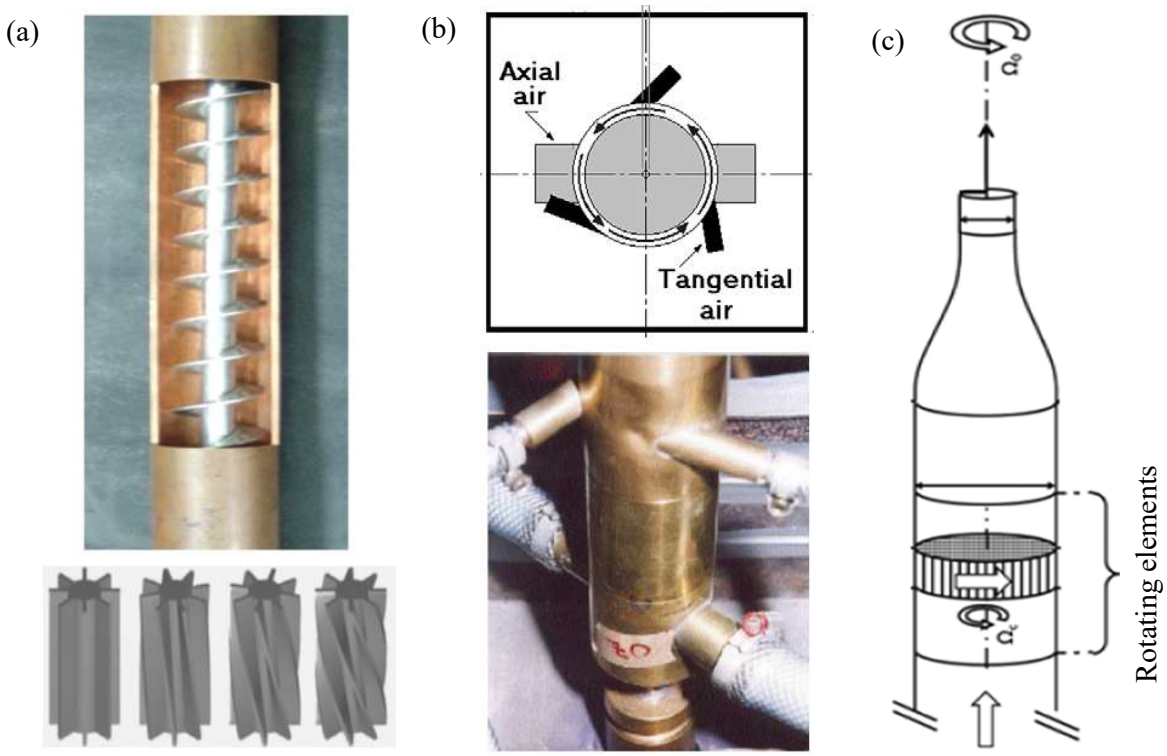

Figure 1.3 Different swirl generating mechanism: (a) geometrical [38, 39] - (top: a single helical insert, and down: typical variants of other inserts), (b) aerodynamical [37, 40] and (c) mechanical [41].

Regardless of the methods to generate swirl, the strength of swirl in the flow is defined by the swirl intensity, commonly known as swirl number. There is no universal definition available that correctly measures swirl intensity, which makes interpretation of swirl flow results difficult. For example, for a swirling (free) jet exiting a round nozzle, the critical swirl intensity for vortex breakdown to occur varies between 0.48 - 0.94 as observed in different studies [25, 42-44]. This variation in swirl intensity is due to the difference in swirl number definitions and variation of swirl flow generation techniques. Although a wide variety of swirl number definitions are used [43], two commonly used swirl number definitions are: the ratio of momentum flux (the ratio of axial flux of tangential momentum to axial flux of axial

momentum [25, 27, 43]) and the ratio of velocity components (tangential-to-axial) at the nozzle exit plane [26, 41, 45]. The detailed mathematical definition of these two and a correlation between them is discussed further in Chapter 3.

1.2. Project motivation

Numerous studies on non-swirling free and impinging jets have been separately investigated in the past [23, 46-48]. However, there is limited research on flow developments and jet spread for both the transitions from free to impinging jets and from non-swirling to swirling jets for the same nozzle and exit conditions. Upstream inflow conditions for a swirl flow may potentially alter the evolution of impinging jets and the heat and mass fluxes at the impingement surface, which have received little attention in the literature. As a result, there is a need to investigate the mean and turbulent flow development for the variation of inflow conditions at the nozzle exit plane. This may partly contribute to explaining the contradicting outcomes on the relationship between surface heat transfer and swirl flow.

The measurement of velocity and turbulent components of highly turbulent, three-dimensional flows, such as swirling flow, particularly at the nozzle exit plane or near the nozzle wall is challenging. Generally, swirl flow measurements are performed using either expensive non-intrusive techniques, such as PIV (Particle Image Velocimetry) or LIF (Laser Induced Fluorescence), or intrusive techniques, such as Constant Temperature Anemometry (CTA) and four-hole pressure probes. Measurements with non-intrusive techniques can be difficult due to restricted optical access or the need for flow seeding. Laser diagnostics may cause a build-up of seed powder scaling onto solid walls that can modify the near wall flow characteristics. In contrast, CTA measurements, among other intrusive techniques, are typically advantageous due to their greater proximity to the wall and capacity to measure both mean and turbulent velocity components from a high frequency (analogue) data series. CTA probes have been successfully applied to both non-swirling and swirling jets [49, 50]. However, their use for velocity measurements is typically limited by a maximum angle between the probe and the mean flow direction, which is commonly referred to as the maximum acceptance angle. For highly turbulent swirling flows, CTA probes (dual-wire and multi-wire) may provide erroneous results due to an inaccurate probe orientation and velocity gradient effects [51]. Previous investigations into the effects of the mean flow direction on the accuracy of measured velocity components have not been reported in the literature. In addition, the literature highlights a lack of systematic testing to establish methodologies for

orienting CTA multi-wire probes in order to increase measurement accuracy in turbulent swirl flows.

Analysing the effects of swirl on the impingement pressure distribution helps build a better understanding of the factors affecting (surface) heat and mass transfer. Moreover, research on the influence of swirl on the wall shear stress distribution is also scarce, which can help describe near-wall flow behaviour. Although a number of studies address the flow-fields of both non-swirling and swirling impinging jets; investigations of the pressure distributions on the impingement surface are relatively limited. In previous studies of impingement pressure from a swirling flow, the jets are developed using an annular nozzle [52, 53]. However, the flow behaviour of an annular nozzle is fundamentally different than a round nozzle due to inherent bluff-body induced flow recirculation.

Previous research into swirling impinging jets (mostly geometrically generated swirl) has predominantly focused on the effects of swirl intensity on the surface heat transfer [17, 54]. These studies have contradictory results in relation to the enhancement of heat transfer due to the addition of swirl, yet these discrepancies are poorly understood. Variation in spatial uniformity of heat transfer that results from swirling flow is also reported in the literature [39, 44]. One of the major difficulties associated with geometrically generated swirling jets is the inclusion of geometry-induced flow perturbations and vortices in the nozzle that disrupts the exact effect of swirl. Another issue for swirling impinging jets is the lack of well-defined boundary conditions at the nozzle exit plane. This research will address the above knowledge gaps by using a specially designed swirl (aerodynamic generated) nozzle, where jets can gradually vary from non-swirling to strongly swirling. The results obtained from this research will significantly improve our current understanding of the relationship between swirl flow and heat transfer on an impingement surface, with potentially positive impacts for industrial applications.

1.3. Project research questions

The brief overview above identifies existing challenges and unresolved issues for swirling flows and impinging jets in relation to their flow development and, heat transfer improvement and its uniformity compared to their non-swirling counterparts. This thesis highlights the development of a ‘swirl nozzle’ that uses an aerodynamically generated swirl flow, which allows transition from non-swirl to high swirl intensity flows for the same mass flow rate or various mass flow rates at the same swirl intensity.

The overall purpose of this work is to study the flow-field and heat transfer in swirling impinging jets by addressing the following research questions:

RQ1: How does a turbulent jet develop when it transitions from free to impinging, and in addition from non-swirling to swirling (for the same inflow, impingement conditions and nozzle geometry)?

RQ2: What inaccuracies are associated with the existing CTA measurement methodology of turbulent swirling flows, and how can they be improved?

RQ3: How does the pressure on the impingement surface vary with swirl intensity for a range of nozzle-to-plate distances and mass flow rates? Also, how does constant swirl intensity influence impingement pressure distribution for varying mass flow rates?

RQ4: How do aerodynamic swirling jets impact on impingement heat transfer characteristics compared to non-swirling jets, for a wide range of characteristic parameters, such as mass flow rates and nozzle-to-plate distance?

RQ5: How do aerodynamically generated swirl flows develop as they impinge on a surface? What factors contribute to non-uniform radial heat transfer distribution on the impingement surface?

1.4. Research methodologies

The above research questions are addressed in this thesis by applying both experimental and numerical methodologies. The experimental methods include hotwire measurements, infrared thermography and flow visualisation. A commercial software package, ANSYS FLUENT (version 14.5), is used for the numerical analysis.

A specially designed nozzle is used in this research to achieve aerodynamically generated swirling jet. Prior to manufacture, the design aspects of the nozzle, such as number of straight sections and orientations of tangential ports (swirler) was tested and optimized by numerical modeling [55].

Hotwire anemometry is used to acquire velocity field and boundary condition data to characterise the flow and provide opportunity for subsequent CFD modelling. The use of hotwire measurements has merit over non-intrusive techniques (PIV, LIF) as they preclude the need to seed flows or require optical access. CTA measurements also provide high frequency (analogue) data series and prevent the build-up of seed powder onto solid walls that can modify near wall turbulence characteristics.

Static pressure measurements on the impingement surface are performed via flush-mounted pressure tappings, which is a well-established method for pressure measurements on a wall or surface [56]. The tapping holes are small (around 1 mm) and distributed over the surface for spatial pressure measurements, where the tappings are connected to manometers.

Flow visualisation near the impingement surface is performed using thin cotton tufts of different colours to qualitatively resolve the flow field behaviour. This method is chosen for its relatively simple setup and can be easily integrated to the pressure measurement arrangement. Two different tuft lengths were also trialled (10 and 20 mm) to identify any discrepancy in the visualisation results due to the tuft length. A series of still images and videos are captured for each test condition.

Steady-state heated thin foil technique [57] via infrared (IR) thermography is used for heat transfer measurement on the impingement surface. Infrared thermography is commonly used with an IR camera, which non-intrusively measures two-dimensional surface temperatures. An IR camera is also advantageous in convective heat transfer analysis compared to standard techniques, such as thermocouples and resistance temperature detectors due to its higher sensitivity and low response time (typically few milliseconds).

The RANS (Reynolds-Averaged Navier Stokes) equations are solved for momentum and energy transport quantities via ANSYS FLUENT and different turbulent models are used to solve flow turbulence. Each model is first tested against experimental data sets derived from the current experiments and the literature. The numerical setup is confirmed after a range of essential testings such as mesh sensitivity analysis (independence), numerical domain and mesh first layer heights.

1.5. Thesis structure

This thesis is presented and organised as 'Thesis with publication" format[1]; and is structured in chapters as follows:

[1] "Thesis with Publication" is an acceptable format of thesis for postgraduate research at ECU policy. The current thesis has been written based on the guideline provided at http://www.ecu.edu.au/GPPS/policies_db/policies_view.php?rec_id= 0000000297. In this format, the submitted thesis can consist of publications that have already been published, are in the process of being published, or a combination of these.

Chapter 1 presents the general overview of the project topic and practical applications of impinging jets, followed by project motivations, the objectives of the thesis and methodology used in this research.

Chapter 2 discusses the effect of upstream inflow conditions on the downstream flow development for non-swirling and swirling, free and impinging jets. Preliminary numerical methodologies and techniques are validated against baseline experimental data sets.

Chapter 3 provides a detailed methodology for improving inaccuracies associated with swirl flow measurements by dual-wire hotwire anemometry.

Chapter 4 is dedicated to the impingement pressure characteristics for both swirling and non-swirling jets. Results of flow visualisation near the impingement surface are also discussed.

Chapter 5 presents experimental measurements of heat transfer using infrared thermography for both swirling and non-swirling impinging jets for the effect of various controlling parameters.

Chapter 6 discusses results from numerical data to better understand the effect of swirl on fluid flow characteristics. Factors affecting impingement heat transfer for both non-swirling and swirling jets are also discussed.

Chapter 7 provides a general discussion of the results presented in each chapter and addresses the research questions for the overall project.

Chapter 8 integrates the findings of all chapters and offers suggestions for possible future works.

1.6. Chapter references

1. Stöhr, M., Boxx, I., Carter, C. and Meier, W., *Dynamics of lean blowout of a swirl-stabilized flame in a gas turbine model combustor*, Proceedings of the Combustion Institute, 33(2), p. 2953-2960, 2011.
2. Eldrainy, Y. A., Aly, H. S., Saqr, K. M. and Jaafar, M. N. M., *A multiple inlet swirler for gas turbine combustors*, International Journal of Aerospace and Mechanical Engineering, 5(2), p. 1-4, 2011.
3. Hu, L. Y., Zhou, L. X., Zhang, J. and Shi, M. X., *Studies on strongly swirling flows in the full space of a volute cyclone separator*, AIChE Journal, 51(3), p. 740-749, 2005.
4. Li, H. and Tomita, Y., *Particle velocity and concentration characteristics in a horizontal dilute swirling flow pneumatic conveying*, Powder Technology, 107(1), p. 144-152, 2000.

5. Kurtbas, I., Durmus, A., Eren, H. and Turgut, E., *Effect of propeller type swirl generators on the entropy generation and efficiency of heat exchangers*, International Journal of Thermal Sciences, 46(3), p. 300-307, 2007.
6. Al-Abdeli, Y. M. and Masri, A. R., *Review of laboratory swirl burners and experiments for model validation*, Experimental Thermal and Fluid Science, 69, p. 178-196, 2015.
7. Horbach, T., Schulz, A. and Bauer, H.-J., *Trailing edge film cooling of gas turbine airfoils—external cooling performance of various internal pin fin configurations*, Journal of Turbomachinery, 133(4), p. 041006, 2011.
8. Agrawal, C., Kumar, R., Gupta, A. and Chatterjee, B., *Effect of jet diameter on the maximum surface heat flux during quenching of hot surface*, Nuclear Engineering and Design, 265, p. 727-736, 2013.
9. Zhang, J.-Z., Tan, X.-M., Liu, B. and Zhu, X.-D., *Investigation for convective heat transfer on grinding work-piece surface subjected to an impinging jet*, Applied Thermal Engineering, 51(1), p. 653-661, 2013.
10. Singh, S. and Chander, S., *Heat transfer characteristics of dual flame with outer swirling and inner non-swirling flame impinging on a flat surface*, International Journal of Heat and Mass Transfer, 77, p. 995-1007, 2014.
11. Singh, S. and Chander, S., *Heat transfer characteristics of dual swirling flame impinging on a flat surface*, International Journal of Thermal Sciences, 89, p. 1-12, 2015.
12. Wannassi, M. and Monnoyer, F., *Fluid flow and convective heat transfer of combined swirling and straight impinging jet arrays*, Applied Thermal Engineering, 78, p. 62-73, 2015.
13. Greco, C. S., Ianiro, A. and Cardone, G., *Time and phase average heat transfer in single and twin circular synthetic impinging air jets*, International Journal of Heat and Mass Transfer, 73, p. 776-788, 2014.
14. Luo, D. D., Zhen, H. S., Leung, C. W. and Cheung, C. S., *Premixed flame impingement heat transfer with induced swirl*, International Journal of Heat and Mass Transfer, 53(19), p. 4333-4336, 2010.
15. Ortega-Casanova, J., Campos, N. and Fernandez-Feria, R., *Experimental study on sand bed excavation by impinging swirling jets*, Journal of Hydraulic Research, 49(5), p. 601-610, 2011.
16. Ichimiya, K. and Tsukamoto, K., *Heat transfer from an inflow-type swirling turbulent impinging jet*, JSME International Journal Series B Fluids and Thermal Engineering, 49(4), p. 995-999, 2006.
17. Ianiro, A. and Cardone, G., *Heat transfer rate and uniformity in multichannel swirling impinging jets*, Applied Thermal Engineering, 49(0), p. 89-98, 2011.
18. Ortega-Casanova, J., *CFD and correlations of the heat transfer from a wall at constant temperature to an impinging swirling jet*, International Journal of Heat and Mass Transfer, 55(21–22), p. 5836-5845, 2012.
19. Amini, Y., Mokhtari, M., Haghshenasfard, M. and Gerdroodbary, M. B., *Heat transfer of swirling impinging jets ejected from Nozzles with twisted tapes utilizing CFD technique*, Case Studies in Thermal Engineering, 6, p. 104-115, 2015.
20. De Bonis, M. V. and Ruocco, G., *An experimental study of the local evolution of moist substrates under jet impingement drying*, International Journal of Thermal Sciences, 50(1), p. 81-87, 2011.
21. Moreira, R. G., *Impingement drying of foods using hot air and superheated steam*, Journal of Food Engineering, 49(4), p. 291-295, 2001.

22. Ratanawilai, T., Nuntadusit, C. and Promtong, N., *Drying characteristics of rubberwood by impinging hot-air and microwave heating*, Wood Research, 60(1), p. 59-70, 2015.
23. Ball, C. G., Fellouah, H. and Pollard, A., *The flow field in turbulent round free jets*, Progress in Aerospace Sciences, 50(0), p. 1-26, 2012.
24. Ozmen, Y. and Baydar, E., *Flow structure and heat transfer characteristics of an unconfined impinging air jet at high jet Reynolds numbers*, Heat and Mass Transfer, 44(11), p. 1315-1322, 2008.
25. Chigier, N. A. and Chervinsky, A., *Experimental investigation of swirling vortex motion in jets*, Journal of Applied Mechanics, 34(2), p. 443-451, 1967.
26. Örlü, R. and Alfredsson, P. H., *An experimental study of the near-field mixing characteristics of a swirling jet*, Flow, Turbulence and Combustion, 80(3), p. 323-350, 2008.
27. Oberleithner, K., Sieber, M., Nayeri, C. N., Paschereit, C. O., et al., *Three-dimensional coherent structures in a swirling jet undergoing vortex breakdown: stability analysis and empirical mode construction*, Journal of Fluid Mechanics, 679, p. 383-414, 2011.
28. Rajaratnam, N., Turbulent jets, Elsevier, Amsterdam, The Netherland, 1976.
29. Gupta, A. K., Lilley, D. G. and Syred, N., *Swirl flows*, Tunbridge Wells, Kent, England, Abacus Press, 1984, 488 p., 1, p., 1984.
30. Rajaratnam, N., Zhu, D. Z. and Rai, S. P., *Turbulence measurements in the impinging region of a circular jet*, Canadian Journal of Civil Engineering, 37(5), p. 782-786, 2010.
31. Carlomagno, G. M. and Ianiro, A., *Thermo-fluid-dynamics of submerged jets impinging at short nozzle-to-plate distance: A review*, Experimental Thermal and Fluid Science, 58, p. 15-35, 2014.
32. Nuntadusit, C., Wae-hayee, M., Bunyajitradulya, A. and Eiamsa-ard, S., *Heat transfer enhancement by multiple swirling impinging jets with twisted-tape swirl generators*, International Communications in Heat and Mass Transfer, 39(1), p. 102-107, 2012.
33. Fenot, M., Dorignac, E. and Lalizel, G., *Heat transfer and flow structure of a multichannel impinging jet*, International Journal of Thermal Sciences, 90, p. 323-338, 2015.
34. Cala, C., Fernandes, E., Heitor, M. and Shtork, S., *Coherent structures in unsteady swirling jet flow*, Experiments in Fluids, 40(2), p. 267-276, 2006.
35. Schimek, S., Moeck, J. P. and Paschereit, C. O., *An experimental investigation of the nonlinear response of an atmospheric swirl-stabilized premixed flame*, Journal of Engineering for Gas Turbines and Power, 133(10), p. 101502 (1-7), 2011.
36. Ianiro, A. and Cardone, G., *Measurement of surface temperature and emissivity with stereo dual-wavelength IR thermography*, Journal of Modern Optics, 57(18), p. 1708-1715, 2010.
37. Al-Abdeli, Y. M., Masri, A. R., Marquez, G. R. and Starner, S. H., *Time-varying behaviour of turbulent swirling nonpremixed flames*, Combustion and Flame, 146(1–2), p. 200-214, 2006.
38. Eiamsa-Ard, S., Thianpong, C. and Eiamsa-Ard, P., *Turbulent heat transfer enhancement by counter/co-swirling flow in a tube fitted with twin twisted tapes*, Experimental Thermal and Fluid Science, 34(1), p. 53-62, 2010.
39. Lee, D. H., Won, S. Y., Kim, Y. T. and Chung, Y. S., *Turbulent heat transfer from a flat surface to a swirling round impinging jet*, International Journal of Heat and Mass Transfer, 45(1), p. 223-227, 2002.

40. Al-Abdeli, Y. M. and Masri, A. R., *Stability characteristics and flowfields of turbulent non-premixed swirling flames*, Combustion Theory and Modelling, 7(4), p. 731-766, 2003.
41. Davoust, S., Jacquin, L. and Leclaire, B., *New results on the structure of turbulence in a mixing layer with and without swirl*, International Journal of Heat and Fluid Flow, 49, p. 11-17, 2014.
42. Farokhi, S., Taghavi, R. and Rice, E. J., *Effect of initial swirl distribution on the evolution of a turbulent jet*, AIAA Journal, 27(6), p. 700-706, 1989.
43. Toh, I., Honnery, D. and Soria, J., *Axial plus tangential entry swirling jet*, Experiments in Fluids, 48(2), p. 309-325, 2010.
44. Nozaki, A., Igarashi, Y. and Hishida, K., *Heat transfer mechanism of a swirling impinging jet in a stagnation region*, Heat Transfer—Asian Research, 32(8), p. 663-673, 2003.
45. Al-Abdeli, Y. M. and Masri, A. R., *Recirculation and flowfield regimes of unconfined non-reacting swirling flows*, Experimental Thermal and Fluid Science, 27(5), p. 655-665, 2003.
46. Mi, J. and Nathan, G. J., *Statistical properties of turbulent free jets issuing from nine differently-shaped nozzles*, Flow, Turbulence and Combustion, 84(4), p. 583-606, 2010.
47. McGuinn, A., Farrelly, R., Persoons, T. and Murray, D. B., *Flow regime characterisation of an impinging axisymmetric synthetic jet*, Experimental Thermal and Fluid Science, 47, p. 241-251, 2013.
48. Yao, S., Guo, Y., Jiang, N. and Liu, J., *An experimental study of a turbulent jet impinging on a flat surface*, International Journal of Heat and Mass Transfer, 83, p. 820-832, 2015.
49. Ng, H. C. H., Monty, J. P., Hutchins, N., Chong, M. S., et al., *Comparison of turbulent channel and pipe flows with varying Reynolds number*, Experiments in Fluids, 51(5), p. 1261-1281, 2011.
50. Leclaire, B. and Jacquin, L., *On the generation of swirling jets: high-Reynolds-number rotating flow in a pipe with a final contraction*, Journal of Fluid Mechanics, 692, p. 78-111, 2012.
51. Kim, J. K., *Investigation of the turbulence characteristics in the swirling flow of a gun-type gas burner with two different hot-wire probes*, Journal of Mechanical Science and Technology, 22(1), p. 180-189, 2008.
52. Yang, H. Q., Kim, T., Lu, T. J. and Ichimiya, K., *Flow structure, wall pressure and heat transfer characteristics of impinging annular jet with/without steady swirling*, International Journal of Heat and Mass Transfer, 53(19–20), p. 4092-4100, 2010.
53. Yang, H., Kim, T. and Lu, T., *Characteristics of annular impinging jets with/without swirling flow by short guide vanes*, Science China Technological Sciences, 54(3), p. 749-757, 2011.
54. Wen, M. and Jang, K., *An impingement cooling on a flat surface by using circular jet with longitudinal swirling strips*, International Journal of Heat and Mass Transfer, 46(24), p. 4657-4667, 2003.
55. Thomas, B., Ahmed, Z. U., Al-Abdeli, Y. M. and Matthews, M. T., *The optimisation of a turbulent swirl nozzle using CFD*, in Proceedings of the Australian Combustion Symposium, 6-8 November Perth, Australia, http://www.anz-combustioninstitute.org/local/papers/ACS2013-Conference-Proceedings.pdf, p. 271-274, 2013.

56. Xu, Z. and Hangan, H., *Scale, boundary and inlet condition effects on impinging jets*, Journal of Wind Engineering and Industrial Aerodynamics, 96(12), p. 2383-2402, 2008.
57. Astarita, T. and Carlomagno, G. M., Infrared Thermography for Thermo-fluid-dynamics, Springer-Verlag, Heidelberg, Berlin, 2013.

Chapter 2

2 The Effect of Inflow Conditions on the Development of Non-swirling Versus Swirling Impinging Turbulent Jets[2]

This chapter discusses the effect of upstream inflow conditions on the downstream flow development for non-swirling and swirling, free and impinging jets. Preliminary numerical methodologies and techniques are validated against baseline experimental data sets.

2.1 Introduction

Impinging jets have received significant attention due to their inherent complex nature and ability to affect convective heat transfer in a variety of applications, ranging from glass tempering [1-3] to turbine blade cooling [4, 5], drying or freezing [6, 7] as well as flame-plate interactions [8-10]. Several reviews of turbulent (axisymmetric) non-swirling impinging jets are available in the literature [11-15]. In a typical flow, the jet impinges directly onto a target surface and the flow field is basically categorized by three broad regions as shown in Figure 2.1; the free jet region, the stagnation or impingement region and the wall jet region. The free jet region consists of an inner potential core and an outer shear layer where fluid from the surroundings is entrained. The potential core is commonly considered to end where the centreline velocity is 95 % of the velocity at the nozzle exit [12, 14], and is found to extend over 4-6 nozzle diameters (D) when impingement occurs relatively far from the nozzle [11, 16]. This aspect of impinging jet development appears to agree with the behaviour of (non-impinging) free jets where the potential core typically ends at 2.5 - 8D [17-20]. In the impingement region, jet impact causes deflection of the flow and a rapid decrease in axial velocity with a corresponding rise in static pressure. However, in flow configurations where the impingement plate is in the near-field ($H/D \leq 2$), the transition from potential core to impingement region occurs at around 1.2 - 1.7D [16, 21-24] which indicates that (non-

[2] This chapter has been published as a full research paper:
Ahmed Z. U., Al-Abdeli, Y. M., Matthews, M. T., Computers & Fluids, **118**, p. 255-273, 2015.
Whilst efforts were made to retain original content of the article, minor changes such as number formats, font size and style were implemented in order to maintain consistency in the formatting style of the thesis.

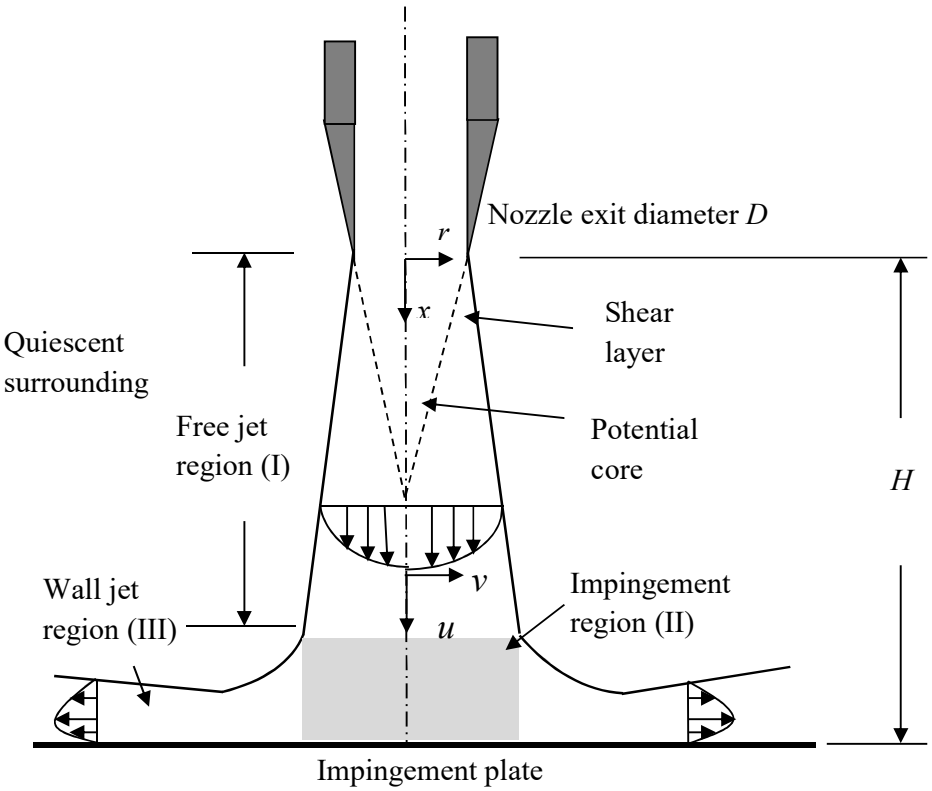

(a)

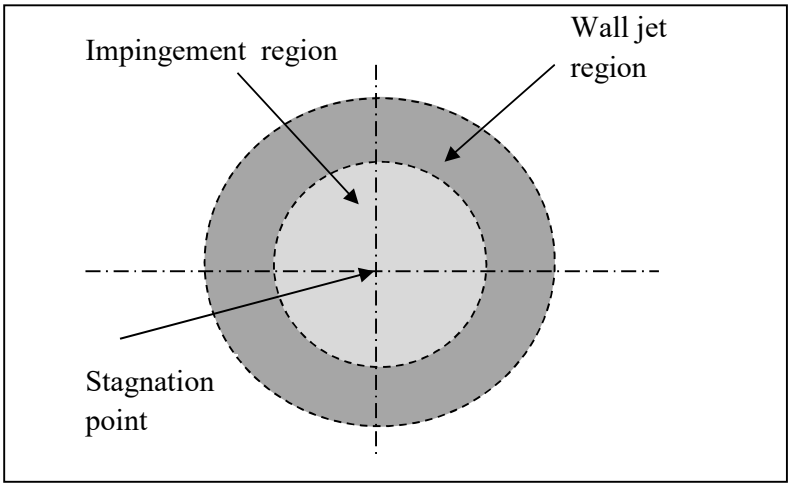

(b)

Figure 2.1 The different regions for (unconfined) axisymmetric jet impingement: (a) side view showing different flow regions; (b) top view on the impingement surface.

swirling) jet development may differ based on the downstream location of impingement. The wall jet region then forms upon axial deceleration of the flow at or near the surface, and the

radial velocity initially rises rapidly (to a maximum near the wall) before falling at larger distances from the wall. The maximum radial velocity in these jets is found to be independent of the Reynolds number and is located at a radial position (r) of approximately $r/D = 1.1$ near the impingement surface. In the wall jet region, the flow also experiences significant entrainment. Many studies [24-27] have focused on the wall jet region, except Tummers et al. [23] who reported detailed measurements of mean flow characteristics and Reynolds stresses in the impingement as well as the wall jet region (up to $r/D = 3.5$). Moreover, no extensive works have been conducted to compare the near-field development between non-swirling and swirling impinging jets. The current study will therefore utilize published data sets to initially validate the numerical models used herein before moving to the analysis of jet impingement on the development and impingement/wall jet regions in both swirling and non-swirling jets.

The imposition of swirl into an impinging jet is expected to affect the development and heat transfer characteristics at the impingement surface, but surprisingly these effects have not been investigated in detail, particularly as impinging jets transition from non-swirling to swirling without the perturbations imposed from geometric swirl generators. Swirl can be imparted in a variety of ways, including the use of vane-type or twisted insert (geometric) generators, or aerodynamically by superimposing a tangential flow onto an axial velocity component without recourse to geometric features. Table 2.1, which summarizes the main attributes of studies conducted on swirling impinging jets over the last decade, clearly shows the predominant use of geometric methods to generate swirl. For jets at relatively short impingement distances ($H/D \leq 2$), the drawback of using geometric inserts is that the "footprints" of these swirl generators manifest themselves at the impingement surface. This makes it difficult to study the fundamental effects of swirl (in an impinging jet), independent of the swirl generation method. The use of geometric, rather than aerodynamic, swirl generation also imposes complexities in relation to the modelling of these flows if intricacies in the form of swirl vanes (or inserts) must also be included. In the context of modelling, the use of aerodynamically induced swirl means avoiding having to account for vane (or insert) induced flow behaviour at the exit plane. Moreover, the literature in this area also appears to indicate some contradictory results as to whether swirl positively [31, 36, 39, 41] or negatively [42, 43] affects heat transfer at the impingement surface, as well as the significance of this impact. This is due to the multitude of geometric generators used.

Table 2.1 Summary of experimental studies into single (turbulent) swirling jets which have been undertaken over the last decade. An asterisk (*) indicates a jet medium other than air.

STUDY	REYNOLDS NUMBER (*Re*)	SWIRL GENERATION METHOD	PARAMETERS INVESTIGATED
Abrantes and Azevedo [28]	21,000	Aerodynamic	$\|V\|$, u_i', *k*, *Nu* *x/D* = 0.25, 2 *S* = 0, 0.5
Alekseenko et al. [29]	8,900	Geometric	$\|V\|$, $<u_i>$, $\overline{u_i'u_i'}$, $\overline{u_i'u'j}$ *x/D* = 3 *S*= 0-1
Bilen et al. [30]	10,000 - 40,000	Geometric	*Nu* *x/D*= 6-14 *S* = 0-0.89
Brown et el. [31]	8,000 - 20,000	Geometric	*Nu* *X/D*= 0.5-10 *S*= 0,0.22, 0.67
Ianiro and Cardone [32]	28,000	Geometric	*Nu* *x/D*= 2-10 *S*= 0-0.8
Kinsella et al.[33]	10,000 - 30,000	Geometric	*Nu* *x/D*= 0.5-6 *S* = NA
Lee et al. [34]	23,000	Geometric	*Nu* *x/D*= 2-10 *S*= 0-0.77
*Nozaki et al. [35]	4,000	Geometric	$<u_c>$, $r^{1/2}$, $<u_i>$, u_i', *Nu* *x/D*= 2 *S*= 0-0.43
Nuntadusit et al.[36]	20,000	Geometric	$<u_i>$, *Nu* *x/D*= 2-10 *S*= 0.4-0.94
*Ortega-Casanova et al. [37]	7,000 - 20,000	Geometric	$<u_i>$ *x/D* = 5, 10, 30 *S* = NA
Senda et al. [38]	8,100	Geometric	$<u_i>$, u_i', *Nu* *x/D*= 0-6 *S*= 0-0.45
Wen and Jang [39]	500 - 27,000	Geometric	*Nu* *x/D*= 3-16 *S* = NA
*Yuan et al. [40]	7,500 - 28,300	Geometric	*Nu* *x/D* = 3 *S* = NA

PARAMETER KEYS:

$|V|$: Time-mean velocity magnitude; $<u_i>$: Time-mean velocity; $<u_c>$: Time-mean centreline axial velocity; u_i': Turbulent velocity fluctuations; $\overline{u_i'u_i'}$: Turbulent normal stress; $\overline{u_i'u'_j}$: Turbulent shear stress; *k* : Turbulent kinetic energy; *Nu* : Nusselt number; *S* : Swirl number; NA : Not Available

Moreover, if long streamwise inserts are used in a nozzle to impart swirl [29, 30, 32, 34, 38, 39], the single impinging jet is converted into a multi-channel jet before impinging on the surface which also raises the question as to whether jet-jet (fluid) interactions augment the effects of swirl [30, 32, 36]. Interestingly, the flow and heat transfer characteristics of these types of impinging jets (even with no swirl) show drastically different results than those of conventional (no insert) impinging jets [33, 34, 36, 38]. These fundamental shortcomings in many earlier (swirling) impinging jet studies are, however, not observed with aerodynamically imparted swirl. For the reasons mentioned above, aerodynamic swirl generation better facilitates a fundamental understanding of swirling impinging jet behaviour.

The present research is part of a larger program that will utilize a specially developed nozzle [44] to generate swirl aerodynamically and study the specific effects of swirl without the perturbation associated with geometric swirl generation. Specifically, this chapter highlights the effects of both inflow conditions (at the nozzle exit plane) and modelling methodologies on the analysis of swirling impinging jet development, when compared to their non-swirling impinging counterparts.

With regard to impinging jets incorporating aerodynamically imparted swirl, Ward and Mahmood [42] investigated the heat transfer coefficients using a heat/mass transfer analogy. Abrantes et al. [28] tested swirling impinging jets at small H/D for Re = 21,000 and a swirl number of S = 0.5 and reported a higher heat transfer distribution for all radial positions at the impingement plate as compared to non-swirling jets, but did not analyse the effects of important flow field parameters such as jet axial decay and spread, or varying swirl number. Whilst Ichimiya and Tsukamoto [45] also studied a swirling impinging jet with aerodynamically generated swirl at Re = 11,500, the swirl intensity was simplistically characterized by the angle of tangential flow entry in their setup which makes it difficult to relate their outcomes in the context of the wider body of swirl research. By reviewing most of the literature published to date, it is evident that prior research into swirling impinging jets (either aerodynamically or geometrically generated) focussed on studying the effects of swirl intensity on heat transfer, with little attention to the effects of upstream (inflow) conditions on jet development, which may explain why different studies have reported varied outcomes on the relationship between surface heat transfer and the introduction of swirl [31, 34, 36, 41-43].

Whilst the use of numerical tools can help greatly advance our understanding of turbulent impinging jets and the factors which affect heat transfer at the impingement surface, these

methods can be challenging to apply due to the three distinct flow regions, the rapid pressure gradients that arise as the jet approaches the impingement surface, and the anisotropic nature of the turbulent structures near the surface. The unavailability of highly resolved flow field data (for benchmarking) as well as clearly defined boundary conditions is another complicating issue. In fact, one of the fundamental difficulties associated with modelling impinging jets stems from the need to describe how the turbulent regions of a decelerating jet interacts with the wall, especially within the wall boundary layer [46]. The inclusion of swirl behaviour into the jet exacerbates the complexities of modelling such turbulent flow fields and increases the need for well resolved inflow conditions. Although the effects of inlet profiles and varied inlet geometry on impinging jet development has been reported by several researchers, both experimentally [27, 47-52] and numerically [53, 54], unlike the present research, these relate only to non-swirling impingement. The diverse range of results reported show that for both the near- and far-field, the time-mean flow field behaviour, turbulence structures and heat transfer coefficients are strongly dependent upon the inflow conditions. The effects of inflow conditions on swirling jets have, however, mostly been investigated for (non-impinging) free jets [55, 56], and very little work has been done to resolve the effects of the conditions at the nozzle exit plane on impinging jet development, heat transfer and pressure distribution at the impingement surface and turbulence characteristics. It is hypothesized that such effects may appear stronger as jets transition from non-swirling to swirling (impinging) jets due to the presence of more adverse streamwise pressure gradients and turbulence levels. Such issues warrant further investigation, particularly as they influence the heat transfer between the jet and the surface [57, 58] and constitute part of the primary motivation for conducting the current numerical study.

There are several turbulence modelling techniques, such as RANS, LES and DNS available for computations of turbulent flows and an up-to-date detail of these techniques are accessible via recent reviews and books [59-63]. Table 2.2 summarises those which have been applied to impinging jets, both non-swirling and swirling. With regard to non-swirling free and impinging jets (with no surface heat transfer interactions involved), Balabel and El-Askary [75] recently applied different k-ε based turbulence models, both linear (standard, v^2-f) and nonlinear (cubic). However, since nonlinear model are highly sensitive to the particulars of the flow analysed, their results cannot be generalized, which warrants further investigation into the effects of different models on the accuracy of modelling swirling impinging flows. Jaramillo et al. [69] also numerically investigated the performance

Table 2.2 Summary of numerical investigations into single non-swirling and swirling (turbulent) impinging jets. An asterisk (*) indicates the jet medium other than air.

STUDY	REYNOLDS NUMBER (*Re*)	TURBULENCE MODELLING	PARAMETERS INVESTIGATED
Angioletti et al. [64]	1,000 - 4, 000	RNG *k*-ε, SST *k*-ω, RSM	|*V*|, *Nu* *x/D* = 4.5 *S* = 0
Behnia et al. [65]	23,000 - 70, 000	STD *k*-ε, v^2-*f*	|*V*|, *Nu*, *k* *x/D* = 2, 6 *S* = 0
Craft et al.[66]	23,000 & 70,000	Low-*Re* *k*-ε, RSM, and two SMC models	|*V*|, u_i', $\overline{u_i'u_j'}$, *k*, *Nu* *x/D* = 2, 6 *S* = 0
Dianat et al. [67]	23,000	STD *k*-ε, RSM	|*V*|, u_i', $\overline{u_i'u_j'}$ *x/D* = 2, 8, 12 *S* = 0
Isman et al. [68]	4,000 - 12,000	STD *k*-ε, RNG *k*-ε, two other nonlinear models	|*V*|, *Nu* *x/D* = 4-10 *S* = 0
Jaramillo et al. [69]	23,000 & 70,0000	Different *k*-ε, *k*-ω models	|*V*|, *Nu* *x/D* = 2, 6 *S* = 0
Merci and Dick [70]	23,000	Low-*Re* *k*-ε, Low-*Re* nonlinear *k*-ε	|*V*|, $\overline{u_i'u_j'}$, *k*, *Nu* *x/D* = 2, 6 *S* = 0
*Ortega-Casanova [71]	7,000 - 18,000	SST *k*-ω	*Nu* *x/D* = 5, 10, 30 *S* = 0.15-0.43
Pulat et al. [72]	4,000 - 12,000	Different *k*-ε and *k*-ω models	*Nu* *x/D* = 6
Ramezanpour [73]	4,000 - 16,000	RNG *k*-ε, RSM	Streamlines, *Nu* *x/D* = 4-10 *S* = 0
Sagot et al. [74]	23,000	Realizable *k*-ε, RNG *k*-ε, STD *k*-ω, SST *k*-ω	*Nu* *x/D* = 2 *S* = 0

PARAMETER KEYS: As shown in Table 2.1

and accuracy of different RANS-based models (explicit algebraic stress models, both linear and non-linear eddy-viscosity models jointly with *k*-ε and *k*-ω platforms) and observed that each model was only able to accurately capture a particular region of the flow field. Similarly, other studies that have considered numerical modelling of non-swirling impinging jets, but with the inclusion of convection heat transfer (e.g. heated jet or surface), also show a lack of generality when comparing the accuracy of different models. In fact, models with

good performance in the round jet case show poor results in the plane jet configuration, which re-emphasizes the sensitivity of models to the particulars of the flow. In this regard, Craft et al. [66] and Dianat et al. [67] studied the performance of different versions of k-ε and Reynolds Stress Model (RSM). In both studies, the RSM is found to be superior among the models considered when predicting the time-mean and time-resolved fluctuating quantities at the stagnation and wall jet regions [66, 67]. Behnia et al. [65, 76] compared the v^2-f model with the standard k-ε model at several H/D (for Re = 23,000, 50,000 and 70,000) and found the v^2-f model to be in good agreement with experiments except in the region close to the wall (0.1-0.5D), where only qualitative behaviour was predicted. Isman et al. [68] on the other hand concluded that the standard k-ε and RNG (Re-Normalization Group) k-ε models, among others including two nonlinear algebraic stress models, agreed well with experiments at both the stagnation and wall jet region but these studies were only again done for non-swirling impinging jets. Qualitative and quantitative comparisons between the computed flow behaviour and that resolved through experiments (e.g. Particle Image Velocimetry - PIV and mass transfer measurements) was also conducted by Angioletti et al. [64] for transitional regime (initially laminar or low turbulence jets). They concluded that although good predictions were achieved by looking at the velocity field using the RNG k-ε and RSM turbulence models for non-swirling impinging jets, all models including k-ω, SST (Shear Stress Transport) and RSM were largely inadequate when evaluating heat exchange at the impingement plate located at H/D = 4.5. Merci and Dick [70], however, showed that a low-Re nonlinear k-ε model is able to better predict the flow field and heat transfer in non-swirling impinging jets compared to a standard k-ε model, but that results derived only qualitatively agree with the v^2-f model. Recently, Sagot et al. [74] considered two k-ε and two k-ω models for non-swirling impinging jet heat transfer and found that SST k-ω agrees well with their experimental data, in agreement with [77]. Although the standard k-ε model has been found to be inaccurate in the past in predicting stagnation region heat transfer, interestingly, a recent work [72] reported significant improvement with standard k-ε models if combined with a two-layer model of enhanced wall treatment. In summary, even though very little work has been done on characterising the effects of different modelling approaches when applied to swirling impinging jets, the diversity of works already done on other flow configurations also makes it hard to anticipate the sensitivity of specific models when applied to turbulent impinging jets. This variation in numerical results is also likely due to the different inflow conditions used across earlier studies (see Table 2.1 and Table 2.2) as well as the inherent

complexities of impinging jets when compared to free jets, particularly with the imposition of swirl.

Although a significant number of numerical studies into non-swirling impinging jets are available and have been summarised above, studies into turbulent swirling impinging jets are relatively scarce, with the few exceptions [71]. In addition, very little work has been conducted into the fundamental development of turbulent jets as they transition from free to impinging, and thereafter from non-swirling to swirling (for the same inflow, impingement conditions and nozzle geometry). With the effects of upstream inflow conditions potentially affecting even free jet development [50, 78-80], there is merit in the current study which looks at the same nozzle geometry at impinging swirl jet transitions and inflow conditions. Of the few comparative experimental studies undertaken between free and impinging (non-swirling) jets, those in axisymmetric configurations by Donaldson and co-workers [81, 82], Popiel and Trass [83] and Looney and Walsh [84] are, however, derived at varied conditions, which makes it difficult to draw summative observations on the fundamental effects of impingement and swirl on jet development. Contributing to this challenging task is the variety of inlet and boundary conditions employed [84-86], many of which are also not completely reported to facilitate modelling or be subject to secondary flow influences, such as recirculation arising from the unique characteristics of the particular apparatus used [81].

By addressing the above noted shortcomings, this chapter attempts to bridge the gap in our fundamental understanding of the transition from non-swirling to swirling (S = 0 - 0.3) impinging jets (at H/D = 2). The study also includes the effect of transition from non-swirling free-to-impinging jets, tangential velocity profiles and turbulence variations at the nozzle exit plane on downstream jet development. This research uses computations based on different RANS turbulence models, which are first tested against experimental data sets derived from the literature. These conditions are selected so as to avoid the perturbation induced to the flow by a stagnant recirculating (vortex breakdown) bubble and the additional effects, on jet spread, which would likely occur at greater swirl numbers or delayed jet impingement ($H/D \geq$ 2).

2.2 Methodology

Figure 2.2 depicts an overall representation of the methodologies used for the validation and testing of the numerical models considered. The RANS approach is implemented with six turbulence models (three k-ε, two k-ω and RSM with linear pressure-strain model), where

time-mean and turbulent flow quantities are solved using the commercial software package ANSYS Fluent (version 14.5). Discussion of grid-density testing, checks for flow asymmetry, upstream boundary or periodic boundary are presented in the ensuing sections. The pressure-based coupled algorithm is used to simultaneously solve the coupled system of continuity and

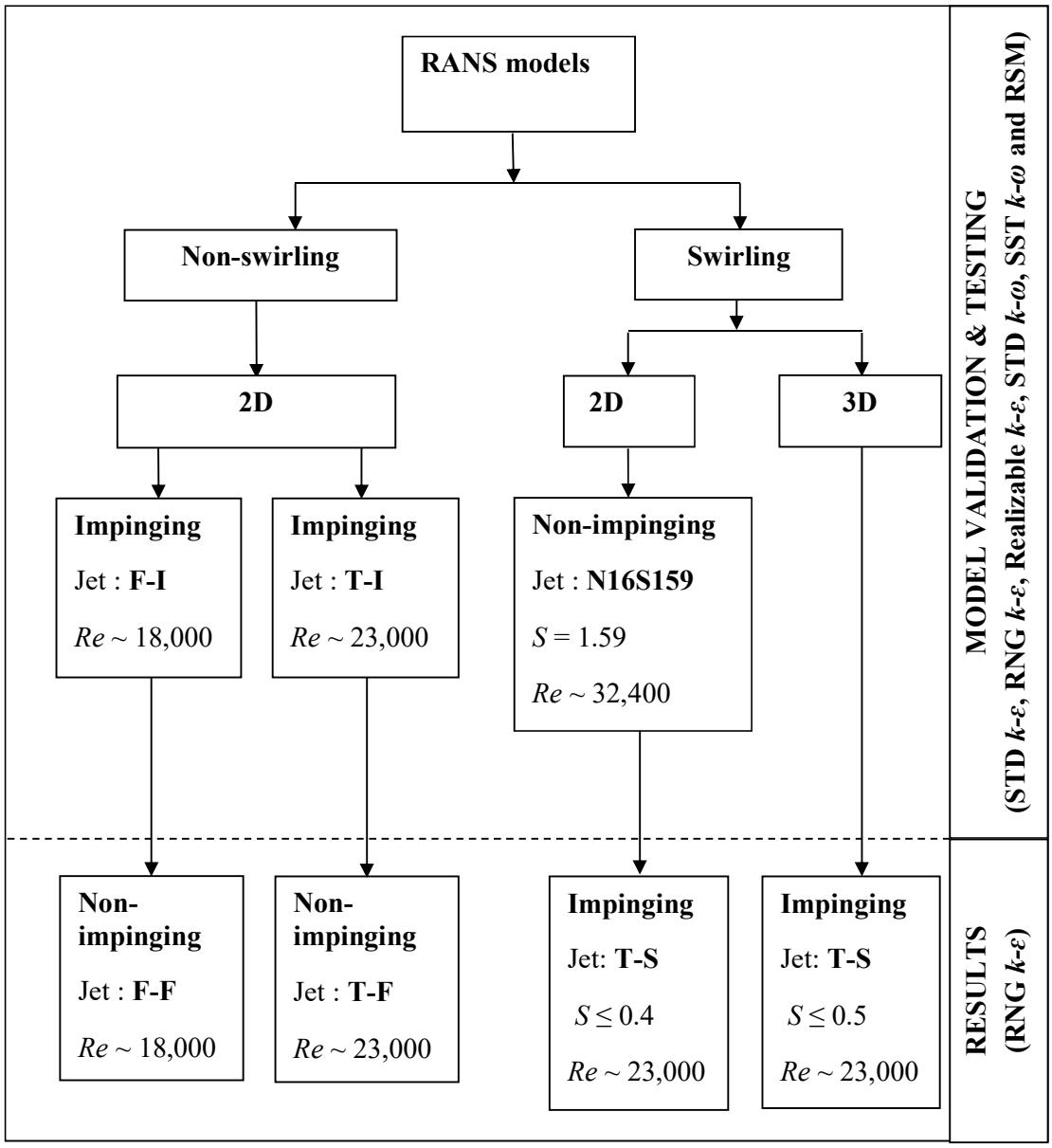

Figure 2.2 The methodology used to develop the models using both 2D (axisymmetric) and 3D computations, validated against benchmark data from the literature: T-I [23], F-I [24] and N16S159 [100, 101].

momentum equations, whereas turbulence quantities are solved separately in a segregated manner; an approach which significantly improves the rate of convergence when compared to a segregated algorithm [87] whereby all variables are solved separately. The PRESTO (PREssure STaggering Option) is applied for the pressure discretization as it is suitable for steep pressure gradients [73] such as those in impinging jets, and the second-order upwind discretization scheme is used for the momentum, turbulent kinetic energy and dissipation equations. Reynolds stress equations (in RSM) are discretised by the second-order upwind scheme. The converged solution is assumed to be achieved when the residuals of the flow parameters are less than 10^{-6}. Before being used to predict the behaviour of turbulent swirling impinging jets, the turbulence models are first tested against baseline (experimental) data sets. This is done for two non-swirling (impinging) jets and a third swirling (non-impinging) jet with the aim of ascertaining the better performing amongst the models in capturing different flow behaviour. Details of the methodology and boundary conditions used for each case tested, using two-dimensional and three-dimensional domains, are described below.

2.2.1 Baseline non-swirling impinging jets: T-I and F-I

Two impinging jets with the same nozzle-to-plate distance T-I [23] and F-I [24] are first considered. The suffix (I) in the naming terminology is used to denote an "impinging" jet. Both flows essentially comprise non-swirling axisymmetric turbulent jets with impingement surfaces located at H/D = 2. Figure 2.3 presents the experimental (inlet profile) data for T-I and F-I, where T-I appears to follow $U_{in}/U_b = 1.23(1-r/R)^{1/5}$. The equivalent "free" jets to these, designated with the suffix (F) are T-F and F-F, employ the same jet diameter (D), bulk flow velocity at the exit plane (U_b) and Reynolds number (Re), but without an impingement plate at H/D = 2. This methodology not only validates the CFD models against highly resolved impinging jet data, but is also extended to establish a comparison of the development in impinging and free jets, both of which are initially non-swirling. Table 2.3 shows the main parameters for these computations.

Preliminary steady-state model testing is done with both 2D-axisymmetric and 3D simulations. In addition to the 2D-axisymmetric simulation against T-I [23], further checks were also done on this test case to see the effect of using 3D simulation on the computed flow. The 3D simulations would also resolve whether any asymmetry evolves when swirl is added or axisymmetry is retained and can be solved with 2D models. To reduce the computational time for the 3D simulations, only part of the flow domain is considered. Figure

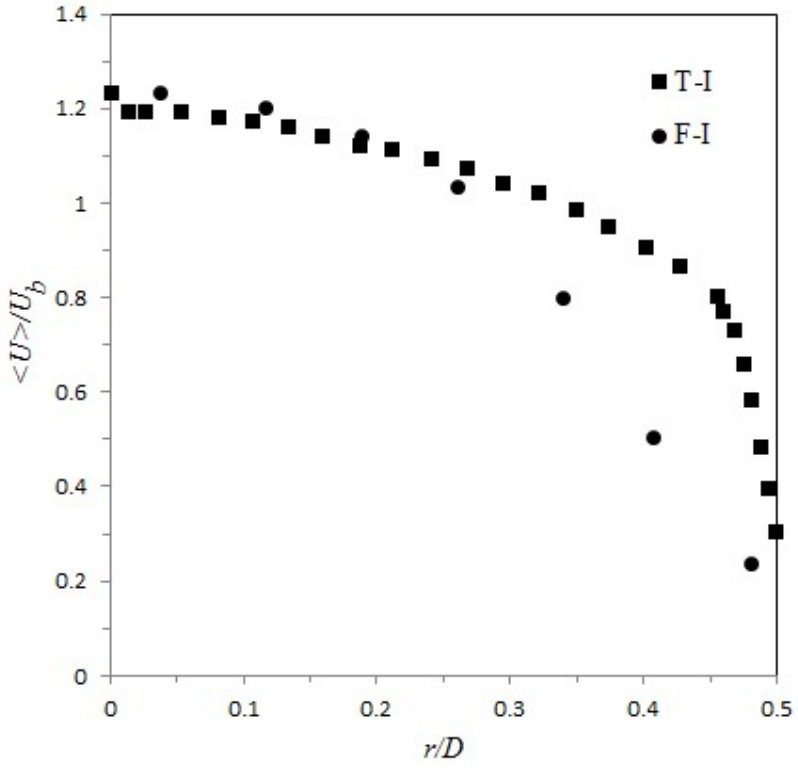

Figure 2.3 Nozzle exit velocity profiles of the benchmark experimental data sets T-I [23] and F-I [24] at $x/D \approx 0.20$ which are used as velocity inlet condition in both 2D and 3D modelling.

Table 2.3 Flow parameters of the baseline jets T-I [23] and F-I [24] and mesh elements used in the computations. Both impinging jets have the same nozzle-to-plate distance ($H/D = 2$).

JET (IMPINGING)	SWIRL NUMBER	D (mm)	U_b (m/s)	Re	MESH CELLS	y^+	VELOCITY INLET AT X= 0	TURBULENT INTENSITY AT INLET
T - I	0	37	9.6	23,000	66,644	0.89	$U_{in}/U_m = (1-r/R)^{1/5}$	2 %
F - I	0	13.3	20	18,000	56,761	1.15	EXPERIMENTAL DATA	5%

PARAMETER KEYS: $U_m = 1.23\,U_b$.

2.4a shows the three-dimensional domain and its boundary conditions. Near to the impingement surface, prismatic cells are used with 15 layers close to the impingement surface and boundary layer growth is set at 1.15 (first mesh layer height is 0.01 mm). Tests

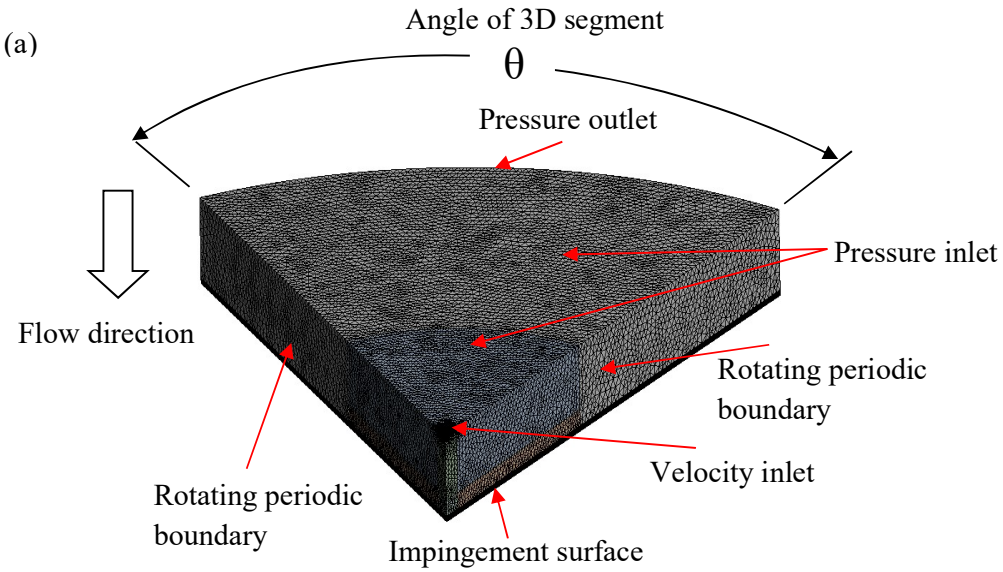

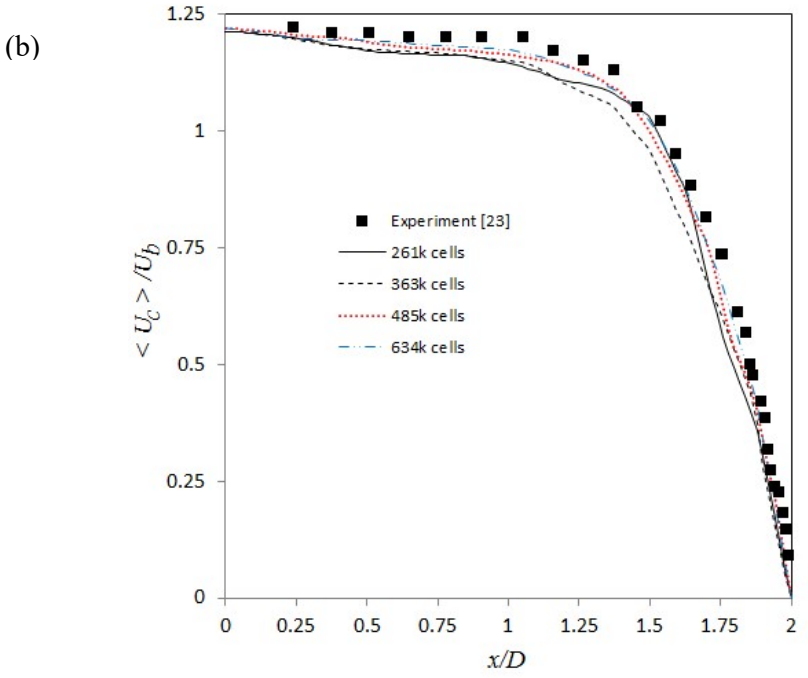

Figure 2.4 (a) Three-dimensional computational domain with mesh and imposed boundary conditions, and (b) Grid independence test with experimental data [23]. A symmetry boundary replaces the rotating periodic boundary in Figure 2.4a for non-swirling flows.

for grid independency are shown in Figure 2.4b and an error of less than 2% for the centerline axial decay of the T-I jet is achieved when using 485, 000 and 634, 000 cells. A mesh with 485,000 cells is chosen for the domain. Another check is also done for the sensitivity of the 3D domain to the size of the flow domain and implemented by comparing results derived using different spatial segments. Figure 2.5 shows the results for a 3D domain spanning one-sixth, one-quarter and one-third of the total domain at a swirl number of $S = 0.5$ (S is defined in section 2.2.2) for comparable mesh densities. Similar computations were also derived for other axial locations (not reported here). These results confirm that no appreciable asymmetry

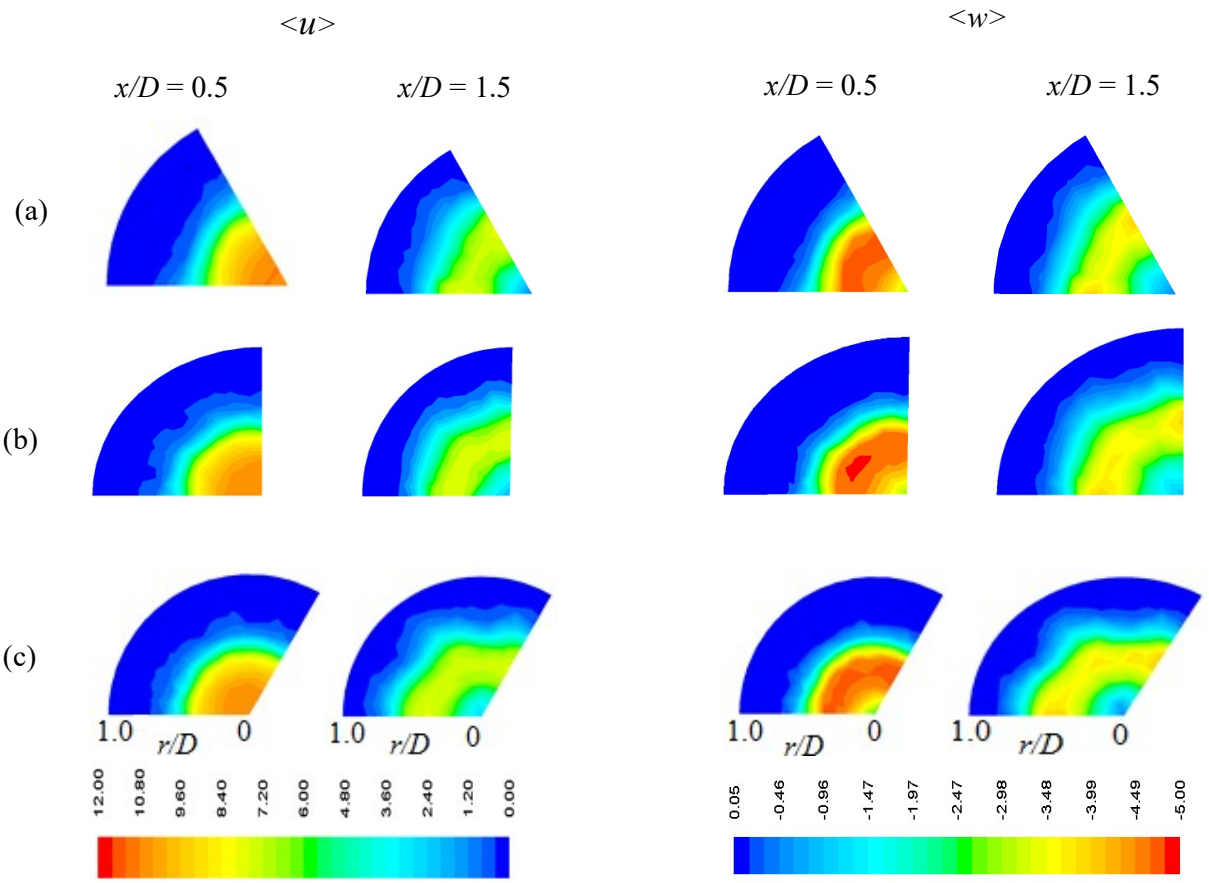

Figure 2.5 Testing the sensitivity of the computed flow behaviours to the size of 3D spatial segment at $S = 0.5$ and $Re = 23, 000$: Left: filled contours of mean axial velocity, and Right: filled contours of mean tangential velocity: (a) one-sixth of full domain ($\theta = 60^0$), (b) one-quarter ($\theta = 90^0$) and (c) one-third ($\theta = 120^0$).

is observed in the 3D simulations. More quantitative comparison between the 2D and 3D domains is also given in the Results and Discussion section, for both swirling and non-swirling impinging jets. Further increases in the 2D spatial domain in the radial direction beyond 10*D* do not lead to noticeable changes in the velocity field. So, the size of the computational domain used is considered adequate. To sufficiently resolve the high velocity gradients, a fine mesh is used at the nozzle exit and an even finer mesh near the impingement surface, whilst grid intensity becomes coarser as the radial distance increases and near the entrainment boundary (top boundary in Figure 2.6). After performing grid independence tests, the number of mesh cells in Table 2.3 is selected to simulate the impinging jets for all two-equation models, but a refined mesh of 176,400 cells is used in RSM as coarser meshes lead to difficulty in attaining a smoother convergence of the residuals.

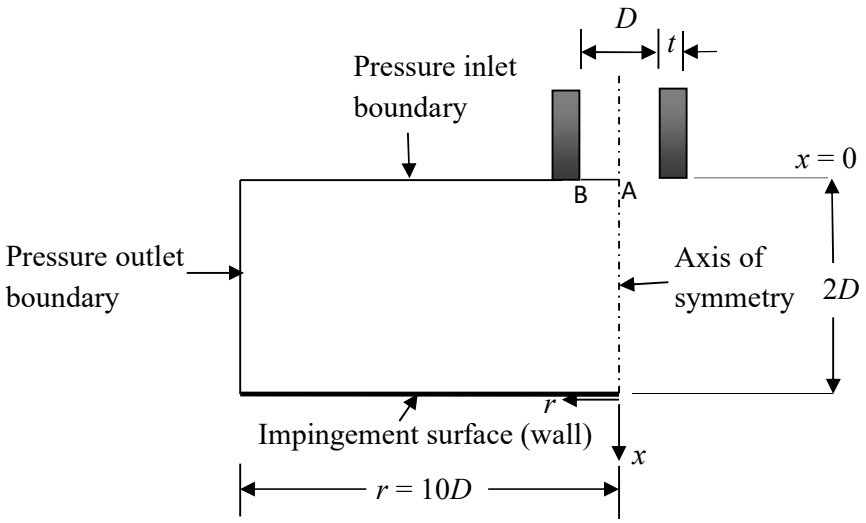

Figure 2.6 Computational domain of all impinging jets investigated (S = 0 - 0.3) and the corresponding boundary conditions for the 2D modelling (jets T-I and F-I).

Figure 2.6 shows the five different types of boundary conditions used to model impinging jets T-I and F-I, namely**:** a velocity inlet at the nozzle exit (i.e. x/D = 0), pressure inlet, pressure outlet, wall and axis of symmetry. Velocity inlet conditions are shown in Table 2.3 with other flow and simulation parameters. Turbulence intensities as well as Reynolds stresses (in RSM) are imposed at the nozzle exit (x/D = 0) based on the corresponding experimental data at about x/D = 0.20. For the pressure inlet, an atmospheric pressure with

zero turbulent kinetic energy and dissipation rate is assumed, whereas for the pressure outlet, atmospheric pressure with turbulence specified by 5% intensity and hydraulic diameter equal to the nozzle exit diameter are applied. Finally, no-slip and axial symmetry conditions at the (impingement) wall and geometric axis are used, respectively.

In turbulent flows, steep gradients close to the wall prohibit resolving flow variables all the way to the solid boundary without using dedicated wall models. In fact, the solution of the mean and turbulent quantities is somewhat dependent on the type of near-wall boundary layer treatment and is more significant in the modelling of impinging jets. Swirl also causes a strong deviation of the velocity profile from the logarithmic law near the wall region which invalidates the standard wall functions for the treatment of the wall boundary condition [88]. For this reason, tests are conducted with different wall functions (standard [89], scalable [87] and non-equilibrium [90]) and Enhanced Wall Treatment (EWT) [91, 92], an improved y^+ insensitive near-wall model, to determine the best near-wall boundary layer treatment that accurately predicts the near wall characteristics of the T-I jet (results not shown here for brevity). In these tests, y^+ (a non-dimensional variable that is proportional to the thickness of the viscous sublayer at the wall) values are chosen appropriately in accordance with the requirement of above near-wall models. It was found that EWT outperforms other wall functions when predicting axial decay and wall shear stress, so EWT is used in the subsequent simulations. In this case, the turbulent viscosity (μ_t), turbulent dissipation (ε) in the near wall cells are specified as proposed by Jongen [92],

$$\phi_{,EWT} = \lambda_\varepsilon \phi + \left(1-\lambda_\varepsilon\right)\phi_{,2l}, \tag{2.1}$$

where ϕ will be replaced by μ_t or ε, and $\phi_{,2l}$ indicates the turbulent quantities in the viscosity-affected near wall region determined by the one-equation model of Wolfstein [93] and Chen and Patel [94]. λ_ε is the blending function which is used to ensure smooth transition between the viscosity-affected (inner) and turbulent (outer) regions (λ_ε = 1 away from walls and λ_ε = 0 in the vicinity of the walls).

Because the height of the first mesh layer plays an important role in resolving the wall characteristics and describing the wall y^+ values, testing was also conducted using different first mesh cell heights. Figure 2.7 shows the shear stress distribution along the wall for different first mesh cell heights and indicates that a height of 0.01 mm results in the best prediction of wall shear stress giving y^+ values around unity in both jet cases T-I and F-I.

These results show qualitatively good agreement with the experiment[3] up to *r/D* = 4. However, a relatively strong deviation is observed around *r/D* = 1.5. Later results (Figure 2.16a) will show increased turbulent kinetic energy at the wall centred at around *r/D*~1.6 which supports the presence of large-scale turbulence in this vicinity. A likely cause for this would be the transition of the flow from stagnation to wall jet region (Figure 2.1). As such, the ineffectiveness of the steady-state RANS models in capturing large-scale structure dynamics (close to the wall and away from the stagnation point) may explain the aforementioned deviation observed in Figure 2.7 near *r/D* = 1.5 [95]. Additionally, the challenges of experimentally resolving flow parameters near a wall (order of 0.1 mm or less) [23, 95], the larger turbulence predicted, and the stronger velocity gradients in this transitional zone may also partly contribute to the discrepancy.

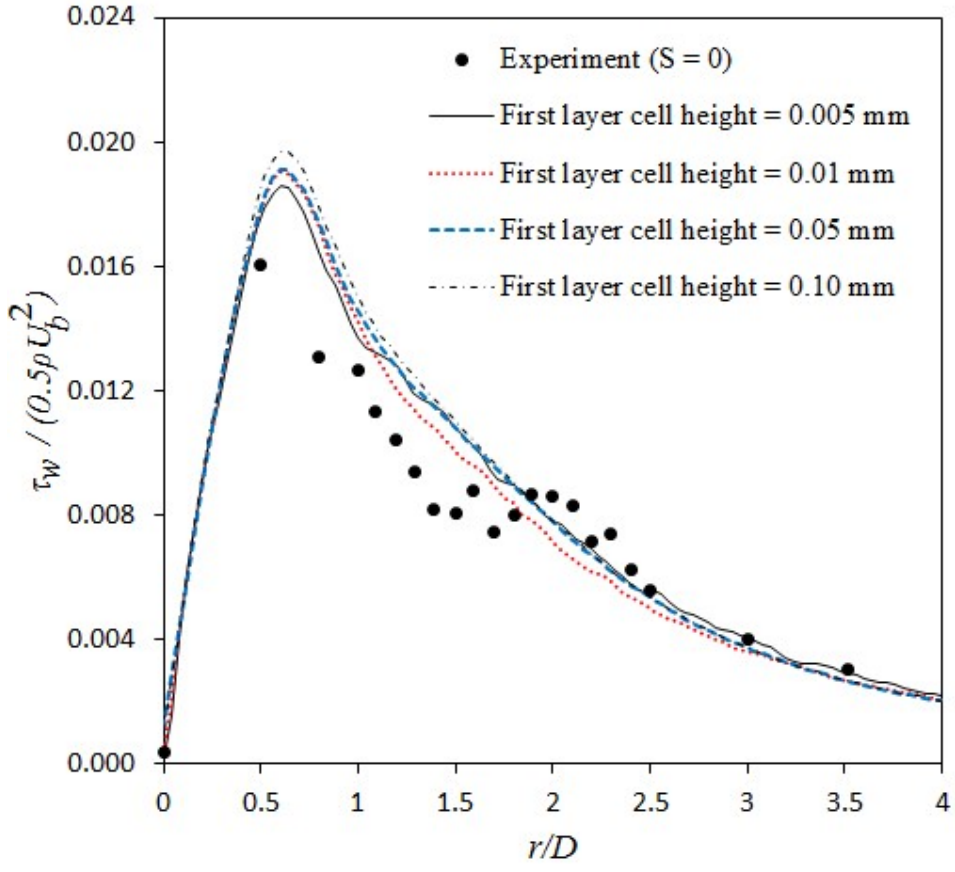

Figure 2.7 A comparison of the normalised wall shear stress profile ($\tau_w / 0.5\rho U_b^2$)[4] between experimental data and numerical simulations of non-swirling ($S = 0$) impinging jet T-I [23].

[3] Experimental data of Tummers et al. [23] had been measured by high-resolution LDA. Wall shear stress was calculated from mean radial velocity components.

[4] In the published version of this chapter, normalisation of wall shear stresses was done by ρU_b^2.

Figure 2.8 presents the numerical predictions of the normalised time-mean axial < u > and radial < v > velocities at three different axial locations using six turbulent models (standard k-ε, RNG k-ε, realizable k-ε, standard k-ω, SST k-ω and the RSM) which are all compared with the experimental data for case T-I [23]. In general, all the models qualitatively and quantitatively agree with the experimental data except the standard and realizable k-ε models, which deviate closer to the impingement surface when predicting the mean radial velocities at

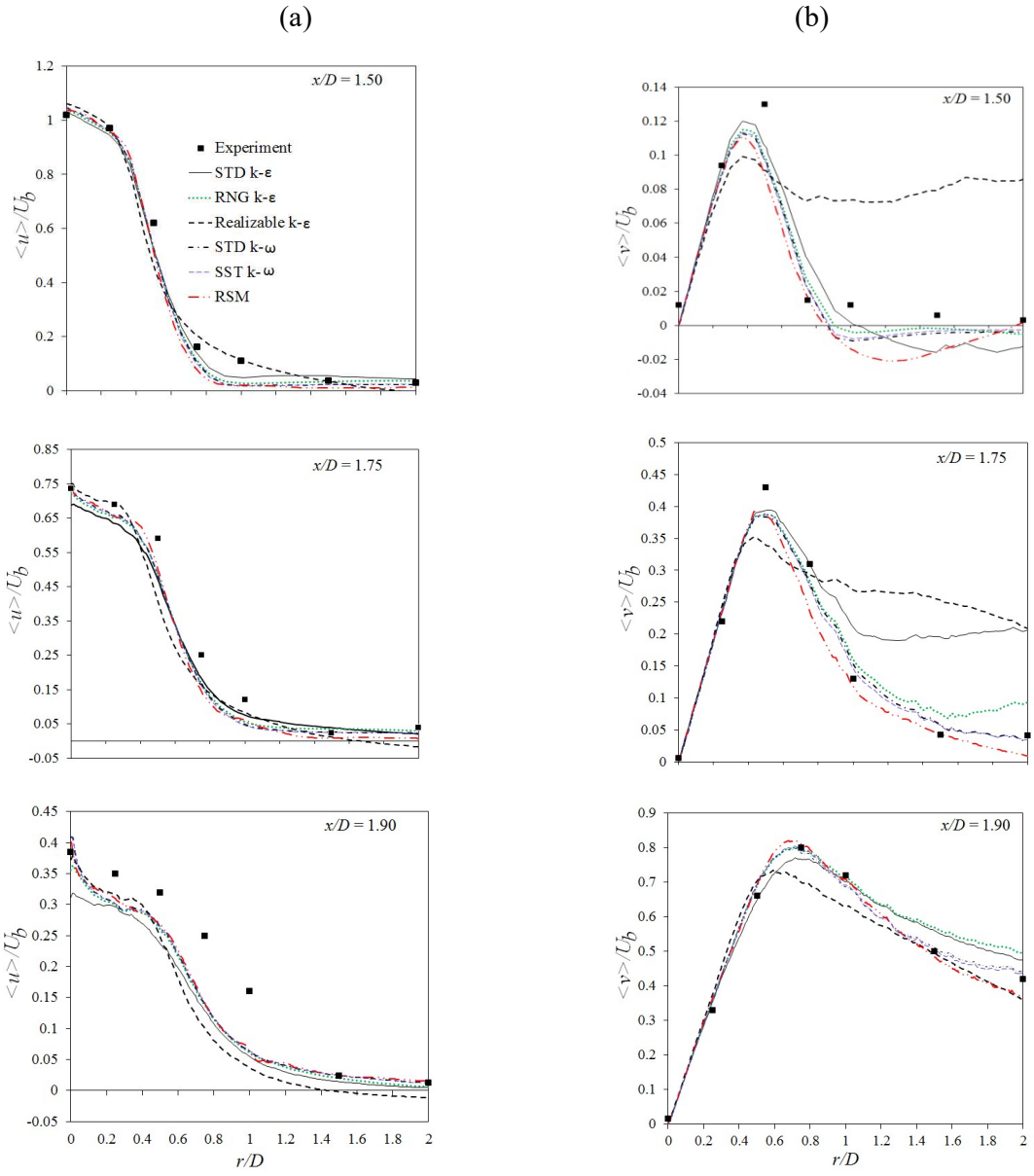

Figure 2.8 Comparison of time-mean flow characteristics for a non-swirling (S = 0) impinging jet experiment T-I [23] using different turbulence models: (a) axial velocity profile, (b) radial velocity profile.

x/D = 1.50 and 1.75. Some quantitative discrepancy is, however, observed in the axial velocity profile (Figure 2.8a) close to the impingement surface (x/D = 1.90). This is believed to be due to the anisotropy associated with the sharp streamline curvatures and increased turbulence nearer to the impingement surface. In addition, some variation in the upstream free jet characteristics, in either the experimental data points derived from the original works or the turbulence properties assumed in the computations, may lead to some discrepancy in the downstream development of the flow. It should be noted that a small amount of negative radial velocity component is predicted at x/D = 1.50 in most of the models, which is in agreement with some recent experimental studies [20, 23-25, 27]. These may arise from the appearance of a small recirculation region outside the boundary layer due to the re-entrainment of the surrounding fluid to the shear layer. Additionally, Figure 2.9 shows a comparison between the models for the turbulent stresses against the experimental data set [23]. It appears from Figures 2.8 and 2.9 that the RNG k-ε model shows superiority as compared to SST k-ω and Reynolds stress models when resolving both the time-mean and turbulence flow characteristics near the impingement region. The standard k-ε model indicates spurious normal and shear stresses near the plate within the impingement region. At r/D = 0.25, all models fail to capture both the normal and shear stresses which may be due to potential differences between the assumed turbulent intensities at the nozzle exit plane x/D = 0. In this regard, whilst the experimental data for turbulence intensity is not uniform over the nozzle radius and peaks nearer to the nozzle wall (as typically found in pipe flows), the computations impose a uniform turbulence intensity (2%) for simplicity over the whole nozzle radius.

In swirling impinging jets, the accurate prediction of time-mean and turbulence characteristics is a challenge because of the inherent complexity of these flows and the anisotropic nature of turbulence in these flows. As mentioned above, existing literature on swirling flows mainly investigates free (non-impinging) jets where LES, RNG k-ε, SST k-ω and Reynolds stress models show varied agreement with experimental data depending on the level of swirl. Outside the scope of LES, RSM has generally been applied in strong swirling (non-impinging) flows [96-98]. However, RSM is also found to be incapable of resolving all the deficiencies of the two-equation models for simulating relatively weak ($S \leq 0.5$) turbulent swirling flows [99-101]. For example, Tsai et al. [100] found that RSM yields a relatively

slower development of axial and swirl velocities compared to a *k-ε* model. RNG *k-ε* model also shows reasonable accuracy in both time-mean and turbulent characteristics at low-to-

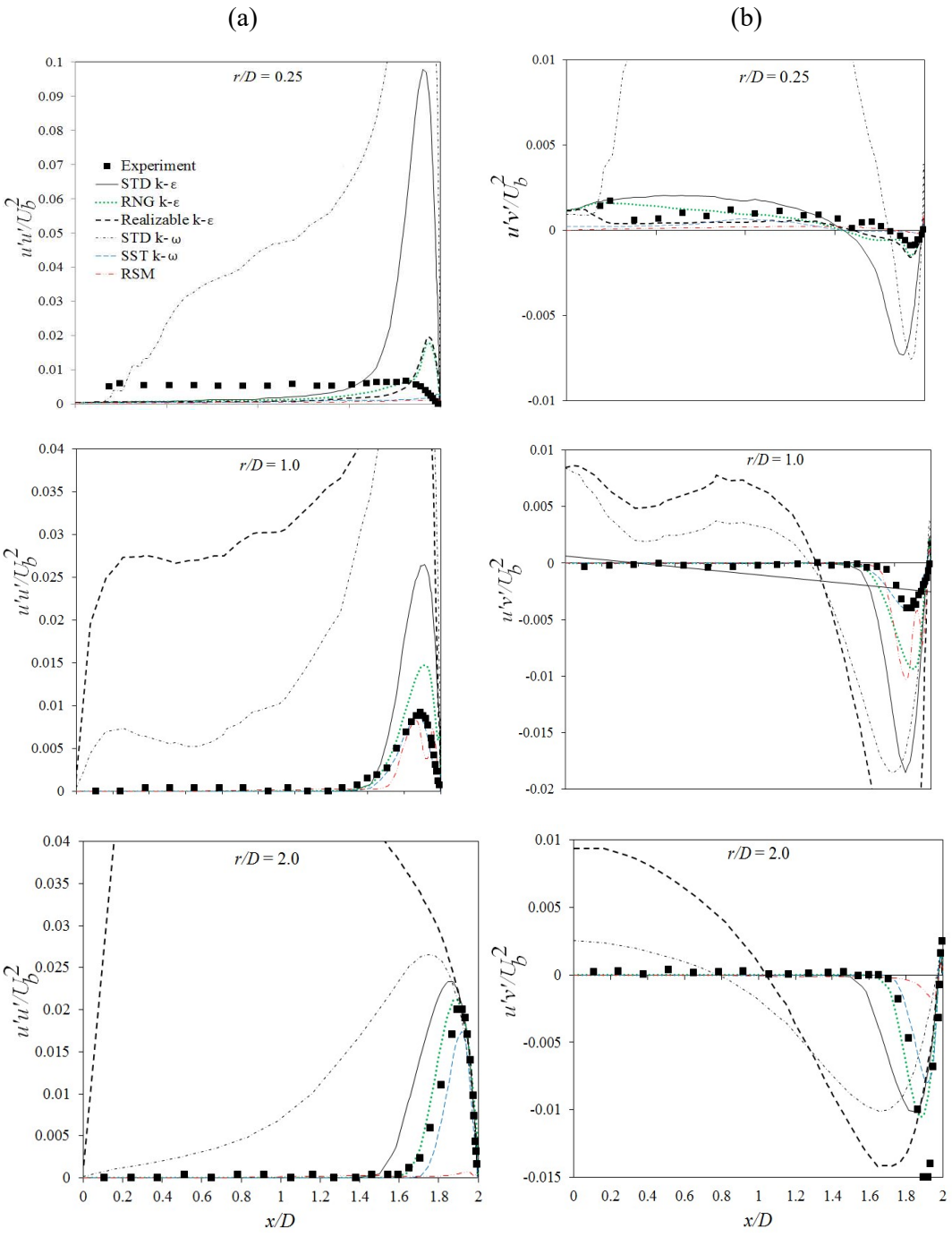

Figure 2.9 Comparison of turbulent flow characteristics for a non-swirling ($S = 0$) impinging jet experiment T-I [23] using different turbulence models: a) Reynolds normal stress, b) Reynolds shear stress.

moderate swirl but only for non-impinging jets [96, 102-104]. As such, the current impingement study is limited to RNG k-ε for the next simulations as it covers non-swirling as well as low-to-moderate swirl flows in the absence of vortex breakdown. RNG k-ε is modified to account for the effect of swirl or rotation by correcting the turbulent viscosity as [105],

$$\mu_t = \mu_{t0}\left(\alpha_s, \Omega, k/\varepsilon\right), \tag{2.2}$$

with μ_{t0} the turbulent viscosity without the swirl modification, Ω the characteristic swirl number and α_s the swirl factor that is assumed as 0.07 [103], typical for weak to medium swirl flows. The RNG k-ε model typically considers curvature corrections and rotations or swirl, but the use of streamline-curvature corrections is found to be of little impact at relatively low swirl flows [106] such as those deployed in the present study.

2.2.2 Baseline swirling non-impinging jet: N16S159

Before presenting the CFD model validation under swirling conditions, it is necessary not only to define swirl number (S) and its incorporation into the models validated, but also the shape of velocity profiles assumed for swirling conditions at the exit plane. In this regard, the ratio of the bulk azimuthal velocity to the bulk axial velocity is utilized to define swirl number S [107-109]:

$$S = \frac{W_b}{U_b} \tag{2.3}$$

where, U_b is shown in Table 2.3 (for each jet) and W_b is obtained from:

$$W_b = \frac{1}{A}\int_A w_{in} dA \tag{2.4}$$

with A being the cross-sectional area of the nozzle and w_{in} as the inlet swirl velocity profile. It is worth noting that although there exist several definitions of swirl number in the literature [55, 109-116], it is common practice to (only) report a single swirl number in relation to identifying each test case. However, the physics of the flow is strongly dependent on the local swirl number which can vary across the exit profile.

In practical systems, different types of swirl-generating methods produce varied profiles which subsequently lead to differing swirl velocity profiles at the nozzle exit. As this research seeks to analyse the effects of various inflow conditions on swirling (and non-swirling)

impinging jet development, it will therefore also investigate three different profiles, namely**:** Uniform Profile (UP), Solid Body rotation (SB) [55, 111, 117, 118] and Parabolic velocity Profile (PP) [119, 120]. To obtain the bulk tangential velocity (W_b) as defined in Equation 2.4, the following swirl velocity profiles are used against each profile:

UP: $$w_{in} = W_m \tag{2.5}$$

SB: $$w_{in} = W_m \left(r / R \right) \tag{2.6}$$

PP: $$w_{in} = W_m \left(r / R \right)^2 \tag{2.7}$$

where, R is the nozzle radius and W_m is the maximum swirl velocity at the exit plane whose magnitudes, in each case, are varied to obtain the same swirl number but for the total streamwise flow (Re).

As the numerical models used have already been validated against experimental data sets for non-swirling impinging jets T-I [23] and F-I [24] (Figures 2.7-2.9), the next step in the methodology is to test the accuracy of the models for turbulent swirling conditions. Although experimental data of swirling (non-impinging) flows without vortex breakdown are available in literature, the inlet conditions are not always well-defined in such data sets. For this an internationally adopted data set [108, 109, 121] which features a highly swirling isothermal jet termed N16S159 (Re = 32,400, S = 1.59) is considered for the validation with the RNG k-ε model.

Figure 2.10 presents a comparison of computed velocity domain for N16S159 against the experimentally derived data [108, 109]. In this flow, the experimental data reveals the relatively high swirl number causes an elongated stagnation zone to form and the central jet which stagnates at around x = 80 mm. The stagnation of the central jet on the centreline, which is also captured in the model being validated, indicates the imminent formation of vortex breakdown on the centreline, although no flow reversal actually occurs. The slight deviations in the near-field of the central jet (x < 80 mm) is attributed to the fact that the experimentally derived boundary conditions for the central jet are only available at x = 6.8 mm [107], but the computations undertaken herein assume a fully developed turbulent profile at x = 0 mm. This validation again indicates that RNG k-ε model is reasonably capable of predicting swirling characteristics qualitatively even at higher swirl flows in the absence of full vortex breakdown.

2.3 Results and discussion

The ensuing presents numerical analysis for the study of turbulent jets, as they develop from free (non-swirling, non-impinging) jets to swirling impinging jets. Figure 2.11 depicts the numerical predictions of centreline velocity decay for two impinging jets with differing inflow conditions (Table 2.3) T-I and F-I and their corresponding free jet counterparts T-F and F-F, respectively. The free jet centreline velocity decay for a third jet at *Re* = 30,000 [16] is also presented to reinforce the general similarity between free and impinging jets in relation to upstream jet development. Superimposing both the impinging and corresponding free jet data (in the same figure) also allows for the influence of the impingement surface (at

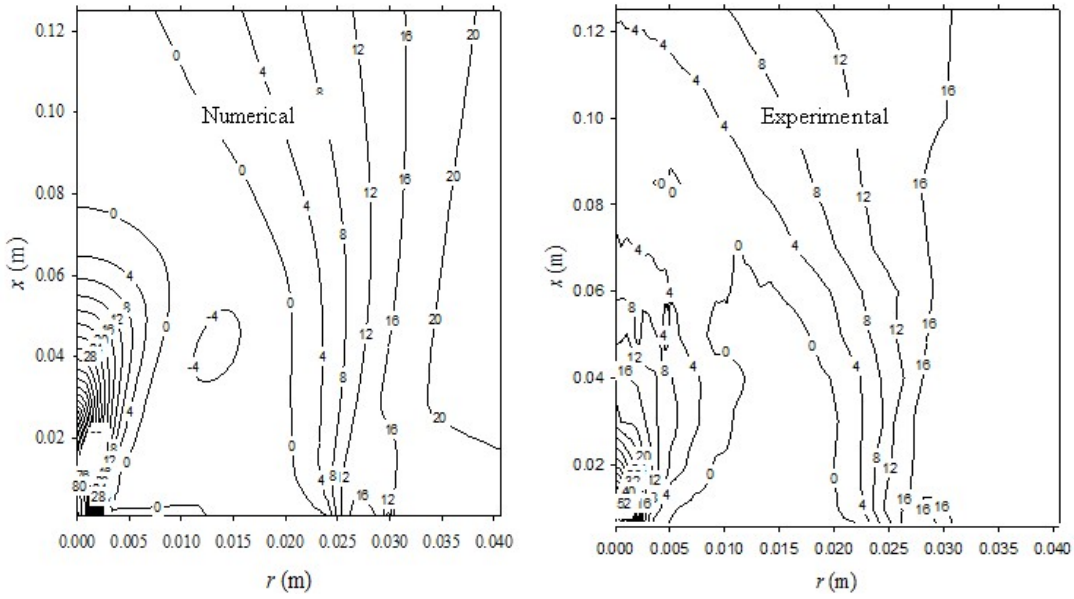

Figure 2.10 Contour plots of computed time-mean axial velocity (m/s) for swirling (*S* = 1.59) isothermal jet N16S159 (*Re* = 32, 400) compared to experimentally derived data [100, 101]. Axisymmetric geometry domain: *r* = 1.8 - 25 mm (bluff-body); *r* = 25 - 30 mm (swirling annulus); and *r* > 30 mm (co-flowing wind tunnel).

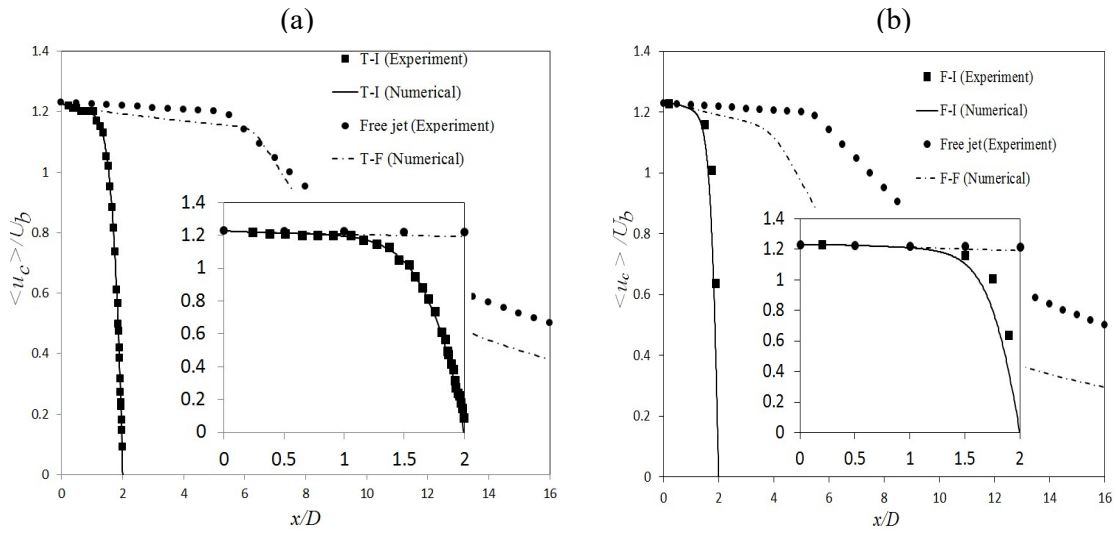

Figure 2.11 Axial velocity decay for impinging jets (experimental data) and their numerically equivalent free jets: (a) T-I [23] and T-F, and (b) F-I [24] and F-F. T-F and F-F are also compared with free jet experimental data [16]. Insets are a magnified view at $x/D \leq 2$.

H/D = 2) on the turbulent jet to be investigated. It is clear that good agreement between the experimental and numerical predictions (for the impinging and free jets) exists up to about x/D = 7 (T-F) and $x/D \approx 4$ (F-F), but discrepancies grow outside the potential core for free jets as they continue to develop. These discrepancies are where strong mixing and entrainment usually occur in free jets and can be attributed to different nozzle exit conditions (Table 2.3). The divergence of numerical results after the potential core for free jets with the experimental data [16] is also attributed to the varied inlet conditions at the nozzle exit, where uniform velocity and zero turbulent intensity are reported by Giralt et al. [16]. The overall observation from the data presented in Figure 2.11 is that across the various conditions depicted, inflow conditions have a stronger effect on the development of free jets compared to impinging jets. Interestingly, in both impinging jets T-I and F-I, a sharp decrease in the velocity decay and deviation from their free jet counterparts (T-F and F-F) only appears to commence at $x/D \approx 1.2$ despite the different inlet conditions. This observation may also help delineate the axial location where an impingement surface starts to affect the potential core of a turbulent jet (for the same inflow conditions), a finding not reported elsewhere.

To further investigate the effects of impingement plates on the development of jets, Figure 2.12 shows the downstream jet spread for both impinging jets T-I and F-I along with their numerically equivalent free jet counterparts. Jet spread is described in this figure via the jet half-radius ($r_{1/2}$) which is the point in the radial direction where the mean axial velocity is

half the mean centreline velocity, i.e. $< u > / < u_c > = 0.5$. Again, it appears that impinging jets deviate from their corresponding free jets at $x/D \approx 1$, followed by a sharp spreading as the jets approach the impingement surface. A wider and longer potential core for T-F is also observed as compared to F-F, by a factor of ~ 1.5 which is attributed to the different inlet boundary conditions (Table 2.3). In summary, the difference in jet inflow conditions at the nozzle exit plane (the Reynolds number, turbulent intensity and velocity profiles) appears to have a more significant influence on the development of the potential core and jet spread in free jets compared to impinging jets. Moreover, in the near-field, impinging jet development follows their corresponding free jets up to $x/D \approx 1$.

In the results presented so far, the focus has been to elucidate the effects of inflow conditions on non-swirling turbulent jet development by comparing between impinging and free jets. Focus now changes to the effects of superimposing swirl onto the impinging jet T-I and how this influences jet development. To first test whether the addition of swirl results in any asymmetry, which may not be reflected in the 2D-axisymmetric simulations, a comparison is undertaken between 3D and 2D-axisymmetric simulations.

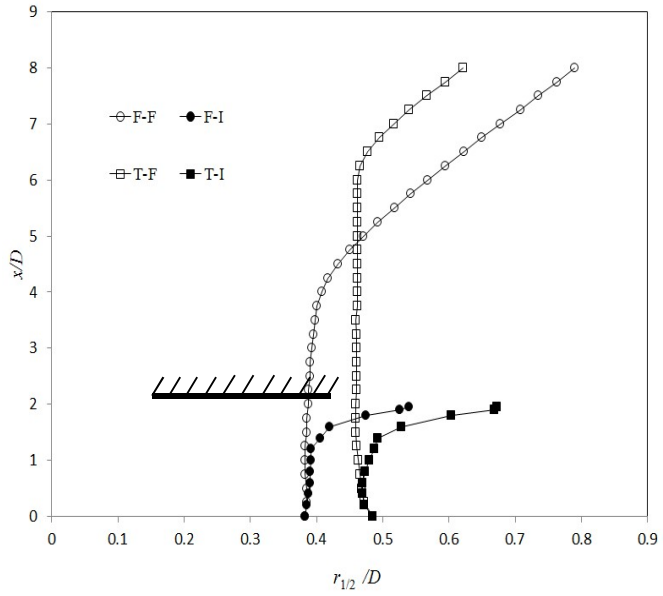

Figure 2.12 Comparison of jet half-radius profiles of impinging jets T-I [23] and F-I [24] and their numerically equivalent free jets T-F and F-F.

In swirling jets where the impingement surface is positioned in the near-field (i.e. $H/D \leq 2$), accurate prediction of centreline velocity decay is challenging as streamwise pressure gradients arise from the dual effects of tangential velocity and the close proximity of the impingement surface. At relatively high swirl, vortex breakdown may also occur. The presence of an impingement surface in the near-field along with the strong streamwise velocity gradients also means that resolving the near wall characteristics becomes a more challenging task. Figure 2.13 shows the effects of different inlet conditions and the imposition of swirl in impinging jets and compares the results between the 3D (left) and 2D-axisymmetric (right) simulations. The normalized centreline velocities $<u_c>$ and the normalized wall shear stresses τ_w are shown in the top and bottom of the figure, respectively. The centreline velocity decay for solid body rotation (SB, Equation 2.6) shows almost the same decay rate and magnitude for both the 3D and 2D-axisymmetric results, except for a slight underestimation at all swirl numbers exhibited in the 3D results. As the jet approaches the wall, the results for both the 3D and 2D modelling show identical results. Similar behaviour for the mean axial velocity decay is also obtained for the PP profile (not shown here for brevity). In contrast, when the inlet conditions at the nozzle exit plane are modelled with a uniform velocity profile (UP, Equation 2.5), greater deviations appear in the axial decay with 2D or 3D modelling. Moreover, when a uniform velocity profile is imposed in a 2D axisymmetric swirl, the onset of vortex breakdown is only predicted at $S = 0.3$ whilst in the 3D case flow reversal begins at $S = 0.4$. Noting the lack of experimental or numerical results for swirling impinging jets in the literature, it is difficult to conclude at this stage the swirl number at which vortex breakdown will occur for impinging jets. These results indicate the need to accurately define the boundary conditions and consider these when studying the effects of swirl on turbulent impinging jets, because this can affect downstream swirling impinging jet development, which is not always adequately done. An example is the study [28] which look at swirl jets (with $H/D = 2$) and report strong recirculation starting from just beyond the nozzle exit for $S = 0.5$, but give no details of the inflow conditions. More notably, the results shown in Figure 2.13 indicate that regardless of inlet velocity profile, for weakly swirling impinging jets where no flow reversal occurs these jets exhibits the same classical behaviour as non-swirling jets ($S = 0$). Figures 2.13a and 2.13b also reveal a strong similarity in the wall shear stress profiles derived for both non-swirling and swirling impinging jets, including the radial position of the maximum wall shear stress. The results, however, show that wall shear stress reduces with increasing swirl number and the location of maximum wall shear stress also shifts radially outward due to the tangential velocity component. However,

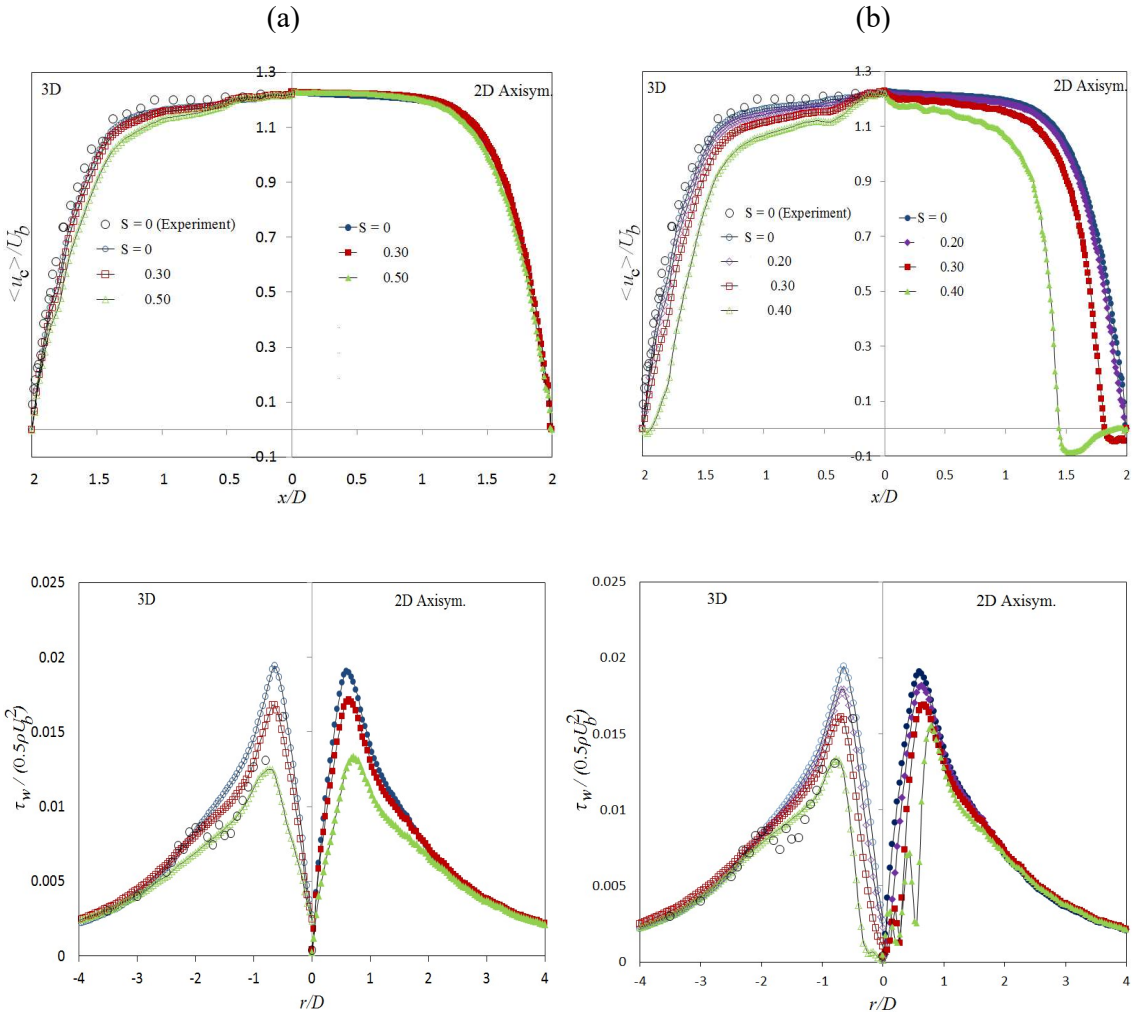

Figure 2.13 A comparison of the effects of three- and two-dimensional axisymmetric simulation on the mean centreline velocity decay (top) and normalised wall shear stress profiles (bottom) at $x/D = 2$ for two inlet tangential velocity conditions at $Re = 23{,}000$: (a) SB (Solid Body rotation) and (b) UP (Uniform velocity Profile).

with the results obtained assuming a uniform velocity profile (UP), the highest swirl value investigated ($S = 0.4$) not only produces flow reversal close to the impingement surface, but also a second weak maxima closer to the impingement point.

The above results therefore indicate that in the case of weakly swirling impinging jets (where vortex breakdown does not occur), the use of 2D-versus-3D or SB-versus-UP velocity profiles makes little difference on the jet development or even shear stresses at the wall. With this in mind, the remaining results in the chapter will be derived using 2D-axisymmetric simulation for $S \leq 3.0$ as they all relate to weakly swirling impinging jets.

Figure 2.14 depicts the swirl flow development near the impingement surface for three swirl velocity profiles UP, SB and PP, where Figures 2.14a and 2.14b show the time-mean axial and time-mean tangential velocity profiles, respectively, for $0.5 \le x/D \le 1.90$. It appears that there is no significant difference in the mean axial velocity in the upstream region (i.e. up to $x/D = 1.5$) for various inlet swirl velocity profiles as well as in comparison with a no-swirl condition [23]. Deviation, however, becomes stronger within $r/D = 0.5$ for the UP profile near the impingement surface, which is attributed to the larger tangential velocity intensity in this region (see Figure 2.14b) which tends to spread the jet radially outward more than the other profiles. Unlike the SB and PP profiles, the maximum axial velocity shifts from the geometric centreline at a radial position $r/D \approx 0.25$ for the UP profile. In contrast, the mean tangential velocity shows slightly different behaviour as it approaches the surface. The rate of decrease of the maximum tangential velocity for the PP profile is the most significant as it is highest in the upstream and lowest near the surface. The radial location of the maximum tangential velocity generally shifts outward, which may affect the heat transfer characteristics away from the stagnation point compared with a non-swirling jet.

The evolutions of the time-mean radial velocity for a weakly swirling jet ($S = 0.3$) for different swirl profiles is illustrated and compared with a non-swirling jet [23] at $Re = 23{,}000$ in Figure 2.15a in the range $0.5 \le x/D \le 1.95$. Interestingly, there is no significant influence of different inlet swirl conditions in predicting radial velocity distributions for swirling jets, even in comparison with non-swirling jets [23] except very close to the impingement surface (i.e. $x/D = 1.95$) for the PP profile where a relatively flat distribution and about 1.5 times smaller velocity peak are observed. The location of the peak also shifts outward (compared with other swirl profiles and non-swirling jets) at approximately $r/D \approx 1.2$ indicating a rather uniform jet spread. A relatively larger negative value near the pipe radius is predicted due to the strong entrainment towards the jet which produces a shear layer, in agreement with swirling jet experiments [110]. Figure 2.15b shows the locus of these peaks when the jet approaches the impingement surface in the range $1.5 \le x/D \le 1.995$. It appears that the maximum radial velocity in the flow occurs at an axial location of $1.98D$ for the numerically predicted non-swirling jet T-I and almost at the same location for weakly swirling jets (for both the SB and UP profiles). For the PP profile, however, the location is at $x/D = 1.95$ and $r/D \approx 1.3$ which is almost 1.5 times radially wider than that of the UP and SB profiles, meaning that swirling jets with a PP profile shows significantly larger jet spreading which may have a positive impact on the heat transfer distribution from the wall.

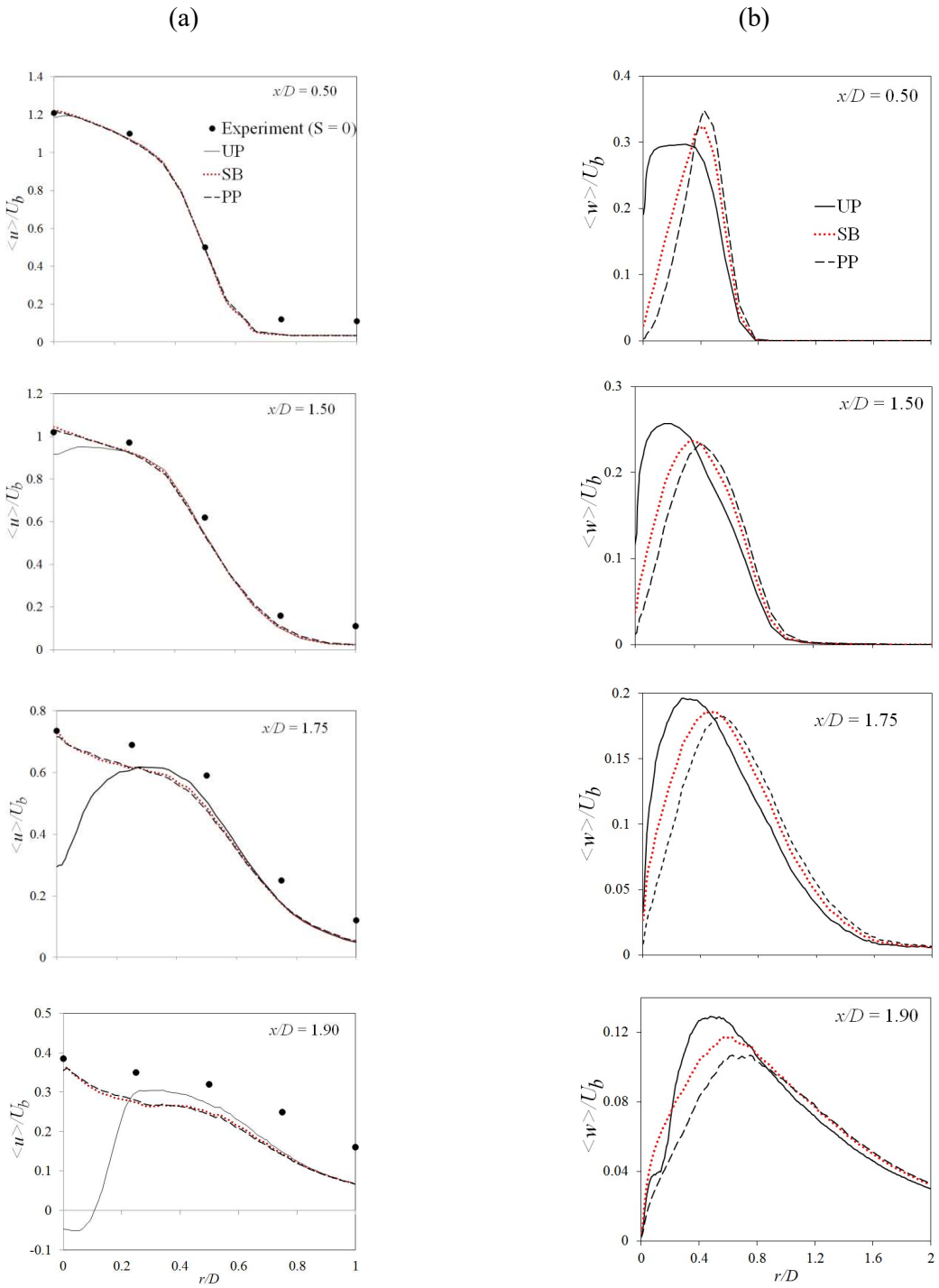

Figure 2.14 The evolving velocity profiles for a weakly swirling jet ($S = 0.3$), (a) time-mean axial velocity and (b) time-mean tangential velocity, for $Re = 23,000$. The time-mean axial velocity data for non-swirling jet ($S = 0$) [23] is added to elucidate the effect of swirl velocity.

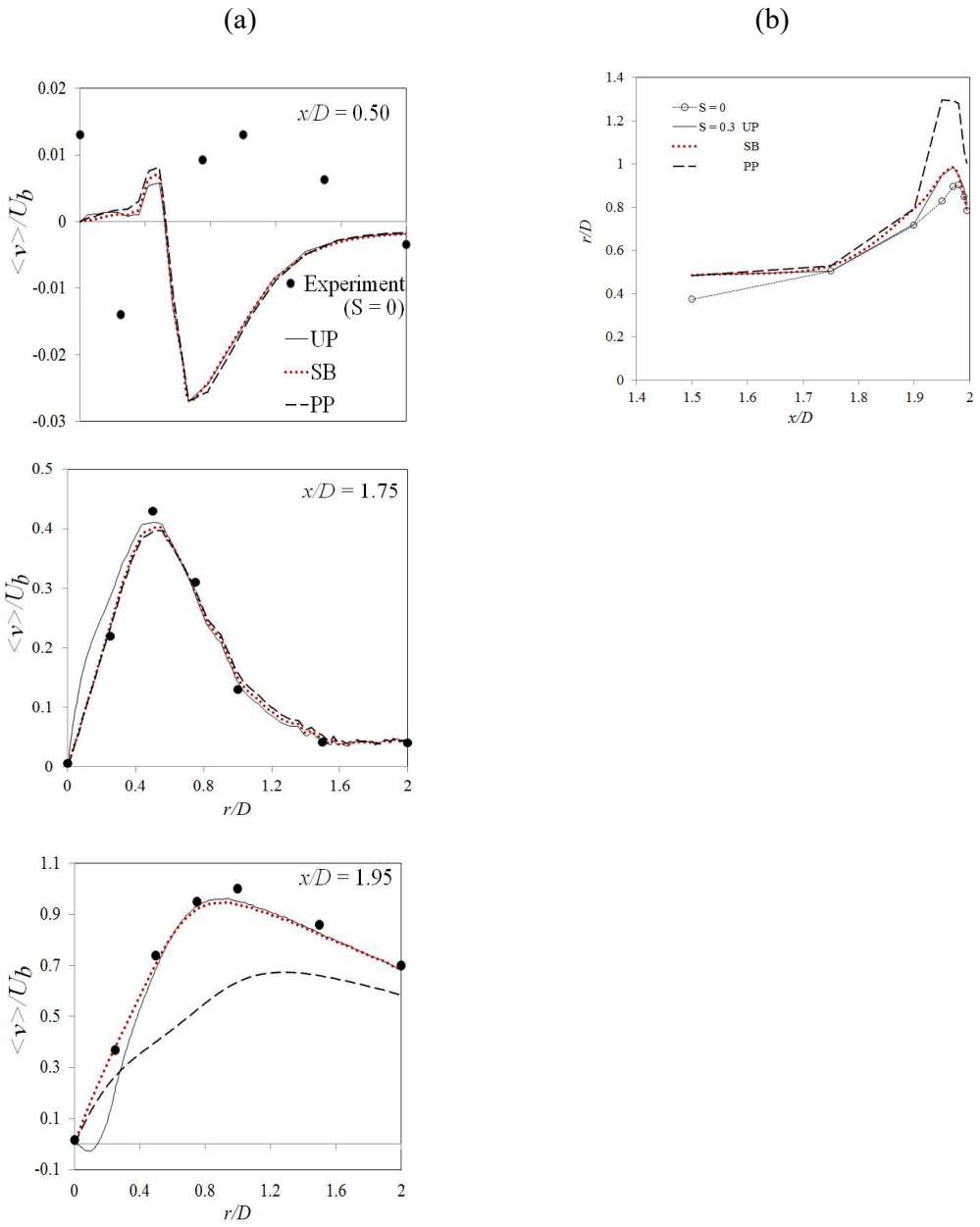

Figure 2.15 A comparison between swirling jet ($S = 0.3$) and non-swirling jet ($S = 0$) [23] for $Re = 23,000$: (a) time-mean radial velocity developments and (b) numerically derived locus of maximum radial velocity near the wall.

Figure 2.16 portrays filled contours of the turbulent kinetic energy at the highest swirl number investigated ($S = 0.3$), at different inlet swirl profiles and turbulence intensities. Results for the PP inlet profile resemble the SB profile and are not shown for brevity. For the same axial inlet velocity profile and turbulence (Figures 2.16a-c), the inclusion of varied

swirl profiles in an impinging jet does not significantly change the turbulent kinetic energy behaviour from its non-swirling counterpart, other than a modest increase close to the nozzle exit. The increased jet spread at S = 0.3, however, influences the location and magnitude of the "eye" of the high intensity turbulent kinetic energy zone in the wall jet region. The results show a shift in the location of this high intensity turbulent kinetic energy zone from $r/D \approx$ 1.75 (at S = 0) to $r/D \approx 2$ at (S = 0.3). This behaviour may also alter the convective heat transfer characteristics between a turbulent swirling impinging jet and the wall and deserves further study. In non-swirling impinging jets, experimental data [122, 123] reveals a local minimum Nusselt number around r/D = 1.4 and a secondary maximum at around r/D = 2. Lytle and Webb [124] argued that a shifted turbulent kinetic energy away from the stagnation region is responsible for the local secondary maxima in Nusselt number. Behnia et al. [65, 76] attempted to numerically study this hypothesis using the v^2-f model. Although an accurate secondary heat transfer peak was not predicted in their results, they attributed such a peak in Nusselt number to the turbulent kinetic energy. For the same Re (23,000) and H/D = 2, Behnia et al. [65, 76] predicted non-dimensional turbulent kinetic energy equal to 0.049, whereas in the current study, this is predicted at 0.035 (for the same radial location). Figures 2.16d-f show the influence of different turbulence intensities (5%, 10% and 15%) on the turbulent kinetic energy. These results indicate that greater turbulence intensities at the nozzle exit translate into significant increases of turbulent kinetic energy at the central impingement region (Figure 2.1a, zone I and II), but does not extend to the wall jet region (Figure 2.1a, zone III). This aspect may also affect heat transfer characteristics in the impingement region. The result again confirms a necessity of adequately resolving inflow conditions for the accurate prediction of heat transfer in swirling impinging flows.

Finally, the effects of swirl on the pressure distribution at the impingement surface, in comparison to a non-swirling jet at an equivalent Re, are investigated. Figure 2.17 shows this analysis for $S \leq 0.3$, whereby the radial distribution for the coefficient of pressure is defined by:

$$C_p = \frac{p - p_\infty}{0.5\rho U_b^2}^{5}, \tag{2.8}$$

where p_∞ is the ambient pressure and p is the static pressure at the surface. The predictions

[5] In the published version of this chapter, normalisation of (gauge) static pressures was done by ρU_b^2 to maintain consistency with wall shear stresses.

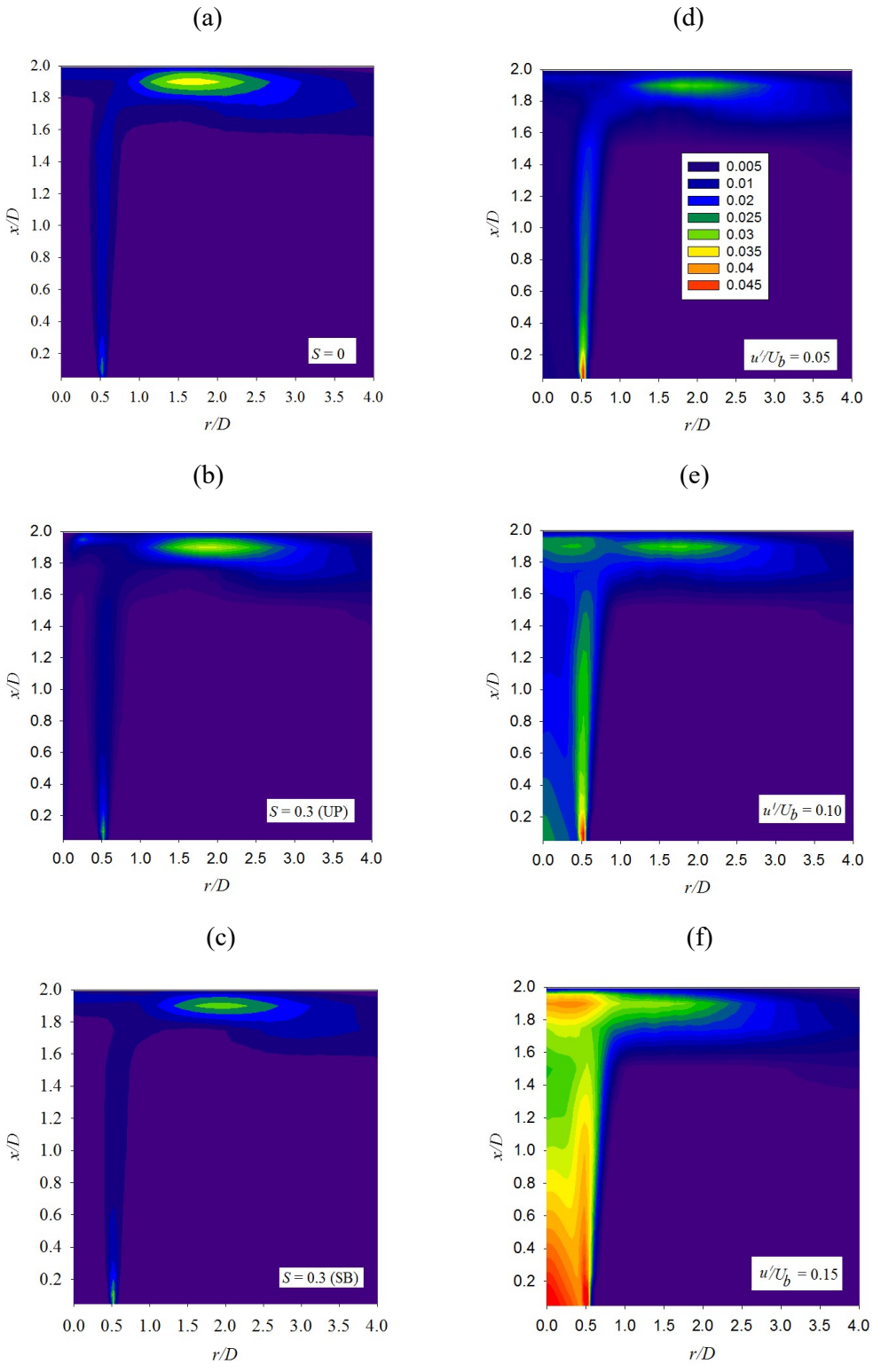

Figure 2.16 Filled contours of turbulent kinetic energy at Re = 23, 000 for different inflow conditions: (a) S = 0, (b) S = 0.3 (UP), (c) S = 0.3 (SB), and (d-f) S = 0.3 (SB). Turbulent kinetic energy is normalised by U_b^2. Same color scale applies for all plots.

(a)

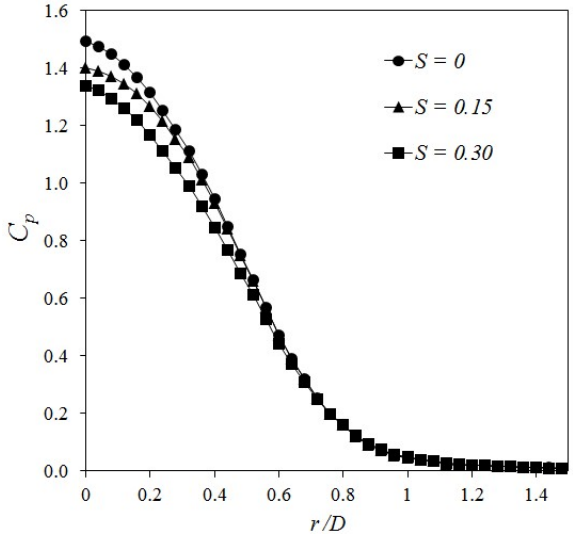

(b)

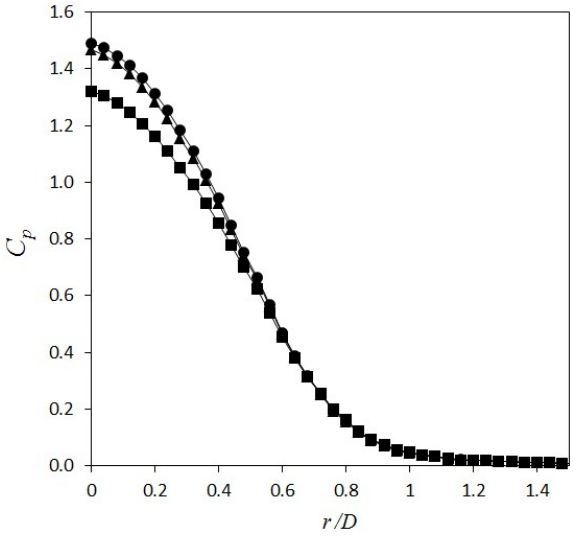

Figure 2.17 Coefficient of pressure (*Cp*) between non-swirling T-I (*S* = 0) and swirling (*S* = 0.3) jets at the impingement surface (*H/D* = 2) for *Re* = 23,000: (a) UP and (b) SB.

show that higher swirl causes a reduction of C_p, particularly inside the impingement region (*r/D* < 0.6), coupled with no significant departure from the non-swirling behaviour beyond this zone. For the swirl numbers and profiles investigated in the current study, the overall behaviour of the coefficient of pressure follows the classical trend for impinging jets. Higher

swirl numbers outside the scope of this data may, however, cause significant deviation in this trend, particularly if flow reversal occurs at higher swirl numbers.

2.4 Conclusions

In this study, both non-swirling and swirling impinging jets along with their corresponding equivalent free jets have been investigated numerically using the commercial software package ANSYS Fluent (version 14.5). The effects of inflow conditions on the transition from free-to-impinging and non-swirling-to-swirling (impinging) jets have been studied largely at Re = 23,000. The analyses and swirl numbers tested have targeted flow conditions whereby no vortex breakdown is expected to occur. The RANS approach with RNG k-ε model is applied to help study the mean flow and turbulent characteristics for these jets. The study first investigates the general performance of six different turbulence models with results validated against baseline (non-swirling) impinging jets T-I [23] and F-I [24] as well as swirling (free) jets [108, 109]. A summary of the conclusions drawn is given below.

- For $x/D \leq 1$, non-swirling (free) and impinging jets appear to develop similarly, both in terms of centreline velocity decay (Figure 2.11) and as well as jet spread (Figure 2.12).
- Differing inflow conditions (Table 2.3) appear to have a larger influence on the downstream development of non-swirling free jets compared to non-swirling impinging jets (Figure 2.12).
- Except where flow reversal through vortex breakdown may occur at relatively large swirl numbers, non-swirling and weakly swirling impinging jets show the same overall behaviour in relation to centreline velocity decay. The imposition of any level of swirl (weak or strong), however, significantly affects the wall shear stress at the impingement surface. The wall shear stress reduces with increasing swirl and the location of the maximum wall shear stress shifts (slightly) radially outwards (Figure 2.13).
- In general, the mean axial and tangential velocities show similar behaviour up to x/D = 1.50 for all inlet swirl velocity profiles (Figure 2.14). The radial location of the maximum tangential velocity shifts radially outward, which may affect heat transfer at the impingement plate as compared to a non-swirling jet for the same Re.

- The locus of the radial velocity peaks for both non-swirling and swirling jets suggest that the maximum radial velocity in the flow occurs at x/D = 1.95-1.98. Among the three swirl velocity profiles tested, swirling jets with the PP inlet profile show significantly larger jet spread which may have an influence on the heat transfer distribution at the impingement plate (Figure 2.15).
- For conditions that do not lead to the onset of vortex breakdown, the inclusion of swirl does not significantly affect the characteristics of the turbulent kinetic energy compared to its non-swirling counterparts. Swirl causes a reduction in the magnitude of turbulent kinetic energy near the impingement surface and a slight shift radially outwards in the wall jet region. For the same swirl number, larger turbulence intensity at the nozzle exit plane significantly alters the turbulent kinetic energy in the central impingement region.
- Computations show that swirl causes a reduction of C_p, particularly around the impingement region (r/D < 0.6), above which no significant departure from the non-swirling behaviour is observed. For the swirl numbers and profiles investigated in the study, the overall behaviour of the coefficient of pressure follows the classical trend for non-swirling impinging jets.

More work is warranted to extend our fundamental understanding of how the above results impact impinging jet heat transfer, under the transition between non-swirling and swirling impinging jets or the impact of swirl conditions if vortex breakdown occurs.

2.5 Chapter references

1. Lee, K. H. and Viskanta, R., *Quenching of flat glass by impinging air jets*, Numerical Heat Transfer, Part A: Applications, 33(1), p. 5-22, 1998.
2. Rantala, M. and Karvinen, R., *Heat transfer under an impinging jet at long nozzle-to-surface distances*, in 13th International Heat Transfer Conference, Sydney, Australia, http://dl.begellhouse.com/journals/IHTC13,0339d661102ccf6d,46a5b51a6bcb2b60.html, p. 12, 2006.
3. Cirillo, F. and Isopi, G. M., *Glass tempering heat transfer coefficient evaluation and air jets parameter optimization*, Applied Thermal Engineering, 29(5–6), p. 1173-1179, 2009.
4. Han, J. C., *Recent studies in turbine blade cooling*, International Journal of Rotating Machinery, 10(6), p. 443-457, 2004.

5. Gupta, S., Chaube, A. and Verma, P., *Review on heat transfer augmentation techniques: Application in gas turbine blade internal cooling*, Journal of Engineering Science and Technology Review, 5(1), p. 57-62, 2012.
6. De Bonis, M. V. and Ruocco, G., *An experimental study of the local evolution of moist substrates under jet impingement drying*, International Journal of Thermal Sciences, 50(1), p. 81-87, 2011.
7. Bond, J. F., Mujumdar, A. S., van Heiningen, A. R. P. and Douglas, W. J. M., *Drying paper by impinging jets of superheated steam. Part 1: Constant drying rate in superheated steam*, The Canadian Journal of Chemical Engineering, 72(3), p. 446-451, 1994.
8. Singh, G., Chander, S. and Ray, A., *Heat transfer characteristics of natural gas/air swirling flame impinging on a flat surface*, Experimental Thermal and Fluid Science, 41(0), p. 165-176, 2012.
9. Yu, B., Kum, S. M., Lee, C. E. and Lee, S., *An experimental study of heat transfer and pollutant emission characteristics at varying distances between the burner and the heat exchanger in a compact combustion system*, Energy, 42(1), p. 350-357, 2012.
10. Hsieh, W. D. and Lin, T. H., *Methane flame stability in a jet impinging onto a wall*, Energy Conversion and Management, 46, p. 727-739, 2005.
11. Gauntner, J. W., Livingood, J. N. B. and Hrycak, P., *Survey of literature on flow characteristics of a single turbulent jet impinging on a flat plate*, in Technical Report, NASA: Washington, D.C., p. 1-22, 1970.
12. Jambunathan, K., Lai, E., Moss, M. A. and Button, B. L., *A review of heat transfer data for single circular jet impingement*, International Journal of Heat and Fluid Flow, 13(2), p. 106-115, 1992.
13. Viskanta, R., *Heat transfer to impinging isothermal gas and flame jets*, Experimental Thermal and Fluid Science, 6(2), p. 111-134, 1993.
14. Livingood, J. N. B. and Hrycak, P., *Impingement heat transfer from turbulent air jets to flat plates: A literature survey*, in Technical report, NASA: Washington, D. C., p. 1-42, 1973.
15. Bradshaw, P. and Love, E. M., *The normal impingement of a circular air jet on a flat surface*, in ARC Report, HM Stationery Office: London, p. 1-8, 1961.
16. Giralt, F., Chia, C. and Trass, O., *Characterization of the impingement region in an axisymmetric turbulent jet*, Industrial & Engineering Chemistry Fundamentals, 16(1), p. 21-28, 1977.
17. Obot, N. Y., Mujumdar, A. S. and Douglas, W. J. M., *Effect of semi-confinement on impingement heat transfer*, in 7th Int. Heat Transfer Conference, Septermber 6-10, Munchen, Germany, p. 395-400, 1982.
18. Maurel, S. and Solliec, C., *A turbulent plane jet impinging nearby and far from a flat plate*, Experiments in Fluids, 31(6), p. 687-696, 2001.
19. Ashforth-Frost, S., Jambunathan, K., Whitney, C. F. and Ball, S. J., *Heat transfer from a flat plate to a turbulent axisymmetric impinging jet*, Proceedings of the Institution of Mechanical Engineers, 211(2), p. 167-167, 1997.
20. Ozmen, Y. and Baydar, E., *Flow structure and heat transfer characteristics of an unconfined impinging air jet at high jet Reynolds numbers*, Heat and Mass Transfer, 44(11), p. 1315-1322, 2008.
21. Rajaratnam, N., Zhu, D. Z. and Rai, S. P., *Turbulence measurements in the impinging region of a circular jet*, Canadian Journal of Civil Engineering, 37(5), p. 782-786, 2010.
22. Beltaos, S. and Rajaratnam, N., *Impinging circular turbulent jets*, Journal of the Hydraulics Division, 100(10), p. 1313-1328, 1974.

23. Tummers, M. J., Jacobse, J. and Voorbrood, S. G. J., *Turbulent flow in the near field of a round impinging jet*, International Journal of Heat and Mass Transfer, 54(23–24), p. 4939-4948, 2011.
24. Fairweather, M. and Hargrave, G., *Experimental investigation of an axisymmetric, impinging turbulent jet. 1. Velocity field*, Experiments in Fluids, 33(3), p. 464-471, 2002.
25. Cooper, D., Jackson, D. C., Launder, B. E. and Liao, G. X., *Impinging jet studies for turbulence model assessment—I. Flow-field experiments*, International Journal of Heat and Mass Transfer, 36(10), p. 2675-2684, 1993.
26. Hargrave, G. K., Williams, T. C., Anandarajah, K. and Halliwell, N. A., *The 3D velocity field of an impacting turbulent jet*, Journal of Physics: Conference Series, 45(0), p. 162-172, 2006.
27. Xu, Z. and Hangan, H., *Scale, boundary and inlet condition effects on impinging jets*, Journal of Wind Engineering and Industrial Aerodynamics, 96(12), p. 2383-2402, 2008.
28. Abrantes, J. K. and Azevedo, L. F. A., *Fluid flow characteristics of a swirl jet Impinging on a flat plate*, in 13th Int Symp on Applications of Laser Techniques to Fluid Mechanics, 26-29 June, Lisbon, Portugal, http://ltces.dem.ist.utl.pt/lxlaser/lxlaser2006/downloads/papers/28_3.pdf, p. 1-12, 2006.
29. Alekseenko, S. V., Bilsky, A. V., Dulin, V. M. and Markovich, D. M., *Experimental study of an impinging jet with different swirl rates*, International Journal of Heat and Fluid Flow, 28(6), p. 1340-1359, 2007.
30. Bilen, K., Bakirci, K., Yapici, S. and Yavuz, T., *Heat transfer from a plate impinging swirl jet*, International Journal of Energy Research, 26(4), p. 305-320, 2002.
31. Brown, K. J., Persoons, T. and Murray, D. B., *Heat transfer characteristics of swirling impinging jets*, in Proceedings of the International Heat Transfer Conference, August 8-13, Washington, DC, USA, p. 1-9, 2010.
32. Ianiro, A. and Cardone, G., *Heat transfer rate and uniformity in multichannel swirling impinging jets*, Applied Thermal Engineering, 49(0), p. 89-98, 2011.
33. Kinsella, C., Donnelly, B., O'Donovan, T. S. and Murray, D. B., *Heat transfer enhancement from a horizontal surface by impinging swirl jets*, in 5th European Thermal-Sciences Conference, The Netherlands, p., 2008.
34. Lee, D. H., Won, S. Y., Kim, Y. T. and Chung, Y. S., *Turbulent heat transfer from a flat surface to a swirling round impinging jet*, International Journal of Heat and Mass Transfer, 45(1), p. 223-227, 2002.
35. Nozaki, A., Igarashi, Y. and Hishida, K., *Heat transfer mechanism of a swirling impinging jet in a stagnation region*, Heat Transfer—Asian Research, 32(8), p. 663-673, 2003.
36. Nuntadusit, C., Wae-hahyee, M., Bunyajitradulya, A. and Shakouch, T., *Heat transfer enhancement for a swirling jet impingement*, in ISFV14 - 14th International Symposium on Flow Visualization, EXCO Daegu, Korea, p. 1-9, 2010.
37. Ortega-Casanova, J., Campos, N. and Fernandez-Feria, R., *Experimental study on sand bed excavation by impinging swirling jets*, Journal of Hydraulic Research, 49(5), p. 601-610, 2011.
38. Senda, M., Inaoka, K., Toyoda, D. and Sato, S., *Heat transfer and fluid flow characteristics in a swirling impinging jet*, Heat Transfer—Asian Research, 34(5), p. 324-335, 2005.

39. Wen, M. and Jang, K., *An impingement cooling on a flat surface by using circular jet with longitudinal swirling strips*, International Journal of Heat and Mass Transfer, 46(24), p. 4657-4667, 2003.
40. Yuan, Z., Chen, Y., Jiang, J. and Ma, C., *Swirling effect of jet impingement on heat transfer from a flat surface to CO2 stream*, Experimental Thermal and Fluid Science, 31(1), p. 55-60, 2006.
41. Huang, L. and El-Genk, M. S., *Heat transfer and flow visualization experiments of swirling, multi-channel, and conventional impinging jets*, International Journal of Heat and Mass Transfer, 41(3), p. 583-600, 1998.
42. Ward, J. and Mahmood, M., *Heat transfer from a turbulent, swirling, impinging jet*, in Heat transfer 1982: Proceedings of the Seventh International Conference, September 6-10, Munich, West Germany, p. 401-407, 1982.
43. Owsenek, B. L., Cziesla, T., Mitra, N. K. and Biswas, G., *Numerical investigation of heat transfer in impinging axial and radial jets with superimposed swirl*, International Journal of Heat and Mass Transfer, 40(1), p. 141-147, 1996.
44. Thomas, B., Ahmed, Z. U., Al-Abdeli, Y. M. and Matthews, M. T., *The optimisation of a turbulent swirl nozzle using CFD*, in Proceedings of the Australian Combustion Symposium, 6-8 November Perth, Australia, http://www.anz-combustioninstitute.org/local/papers/ACS2013-Conference-Proceedings.pdf, p. 271-274, 2013.
45. Ichimiya, K. and Tsukamoto, K., *Heat transfer from an inflow-type swirling turbulent impinging jet*, JSME International Journal Series B Fluids and Thermal Engineering, 49(4), p. 995-999, 2006.
46. Zuckerman, N. and Lior, N., *Jet impingement heat transfer: Physics, Correlations, and Numerical modeling*, in Advances in Heat Transfer, editor: G. A. Greene, J. P. Hartnett, A. B. C. Young, et al., Elsevier. p. 565-631, 2006.
47. Deo, R. C., Mi, J. and Nathan, G. J., *The influence of nozzle-exit geometric profile on statistical properties of a turbulent plane jet*, Experimental Thermal and Fluid Science, 32(2), p. 545-559, 2007.
48. Ferdman, E., Otugen, M. V. and Kim, S., *Effect of initial velocity profile on the development of round jets*, Journal of Propulsion and Power, 16(4), p. 676-686, 2000.
49. Garimella, S. V. and Nenaydykh, B., *Nozzle-geometry effects in liquid jet impingement heat transfer*, International Journal of Heat and Mass Transfer, 39(14), p. 2915-2923, 1996.
50. Mi, J. and Nathan, G. J., *Statistical properties of turbulent free jets issuing from nine differently-shaped nozzles*, Flow, Turbulence and Combustion, 84(4), p. 583-606, 2010.
51. Obot, N. T., Graska, M. L. and Trabold, T. A., *The near field behavior of round jets at moderate Reynolds numbers*, The Canadian Journal of Chemical Engineering, 62(5), p. 587-593, 1984.
52. Xu, G. and Antonia, R., *Effect of different initial conditions on a turbulent round free jet*, Experiments in Fluids, 33(5), p. 677-683, 2002.
53. Faghani, E., Maddahian, R., Faghani, P. and Farhanieh, B., *Numerical investigation of turbulent free jet flows issuing from rectangular nozzles: the influence of small aspect ratio*, Archive of Applied Mechanics, 80(7), p. 727-745, 2010.
54. Shuja, S. Z., Yilbas, B. S. and Budair, M. O., *Influence of conical and annular nozzle geometric configurations on flow and heat transfer characteristics due to flow impingement onto a flat plate*, Numerical Heat Transfer, Part A: Applications, 48(9), p. 917-939, 2005.

55. Farokhi, S., Taghavi, R. and Rice, E. J., *Effect of initial swirl distribution on the evolution of a turbulent jet*, AIAA Journal, 27(6), p. 700-706, 1989.
56. Dong, M. and Lilley, D. G., *Inlet velocity profile effects on turbulent swirling flow predictions*, Journal of Propulsion and Power, 10(2), p. 155-160, 1994.
57. Carlomagno, G. M. and Cardone, G., *Infrared thermography for convective heat transfer measurements*, Experiments in Fluids, 49(6), p. 1187-1218, 2010.
58. Meola, C., de Luca, L. and Carlomagno, G. M., *Influence of shear layer dynamics on impingement heat transfer*, Experimental Thermal and Fluid Science, 13(1), p. 29-37, 1996.
59. Batten, P., Goldberg, U., Peroomian, O. and Chakravarthy, S., *Recommendations and best practice for the current state of the art in turbulence modelling*, International Journal of Computational Fluid Dynamics, 23(4), p. 363-374, 2009.
60. Dewan, A., Dutta, R. and Srinivasan, B., *Recent trends in computation of turbulent jet impingement heat transfer*, Heat Transfer Engineering, 33(4-5), p. 447-460, 2012.
61. Clark, K. M. and Loth, E., *A multi-scale LES technique for coupling near-field and far-field domains for a jet flow*, Computers & Fluids, 88(0), p. 262-271, 2013.
62. Tucker, P. G., *Turbulence and Its Modelling*, in Unsteady Computational Fluid Dynamics in Aeronautics, editor, Springer Netherlands. p. 93-148, 2014.
63. Argyropoulos, C. D. and Markatos, N. C., *Recent advances on the numerical modelling of turbulent flows*, Applied Mathematical Modelling, 39(2), p. 693-732, 2015.
64. Angioletti, M., Nino, E. and Ruocco, G., *CFD turbulent modelling of jet impingement and its validation by particle image velocimetry and mass transfer measurements*, International Journal of Thermal Sciences, 44(4), p. 349-356, 2005.
65. Behnia, M., Parneix, S. and Durbin, P. A., *Prediction of heat transfer in an axisymmetric turbulent jet impinging on a flat plate*, International Journal of Heat and Mass Transfer, 41(12), p. 1845-1855, 1998.
66. Craft, T. J., Graham, L. J. W. and Launder, B. E., *Impinging jet studies for turbulence model assessment—II. An examination of the performance of four turbulence models*, International Journal of Heat and Mass Transfer, 36(10), p. 2685-2697, 1993.
67. Dianat, M., Fairweather, M. and Jones, W. P., *Predictions of axisymmetric and two-dimensional impinging turbulent jets*, International Journal of Heat and Fluid Flow, 17(6), p. 530-538, 1996.
68. Isman, M. K., Pulat, E., Etemoglu, A. B. and Can, M., *Numerical investigation of turbulent impinging jet cooling of a constant heat flux surface*, Numerical Heat Transfer, Part A: Applications, 53(10), p. 1109-1132, 2008.
69. Jaramillo, J. E., Pérez-Segarra, C. D., Rodriguez, I. and Oliva, A., *Numerical study of plane and round impinging jets using RANS models*, Numerical Heat Transfer, Part B: Fundamentals, 54(3), p. 213-237, 2008.
70. Merci, B. and Dick, E., *Heat transfer predictions with a cubic k–ε model for axisymmetric turbulent jets impinging onto a flat plate*, International Journal of Heat and Mass Transfer, 46(3), p. 469-480, 2003.
71. Ortega-Casanova, J., *CFD and correlations of the heat transfer from a wall at constant temperature to an impinging swirling jet*, International Journal of Heat and Mass Transfer, 55(21–22), p. 5836-5845, 2012.
72. Pulat, E., Isman, M. K., Etemoglu, A. B. and Can, M., *Effect of turbulence models and near-wall modeling approaches on numerical results in impingement heat transfer*, Numerical Heat Transfer, Part B: Fundamentals, 60(6), p. 486-519, 2011.

73. Ramezanpour, A., Mirzaee, I., Firth, D. and Shirvani, H., *A numerical heat transfer study of slot jet impinging on an inclined plate*, International Journal of Numerical Methods for Heat & Fluid Flow, 17(7), p. 661-676, 2007.
74. Sagot, B., Antonini, G., Christgen, A. and Buron, F., *Jet impingement heat transfer on a flat plate at a constant wall temperature*, International Journal of Thermal Sciences, 47(12), p. 1610-1619, 2008.
75. Balabel, A. and El-Askary, W. A., *On the performance of linear and nonlinear turbulence models in various jet flow applications*, European Journal of Mechanics - B/Fluids, 30(3), p. 325-340, 2011.
76. Behnia, M., Parneix, S., Shabany, Y. and Durbin, P. A., *Numerical study of turbulent heat transfer in confined and unconfined impinging jets*, International Journal of Heat and Fluid Flow, 20(1), p. 1-9, 1999.
77. Badra, J., Masri, A. R. and Behnia, M., *Enhanced transient heat transfer from arrays of jets impinging on a moving plate*, Heat Transfer Engineering, 34(4), p. 361-371, 2013.
78. O'Neill, P., Soria, J. and Honnery, D., *The stability of low Reynolds number round jets*, Experiments in Fluids, 36(3), p. 473-483, 2004.
79. Otobe, Y., Kashimura, H., Matsuo, S., Setoguchi, T., et al., *Influence of nozzle geometry on the near-field structure of a highly underexpanded sonic jet*, Journal of Fluids and Structures, 24(2), p. 281-293, 2008.
80. Ball, C. G., Fellouah, H. and Pollard, A., *The flow field in turbulent round free jets*, Progress in Aerospace Sciences, 50(0), p. 1-26, 2012.
81. Donaldson, C. D. and Snedeker, R. S., *A study of free jet impingement. Part 1. Mean properties of free and impinging jets*, Journal of Fluid Mechanics, 45(02), p. 281-319, 1971.
82. Donaldson, C. D., Snedeker, R. S. and Margolis, D. P., *A study of free jet impingement. Part 2. Free jet turbulent structure and impingement heat transfer*, Journal of Fluid Mechanics, 45(03), p. 477-512, 1971.
83. Popiel, C. O. and Trass, O., *Visualization of a free and impinging round jet*, Experimental Thermal and Fluid Science, 4(3), p. 253-264, 1991.
84. Looney, M. K. and Walsh, J. J., *Mean-flow and turbulent characteristics of free and impinging jet flows*, Journal of Fluid Mechanics, 147, p. 397-429, 1984.
85. Kotsovinos, N. E., *A note on the spreading rate and virtual origin of a plane turbulent jet*, Journal of Fluid Mechanics, 77(02), p. 305-311, 1976.
86. Bradshaw, P., *Effect of external disturbances on the spreading rate of a plane turbulent jet*, Journal of Fluid Mechanics, 80(04), p. 795-797, 1977.
87. *ANSYS, Inc., ANSYS FLUENT (version 14.5)*. http://www.ansys.com/Products/Simulation+Technology/Fluid+Dynamics/Fluid+Dynamics+Products/ANSYS+Fluent, Date Accessed: 13 May, 2013, 2012.
88. Jakirlic, S., Hanjalic, K. and Tropea, C., *Modeling rotating and swirling turbulent flows: a perpetual challenge*, AIAA journal, 40(10), p. 1984-1996, 2002.
89. Launder, B. E. and Spalding, D. B., *The numerical computation of turbulent flows*, Computer Methods in Applied Mechanics and Engineering, 3(2), p. 269-289, 1974.
90. Kim, S. E. and Choudhury, D., *A near-wall treatment using wall functions sensitized to pressure gradient*, ASME FED, Separated and Complex Flows, ASME, 217, p., 1995.
91. Kader, B. A., *Temperature and concentration profiles in fully turbulent boundary layers*, International Journal of Heat and Mass Transfer, 24(9), p. 1541-1544, 1981.
92. Jongen, T., *Simulation and modelling of turbulent incompressible flows*, PhD, in EPF Lausanne: Lausanne, Switzerland, p., 1992.

93. Wolfshtein, M., *The velocity and temperature distribution in one-dimensional flow with turbulence augmentation and pressure gradient*, International Journal of Heat and Mass Transfer, 12(3), p. 301-318, 1969.
94. Chen, H. C. and Patel, V. C., *Near-wall turbulence models for complex flows including separation*, AIAA Journal, 26(6), p. 641-648, 1988.
95. El Hassan, M., Assoum, H. H., Sobolik, V., Vétel, J., et al., *Experimental investigation of the wall shear stress and the vortex dynamics in a circular impinging jet*, Experiments in Fluids, 52(6), p. 1475-1489, 2012.
96. Xia, J. L., Yadigaroglu, G., Liu, Y. S., Schmidli, J., et al., *Numerical and experimental study of swirling flow in a model combustor*, International Journal of Heat and Mass Transfer, 41(11), p. 1485-1497, 1998.
97. Wang, J., Priestman, G. H. and Tippetts, J. R., *Modelling of strongly swirling flows in a complex geometry using unstructured meshes*, International Journal of Numerical Methods for Heat & Fluid Flow, 16(8), p. 910-926, 2006.
98. Jawarneh, A. M. and Vatistas, G. H., *Reynolds stress model in the prediction of confined turbulent swirling flows*, Journal of Fluids Engineering, 128(6), p. 1377-1382, 2006.
99. Jones, W. P. and Pascau, A., *Calculation of confined swirling flows with a second moment closure*, Journal of Fluids Engineering, 111(3), p. 248-255, 1989.
100. Tsai, J. H., Lin, C. A. and Lu, C. M., *Modelling dum combustor flows with and without swirl at the inlet using Reynolds stress models*, International Journal of Numerical Methods for Heat & Fluid Flow, 5(7), p. 577-588, 1995.
101. Lu, P. and Semião, V., *A new second-moment closure approach for turbulent swirling confined flows*, International Journal for Numerical Methods in Fluids, 41(2), p. 133-150, 2003.
102. Shamami, K. K. and Birouk, M., *Assessment of the performances of RANS models for simulating swirling flows in a can-combustor*, Open Aerospace Engineering Journal, 1, p. 8-27, 2008.
103. Gupta, A. and Kumar, R., *Three-dimensional turbulent swirling flow in a cylinder: Experiments and computations*, International Journal of Heat and Fluid Flow, 28(2), p. 249-261, 2007.
104. Vondál, J. and Hájek, J., *Prediction of flow through swirl generator and validation by measured data*, Journal of Physics: Conference Series, 318(2), p. 022026, 2011.
105. Choudhury, D., *Introduction to Renormalization Group method and turbulence modelling*, in Technical Memorandum, TM - 107, Fluent Inc., p. 1-68, 1993.
106. Yaras, M. I. and Grosvenor, A. D., *Evaluation of one- and two-equation low-Re turbulence models. Part I—Axisymmetric separating and swirling flows*, International Journal for Numerical Methods in Fluids, 42(12), p. 1293-1319, 2003.
107. Al-Abdeli, Y. M. and Masri, A. R., *Stability characteristics and flowfields of turbulent non-premixed swirling flames*, Combustion Theory and Modelling, 7(4), p. 731-766, 2003.
108. Al-Abdeli, Y. M. and Masri, A. R., *Recirculation and flowfield regimes of unconfined non-reacting swirling flows*, Experimental Thermal and Fluid Science, 27(5), p. 655-665, 2003.
109. Al-Abdeli, Y. M., *Experiments in turbulent swirling non-premixed flames and isothermal flows*, PhD Thesis, in The University of Sydney: Sydney, p., 2004.
110. Toh, I., Honnery, D. and Soria, J., *Axial plus tangential entry swirling jet*, Experiments in Fluids, 48(2), p. 309-325, 2010.

111. Örlü, R. and Alfredsson, P. H., *An experimental study of the near-field mixing characteristics of a swirling jet*, Flow, Turbulence and Combustion, 80(3), p. 323-350, 2008.
112. Chigier, N. A. and Beer, J. M., *Velocity and static-pressure distributions in swirling air jets issuing from annular and divergent nozzles*, Journal of Basic Engineering, 86(4), p. 788-796, 1964.
113. Chigier, N. A. and Chervinsky, A., *Experimental investigation of swirling vortex motion in jets*, Journal of Applied Mechanics, 34(2), p. 443-451, 1967.
114. Sislian, J. P. and Cusworth, R. A., *Measurements of mean velocity and turbulent intensities in a free isothermal swirling jet*, AIAA journal, 24(2), p. 303-309, 1986.
115. Panda, J. and McLaughlin, D. K., *Experiments on the instabilities of a swirling jet*, Physics of Fluids, 6(1), p. 263-276, 1994.
116. Guo, B., Fletcher, D. F., Marquez, G., Al-Abdeli, Y. M., et al., *RANS calculation and measurements of instabilities in swirl-stabilized jets and flames*, in 2003 Australian Symposium on Combustion & The 8th Australian Flame Days, Monash University, Australia, p., 2003.
117. Weber, R., Visser, B. M. and Boysan, F., *Assessment of turbulence modeling for engineering prediction of swirling vortices in the near burner zone*, International Journal of Heat and Fluid Flow, 11(3), p. 225-235, 1990.
118. Najafi, A. F., Saidi, M. H., Sadeghipour, M. S. and Souhar, M., *Numerical analysis of turbulent swirling decay pipe flow*, International Communications in Heat and Mass Transfer, 32(5), p. 627-638, 2005.
119. Sander, G. F. and Lilley, D. G., *The Performance of an Annular Vane Swirler*, AIAA Paper, (83-1326), p. 27-29, 1983.
120. Maciel, Y., Facciolo, L., Duwig, C., Fuchs, L., et al., *Near-field dynamics of a turbulent round jet with moderate swirl*, International Journal of Heat and Fluid Flow, 29(3), p. 675-686, 2008.
121. *TNF Workshop Database*, [cited; Sandia National Laboratories, http://www.sandia.gov/TNF/swirlflames.html, Access Date: 15 January 2013, 2010.
122. Baughn, J. W. and Shimizu, S., *Heat transfer measurements from a surface with uniform heat flux and an impinging jet*, Journal of Heat Transfer, 111(4), p. 1096-1098, 1989.
123. Baughn, J. W., Hechanova, A. E. and Yan, X., *An experimental study of entrainment effects on the heat transfer from a flat surface to a heated circular impinging jet*, Journal of Heat Transfer (Transactions of the ASME, Series C), 113(4), p., 1991.
124. Lytle, D. and Webb, B. W., *Air jet impingement heat transfer at low nozzle-plate spacings*, International Journal of Heat and Mass Transfer, 37(12), p. 1687-1697, 1994.

Chapter 3

3 Corrections of dual-wire CTA data in turbulent swirling and non-swirling jets[6]

This chapter provides a detailed methodology for improving inaccuracies associated with swirl flow measurements by dual-wire hotwire anemometry.

3.1 Introduction

Constant Temperature Anemometers (CTA), also commonly referred to as hotwire anemometers have been extensively used for many years to measure velocity components and their fluctuations in axisymmetric gaseous jets. CTA applications include many other complex flow studies such as, turbulent boundary layers, wakes, swirling combustors and instabilities [1-4], due to their economical and efficient use compared to PIV or LIF. Data acquired by hotwire anemometers in such complex flows are also useful for imposing boundary conditions in numerical simulations and/or validating different CFD models. Resolving boundary conditions at the nozzle exit plane of a turbulent (non-swirling or swirling) jet typically requires data acquisition in the axial, radial and tangential (azimuthal) directions coupled with the post-processing of data using correlations that decompose raw voltages into mean velocities and turbulence components [5-7]. However, the accuracy of the post-processed CTA data is strongly affected by the orientation of the mean flow angle (α) with respect to the probe axis and the velocity gradient effect as shown in Figure 3.1. Velocity measurements with CTA probes are typically limited by the maximum acceptance angle (α_{max}), which is defined as the largest measurable angle of a velocity vector around the probe axis for a CTA probe. The maximum acceptance angle is usually identified from the geometry and orientations of sensor wires of a probe and is presented in Table 3.1 for different types of CTA sensors. In many turbulent swirling jets, the radial distribution of

[6] This chapter has been published as a full research paper:
Ahmed Z. U., Al-Abdeli, Y. M., Guzzomi, F. G., Experimental Thermal and Fluid Sciene, 70, p. 166-175, 2016.
Whilst efforts were made to retain original content of the article, minor changes such as number formats, font size style were implemented in order to maintain consistency in the formatting style of the thesis.

tangential velocity (<*w*>) at the nozzle exit plane is likely to take the form of a forced vortex (solid body rotation), free vortex or a combination of both [8, 9]. Whilst common practice is to attribute a single swirl number to each combination of tangential and axial flow conditions through a nozzle [10], some of these definitions appear more commonly in the literature. The widely used definition of swirl number is based on the ratio of axial flux of tangential momentum to the axial flux of axial momentum [11]. There also exists a more simplified expression for swirl number S (which is used in this study) as defined by the ratio of bulk tangential-to axial-velocity [9, 12, 13]:

$$S = \frac{W_b}{U_b}, \tag{3.1}$$

where, U_b, W_b are the bulk axial and bulk tangential velocities, respectively and typically

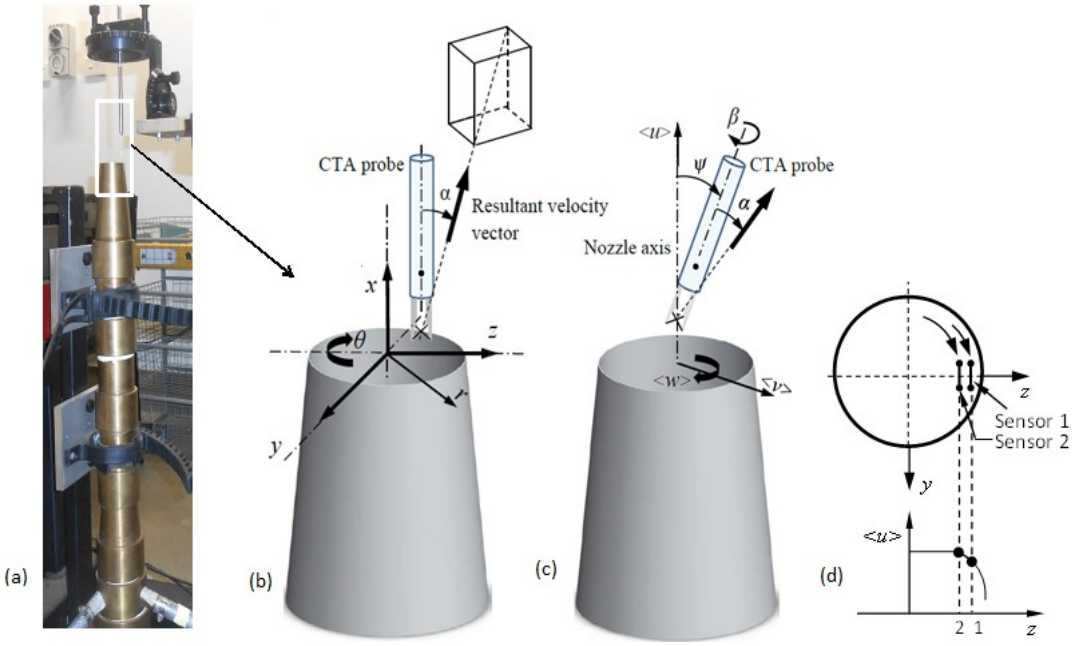

Figure 3.1 (a) Swirl nozzle with CTA probe holder held by yaw/pitch/roll manipulator; (b) and (c) detailed view of the nozzle exit plane with the coordinate system and angle definitions; and (d) top view on exit plane showing velocity gradient effects near solid boundaries [Key- α: Resultant velocity vector with respect to the probe axis; β: roll angle; ψ: probe inclination angle with respect to the nozzle axis and θ: azimuthal angle around nozzle].

determined across the nozzle exit plane. In practice, the exact value of swirl number depends on its definition and swirl generation methods. With the above in mind, the consequences are a significant radial variation of the mean flow angle at the exit plane which occurs due to changes in $\langle w \rangle$, even if the axial velocity ($\langle u \rangle$) follows a uniform radial profile. As such, radial variation of $\langle u \rangle$ and $\langle w \rangle$ creates position dependent (localised) swirl numbers and resultant velocity vector angles which affect the accuracy of CTA measurements. Additionally, the existence of high velocity gradients and turbulence levels near the walls of a nozzle adds further measurement discrepancies due to the boundary layers. Although a number of excellent (general) studies into the application of CTA exist in the literature [5, 14-16], an investigation into the effects of the mean flow direction on the accuracy of measured velocity components (for a turbulent swirling jet) has not been reported and is the focus of this present research.

In addition to extensive use of laser-based non-intrusive techniques to resolve turbulent swirling isothermal jets [17, 18], intrusive techniques such as CTA measurements using single- [19, 20], dual- (X-) [21-23] and multi-wire (tri-wire, four-wire) hotwire probes [24] as well as multi-hole pressure probes [25-28] have also been used. Although the mean flow directions can be measured by multi-hole pressure probes, the relative size of these probes (typically 3-6 mm) may alter the flow field and create local regions of recirculation in swirl flows [26]. Moreover, inability to measure turbulence makes the use of multi-hole pressure probes less popular in recent times as turbulence significantly influences the flow and surface flux characteristics in impinging and swirling jets, and often is a prerequisite in simulations of complex flows. In contrast, the use of CTA measurements has some merit over non-intrusive techniques as they preclude the need to seed flows or require optical access. CTA measurements also provide high frequency (analogue) data series and prevent the build up of seed powder (as used with laser diagnostics) onto solid walls which can modify near wall turbulence characteristics. However, for three-dimensional and highly turbulent flows measurements with CTA probes [19, 20] are typically challenging and susceptible to inaccuracies. These inaccuracies are due to inconsistent orientation of the probe axis relative to the flow direction as well as near wall measurements that magnify velocity gradient effects, which provide variation of cooling wires [24]. Numerous studies using multi-wire probes to measure three-dimensional turbulent flows, in both non-swirling and swirling jets, are available in the literature [3, 24, 29, 30]. The large probe size and wire separations (about 2-4.5 mm), limited probe acceptance angle, intensive calibration procedures and likely prong-

induced wakes, limit the use of multi-wire probes in swirl flow measurements since both the mean flow direction and velocity gradient effects change with radial position [3, 5, 22, 24]. As such, probes with smaller wire separations such as the dual-wire may have reduced flow perturbations and better spatial resolution than multi-wire probes. Therefore, the current study uses a dual-wire probe in swirling jets with the aim of quantifying the detrimental effects associated with velocity gradients which arise from wire separation and measurements undertaken outside the probe acceptance angle. The techniques implemented in this study may also be used for multi-wire probes.

When establishing boundary conditions of non-recirculating swirl jets at the nozzle exit plane (x = 0 mm), the radial velocity component ($<v>$) can be relatively insignificant compared to other velocity components [31-35]. Consequently, in many instances only two velocity components ($<u>$, $<w>$) are resolved using dual-wires (X-wire probes) [21-23, 31, 35-37]. Most CTA studies with X-wire probes apply sensor calibrations using the look-up-matrix method that establishes a set of voltage-velocity pairs followed by a two-stage interpolation scheme [5]. This method is time intensive and the calibration accuracy is dependent on the velocity component and its fluctuation normal to the probe wire-prong plane; widely referred to as the out-of-plane contaminations [5]. Whilst this error can be reduced by using a position dependent probe inclination angle (ψ) or rotation angle (β) such that the mean flow direction (α) is within the probe acceptance angle (Table 3.1), this approach used for dual-wire probes has not been adequately described in the literature. Although some near-wall turbulent boundary layer studies [36-38], including Ribeiro and Whitelaw [35] for weakly swirling (S = 0.26) coaxial jets, have detailed methodologies to identify dominant flow directions by orienting (in yaw) the X-wire probe, such methods are not accurate when the swirl intensity and/or turbulence is high [39]. Moreover, these earlier works [35, 36] have neither investigated the velocity gradient effects nor the impact of a radially varying mean flow direction on measurements undertaken with these probes. CTA measurements in highly swirling flows are further complicated as the resultant flow direction (represented by α in Figure 3.1) may reach up to 45^o from the probe axis [21]. However, X-wire probe calibrations are often performed over a smaller angular range ($\psi = \pm$ 30^o) by varying the probe inclination angle in relation to an axial (non-swirling) flow [21, 23]. In addition to considering variations of α, the use of multi-wire probes (dual- or tri-wires) in near-wall flows results in individual sensors being subjected to strong velocity gradients across their small radial separation [40]. The above challenges associated with applying X-wire probes in swirling flows, warrants detailed analysis to better understand the factors

affecting their measurement accuracy. Whilst the experimental methodologies described in the present research extend the observations made beyond low swirl, this study also avoids the use of a coaxial nozzle in order to avoid cross-interference between both effects which may be magnified with the presence of annular jets.

The above discussion highlights that there is a lack of systematic testing to establish methodologies for orienting CTA X-wire probes to increase measurement accuracy in turbulent swirl flows for a range of Reynolds numbers (the ratio of inertia force to viscous force, defined in Equation 3.9). This research addresses this knowledge gap by investigating the effects of X-wire probe inclination and velocity gradient on measurement accuracy.

3.2 Experimental techniques

3.2.1 CTA system

A three-channel hotwire anemometer system (Dantec Dynamics, Denmark) is used in this study. The system comprises a Streamline main frame (model: 90N10), three CTA modules each dedicated to an individual sensor/wire (model: 90C10), one module (model: 90C20) for fluctuating temperature measurements, a gaseous (jet) calibration system (model: 90H10), a pitch/yaw/roll manipulator (model: 90H03) and an air filter unit (model: 90H04). Data acquisition and post-processing is achieved using Streamware (version 5.12). Raw voltages are sampled from each sensor using a data acquisition board (National Instruments, model: NI-PCI6143), which allows 16-bit data resolution at a peak sampling rate of 250 kHz/channel and is interfaced with the main frame (model: 90N10). Changes in ambient temperature over the duration of the experimental data acquisition are estimated at ± 3^{o}C. A system temperature probe (model: 90P10) is integrated with the main frame to compensate for the temperature variations. The correction formula used in conjunction with the temperature probe to compensate for anemometer output is [41]:

$$E_{corr} = \sqrt{\frac{T_w - T_{ref}}{T_w - T_\infty}} E \,. \tag{3.2}$$

E is the (raw) acquired voltage, T_w, T_{ref} and T_∞ are the hot sensor temperature, ambient reference temperature (at which calibration was performed) and the instantaneous ambient temperature during the experiment, respectively. The Streamline calibration system is used for velocity and directional calibrations of the hotwire probes in the range of 0.50 – 25 m/s and ψ = -40^{o} to +40^{o} respectively, in a uniform non-swirling (axial) flow. Directional

calibration accounts for heat dissipation in the tangential direction of the sensor and is achieved by rotating the probe through a set of yaw angles. At each angular position, yaw factors for each sensor wire are derived using a system of cooling velocity equations, but this standard (OEM) calibration is performed at a uniform (non-swirling) axial flow, where α is within the probe acceptance angle (Table 3.1). The average yaw factors at all angular positions for each sensor wire are then applied during velocity decomposition in the probe coordinate system. Calibration velocities from the voltage signals of each wire are obtained from a fourth order polynomial. The probe manufacturer designated calibrations for velocity and directions do not account for the effects of swirl in modifying the mean flow angle (α) or assessing the inaccuracies that arise if the angle approaches or exceeds α_{max} of the X-wire probe.

Table 3.1 Major specifications for different wire sensors probe. Source [41]

TYPES OF PROBES	*WIRE SEPARATION /MEASUREMENT VOLUME SIZE* (mm)	*PROBE ACCEPTANCE ANGLE* (deg.)
Single-wire (55P11)	-	$\pm 90^{o}$
Dual-wire (X-wire) (55P61)	1	$\pm 45^{o}$
Tri-wire (55P91)	3	$\pm 35^{o}$

Hotwire probes fitted with a single-wire (model: 55P11) and dual-wire (X-wire) (model: 55P61) are used in this study. Both feature tungsten wire sensors (diameter d = 5μm and length l = 1.25 mm) held in a probe body. This sensor geometry has an aspect ratio l/d > 200, which is consistent with recommendations by Liagrini and Bradshaw [42] to minimise end-conduction effects. For each data point presented in this research, CTA signals are acquired for 2 seconds at a sampling frequency of 60 kHz/channel and low-pass filtered at 30 kHz, which gives the sampling resolution of $0.006D/U_f$ with U_f the bulk volumetric flow rate (defined later in Section 2.6). The combination of relatively short sampling period and high sampling rate ensures measurements are less susceptible to any perturbations in volumetric flow rates arising from the use of flow meters. An overheat ratio of 0.8 approximates the sensor wire temperature to be 250^{o}C. Although this study focuses on the dual-wire probe, the single-wire probe is used first to resolve the approximate direction of the resultant velocity vector by orienting it at different radial locations across the nozzle exit plane and determining

the angle ψ where a peak velocity reading occurs. The X-wire probe is subsequently used to measure the axial (<u>) and tangential (<w>) components and identify the effects of localised orientation (ψ) and rotation (β) on the measurements.

3.2.2 Swirl nozzle

Figure 3.1a shows the gaseous jet nozzle used in the experiment that is designed to generate both non-swirling and swirling turbulent flows. At the exit plane, the nozzle ends with a diameter of D = 40 mm and a sharp edge (~ 0.2 mm) to avoid flow separation at or near the nozzle periphery. The nozzle induces swirl aerodynamically (i.e. does not use radial vanes or helical inserts) using three tangential ports located at x = -573 mm (x/D = -14.73), upstream of the exit plane (x/D = 0). This rotational stream is also augmented with axial streams, delivered from two radially opposed ports at x = -687 mm (x/D = -17.18). The axial streams pass through flow conditioning layers (mesh screens and aluminium honeycombs) before reaching the tangential ports to reduce large-scale turbulence. Thus the total volumetric flow (Q_T) at the exit plane is the sum of the flow from two axial ports (Q_a) and the three tangential ports (Q_t). Further detail on the preliminary CFD optimisation of the nozzle and its detailed boundary condition features are available in the author's other studies [12, 43]. Dry (filtered) air is supplied to the nozzle throughout the testing using pressure regulated (calibrated) flow meters and the nozzle operates in a quiescent environment.

The hotwire probe is positioned using a manual traversing mechanism that allows displacement in two mutually perpendicular directions (Cartesian y- and z-axes) with a resolution of 0.02 mm (0.016l). The alignment of the CTA probe axis with the geometric centreline of swirl nozzle is approximated to be within 0.1 mm (0.08l) and vertical displacement (Cartesian x-axis) is achieved by a separate mechanism with an accuracy of 0.5 mm (0.4l). Horizontal alignment of the nozzle exit plane and the CTA probe is ascertained using a 2D spirit–level and a spherical bubble. The entire setup and positioning mechanisms are mounted to a heavy pedestal with ground level damping.

3.2.3 Velocity and directional response

CTA measurements infer the probe axis should coincide with the mean flow direction to achieve a reasonable level of accuracy. Such an alignment of the probe with the mean flow is, however, often difficult to maintain in many turbulent three-dimensional (non-swirl) flows as well as more complex swirl flows. To minimise errors associated with the misalignment of the probe with the mean flow, the standard procedure commonly used first measures a non-

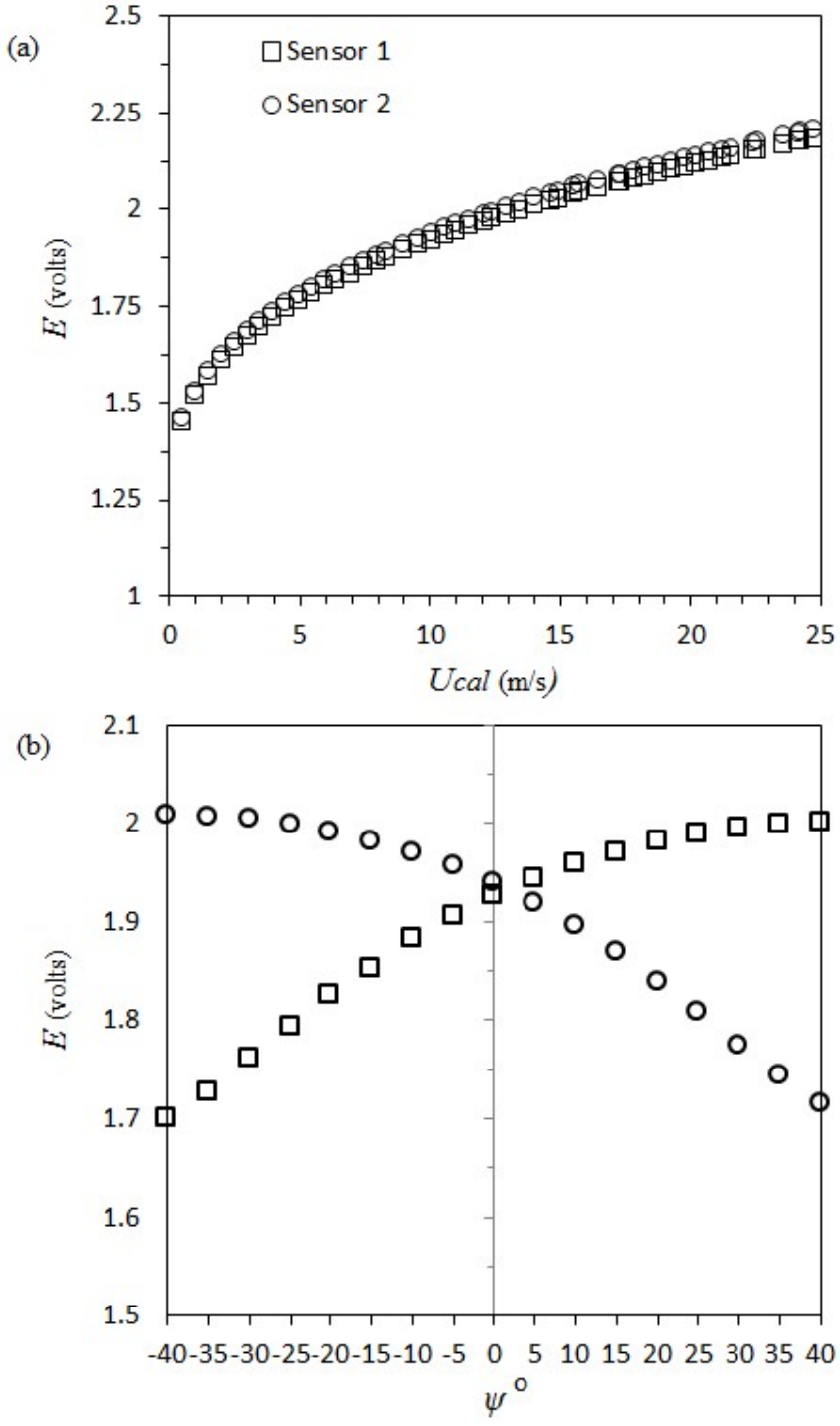

Figure 3.2 Data (raw) acquired using the standard calibrator system (x = 0 mm) (a) Velocity calibration (X-wire probe): variation of sensor voltage E versus calibrator bulk flow speed ($Ucal$) for $\psi = 0^{o}$, (b) Directional calibration (X-wire probe): variation of sensor voltage E versus probe inclination angle (ψ) for $Ucal$ = 12 m/s.

inclined sensor's response over different velocities. This is followed with directional sensitivity by inclining the X-wire probe against a non-swirling flow issued from the same calibrator across a range of angles, as shown in Figure 3.2. The errors associated with such checks for various angles are discussed later in this chapter (Figure 3.3). The data presented in Figure 3.2 shows the temperature corrected calibration curves for uncorrelated velocity (Figure 3.2a) and directional sensitivity (Figure 3.2b) against the acquired voltage (E) for the X-wire probe. This velocity calibration is uncorrelated because the individual sensor data has not been decomposed into velocity components. It is evident that in a non-swirling flow, both sensors follow the same relationship between the voltage and the calibration velocity ($Ucal$). The directional response also shows a similar pattern with the response almost merging together at $\psi = 0^o$ due to the equal velocity vector angle between both sensors and the probe axis. For the same relative orientation (ψ), the variation between readings from the two sensors is less than 1% over the tested velocity range.

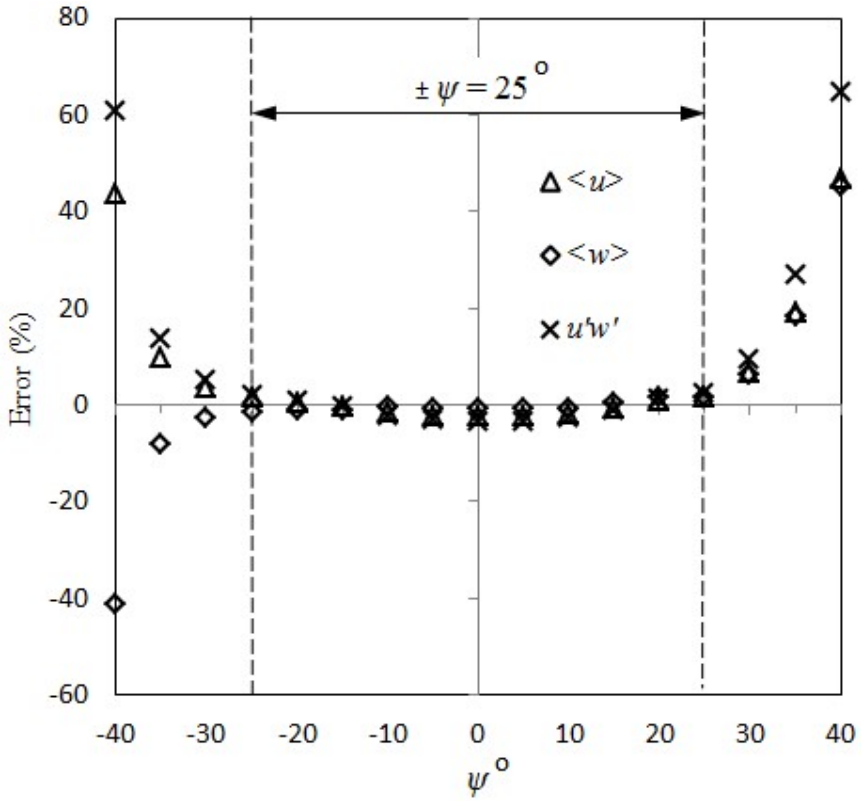

Figure 3.3 Post-processed velocity data acquired using the standard calibrator system (x = 0 mm). The errors due to the directional response for the axial (<u>), tangential (<w>) velocity components and shear stress for the X-wire probe.

By using the same calibration system but orienting the X-wire probe axis, it is possible to obtain the decomposed velocity components and Reynolds shear stress over different probe inclination angles ψ, depicted in Figure 3.3. The maximum error for both velocity components ($<u>$ and $<w>$) and shear stresses ($\overline{u'w'}$) are less than 2% for $\psi \leq \pm 25^{o}$, where beyond this limit the error increases rapidly and exceeds 40% at $\psi = \pm 40^{o}$. Because the data presented in Figure 3.3 is acquired in the axial flow supplied by the calibrator, these results clearly show that if the probe axis is not adequately aligned with the mean flow direction within $\pm 25^{o}$, significant deviation may result. This demonstrates the need to explore the effects of swirl number on probe response, where the resultant velocity vector can vary appreciably in the radial direction and ultimately how the accuracy can be improved through applying angular orientation (ψ).

To systematically study the effects of mean flow direction and (shear layer) velocity gradients in relation to both non-swirling ($S = 0$) and swirling flows ($S = 0.27$-1.05) using both the single-wire and X-wire probes, the methods described next are tested in conjunction with the swirl nozzle presented in Figure 3.1.

3.2.4 Probe alignment and mean flow direction

The first step for a reliable CTA measurement in turbulent jets is to ensure the mean flow direction is within the acceptance cone of the X-wire probe. In many instances, however, measurements are performed to a lower angle than the maximum acceptance angle to minimise errors. The results in Section 2.3 imply that a reasonable accuracy can be achieved when the mean flow direction is maintained within $\pm 25^{o}$, although the acceptance cone for the X-wire probe is much higher than this value. To achieve this, the single-wire probe is used first to estimate the mean flow direction over the radial extent of the given swirl nozzle at the exit plane. Subsequently, X-wire probe is also used to ensure the mean flow direction is within $\pm 25^{o}$ for all swirl numbers. The conceptual methodology to align the flow using single-wire probe (only) is similar to Ribeiro and Whitelaw [35] for weakly swirling flows. When swirl number or turbulence increases the use of single-wire probes (only) may not be reliable due to the sharp increase of inaccuracies with higher turbulence and out-of-plane velocity errors [39, 44]. As such, this study uses both single- and X-wire probe for a reliable CTA measurements for a wider range of swirl numbers. The methodology adopted in the research also estimates the probe inclination angle required for a given swirl number and the radial variation of the mean flow angles across the nozzle radius.

At a specific radial location, the single-wire probe is yawed over $\psi = 0^o$ to 80^o and data is acquired at 5^o increments. For any bulk swirl and Reynolds number, the variation of α over different radial locations can then be determined at $\beta = 0^o$. The resultant velocity vector angle (α) corresponds to ψ, where the sensor signal (voltage) is a maximum because the sensor is subjected to peak convective heat loss at this angular orientation. To further resolve the effects of probe rotation (β) on ψ, the single-wire probe is also rotated through roll angles of $\beta = \pm 40^o$, similar to Ribeiro and Whitelaw [35], after incling the probe at the approximated ψ. The results show that such a procedure is effective in low swirl number flows where turbulence is typically small and out-of-plane contaminations are negligible. However, in higher swirl number flows, the initial velocity vector angle estimated by the single-wire probe may not be accurate due to the single-wire limitations, as mentioned above. As a result, at higher swirl numbers, the resultant flow direction is determined by using the instantaneous velocities from the X-wire probe after inclining the probe at a certain angle (ψ) for a given swirl number. In this regard, the following expression may be used to identify α for the X-wire probe [45],

$$\frac{u_{1,e} - u_{2,e}}{u_{1,e} + u_{2,e}} = \tan\alpha \ , \tag{3.3}$$

where, $u_{1,e}$ and $u_{2,e}$ are the instantaneous effective cooling velocities of wire 1 and wire 2, respectively, and α is the angle between the mean flow direction and the probe axis (to be determined). Once α is calculated using Equation (3.3) and it remains within 25^o at any radial location, the axial and tangential velocity components and their turbulence components are finally obtained in the laboratory coordinate system (Figure 3.1) by using the following matrix transformation:

$$\begin{bmatrix} <u> \\ <w> \end{bmatrix} = \begin{bmatrix} \cos\psi & -\sin\psi \\ \sin\psi & \cos\psi \end{bmatrix} \begin{bmatrix} <u_p> \\ <w_p> \end{bmatrix}, \tag{3.4}$$

where $<u_p>$, $<w_p>$ are CTA components resolved with the probe coordinate system. It is worth noting that the total velocity vector angle with respect to the vertical axis (i.e. the laboratory x-axis) is the sum of α and ψ.

3.2.5 Velocity gradient effects

Whilst the aforementioned methodologies help quantify (and mitigate against) inaccuracies originating from excessive or misaligned probe angular orientation ψ with α,

they do not help quantify the superimposed effects of velocity gradients. Figure 3.1d shows that a larger separation between different sensors (i.e., poor spatial resolution of X-wire probes), can lead to individual sensor wires being subject to differing cooling velocities. This happens particularly within the shear layer in the outer part of a nozzle or channel flow due to the presence of solid walls. The error in hotwire measurements due to shear layer (at the nozzle exit plane) in the direction of the wall are corrected by expanding the effective cooling velocity for the two wires in series. The desired (corrected) mean velocities (<u> and <w>) for velocity gradient effects in the shear layer can be determined iteratively using the following equations [46, 47]:

$$< u_X >=< u > + \frac{\Delta}{2}\frac{\partial < w >}{\partial r} + \frac{1}{2}\left(\frac{\Delta}{2}\right)^2 \frac{\partial^2 < u >}{\partial r^2} + \mathrm{O}\left(\Delta^3\right) \tag{3.5}$$

$$< w_X >=< w > + \frac{\Delta}{2}\frac{\partial < u >}{\partial r} + \frac{1}{2}\left(\frac{\Delta}{2}\right)^2 \frac{\partial^2 < w >}{\partial r^2} + \mathrm{O}\left(\Delta^3\right). \tag{3.6}$$

In Equations (3.5) and (3.6), $< u_X >$ and $< w_X >$ represent the X-wire probe measured (uncorrected) mean axial and azimuthal velocity, respectively. The separation distance between the two wires is Δ. When the probe advances towards a solid wall, in addition to the (fixed) velocity gradient effect due to wire separation, different signal responses will arise from each wire as the solid walls are approached. These may be treated as an additional (virtual) distance between the wires [46] with the consequence of artificially magnifying the non-axial velocity component in non-swirling flows as the probe advances towards solid walls. Talamelli et al. [46] also suggested that probe geometrical imperfections can be accommodated via the wire separation distance Δ. To achieve this, the distance Δ is first determined at radial positions commensurate with the shear layer using the Equation (3.6) by assuming $< w >= 0$ in a non-swirling flow and utilising both both single- and X-wire probe data in the same flow condition (i.e. without any modifying the flow settings). In this manner, $\frac{\partial < u >}{\partial r}$ can be calculated from Equation (3.6) using the single-wire probe data and the same equation is used to solve for Δ at each radial location by neglecting the second order term. Once Δ is obtained for each radial location in the shear layer, $< u >$ and $< w >$ are determined iteratively by considering the second order terms from Equations (3.5) and (3.6). This methodology is graphically presented through the flow chart which appears in the Appendix. Finally, it should be mentioned that velocity gradient effects also arising from non-uniform temperature distributions along the length of the wires, are not considered in the present study

since wire lengths have been typically very small with a (X-probe) sensor aspect ratio $l/d >$ 200 [5]. Moreover, variations of velocity along the wire length (1.25 mm) are not expected to differ appreciably for a nozzle of relatively large diameter (40 mm).

3.2.6 Test conditions

Table 3.2 presents the swirl conditions used in this chapter. The swirl number (S) is determined using Equation (3.1) whereby bulk axial and tangential velocities are measured by integrating CTA resolved data[7] (acquired at $x/D = 0.025$) across the nozzle radius (R):

$$U_b = \frac{2}{R^2}\int_0^R r < u > dr, \tag{3.7}$$

$$W_b = \frac{2}{R^2}\int_0^R r < w > dr. \tag{3.8}$$

The Reynolds number (Re) is defined as,

$$Re = \frac{U_f D}{\nu}, \tag{3.9}$$

where, D is the nozzle diameter (40 mm) and ν is the kinematic viscosity of air (15.11 x 10^{-6} m^2/s) and U_f is the velocity calculated from the total volume flow rate:

$$U_f = \frac{4Q}{\pi D^2}. \tag{3.10}$$

The total flow (volume) Q is the sum of the axial and tangential flows (Figure 3.1a) that is fed into the nozzle via their respective flowmeters. In aerodynamically generated swirl flows, the ratio between the total tangential flow to the total flow (Q_t / Q_T) plays a major role [12] in producing a specific swirl number for the same total flow (or Reynolds number). However, the relationship between Q_t / Q_T and swirl number (S) is not necessarily linear due to the complex internal flow from multiple inlet streams and pressure drops along the length of the nozzle. Figure 3.4 shows the relationship between S and Re against Q_t / Q_T.

[7] The accuracy of X-wire CTA probe measurements is available in the second paragraph of section 4.2.2.

Table 3.2 Test conditions obtained from the swirl nozzle.

No.	Re $\left(U_f D/\nu\right)$	U_b (m/s)	W_b (m/s)	S $\left(W_b/U_b\right)$	u'/U_b (%)
1	35,000 ± 4%	13.26	0.00	0.00	5.35
2		13.14	3.50	0.27	9.35
3		13.74	6.18	0.45	9.78
4		13.71	10.51	0.77	11.88
5		17.39	14.43	0.83	27.41
6		17.57	18.39	1.05	36.89
7	24,600 ± 3%	9.32	0.00	0.00	6.30
8		9.10	2.81	0.31	10.83
9		9.91	5.79	0.58	17.36
10		11.00	7.01	0.64	21.11
11		11.55	8.36	0.72	24.31
12		11.00	9.34	0.85	26.93
13	11,600 ± 6%	4.39	0.00	0.00	5.79
14		4.28	1.15	0.27	9.61
15		5.03	1.63	0.32	11.20
16		4.95	2.92	0.59	18.13
17		5.08	3.75	0.74	24.42

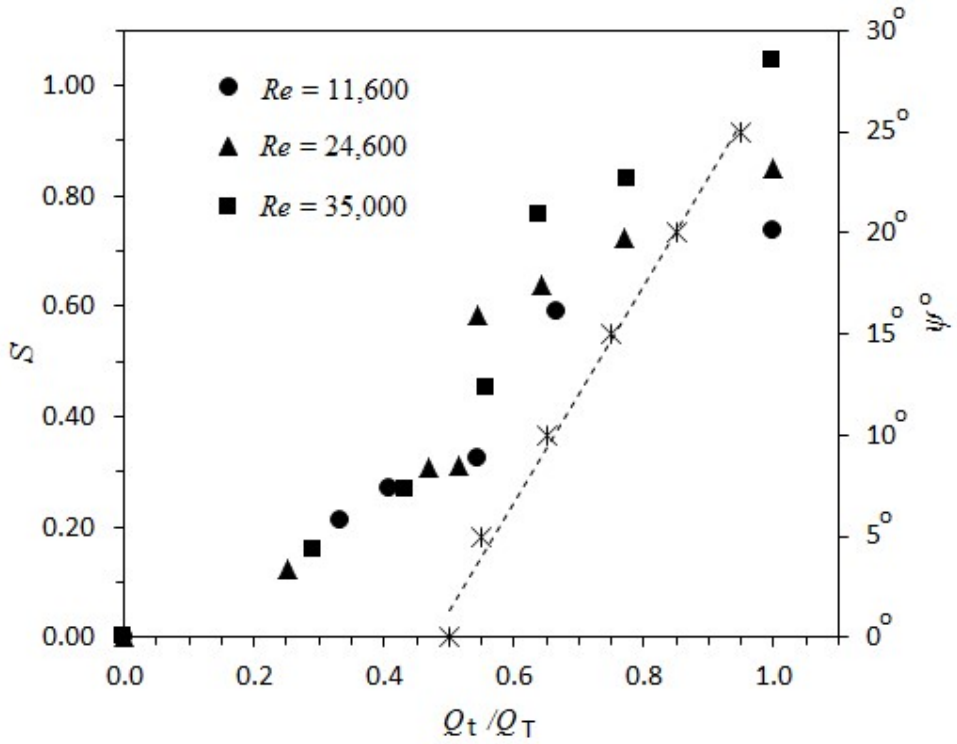

Figure 3.4 Data acquired using the swirl nozzle (x = 1 mm). Variations of swirl number (S) versus (Q_t/Q_T) for different Reynolds numbers (Re = 11,600 – 35,000). The data shown in (*) marker with the trend line and the second (right-hand) axis is used later in conjunction with Figure 3.7.

The uncertainty in *Re*, shown in Table 3.2, is estimated as follows [48, 49]:

$$\varepsilon = \pm\sqrt{\varepsilon_s^2 + \varepsilon_r^2}\ , \tag{3.11}$$

where, the systematic error, ε_s is determined from hotwire calibrations and the difference between CTA data and a polynomial fit for the volume flow rate. ε_r is the random error determined by:

$$\varepsilon_r = \sqrt{\varepsilon_{r,Qa}^2 + \varepsilon_{r,Qt}^2}\ , \tag{3.12}$$

where, $\varepsilon_{r,Qa}$ and $\varepsilon_{r,Qt}$ are the standard uncertainty associated with the axial and tangential flows respectively. These uncertainties are determined by the method described in [50] for a flow that consists of several flowmeters (correlated or uncorrelated).

3.3 Results and discussion

The significance of applying hotwire sensor corrections to compensate for the effects of probe alignments (ψ) for dual-wire probes in swirling jets is discussed first. Velocity gradient effects near solid walls (shear layer region) of a non-swirling flow ($S = 0$) is then presented.

3.3.1 Effect of probe alignment and mean flow direction

Errors associated with the misalignment of the dual-wire probe for increasing swirl number can be improved via the techniques described in the Section 2.4. Before presenting the analysis for the effects of swirl on the mean flow direction and realignmnent of X-wire CTA probes, a single-wire CTA sensor is first used and oriented preliminarily across a series of inclination angle (ψ) at low (S = 0.27) and high (S = 1.05) swirl numbers for the highest Reynolds number (*Re* = 35,000), depicted in Figure 3.5. This preliminary data is used to show the range of probe inclination angles (ψ) for various radial locations at the swirl nozzle exit plane. Whilst this data cannot resolve the various velocity components, the single-wire probe orientation does succeed in capturing the mean velocity direction. For this reason, the data plotted in Figure 3.5 shows the sensor signal (*E*). Figure 3.6a indicates that for $S = 0.27$ the peak sensor voltage is obtained at inclination angles not exceeding $\psi = 20^o$; i.e. well within the acceptance angle of an X-wire probe (Table 3.1). Furthermore, probe rotation around its own axis (β) also shows negligible effects (not reported in the figure), which

indicates the mean flow direction (α) at different radial locations is closely aligned with the CTA probe axis. These tests also show that for a relatively low swirl number (S = 0.27), X-

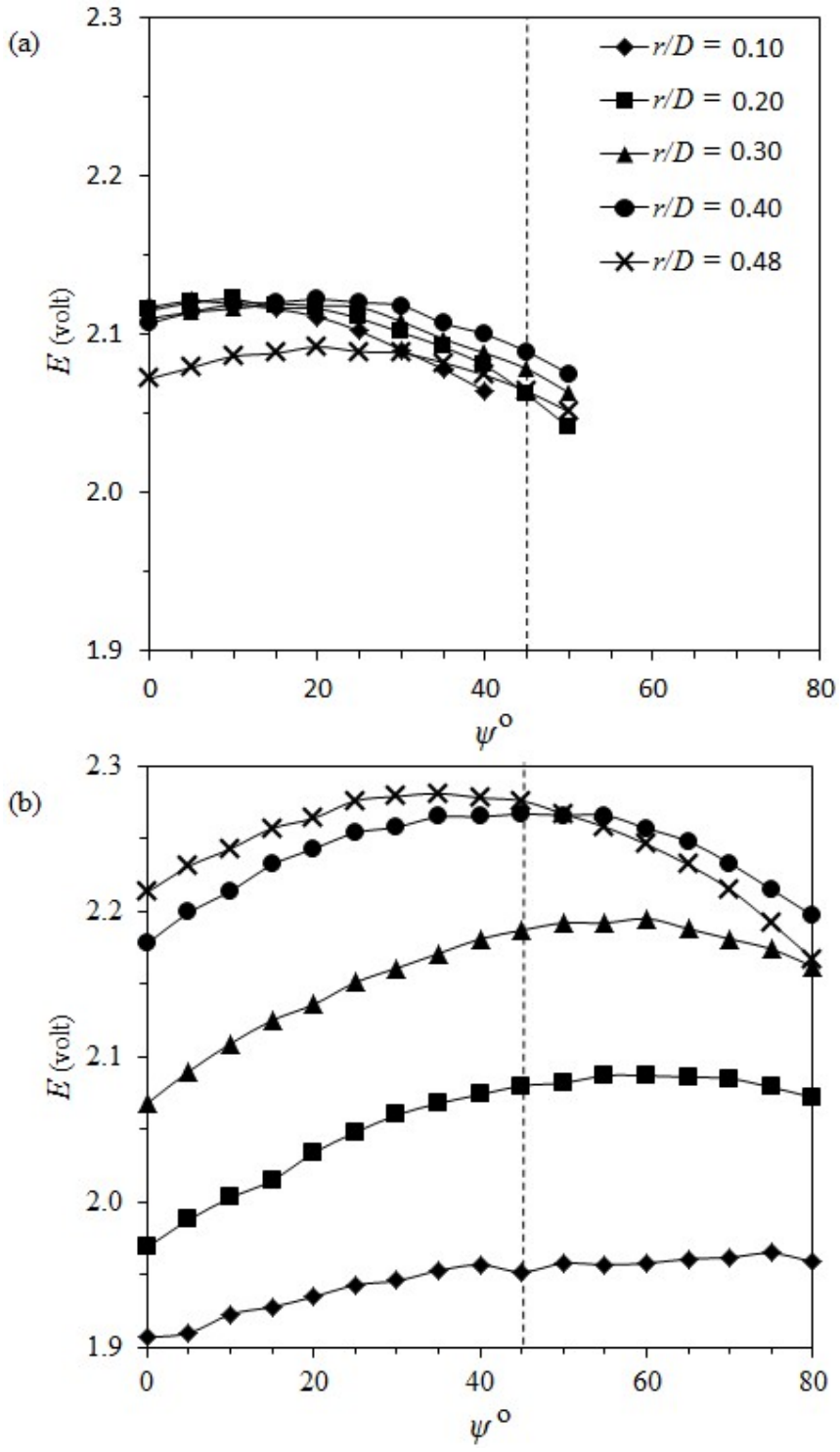

Figure 3.5 Data acquired using the swirl nozzle (x = 1 mm) for Re = 35,000. Mean velocity vector angle approximated by single-wire probe: (a) S = 0.27, (b) S = 1.05. The dashed

vertical line designates the upper limit of the acceptance angle (Table 3.1) for an X-wire probe (at $\psi = 0^o$).

wire probe inclination may not lead to more accurate measurements (whilst traversing the probe across the nozzle exit plane). In this regard, the data acquired will be within the dynamic range of each sensor (Figure 3.3). In contrast, Figure 3.5b shows that for strongly swirling flows (S = 1.05) the measured profiles indicate that the mean velocity vector directions are at $\psi \geq 45^o$, particularly at radial locations closer to the nozzle centreline ($r/D \leq$ 0.3). At these conditions, the use of an X-wire probe without inclination can result with the mean flow direction exceeding the acceptance angle limit (Table 3.1 and Figure 3.3). The above observations demonstrate there is more necessity for probe inclination at higher swirl numbers to ensure the angle (α) is well within the acceptance angle to improve data reliability. Figure 3.6 also presents the variation of ψ in a moderately swirling flow (S = 0.74) but at a lower Reynolds number (11,600). These results show the mean flow direction, represented by the data points where the sensor signal is a maximum, lies between $\psi = 35^o$ and 50^o for all tested radial locations. These results further reinforce the need to incline the X-wire probe (even) for moderate swirl and Reynolds numbers. The data presented in Figures 3.5 and 3.6 should be only taken as a preliminary analysis because single-wire probes are more accurate for low turbulence (swirl numbers), where anisotropic turbulence and out-of-plane contaminations are relatively minimal [39, 51].

Based on the preliminary analysis of variation in the mean flow direction, a series of probe inclinations are then applied to a dual-wire probe in a swirling flow. The aim is to then determine whether the angle (α) remains within 25^o across the measurement plane to improve data accuracy (Figure 3.3). Figure 3.7 illustrates the mean flow angle (α) with swirl number (S) for Re = 35,000 (Figure 3.7a) and Re = 11,600 (Figure 3.7b) for radial variation ($-0.25 \leq r/D \leq 0.48$). In this regard, the angle (α) is obtained using Equation 3.3 after inclining the X-wire probe to experimentally resolved (pre-set) values of ψ = 0, 5, 10, 15 or 25^o. The value of probe inclination (ψ) for each swirl number (S) was found to be directly proportional to both swirl number and the ratio Q_t / Q_T as shown in Table 3.3 and the second (right-hand) axis of Figure 3.4. At relatively low swirl numbers (S = 0.27), Figure 3.7a shows that the mean flow angle (α) increases linearly with radial position (r) and is less than 15^o except close to the nozzle wall where α abruptly increases due to the shear layer effect. At larger swirl numbers (S = 0.45–1.05), the angle (α) also increases linearly up to a threshold value and then decays. The location of this critical r/D position depends on the swirl number. Thus, by inclining the

axis of the X-wire probe to approach α with the assistance of preliminary data presented in Figures 3.5 and 3.6, it is possible to realign the probe for higher data yield and accuracy. This methodology helps ensure the mean flow direction is within the accurate measurement range of the probe. In this manner, for the specific conditions tested in this chapter, the mean flow direction does not exceed $\alpha = 20^o$ even for the highest swirl number used (S = 1.05). By applying the above methodology to realign the probe axis to ψ, the data acquired is expected to be within the dynamic range of the probe (Figure 3.3). A slight increase in α does occur near the wall due to the shear layer but this angle ($\alpha = 25^o$) still remains within the dynamic range. Figure 3.7b also shows the relationship between α and ψ over the nozzle radius at Re = 11,600. Almost similar qualitative variations with swirl number are observed. However, these start at smaller swirl numbers compared to those resolved at a higher Reynolds number as shown in Figure 3.7a.

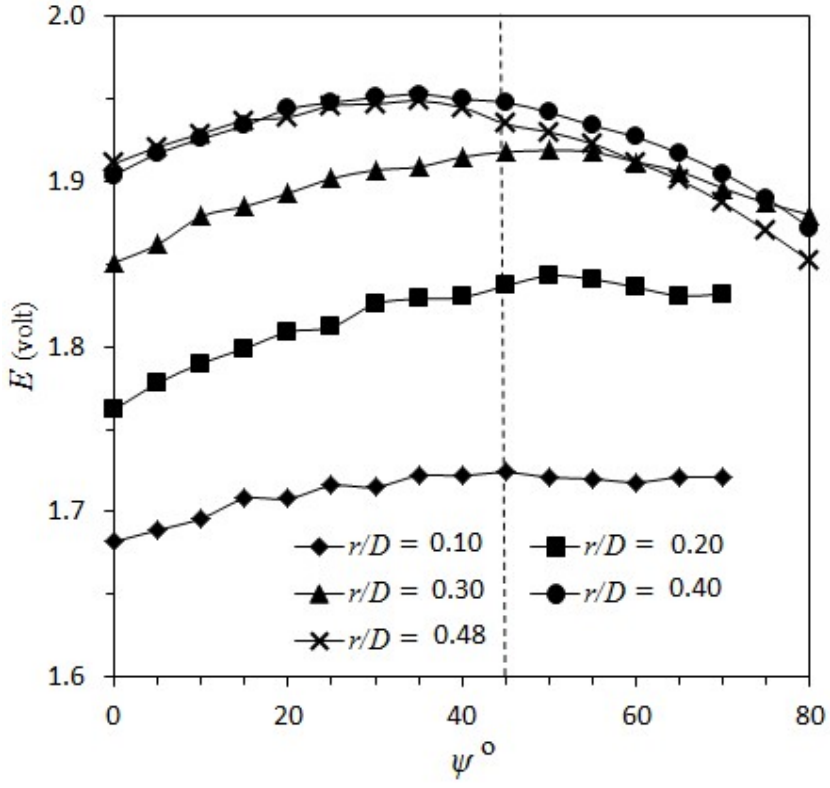

Figure 3.6 Data acquired using the swirl nozzle (x = 1 mm) for Re = 11,600 and S = 0.74. Mean velocity vector angle approximated by single-wire probe. The dashed vertical line designates the upper limit of the acceptance angle (Table 3.1) for an X-wire probe (at $\psi = 0^o$).

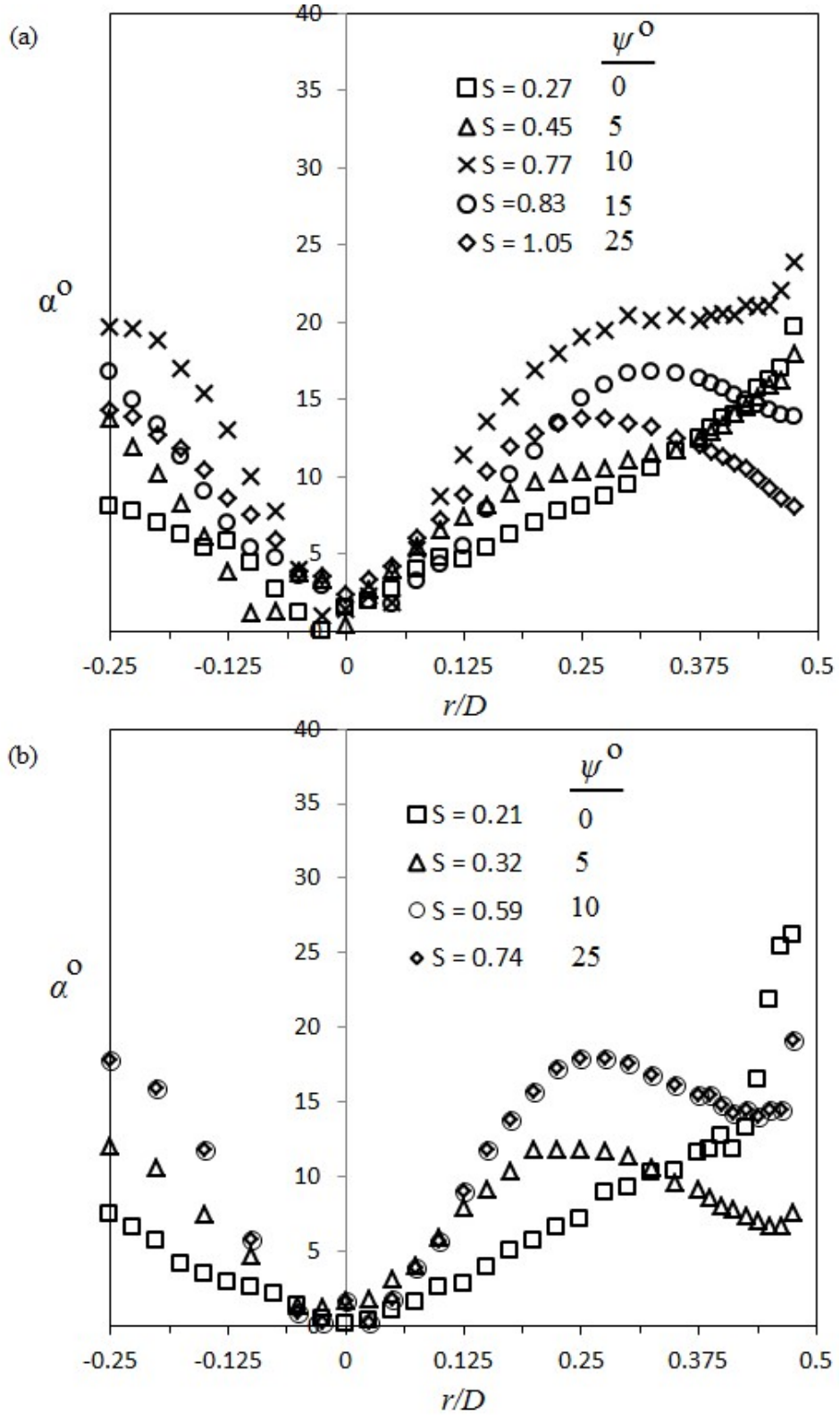

Figure 3.7 Data acquired using the swirl nozzle (x = 1 mm) for (a) Re = 35,000 and (b) Re = 11,600. Mean velocity vector angle experiences by the X-probe after its inclination to $\psi = 0^{o}$ to 25^{o}. Values for ψ are derived as shown in the second (right-hand) axis of Figure 3.4.

3.3.2 Velocity gradient effects

The velocity gradient effect is corrected using the technique highlighted in Section 2.5. Figure 3.8 presents both uncorrected ($<u_X>$) and corrected ($<u>$) velocity data using Equations (3.5) and (3.6) over three Reynolds numbers (11,600, 24,600 and 35,000). The relative effect of the velocity gradient correction (coloured dotted line against the right-hand vertical axis) clearly improves as the wall is approached and becomes more significant for higher Reynolds number flows. This is believed to be due to the thickening of the shear layer generated from the nozzle wall as the Reynolds number increases. Without such corrections, the bulk velocity U_b would be underestimated by around 2% at the highest *Re* shown. Additionally, as the separation distance between the wires increases or the nozzle diameter decreases, the velocity gradient effect is expected to become more influential.

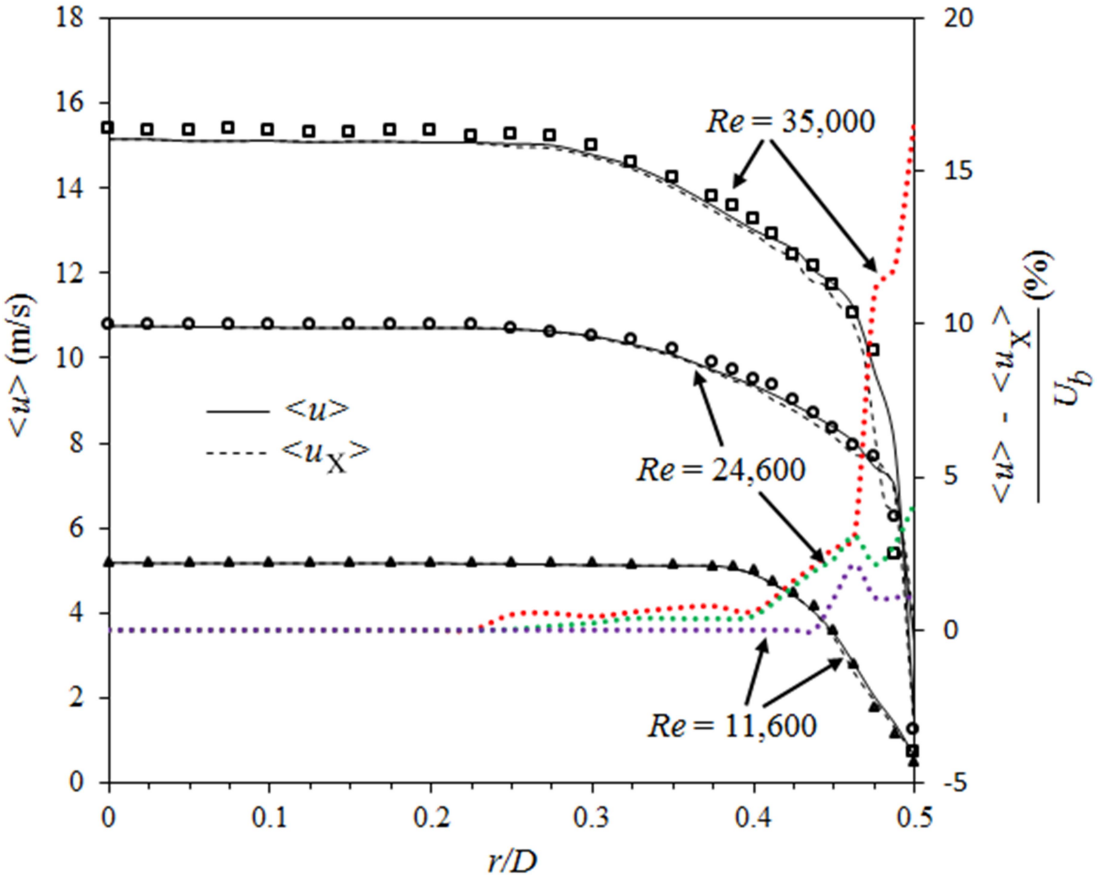

Figure 3.8 Data acquired using the swirl nozzle (S = 0, x = 1 mm). The significance of correcting X-wire probe data for velocity gradient effects (via Equations 3.4 and 3.5) close to the wall is highlighted for different Reynolds numbers. Markers correspond to each *Re* values indicate single-wire probe data. Coloured dotted lines correspond to right-hand axis.

3.4 Conclusions

Uncertainties in X-wire measurements usually arise from different sources; which include the finite probe size, out-of-plane contaminations, high turbulence intensity in the incoming flow, temperature drift and calibration inaccuracies. This study addresses a methodology to minimise two (significant) sources of error when applying dual-wire CTA probes, namely probe misalignment with the mean flow direction and the velocity gradient effect (in the shear layer) using both single- and X-wire probes. To date, the former effect has only been discussed in weakly swirling flows [35]. A systematic methodology is described (Section 2.4), for both low and higher swirling flows, to ensure the mean flow direction falls within a certain angular range ($< \pm 25^{o}$). This method minimises errors associated with inadequately aligning the probe axis to the dominant flow direction. The error associated with the velocity gradient effect is improved from the measured (uncorrected) X-wire probe data by series expanding the effective cooling velocity for the two wires and solving the resulting relations between the uncorrected and corrected velocity components iteratively (Section 2.5).The significance of the work presented is that it can help improve measurement accuracy when using CTA dual-wire probes, which is an issue largely overlooked in earlier swirling and non-swirling jet studies [16, 21, 39, 52, 53]. This study has utilised a nozzle (D/l = 32) featuring an aerodynamically generated swirling flow over low-to-high swirl numbers and Re = 11,600 to 35,000. The dual-wire probe applied has a wire separation distance of 0.8l.

The results of the study are summarised below.

- Single-wire data measurements show that for a low swirl number (S = 0.27), the mean flow direction (α) appears to stay well inside the maximum acceptance angle for the dual-wire probe, over all radial locations considered (Figure 3.5a). At relatively higher swirl numbers, the flow direction mostly approaches the maximum acceptance angle and depends on the radial position (Figures 3.5b and 3.6). These results suggests the need to consider probe inclination (ψ) at higher (global) swirl numbers and/or for radial locations where α exceeds the acceptance angle of dual-wire probes.
- For a dual-wire probe and by using Equation (3.3), methods are presented to ensure that $\alpha \leq \pm 25^{o}$ (Figure 3.3) using minimal probe inclination (ψ) when tests for weak to relatively strong swirl numbers (S = 0.21 to 1.05).
- The probe inclination angles that are experimentally resolved (ψ) are found to be largely proportional to the ratio of tangential-to-total flow (Q_t/Q_T) and swirl number

(*S*), as shown in Figures 3.3 and 3.7. However, the correlations presented in Figure 3.4 are nozzle dependent.

The impact of velocity gradient corrections applied to dual-wire CTA probes becomes more apparent as the Reynolds number increases and start to manifest themselves as early as $r/D \sim 0.25$. For smaller D/l and longer wire sensors, the corrections due to the velocity gradient effect may be more significant due to the poorer spatial resolution of the probe.

3.5 Chapter references

1. Ng, H. C. H., Monty, J. P., Hutchins, N., Chong, M. S., et al., *Comparison of turbulent channel and pipe flows with varying Reynolds number*, Experiments in Fluids, 51(5), p. 1261-1281, 2011.
2. Vukoslavčević, P. V. and Wallace, J. M., *On the accuracy of simultaneously measuring velocity component statistics in turbulent wall flows with arrays of three or four hot-wire sensors*, Experiments in Fluids, 51(6), p. 1509-1519, 2011.
3. Doebbeling, K., Lenze, B. and Leuckel, W., *Four-sensor hot-wire probe measurements of the isothermal flow in a model combustion chamber at different levels of swirl*, Experimental Thermal and Fluid Science, 5(3), p. 381-389, 1992.
4. Hosseini, Z., Bourgeois, J. A. and Martinuzzi, R. J., *Large-scale structures in dipole and quadrupole wakes of a wall-mounted finite rectangular cylinder*, Experiments in Fluids, 54(9), p. 1-16, 2013.
5. Bruun, H. H., Hot-wire anemometry: principles and signal analysis, Oxford University Press, Oxford, 1995.
6. Sherif, S. A. and Pletcher, R. H., *An analytical procedure for predicting the response of constant-temperature hot-wire and film anemometers*, Measurement, 25(3), p. 193-201, 1999.
7. Fingerson, L. M. and Freymuth, P., *Thermal Anemometers*, in Fluid Mechanics Measurements (2nd Ed.), editor: Goldstein, R. J., Taylor & Francis, London. p., 1996.
8. Sloan, D. G., Smith, P. J. and Smoot, L. D., *Modeling of swirl in turbulent flow systems*, Progress in Energy and Combustion Science, 12(3), p. 163-250, 1986.
9. Ahmed, Z. U., Al-Abdeli, Y. M. and Matthews, M. T., *The effect of inflow conditions on the development of non-swirling versus swirling impinging turbulent jets*, Computers & Fluids, 118, p. 255-273, 2015.
10. Toh, I., Honnery, D. and Soria, J., *Axial plus tangential entry swirling jet*, Experiments in Fluids, 48(2), p. 309-325, 2010.
11. Chigier, N. A. and Chervinsky, A., *Experimental investigation of swirling vortex motion in jets*, Journal of Applied Mechanics, 34(2), p. 443-451, 1967.
12. Ahmed, Z. U., Al-Abdeli, Y. M. and Guzzomi, F. G., *Impingement pressure characteristics of swirling and non-swirling turbulent jets*, Experimental Thermal and Fluid Science, 68, p. 722-732, 2015.
13. Al-Abdeli, Y. M. and Masri, A. R., *Stability characteristics and flowfields of turbulent non-premixed swirling flames*, Combustion Theory and Modelling, 7(4), p. 731-766, 2003.

14. Tsuji, T. and Nagano, Y., *An anemometry technique for turbulence measurements at low velocities*, Experiments in Fluids, 7, p. 547-559, 1989.
15. Burattini, P. and Antonia, R. A., *The effect of different X-wire calibration schemes on some turbulence statistics*, Experiments in Fluids, 38(1), p. 80-89, 2005.
16. Müller, U. R., *Measurement of the Reynolds stresses and the mean-flow field in a three-dimensional pressure-driven boundary layer*, Journal of Fluid Mechanics, 119, p. 121-153, 1982.
17. Al-Abdeli, Y. M. and Masri, A. R., *Recirculation and flowfield regimes of unconfined non-reacting swirling flows*, Experimental Thermal and Fluid Science, 27(5), p. 655-665, 2003.
18. Al-Abdeli, Y. M., *Experiments in turbulent swirling non-premixed flames and isothermal flows*, PhD Thesis, in The University of Sydney: Sydney, p., 2004.
19. Chang, F. and Dhir, V. K., *Turbulent flow field in tangentially injected swirl flows in tubes*, International Journal of Heat and Fluid Flow, 15(5), p. 346-356, 1994.
20. Fitouri, A., Khan, M. K. and Bruun, H. H., *A multiposition hot-wire technique for the study of swirling flows in vortex chambers*, Experimental Thermal and Fluid Science, 10(1), p. 142-151, 1995.
21. Champagne, F. H. and Kromat, S., *Experiments on the formation of a recirculation zone in swirling coaxial jets*, Experiments in Fluids, 29(5), p. 494-504, 2000.
22. Örlü, R. and Alfredsson, P. H., *An experimental study of the near-field mixing characteristics of a swirling jet*, Flow, Turbulence and Combustion, 80(3), p. 323-350, 2008.
23. Leclaire, B. and Jacquin, L., *On the generation of swirling jets: high-Reynolds-number rotating flow in a pipe with a final contraction*, Journal of Fluid Mechanics, 692, p. 78-111, 2012.
24. Kim, J. K., *Investigation of the turbulence characteristics in the swirling flow of a gun-type gas burner with two different hot-wire probes*, Journal of Mechanical Science and Technology, 22(1), p. 180-189, 2008.
25. Farokhi, S., Taghavi, R. and Rice, E. J., *Effect of initial swirl distribution on the evolution of a turbulent jet*, AIAA Journal, 27(6), p. 700-706, 1989.
26. Gilchrist, R. T. and Naughton, J. W., *Experimental study of incompressible jets with different initial swirl distributions: mean results*, AIAA journal, 43(4), p. 741-751, 2005.
27. Benišek, M. H., Lečić, M. R., Ilić, D. B. and Čantrak, Đ. S., *Application of new classical probes in swirl fluid flow measurements*, Experimental Techniques, 34(3), p. 74-81, 2010.
28. Samet, M. and Einav, S., *Mean value measurements of a turbulent swirling-jet*, AIAA journal, 26(5), p. 619-621, 1988.
29. Samet, M. and Einav, S., *A hot-wire technique for simultaneous measurement of instantaneous velocities in 3D flows*, Journal of Physics E: Scientific Instruments, 20(6), p. 683, 1987.
30. Pompeo, L. and Thomann, H., *Quadruple hot-wire probes in a simulated wall flow*, Experiments in Fluids, 14(3), p. 145-152, 1993.
31. Kitoh, O., *Experimental study of turbulent swirling flow in a straight pipe*, Journal of Fluid Mechanics, 225(0), p. 445-479, 1991.
32. Lečić, M. R., Ćoćić, A. S. and Čantrak, S. M., *Original measuring and calibration equipment for investigation of turbulent swirling flow in circular pipe*, Experimental Techniques, 38(3), p. 54-62, 2014.
33. Algifri, A. H., Bhardwaj, R. K. and Rao, Y. V. N., *Turbulence measurements in decaying swirl flow in a pipe*, Applied Scientific Research, 45(3), p. 233-250, 1988.

34. Alekseenko, S. V., Bilsky, A. V., Dulin, V. M. and Markovich, D. M., *Experimental study of an impinging jet with different swirl rates*, International Journal of Heat and Fluid Flow, 28(6), p. 1340-1359, 2007.
35. Ribeiro, M. M. and Whitelaw, J. H., *Coaxial jets with and without swirl*, Journal of Fluid Mechanics, 96(part 4), p. 769-795, 1980.
36. Clausen, P. D., Koh, S. G. and Wood, D. H., *Measurements of a swirling turbulent boundary layer developing in a conical diffuser*, Experimental Thermal and Fluid Science, 6(1), p. 39-48, 1993.
37. Wood, D. H., Mehta, R. D. and Koh, S. G., *Structure of a swirling turbulent mixing layer*, Experimental Thermal and Fluid Science, 5(2), p. 196-202, 1992.
38. Bissonnette, L. R. and Mellor, G. L., *Experiments on the behaviour of an axisymmetric turbulent boundary layer with a sudden circumferential strain*, Journal of Fluid Mechanics, 63(02), p. 369-413, 1974.
39. Vu, B. T. and Gouldin, F. C., *Flow measurements in a model swirl combustor*, AIAA Journal, 20(5), p. 642-651, 1982.
40. Johnson, F. D. and Eckelmann, H., *A variable angle method of calibration for X-probes applied to wall-bounded turbulent shear flow*, Experiments in Fluids, 2(3), p. 121-130, 1984.
41. Jorgensen, F. E., *How to measure turbulence with Hot-Wire anemometers*, in Dantec Dynamics, Skovlunde, Denmark, p., 2004.
42. Ligrani, P. M. and Bradshaw, P., *Spatial resolution and measurement of turbulence in the viscous sublayer using subminiature hot-wire probes*, Experiments in Fluids, 5(6), p. 407-417, 1987.
43. Thomas, B., Ahmed, Z. U., Al-Abdeli, Y. M. and Matthews, M. T., *The optimisation of a turbulent swirl nozzle using CFD*, in Proceedings of the Australian Combustion Symposium, 6-8 November Perth, Australia, http://www.anz-combustioninstitute.org/local/papers/ACS2013-Conference-Proceedings.pdf, p. 271-274, 2013.
44. Ovink, R., Lamers, A. P. G. G., van Steenhoven, A. A. and Hoeijmakers, H. W. M., *A method of correction for the binormal velocity fluctuation using the look-up inversion method for hot-wire anemometry*, Measurement Science and Technology, 12(8), p. 1208, 2001.
45. Müller, U. R., *Comparison of turbulence measurements with single, X and triple hot-wire probes*, Experiments in Fluids, 13(2-3), p. 208-216, 1992.
46. Talamelli, A., Westin, K. J. A. and Alfredsson, P. H., *An experimental investigation of the response of hot-wire X-probes in shear flows*, Experiments in Fluids, 28(5), p. 425-435, 2000.
47. Facciolo, L., *A study on axially rotating pipe and swirling jet flows*, PhD, in Department of Mechanics, Royal Institute of Technology: Stockholm, Sweden, p., 2006.
48. Moffat, R. J., *Describing the uncertainties in experimental results*, Experimental Thermal and Fluid Science, 1(1), p. 3-17, 1988.
49. Montgomery, D. C. and Runger, G. C., Applied statistics and probability for engineers, 5th, John Wiley & Sons, Hoboken, NJ, 2011.
50. Dieck, R. H., Steele, W. G. and Osolsobe, G., *Test uncertainty. ASME PTC 19.1-2005*, in American Society of Mechanical Engineers: New York, NY, p., 2005.
51. Clausen, P. D. and Wood, D. H., *The correction of X-probe results for transverse contamination*, Journal of Fluids Engineering, 111(2), p. 226-229, 1989.

52. Nagano, Y. and Tsuji, T., *Recent developments in hot-and cold-wire techniques for measurements in turbulent shear flows near walls*, Experimental Thermal and Fluid Science, 9(2), p. 94-110, 1994.
53. Mehta, R. D., Wood, D. H. and Clausen, P. D., *Some effects of swirl on turbulent mixing layer development*, Physics of Fluids A: Fluid Dynamics, 3(11), p. 2716-2724, 1991.

3.6 Chapter appendices

The graphical representation of the velocity gradient correction using Equations (3.5) and (3.6) by the use of both single-wire and X-wire probes is shown below.

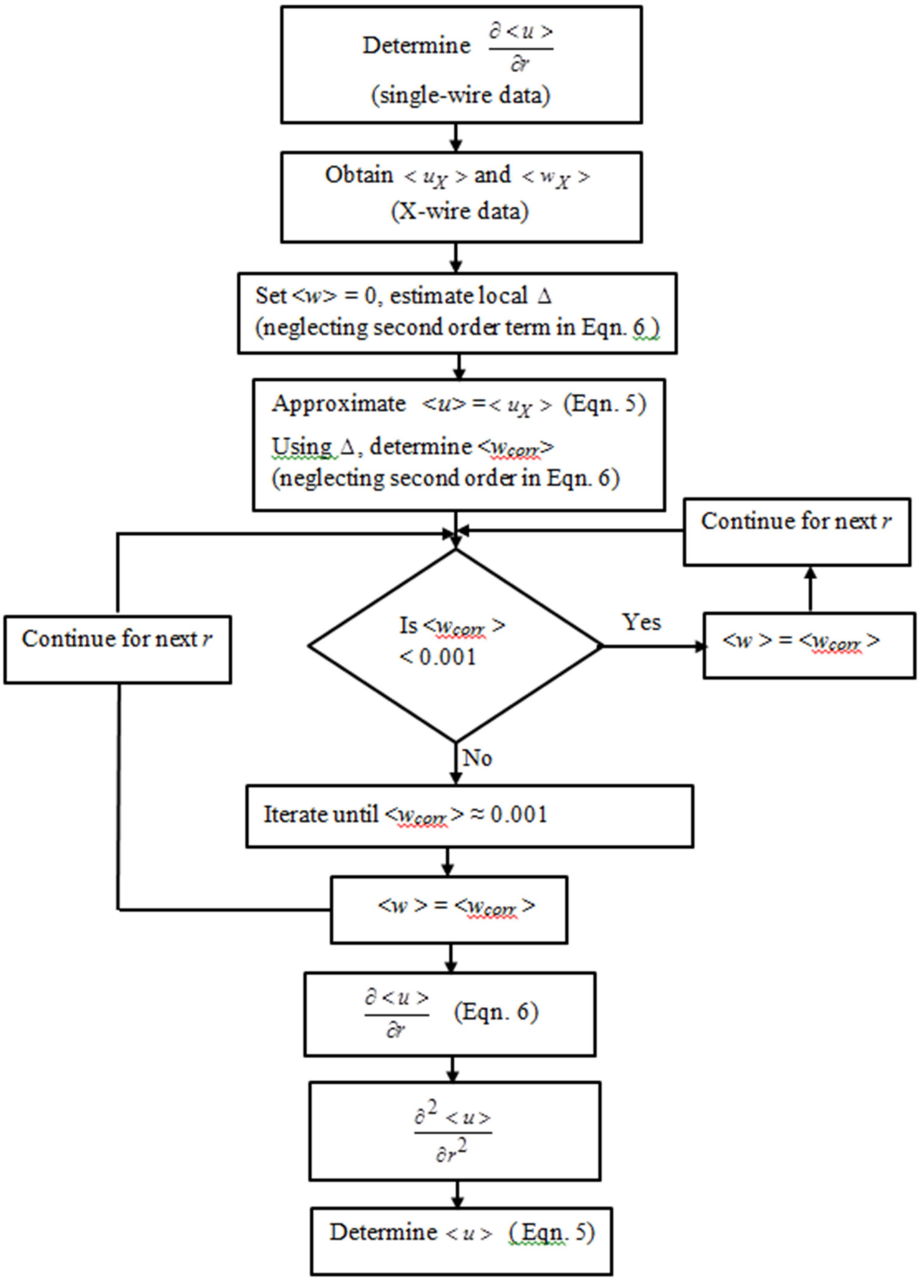

Chapter 4

4 Impingement Pressure Characteristics of Swirling and Non-swirling Turbulent Jets[8]

This chapter is dedicated to the impingement pressure characteristics for both swirling and non-swirling jets. Results of flow visualisation near the impingement surface are also discussed.

4.1 Introduction

Impinging jets are widespread in industrial applications due to their ability to affect heat and mass transfer rates on surfaces [1-4]. In a typical impingement jet, the flow field is divided into three regions, namely the free jet region, the stagnation (or impingement) region and the wall jet region. The free jet region that occupies most of the flow domain is largely characterised by both the (conical) potential core around the axis where the axial velocity is 95% of centreline velocity at the nozzle exit [5] and its shear layer. In the impingement region, on or close to the impingement surface and symmetrical about the geometric centreline, jet impact causes streamline curvature towards radially outward direction and a rapid decrease in axial velocity with a corresponding rise in static pressure. The wall jet region, which is further out (radially), then forms around the impingement region where the axial deceleration of the flow causes lateral spread near the surface. Although excellent historical [6-9] and recent [10-13] treatise exist on the flow field characteristics of turbulent impinging jets and the characteristics of three distinctive flow regions, relatively fewer works have attempted to resolve the pressure distribution in the stagnation and wall jet regions or the effects of relatively high swirl on the potential core. The impartation of swirl into an impinging jet further complicates the flow field with fundamental interpretation becoming more challenging if swirl is generated geometrically by means of helical inserts or guide

[8] This chapter has been published as a full research paper:
Ahmed Z. U., Al-Abdeli, Y. M., Guzzomi, F. G., Experimental Thermal and Fluid Sciene, 68, p. 722-732, 2015.
Whilst efforts were made to retain original content of the article, minor changes such as number formats, font size style were implemented in order to maintain consistency in the formatting style of the thesis.

vanes. This is because geometrical swirl generation causes dead zones to form on the axis and limits the range of swirl numbers, results in a bifurcation of a single jet into multiple jets [14-17], is likely to distort the flow and alter heat transfer characteristics as well as impingement pressure distribution. Adding to this complexity is the anticipated role of swirl induced flow reversal and/or instability at certain free jet conditions [18, 19]. These geometry induced flow perturbations may be avoided through aerodynamically generated swirl flows (i.e., without any inserts or guide vanes), which is the focus of the present study.

Existing research on swirling impinging jets largely populated with surface heat transfer characteristics and studies have reported varied outcomes in relation to the effects of swirl on impingement surface heat transfer. Lee et al. [15] as well as Ianiro and Cardone [17] observed a reduction in heat transfer with swirl, which may be affected by flow blockages formed around the centreline from the use of geometric swirl generation (helical inserts). In contrast, Wen and Jang [20] as well as Ichimiya and Sukamoto [21] discovered enhanced heat transfer at the surface (around the stagnation point). This finding may be attributed to swirl induced mixing via the formation of vortices on the impingement surface and larger entrainment of (cool) ambient air. As such, there appears to be a fundamental disparity in the understanding of whether swirl improves or deteriorates impingement heat transfer and remains an issue worthy of further investigation. Moreover, despite numerous research into impinging non-swirling turbulent jets, it is evident that there is limited reporting of the (surface) pressure field which would help in validating turbulence models in computations, particularly near-wall flow features or surface characteristics. Pressure distributions were overlooked in the majority of earlier studies because the focus was on heat transfer. Notably, resolving pressure distributions along the impingement surface may also influence boundary layer development and help characterise the nature of jet spread. Bayder and Ozmen [22] identified a relationship between pressure distribution and turbulence intensity and its effect on the transition from laminar to turbulent boundary layer flow in the wall jet region of non-swirling impinging jets. Likewise, Katti and Prabhu [11] used pressure data to propose a theoretical relationship between wall static pressure and heat transfer at the stagnation point for a single Reynolds number (*Re*) and nozzle-to-plate distance (*H*). The following is a brief overview of the research conducted to date on the pressure distribution of turbulent (gaseous) impinging jets, for both swirling and non-swirling conditions.

In non-swirling jets with large nozzle-to-plate distances ($H > 8.3D$) the stagnation pressure (P_S) is inversely proportional to the square of the impingement distance i.e.

$P_S \alpha (H/D)^{-2}$, where D is the nozzle diameter [7, 23]. However, in the near field and for small nozzle-to-plate distances ($H \leq 5.5D$), P_S does not vary with H/D and approximates to the dynamic pressure, which agrees with the experiment by Giralt et al. [8]. At $H \leq 5.5D$, Beltaos and Rajaratnam [7, 23] identified the impingement region to extend up to $1.2D$ from the impingement wall and $r/D \approx 1.4$ from the stagnation point where the pressure drops to the ambient value. However, other results have indicated that when the impingement surface is positioned very close to the nozzle ($H \leq 0.5D$), a constant pressure zone (equal to P_S) is developed around the stagnation point, where this zone grows with decreasing H values [24]. Lytle and Webb [24] also reported that the stagnation pressure and radial pressure distribution were not significantly dependent on Re and H in non-swirling jets except very close to the nozzle exit plane ($H = 0.2D$), which agrees with recent experimental and numerical studies [11, 22, 25, 26]. For impingement at $H = 0.2D$, the impingement surface pressure is about three times larger than pressure at other H values and is attributed to the rapid decrease of axial velocity as the jet transcends the impingement zone. At $H = 0.2D$, there is a slight decrease in P_S with increasing Re but no explanation was reported in the literature [22]. Finally, sharp pressure drops have been observed at $r/D \approx 0.5$, where the pressure drop occurs more distant (radially) from the geometric centreline with increasing Re. As such, it is evident that even for non-swirling impinging jets at $H \leq 6D$, some uncertainty exists on the effects of H on P_S and the underlying flow dynamic effects at such flow conditions.

The effect of swirl on the pressure distribution of turbulent impinging jets is scarce in the literature. Apart from experimental investigations into the surface pressure distribution of annular swirling jets [27, 28], which impose fundamentally different flow behaviour due to multiple shear layers, there is little data for pressure distributions of turbulent swirling jets. Most swirling impinging jet studies largely deal with the mean and turbulent velocity characteristics upstream of the impingement surface [16, 29-33]. These studies reveal that the formation of flow recirculation between the nozzle exit and the impingement surface depends on the swirl number ($0.3 \leq S \leq 0.5$) and the impingement distance ($H = 2D - 6D$). However, in almost all of these studies, swirl is generated geometrically by helical inserts or guide vanes inside a nozzle. This causes the formation of dead zones on the flow centreline and may also lead to vane-induced trailing vortices which may further complicate interpretations of the link between swirl and pressure distribution on the impingement surface.

This research uses an aerodynamically generated swirling jet which seamlessly transitions from non-swirling to highly swirling flows for the same Reynolds number (*Re*). Analysing the effects of swirl on the impingement pressure distribution helps provide a fundamental understanding of the factors affecting (surface) heat and mass transfer. Methods used in this chapter include performing pressure field measurements combined with flow visualisations at the impingement surface. In addition, Constant Temperature Anemometry (CTA) is used to acquire velocity field and boundary condition data so as to provide opportunity for subsequent CFD modelling. Test conditions investigated span a range of swirl (S = 0 to 1.05) and Reynolds numbers (Re =11,600 to 35,000) as well as impingement distances (H = 1D to 6D). Section 2 details the swirl nozzle, experimental set-up, test cases and the jet inlet velocity profiles. Section 3 discusses the results followed by the conclusions in Section 4

4.2 Experimental techniques

4.2.1 Swirl nozzle

Figure 4.1 shows an illustration of the swirl nozzle used in this study along with the coordinate system, where x indicates the streamwise direction and y-z defines the nozzle exit plane at x = 0 mm. The brass nozzle is modular and assembled from seven sections (A, T, C, 3 x S and N). The lower axial section (A) is 50 mm in diameter and includes two diametrically opposed ports with a settling chamber occupied by two layers of 20 mm hexagonal aluminium honeycomb (3 mm cells) and four mesh screens (0.8 mm wire diameter). Flow conditioning reduces large-scale turbulence and straightens the flow [34, 35]. The emerging axial flow then enters section T, which introduces the swirling motion via three tangential ports of 12 mm diameter. Aerodynamic swirl generation helps avoid trailing vortices from radial vanes [33] and allow a seamless transition from non-swirling to swirling jet flows. In addition, this technique avoids the complications arising from dead (central) ribs associated with geometrical swirl generation [16, 27]. Aerodynamic swirl generator design adopted here allows varying swirl numbers independent of Reynolds number to be tested. The contraction section (C) is designed to aid flow coalescence and has a smooth internal contour that ends at zero (straight) gradient. Section C is based on a cubic polynomial contour (defined below), which minimises boundary layer separation and improves flow uniformity after the contraction [34, 36-38]:

$$R_c = \frac{D_i}{2} - \frac{3}{2}(D_i - D_e)\left(\frac{x}{L}\right)^2 + (D_i - D_e)\left(\frac{x}{L}\right)^3, \tag{4.1}$$

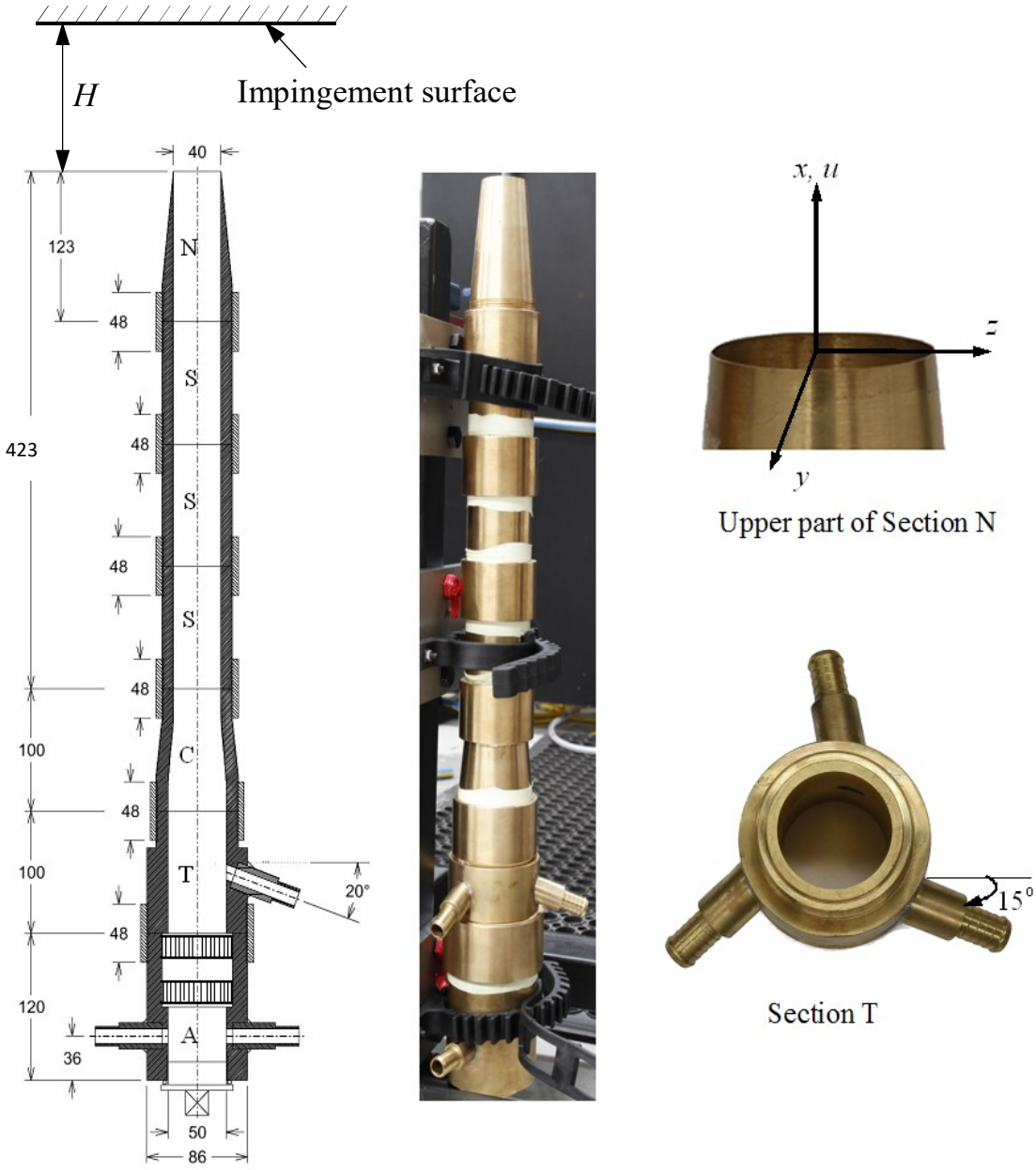

Figure 4.1 Swirl nozzle with both CAD and post manufactured view as well as the co-ordinate system used in the chapter.

where R_c is the radius of the nozzle contraction section and is a function of x, D_i and D_e (D_i and D_e are the contraction inlet and exit diameters, respectively). The resultant area contraction ratio over the section (C) is 1.56. After the contraction, three identical sections (S) are used to further improve flow uniformity before the nozzle exit plane. The number of S sections was found in a separate (preliminary) numerical study [39]. The final nozzle section

(N) is 40 mm diameter at the exit plane and ends with a sharp-edge (estimated at 0.2 mm wall thickness) to avoid flow separation at (or near) the exit. Dry air is fed into the swirl nozzle via an air compressor and calibrated flow meters regulate axial and tangential streams into sections A and T. The nozzle is operated in quiescent surroundings.

4.2.2 CTA system

A dual-wire (X-wire) probe (DANTEC, model: 55P61) is used to resolve the boundary conditions near the nozzle exit plane (x/D = 0.025). A single-wire probe (DANTEC, model: 55P11) was used to reveal if any flow asymmetry is present at the nozzle exit for S = 0 - 1.05. The single-wire probe has a much smaller probe volume and allows flow measurements very close to the nozzle wall. Symmetry checks at the nozzle exit plane were done by orientating this sensor parallel to the nozzle wall and traversing the sensor circumferentially at different radii (r). The CTA probes are traversed in the horizontal plane (y and z directions with a resolution: 0.02 mm) and in the vertical direction (x direction with a resolution: 0.5 mm). To obtain axial ($<u>$) and tangential ($<w>$) velocity profiles at the nozzle exit plane, the probe body was positioned parallel to the x-axis with the wires aligned in the x-y plane. The radial velocity component ($<v>$) for non-recirculating swirling flows is small at the nozzle exit plane compared to $<u>$ and $<w>$ [16, 40-42], and consequently it is not reported in this study. To improve CTA measurement accuracy, the data acquired at the nozzle exit terminates at 1 mm away from the nozzle wall to reduce errors from strong shear and wall effects near the solid boundary.

To estimate the accuracy of CTA measurements, pitot-static tube and hotwire anemometry measurements were compared for non-swirl flows and the error was found to be less than 2% (centreline velocity). For swirling flows, a single-wire probe was used along the nozzle centreline and compared to X-wire probe data in the range x/D = 0.025 - 6 for the same flow conditions. The deviations between the data were approximately 2% and 4% for low and higher swirl numbers, respectively, whereby CTA measurements also included checks for velocity gradients and sensor directional response.

4.2.3 Impingement pressure plate

Figure 4.2 shows the nozzle and impingement plate assembly with a built-in perspex plate, 12 mm thick and 450 mm square, which is used for impingement pressure measurements. Static pressure is measured from pressure tappings (1.6 mm diameter), as shown in Figure 4.2a. The pressure tappings are connected to a digital micromanometer (TSI,

(a)

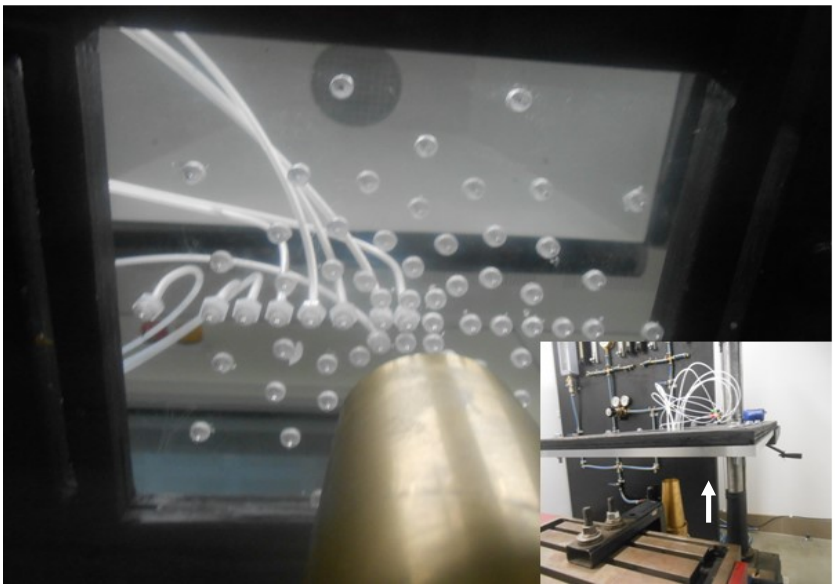

(b)

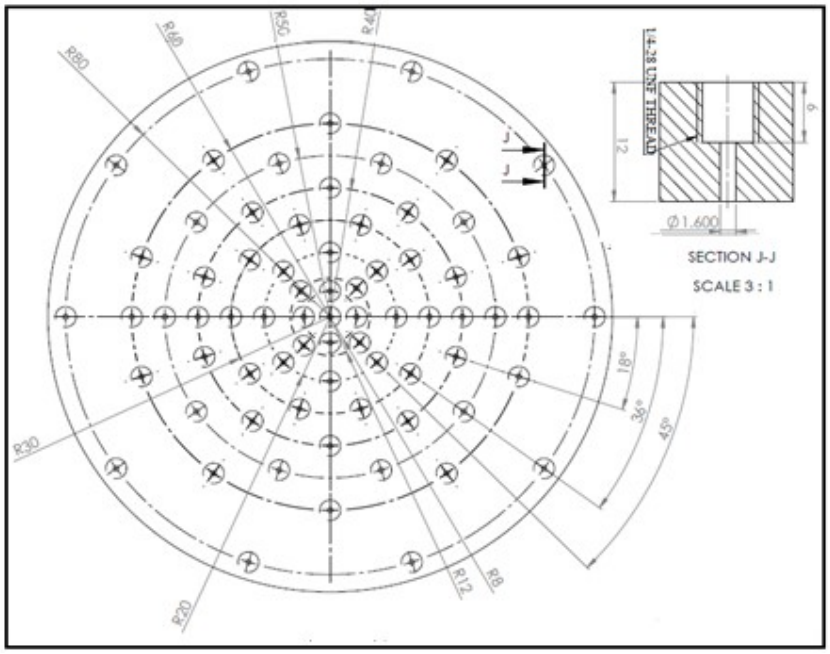

Figure 4.2 (a) Experimental setup for pressure measurement (inset) with a closer photograph of impingement plate concentric circles in relation to the nozzle, (b) CAD design of concentric circles onto plate.

model: 5815) via 1.6 mm LDPE tubing and a 10 position stream selector (Chromalytic, model: C25-6180), to allow quick sampling from different tappings. The digital

micromanometer has a pressure range of ±3.7 kPa with a resolution of 0.1 Pa. To check for pressure drop across the stream selector, pressure measurements were conducted (with and without the stream selector) at a given flow and negligible pressure loss was observed. The circumferential pressure distribution was measured by 71 flush mounted taps, distributed over nine concentric circles at *r/D* = 0 to 2 centred about the plate's geometric centre (Figure 4.2b). Flow axisymmetry on the impingement surface was ascertained by measuring circumferential pressure profiles at two radii (*r/D* = 0.5 and 1) for *H* = 2*D* to 6*D*. Such tests revealed that at any given concentric circle, the pressure data variation was less than ±5% of the circumferentially averaged value for both non-swirling and swirling flows. The maximum uncertainty in pressure measurements was found to be within ±1 Pa over a range of -39.2 to 137.8 Pa.

Pressure measurements are presented by coefficient of pressure (*Cp*), which is the difference between the local static pressure and the freestream (ambient) pressure, normalised by the dynamic pressure. The coefficient of pressure is defined mathematically by:

$$Cp = \frac{P - P_\infty}{1/2\rho U_b^2}\,^{9}, \tag{4.2}$$

where, P, P_∞ are the local surface static pressure, the ambient pressure, respectively, ρ is the air density (1.204 kg/m^3) and U_b is the bulk velocity (defined in Equation 4.6) of non-swirling flows. Alternatively, U_b of non-swirling flows is equal to U_f (Equation 4.3), which the velocity obtained from the total volume flow rate from all ports divided by the nozzle exit area.

4.2.4 Flow visualisations

Flow visualisation was used to qualitatively resolve the flow behaviour of the stagnation and wall jet regions. To facilitate this, thin cotton tufts were inserted through the tappings of the same impingement surface at each concentric circle. During these flow visualisations, no pressure readings were acquired. To increase visibility, different colours were assigned to tufts occupying each concentric circle on the impingement plate. Two different tuft lengths were also trialled (10 and 20 mm) to identify any discrepancy in the visualisation results due to the tuft length. No such perturbation was observed, however a tuft length of 20 mm

[9] In the published version of this chapter, normalisation of (gauge) static pressures was done by $0.5\rho U_f^2$.

provided better tuft visualisation in still images and videos. Flow visualisations are spanned different swirl numbers (S = 0 to 1.05) for H = 1D to 6D and for two Reynolds numbers (Re = 11,600 and 35,000). To identify any reversed flow in the central region of the jet, tufts suspended on a thin probe were also traversed between the impingement surface and the nozzle exit for all nozzle-to-plate distances at the highest swirl number.

4.2.5 Test conditions

In this study, the swirling flows are characterised by two non-dimensional parameters, namely Reynolds number (Re) and swirl number (S). The Reynolds number is obtained from the volumetric flow rate that arises from both the axial (Section A) and tangential (Section T) inlet ports, defined by:

$$Re = \frac{4Q}{\pi D \nu} = \frac{U_f D}{\nu}, \tag{4.3}$$

where, Q is the total volume flow rate in the nozzle and ν is the kinematic viscosity of air (15.11 x 10^{-6} m^2/s). The common definition for swirl number, S^*, is derived from conservation equations and expressed as the ratio of the axial flux of tangential momentum G_θ to the axial flux of axial momentum G_x as shown in Equation (4.4) [43-45]:

$$S^* = \frac{G_\theta}{RG_x} \simeq \frac{\int_0^R < u >< w > r^2 dr}{R\int_0^R (< u >^2 - \frac{1}{2} < w >^2) r dr}, \tag{4.4}$$

where R is the nozzle radius. Since calculating S^* involves the integration of <w> and <u> profiles across the nozzle exit plane (r = 0 to R), two swirling flows with markedly different radial velocity profiles can still be described by the same S^* [46]. With downstream jet development affected by the shape of velocity profile [13] and transitions into vortex breakdown not solely a function of high swirl numbers [18], an alternative approach is to derive a swirl intensity that accommodates the velocity profiles at the exit plane [47-50], as will be presented in the ensuing Section 2.6. Similarly from this context, a single swirl number may also be expressed as shown in Equation (4.5),

$$S = \frac{W_b}{U_b}, \tag{4.5}$$

where, U_b, W_b are the bulk axial and tangential velocities, respectively and are obtained by:

$$U_b = \frac{2}{R^2}\int_0^R r < u > dr, \tag{4.6}$$

$$W_b = \frac{2}{R^2}\int_0^R r < w > dr, \tag{4.7}$$

Typically there is a linear relationship between the momentum flux based swirl number (S^*) and the velocity based swirl number (S), $S = CS^*$, where the constant C varies in different studies [50-52]. This may be due to the different nozzle geometries and swirl generating mechanisms in these experimental studies. Figure 4.3 presents the relationship between S and S^* which is specific to the current nozzle. These results show a nonlinear relationship between the swirl numbers ($S^* = 0.980S^2+0.384S$) that is independent of Re. Table 4.1 shows the different impinging jets cases that were tested for a range of swirling flows at different Reynolds number.

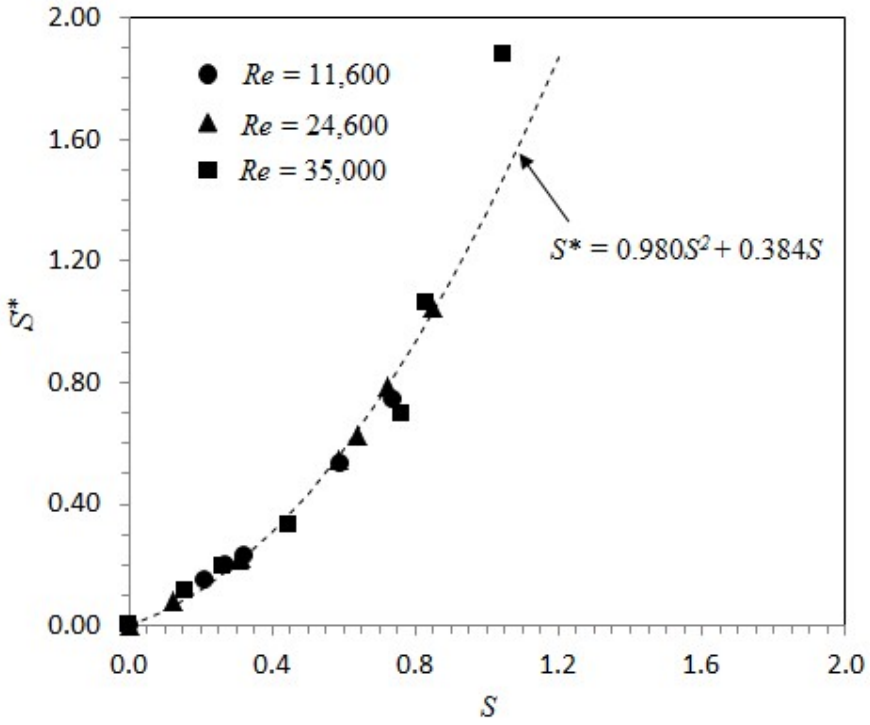

Figure 4.3 Relationship between the swirl number adopted in the present study ($S = W_b/U_b$) with the swirl number from the literature S^* [43-45] for three different Reynolds numbers (Re = 11,600 to 35,000). Swirl numbers are calculated from the data measured at x/D = 0.025.

4.2.6 Inlet conditions

Resolving inlet boundary condition i.e velocity and turbulence data at the nozzle exit helps characterise the swirl number and establish a means for comparison results among different studies. It is also essential for any numerical simulations to identify first for an accurate analysis for complex flows such as swirl flows.

Figure 4.4 shows the raw CTA data (E, in volt) used to identify the presence of any non-uniformity around the nozzle at the exit plane (x/D = 0.025). The data was measured at twelve positions around the circumference in both non-swirling and swirling jets over two radii (r = 10 mm, 15 mm) with the peak flow rate applied (Re = 35,000). This data, which is normalised by the mean value (E_m), shows excellent uniformity across the exit plane with deviations are within ±1% over 360^o for non-swirling (S = 0) and swirling flows (S = 0.27 – 1.05).

Table 4.1 Impinging jets tested

IMPINGING JET CASE	Re	U_b (m/s)	W_b (m/s)	S
I35S000	35,000	13.26	0.00	0.00
I35S016		12.99	2.04	0.16
I35S027		13.14	3.50	0.27
I35S045		13.74	6.18	0.45
I35S077		13.71	10.51	0.77
I35S083		17.39	14.43	0.83
I35S105		17.57	18.39	1.05
I24S000	24,600	9.32	0.00	0.00
I24S012		9.26	1.15	0.12
I24S031		9.10	2.81	0.31
I24S058		9.91	5.79	0.58
I24S064		11.00	7.01	0.64
I24S072		11.55	8.36	0.72
I24S085		11.00	9.34	0.85
I11S000	11,600	4.39	0.00	0.00
I11S021		4.31	0.91	0.21
I11S027		4.28	1.15	0.27
I11S032		5.03	1.63	0.32
I11S059		4.95	2.92	0.59
I11S074		5.08	3.75	0.74

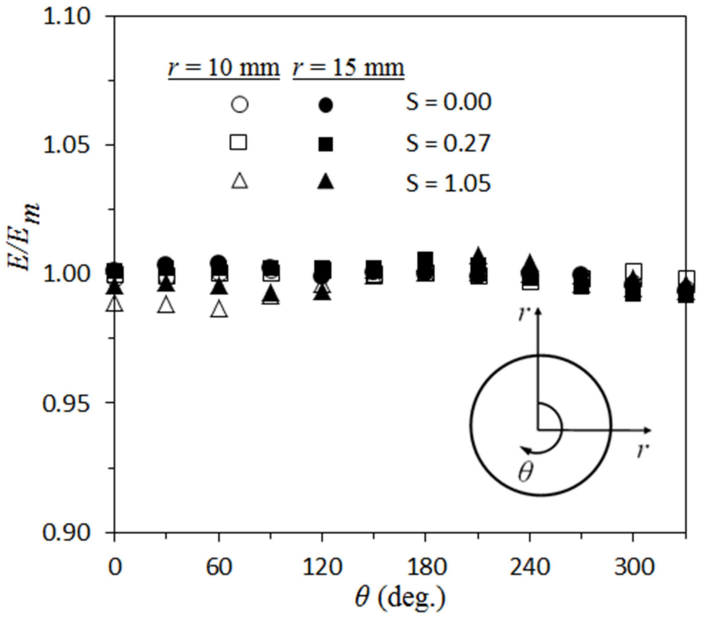

Figure 4.4 Circumferential distribution of CTA data for the highest flow (Re = 35,000) over S = 0 to 1.05. Data measured at x/D = 0.025 for two radial locations (r = 10 mm, 15 mm) is shown.

Figure 4.5 depicts the radial distribution of axial and tangential velocity components and the corresponding local swirl number profiles at x/D = 0.025 for Re = 35,000. The velocity components are normalized (unless shown otherwise on the plots) by the bulk axial velocity (U_b) of the non-swirling test case (I35S000). At no swirl (S = 0), the axial velocity <u> remains reasonably constant up to $r/D \approx 0.35$ and then decreases for the proximity of the shear layer due to the nozzle wall (r = 20 mm). For weak swirl ($S \leq 0.27$), <u> shows similar trends to a non-swirling jet and the <w> profile is akin to solid body rotation (showing a linear relationship with the radial distance). However, at the higher swirl numbers ($S \geq 0.83$), <u> shows drastically different flow behaviour with a deviation from the near-uniform distribution and a larger portion of the fluid is forced towards the nozzle wall from the central region. This behaviour can be attributed to the strong tangential flow that induces centrifugal forces within the flow field and results in a reduction of axial velocity near the nozzle axis (r/D = 0). The tangential velocity increases linearly before reaching a peak near the nozzle wall and then decays with r/D. These trends observed for <u> and <w> are similar for other turbulent swirl flows from circular nozzles [51, 53, 54]. It appears that a transitional swirl number range exists over $0.45 \leq S \leq 0.77$, where the tangential velocity distribution shows a combined profile: forced vortex in the core region and a free vortex in the outer region. The

radial variation of the tangential velocity for $S = 0.45$ to 0.77 is closely approximated by the vortex model proposed in Algifri et al. [42] as well as Semaan and Naughton [55], where the constant C (equal to 4.5 in this study) characterises the shape of the distribution:

$$< w >= \frac{\left(< w > \times r / R\right)_{\max}}{r / R}\left(1 - e^{-C(r/R)^2}\right). \tag{4.8}$$

Figure 4.5 also depicts the local swirl number distribution. For swirl numbers up to $S = 0.77$, the profiles closely follow the tangential velocity profiles due to relatively uniform axial velocities. At $S \geq 0.83$, the localised maxima of the swirl number is found to move inwards towards the centerline axis. The ensuing pressure distribution data at the impingement plate will also reveal a change in behavior around $S = 0.77$. It is also worth noting that whilst variation of $<w>/U_b$ and $<w>/<u>$ is gradual over the swirl number range, the trend of $<u>/U_b$ appears to undergo a more abrupt change at $S = 0.77$. However, later results will show (Figure 4.7) there is no data to support the occurrence of vortex breakdown. Data acquired at Re = 24,600 (cases I24S000 – I24085) and Re = 11,600 (cases I11S000 I11S074)[10] shows fundamentally the same behavior observed at Re = 35,000. However, as the Reynolds number decreases to Re = 24,600 and then 11,600, the abrupt change in trends for velocity profiles occur at the lower swirl number of $S = 0.58$ and then $S = 0.32$, respectively. This reinforces the need to define boundary conditions at the nozzle exit in order to interpret flow dynamics at the impingement surface. These results also highlight the importance of avoiding inserts or guide-vanes to generate swirl as their inherent "dead" zones at the jet axis could alter fundamental jet impingement characteristics.

Figure 4.6 illustrates the turbulent intensities at the nozzle exit. The axial turbulence intensities (u'/U_b) do not change significantly up to $r/D \sim 0.25$ for all flow conditions. This data also reveals that the turbulence intensities increase near the nozzle wall for both low and high swirl values, which is attributed to the shear layer in this region. The turbulence intensity magnitude increases with swirl number, with intensities less than 20% for $S < 0.83$. This increase may be due to the enhanced mixing between axial and tangential streams at higher swirl numbers. The distribution of the tangential turbulence intensity (w'/U_b) is similar to the axial turbulence intensity except for the two highest swirl conditions, where the tangential turbulence intensity is high in the outer region of the jet. This high intensity is attributed to the intense mixing and strong velocity gradients at high swirl. It may also be due

[10] Plots for both cases are presented in the Supplementary Material (Figure 4.S-1 and Figure 4.S-2)

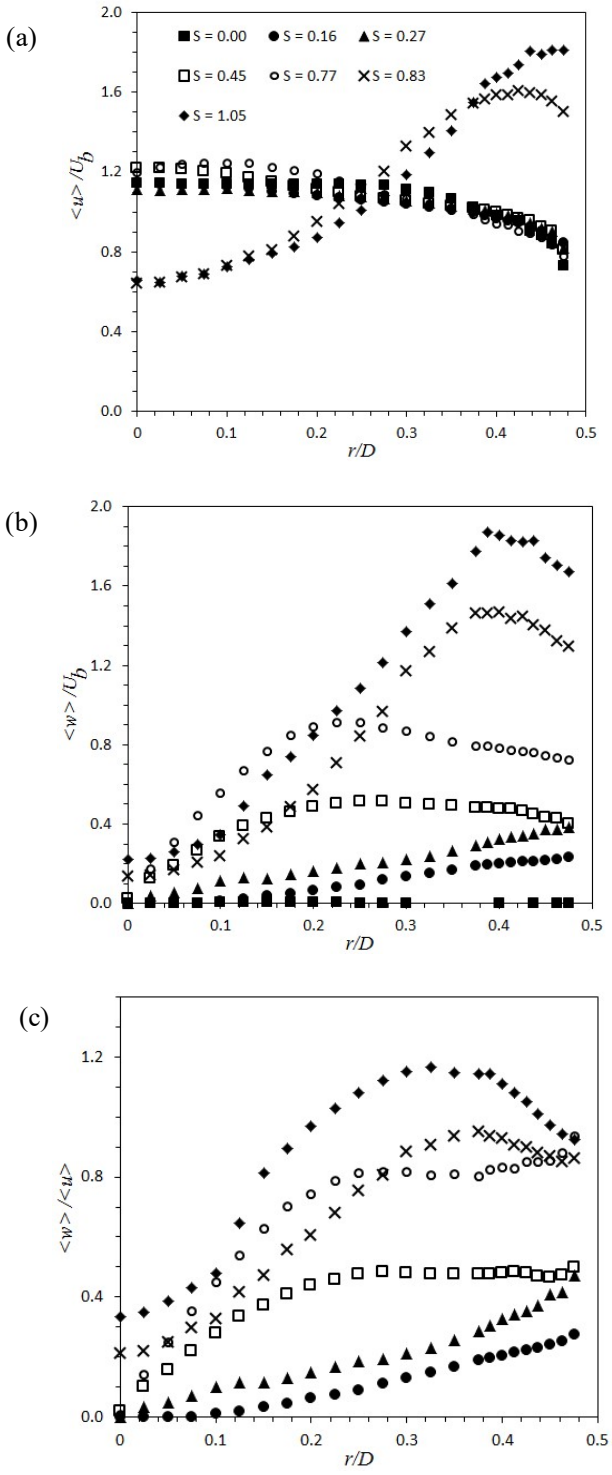

Figure 4.5 Velocity profiles measured at the nozzle exit plane (x/D = 0.025) for both non-swirling (S = 0.00) and swirling jets (S = 0.16 – 1.05) at Re = 35,000: (a) axial velocity, (b) tangential velocity and (c) local swirl profiles.

to CTA probe interference, which although only reported at relatively weak swirl numbers [48], is also expected to be magnified with increased swirl.

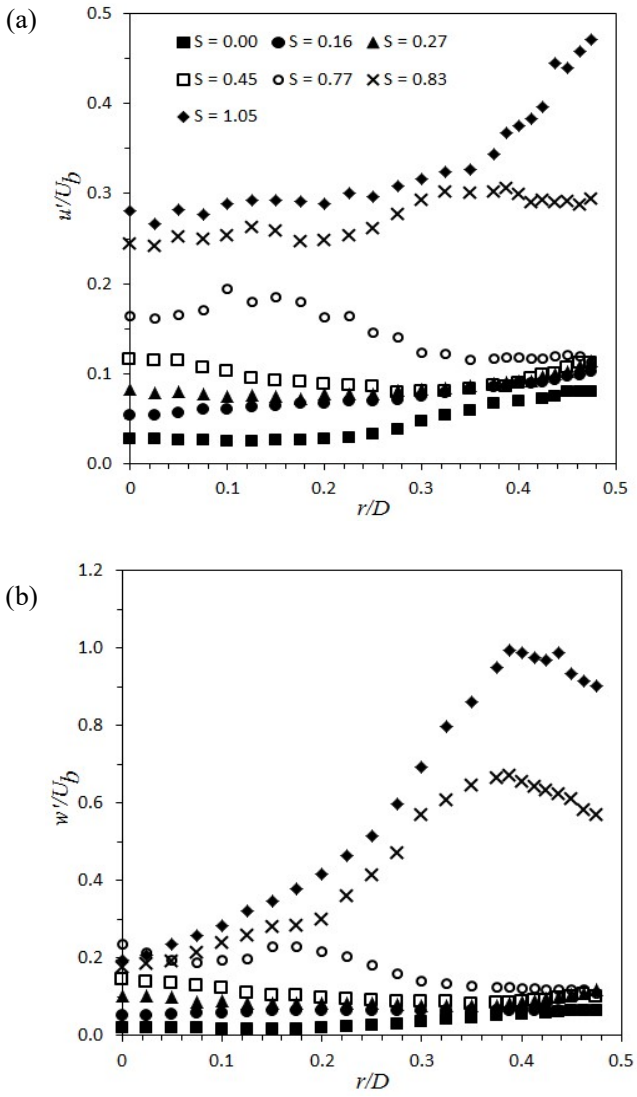

Figure 4.6 Turbulence intensities measured at the nozzle exit (x/D = 0.025) for both non-swirling (S = 0) and swirling jets (S = 0.16 – 1.05) at Re = 35,000: (a) axial and (b) tangential turbulence intensity profiles.

4.3 Results and discussion

Figure 4.7 depicts the decay of the mean axial velocity for the equivalent free (non-impinging) jets for S = 0 - 1.05 at Re = 35,000. The data shows a shortening of the potential

core length from $x = 5D$ to $x = 2D$ at small swirl numbers ($S = 0.16$), in comparison to a non-swirling jet ($S = 0$). For $S \geq 0.27$, the core length reduces more drastically with increasing swirl number and the potential core terminates close to the nozzle exit, which indicates increased jet dispersion due to swirl. The decrease in core length shown in Figure 4.7 is attributed to the increase in centrifugal forces and axial pressure gradient with higher swirl. The hyperbolic decay prevails after $x = 2D$, where $\langle u_c \rangle$ is proportional to $1/x$, in agreement with other classical studies [51, 56] and conservation equations. The maximum value of $\langle u \rangle$ is displaced from the x-axis at the highest swirl number. The absence of a distinctive trough-like decay, indicative of a flow approaching centreline stagnation, does not support evidence for clear vortex breakdown occurring (or being approached) from this data [57]. More tests are warranted to further validate this.

Figure 4.8 demonstrates the effect of swirl on the radial distributions of (impingement surface) static pressure for the range $0 \leq S \leq 1.05$ and $H = 1D$ to $6D$ at $Re = 35{,}000$. For all H positions and for low swirl numbers ($S \leq 0.27$), Cp decreases (with radial distance) from a maximum at the stagnation point and shows a Gaussian-like distribution, with maximum Cp at the centreline similar to non-swirling flows. However, the maximum Cp value shifts (radially) from the stagnation point for medium swirl numbers ($S = 0.45$) and at $H = 1D$, whereas the shift initiates at $S = 0.77$ for other H values. The radial position of the maximum Cp moves outward due to the higher centrifugal effects as swirl number increases. A flatter

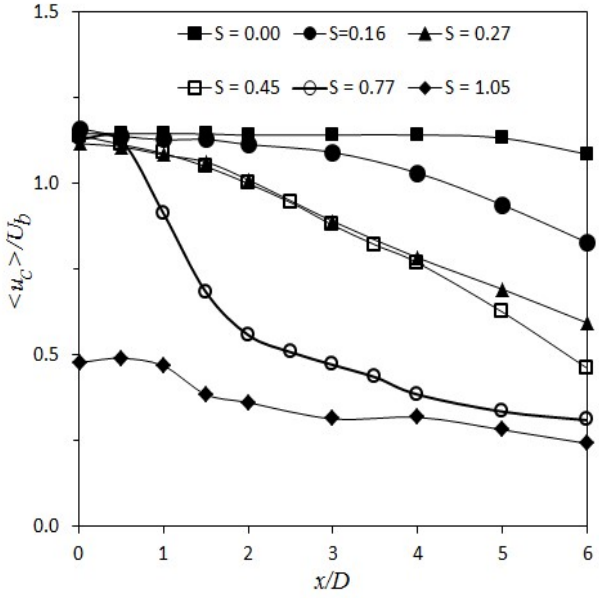

Figure 4.7 Normalised centreline velocity decay at $Re = 35{,}000$ for non-swirling ($S = 0$) and swirling ($S = 0.16 – 1.05$) free jets. Normalisation is by U_b measured at $x/D = 0.025$.

Cp distribution is observed for $H \geq 2D$ when $S \geq 0.77$, which is attributed to the radial spread of the jet. The reduction in stagnation pressure with swirl number for all *H* at a given *Re*, closely follows the quadratic equation:

$$\frac{P_S}{P_S(S=0)} = \mathrm{A}S^2 + \mathrm{B}S + 1, \tag{4.9}$$

where, A and B are constants that are dependent on *H*. The reduction is largely attributed to the axial deceleration of the swirl flow. Figure 4.8 also demonstrates a negative wall pressure coefficient near the stagnation region for $H = 1D$ that disappears for larger *H* values. This indicates flow separation from the impingement surface near the stagnation point for $H = 1D$. The wall static pressure increases in the radial direction (from the stagnation point) before reaching a maximum and then decaying. This suggests that the radial pressure gradient $\frac{\partial p}{\partial r} > 0$ and $\frac{\partial p}{\partial r} < 0$ before and after the peak static pressure, respectively and highlights two separate flow phenomena that may exist on (or near) the impingement surface surrounding the pressure peak. This is supported by Senda et al. [31] who found a radial inflow within $0.1D$ of the impingement surface up to $H = 4D$ for $S = 0.45$. In general, for non-swirling flow, *Cp* is almost independent of *H* up to $H = 4D$ (depicted in Figure 4.8), agrees with other studies [11, 22, 25], and is likely the distance within the potential core region and hence variation in pressure is not significant. However, for swirling flow, *Cp* reduces with *H* in the inner region of the flow and increases in the radial direction for the outer region. This characteristic highlights the increased radial extent of the impingement region and surface characteristics, such as wall shear stress and heat transfer may ultimately be affected at higher swirl intensity. Surface pressure profiles for medium-to-strong swirl flow revert to non-swirl flow behaviour with increasing *H*, where peaks outside the stagnation point become weaker and eventually diminish for $H = 6D$. At larger *H*, the jet's kinetic energy should reduce as the jet approaches the surface and undergoes a reduction of $\langle w \rangle$ due to stronger dissipative effects from flow mixing with the surrounding fluid [33]. This leads to the weaker centrifugal force causing jet spread. Moreover, the effect of swirl is more evident in the near-field ($H = 1D$) as *S* causes more abrupt change in *Cp* trend at this distance compared to other downstream distances ($H = 2D – 6D$).

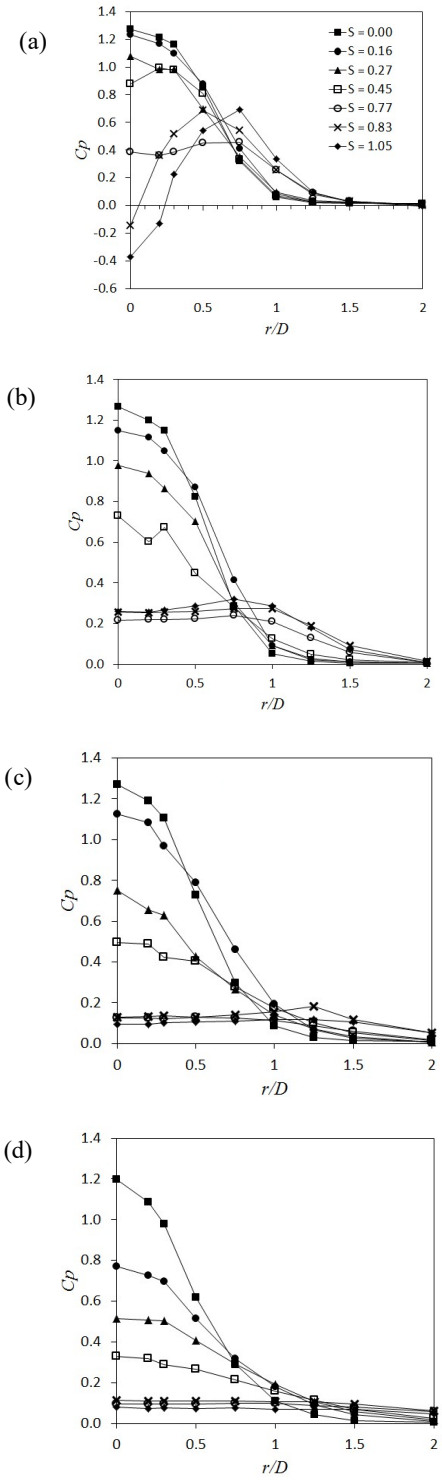

Figure 4.8 The effect of nozzle-to-plate distance and swirl number at *Re* = 35,000 on the impingement surface pressure distribution: (a) *H* = 1*D*, (b) *H* = 2*D*, (c) *H* = 4*D* and (d) *H* = 6*D*.

Figure 4.9 depicts the effect of *Re* on wall pressure distributions for the same swirl numbers in the range $S = 0 – 0.74$ (Table 4.1). Since *Cp* cannot be used as a non-dimensional parameter to compare wall pressures at different *Re*, due to the varying dynamic pressures in each case, the wall static pressure is normalized by the maximum pressure in the radial distribution (not necessarily at the stagnation point) for a given *S*. For non-swirling ($S = 0$) and low swirl conditions ($S = 0.29$), the pressure distribution is found to be independent of *Re*. For $S = 0.52$, the wall pressure is found to vary between different Reynolds numbers up to $r/D = 2$; a peak is located away from the stagnation region for the lowest *Re* whilst a peak appears on the centreline axis for the remaining cases. This is attributed to the varied axial and tangential velocity profiles in the upstream at different *Re* even though the swirl number (*S*) remains unchanged (Figures 4.5, 4.S-1 and 4.S-2). The result is an expected influence on the downstream flow development and characteristics at the impingement surface. At higher swirl ($S = 0.74$), similarity of pressure profiles recurs again particularly for lower *Re* (11,600 and 24,600) and a dependency of the pressure profile on higher *Re* only exists for $r/D < 0.75$. This merging tendency of the pressure trends at higher swirl is due to the similar upstream profiles of $\langle u \rangle/U_b$ and $\langle w \rangle/U_b$ for *Re* = 11,600 and 24,600, compared to *Re* = 35,000. At the exit plane (x/D=0.025), these velocity profiles are largely dependant on the combined flow through the three tangential ports (Q_t) relative to the total flows via the tangential and axial ports (Q_T) together. At a nomimal swirl number of $S = 0.52$, Q_t/Q_T equals to 0.67 for *Re* = 11,600 but different at around 0.55 for both *Re* = 24,600 and 35,000, respectively.

Figure 4.10 illustrates the flow visualisation results near the impingement surface up to $r/D = 2$ for *Re* = 35,000, $H = 1D$ and $S = 0.27, 1.05$. The results from the r-θ plane (Figure 4.10a) reveal that tufts are largely oriented radially with a little inclination towards the tangential direction on the impingement surface for low swirl ($S = 0.27$). This clearly deviates from the unidirectional (radially outward) flow for $S = 0$ (not detailed here for brevity). The visualisation in the r-x plane (Figure 4.10b) shows no reverse flow behavior near the impingement surface with tufts pointing outwards and away from the stagnation point. In contrast, for high swirl ($S = 1.05$) an entirely different flow characteristic is observed around the geometric stagnation point (Figure 4.10c and Figure 4.10d), with three different radial regions being identified. In the region closest to the stagnation point and spanning $r/D \leq 0.5$, Figure 4.10c shows tufts which are no longer oriented radially outward, as in the low swirl case, but directed towards the stagnation point and inclined in the tangential direction (clockwise). In this region, Figure 4.10d predominantly indicates flow separation at the

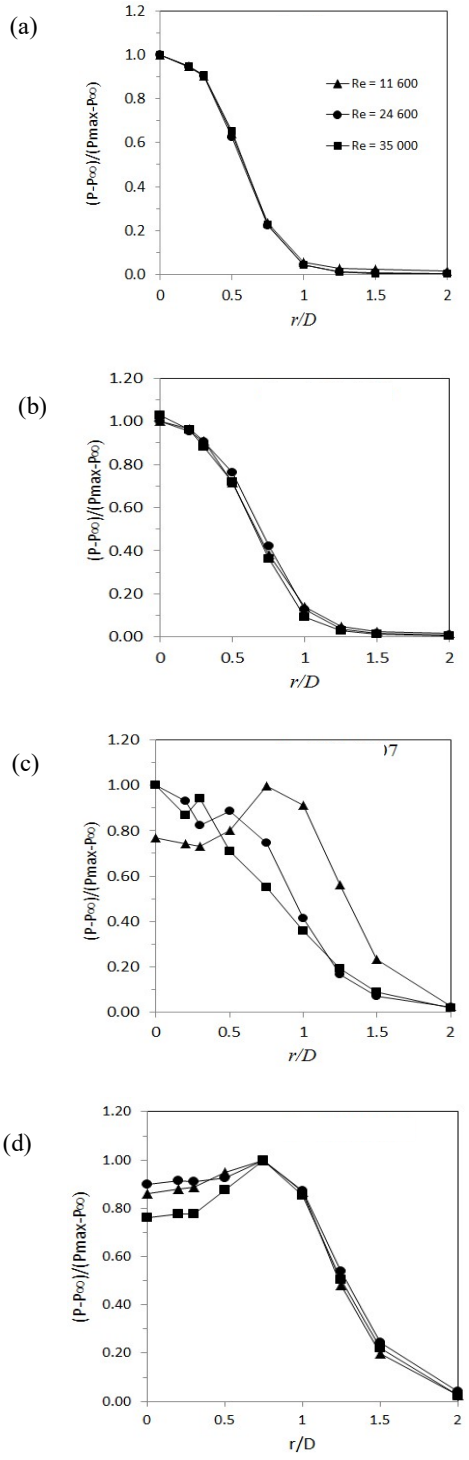

Figure 4.9 The effect of Reynolds number and swirl number at $H = 2D$ on the impingement pressure distribution: (a) $S = 0$, (b) $S = 0.29 \pm 0.03$, (c) $S = 0.52 \pm 0.07$ and (d) $S = 0.74 \pm 0.02$. The numbers after (±) indicates swirl number variations over the range $Re = 11{,}600 – 35{,}000$.

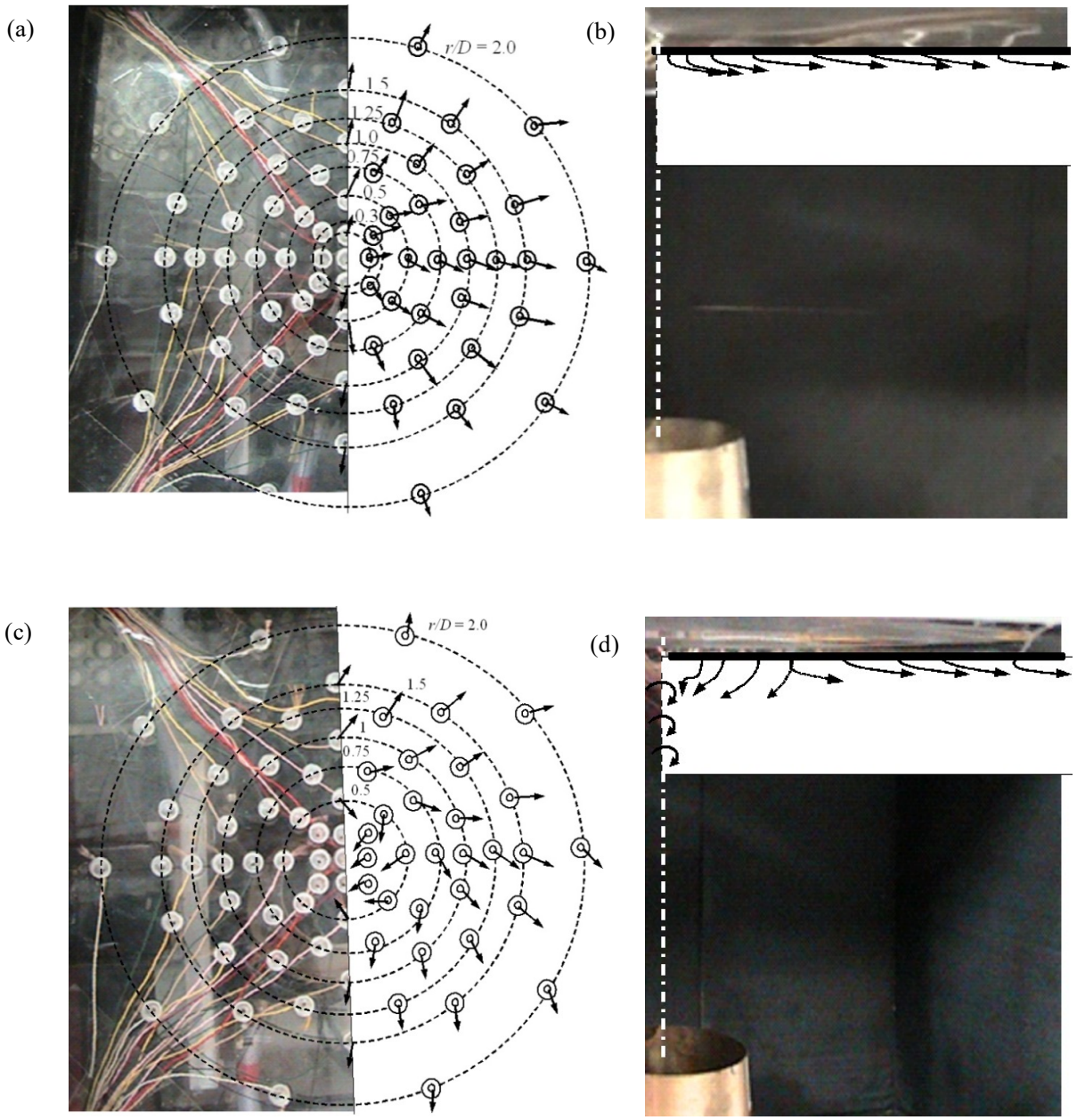

Figure 4.10 Flow visualizations on the impingement surface for Re = 35,000 and H = 1D. Image (a,b) S = 0.27; Image (c,d) S = 1.05. The impingement surface is smooth, whereby the long strings shown are on the reverse (back) side which is not subject to jet flow. Figures b and d depict the general orientation of tufts as visualized through digital movies (actual tufts are not shown due to limited visibility).

stagnation surface with tufts pointing upstream and towards the centreline. The results from both Figures 4.10c and 4.10d support the likelihood of a flow reversal or separation which also rotates with swirl in this zone. In the furthermost region from the stagnation point spanning $r/D \geq 1.0$, Figure 4.10c shows that tufts are susceptible to some tangential

alignment similar to the low swirl case. The transition between these two zones occurs at $0.5 < r/D \leq 0.75$.

The above findings are consistent with the experimental results shown in Figures 4.8 and 4.9, where negative *Cp* values were observed around the stagnation point at $H = 1D$ and it also confirms the inward flow direction at the transition region. Although flow visualisation for $S = 1.05$ at $H = 1D$ and $2D$ (not shown) demonstrate almost similar features, the existence of negative *Cp* for $H = 1D$ can be explained by the flow separation (flow reversal) at the stagnation zone. The flow reversal zone, appeared between the impingement surface and the nozzle, may originate at the impingement surface. For $H = 2D$, flow reversal may have started some distance away from the impingement surface without any flow separation at the impingement wall. Visual inspections from traversing a set of tufts from the impingement surface towards the nozzle exit supports this explanation, where the occurrence of reversed flow is found to depend on *H* and this agrees with similar studies [16, 31]. The exact nature or detailed extent of the reverse flow region cannot be accurately characterised by simply using tufts and needs more investigation for turbulent impinging jets with aerodynamically generated swirl.

4.4 Conclusions

An incompressible turbulent swirling air jet was investigated experimentally for the effect of swirl in the range $0 \leq S \leq 1.05$ for $H = 1D - 6D$ and $Re = 11{,}600 - 35{,}000$. A CTA anemometer is used to measure the time-mean and turbulence velocity components at the exit plane of the swirl nozzle to characterise the inlet conditions of the flow. Surface pressure measurements were conducted by using a digital micromanometer via flush-mounted pressure taps on the impingement plate. The results of these experiments are summarised below:

- The stagnation pressure reduction with swirl is found to be nonlinear and closely follows a quadratic relationship for a given *Re*. For low swirl values ($S \leq 0.27$), the behaviour of *Cp* is similar to non-swirling flows ($S = 0$) for small impingement distances. The maximum *Cp* shifts away from the stagnation point with stronger swirl. A flatter *Cp* profile with a weak peak is evident when *S* further increases, for beyond $H = 2D$.

- A negative wall pressure coefficient occurs near the stagnation region at $H = 1D$ due to the rotating reversed flow separation from the impingement surface, which disappears at larger H values (Cases I35S083 and I35S105).
- For low swirls ($S \leq 0.29$), the pressure is independent of Re and for larger swirl, the pressure varies with Re up to $r/D = 2$ for $S \approx 0.52$ and $r/D < 0.75$ for $S \approx 0.74$ (Figure 4.9).
- Unlike for non-swirling flows, a combined radial and weak tangential flow on the impingement surface is observed for low swirl ($S = 0.27$). In contrast, for strong swirl ($S = 1.05$), three different regions are identified on the impingement surface from the stagnation point: an inward rotating flow at $r/D \leq 0.5$, a transition region at $0.5 < r/D \leq 0.75$ and an outward directed flow region at $r/D \geq 1.0$ (Figure 4.10).

4.5 Chapter references

1. Lee, K. H. and Viskanta, R., *Quenching of flat glass by impinging air jets*, Numerical Heat Transfer, Part A: Applications, 33(1), p. 5-22, 1998.
2. Han, J. C., *Recent studies in turbine blade cooling*, International Journal of Rotating Machinery, 10(6), p. 443-457, 2004.
3. De Bonis, M. V. and Ruocco, G., *An experimental study of the local evolution of moist substrates under jet impingement drying*, International Journal of Thermal Sciences, 50(1), p. 81-87, 2011.
4. Singh, G., Chander, S. and Ray, A., *Heat transfer characteristics of natural gas/air swirling flame impinging on a flat surface*, Experimental Thermal and Fluid Science, 41(0), p. 165-176, 2012.
5. Jambunathan, K., Lai, E., Moss, M. A. and Button, B. L., *A review of heat transfer data for single circular jet impingement*, International Journal of Heat and Fluid Flow, 13(2), p. 106-115, 1992.
6. Gauntner, J. W., Livingood, J. N. B. and Hrycak, P., *Survey of literature on flow characteristics of a single turbulent jet impinging on a flat plate*, in Technical Report, NASA: Washington, D.C., p. 1-22, 1970.
7. Beltaos, S. and Rajaratnam, N., *Impinging circular turbulent jets*, Journal of the Hydraulics Division, 100(10), p. 1313-1328, 1974.
8. Giralt, F., Chia, C. and Trass, O., *Characterization of the impingement region in an axisymmetric turbulent jet*, Industrial & Engineering Chemistry Fundamentals, 16(1), p. 21-28, 1977.
9. Rajaratnam, N., Turbulent jets, Elsevier, Amsterdam, The Netherland, 1976.
10. Hargrave, G. K., Williams, T. C., Anandarajah, K. and Halliwell, N. A., *The 3D velocity field of an impacting turbulent jet*, Journal of Physics: Conference Series, 45(0), p. 162-172, 2006.
11. Katti, V. and Prabhu, S. V., *Experimental study and theoretical analysis of local heat transfer distribution between smooth flat surface and impinging air jet from a circular straight pipe nozzle*, International Journal of Heat and Mass Transfer, 51(17–18), p. 4480-4495, 2008.

12. Tummers, M. J., Jacobse, J. and Voorbrood, S. G. J., *Turbulent flow in the near field of a round impinging jet*, International Journal of Heat and Mass Transfer, 54(23–24), p. 4939-4948, 2011.
13. Ahmed, Z. U., Al-Abdeli, Y. M. and Matthews, M. T., *The effect of inflow conditions on the development of non-swirling versus swirling impinging turbulent jets*, Computers & Fluids, 118, p. 255-273, 2015.
14. Bilen, K., Bakirci, K., Yapici, S. and Yavuz, T., *Heat transfer from a plate impinging swirl jet*, International Journal of Energy Research, 26(4), p. 305-320, 2002.
15. Lee, D. H., Won, S. Y., Kim, Y. T. and Chung, Y. S., *Turbulent heat transfer from a flat surface to a swirling round impinging jet*, International Journal of Heat and Mass Transfer, 45(1), p. 223-227, 2002.
16. Alekseenko, S. V., Bilsky, A. V., Dulin, V. M. and Markovich, D. M., *Experimental study of an impinging jet with different swirl rates*, International Journal of Heat and Fluid Flow, 28(6), p. 1340-1359, 2007.
17. Ianiro, A. and Cardone, G., *Heat transfer rate and uniformity in multichannel swirling impinging jets*, Applied Thermal Engineering, 49(0), p. 89-98, 2011.
18. Al-Abdeli, Y. M. and Masri, A. R., *Recirculation and flowfield regimes of unconfined non-reacting swirling flows*, Experimental Thermal and Fluid Science, 27(5), p. 655-665, 2003.
19. Al-Abdeli, Y. M. and Masri, A. R., *Turbulent swirling natural gas flames: Stability characteristics, unsteady behavior and vortex breakdown*, Combustion Science and Technology, 179(1-2), p. 207-225, 2007.
20. Wen, M. and Jang, K., *An impingement cooling on a flat surface by using circular jet with longitudinal swirling strips*, International Journal of Heat and Mass Transfer, 46(24), p. 4657-4667, 2003.
21. Ichimiya, K. and Tsukamoto, K., *Heat transfer from an inflow-type swirling turbulent impinging jet*, JSME International Journal Series B Fluids and Thermal Engineering, 49(4), p. 995-999, 2006.
22. Baydar, E. and Ozmen, Y., *An experimental investigation on flow structures of confined and unconfined impinging air jets*, Heat and Mass Transfer, 42(4), p. 338-346, 2006.
23. Beltaos, S. and Rajaratnam, N., *Impingement of axisymmetric developing jets*, Journal of Hydraulic Research, 15(4), p. 311-326, 1977.
24. Lytle, D. and Webb, B. W., *Air jet impingement heat transfer at low nozzle-plate spacings*, International Journal of Heat and Mass Transfer, 37(12), p. 1687-1697, 1994.
25. Ozmen, Y. and Baydar, E., *Flow structure and heat transfer characteristics of an unconfined impinging air jet at high jet Reynolds numbers*, Heat and Mass Transfer, 44(11), p. 1315-1322, 2008.
26. Tong, A. Y., *A numerical study on the hydrodynamics and heat transfer of a circular liquid jet impinging onto a substrate*, Numerical Heat Transfer: Part A: Applications, 44(1), p. 1-19, 2003.
27. Yang, H. Q., Kim, T., Lu, T. J. and Ichimiya, K., *Flow structure, wall pressure and heat transfer characteristics of impinging annular jet with/without steady swirling*, International Journal of Heat and Mass Transfer, 53(19–20), p. 4092-4100, 2010.
28. Yang, H., Kim, T. and Lu, T., *Characteristics of annular impinging jets with/without swirling flow by short guide vanes*, Science China Technological Sciences, 54(3), p. 749-757, 2011.
29. Abrantes, J. K. and Azevedo, L. F. A., *Fluid flow characteristics of a swirl jet Impinging on a flat plate*, in 13th Int Symp on Applications of Laser Techniques to

Fluid Mechanics, 26-29 June, Lisbon, Portugal, http://ltces.dem.ist.utl.pt/lxlaser/lxlaser2006/downloads/papers/28_3.pdf, p. 1-12, 2006.
30. Nozaki, A., Igarashi, Y. and Hishida, K., *Heat transfer mechanism of a swirling impinging jet in a stagnation region*, Heat Transfer—Asian Research, 32(8), p. 663-673, 2003.
31. Senda, M., Inaoka, K., Toyoda, D. and Sato, S., *Heat transfer and fluid flow characteristics in a swirling impinging jet*, Heat Transfer—Asian Research, 34(5), p. 324-335, 2005.
32. Ortega-Casanova, J., Campos, N. and Fernandez-Feria, R., *Experimental study on sand bed excavation by impinging swirling jets*, Journal of Hydraulic Research, 49(5), p. 601-610, 2011.
33. Felli, M., Falchi, M. and Pereira, F., *Distance effect on the behavior of an impinging swirling jet by PIV and flow visualizations*, Experiments in Fluids, 48(2), p. 197-209, 2010.
34. Hussain, A. K. M. F. and Ramjee, V., *Effects of the axisymmetric contraction shape on incompressible turbulent flow*, Journal of Fluids Engineering, 98(1), p. 58-68, 1976.
35. Scheiman, J. and Brooks, J. D., *Comparison of experimental and theoretical turbulence reduction from screens, honeycomb, and honeycomb-screen combinations*, Journal of Aircraft, 18(8), p. 638-643, 1981.
36. Watmuff, J. H., *Wind tunnel contraction design*, in 9th Australasian Fluid Mechanics Conference, 8-12 December, Auckland, http://www.afms.org.au/proceedings.html#proceedings, p. 472-475, 1986.
37. Morel, T., *Comprehensive design of axisymmetric wind tunnel contractions*, Journal of Fluids Engineering, 97(2), p. 225-233, 1975.
38. Mikhail, M. N., *Optimum design of wind tunnel contractions*, AIAA Journal, 17(5), p. 471-477, 1979.
39. Thomas, B., Ahmed, Z. U., Al-Abdeli, Y. M. and Matthews, M. T., *The optimisation of a turbulent swirl nozzle using CFD*, in Proceedings of the Australian Combustion Symposium, 6-8 November Perth, Australia, http://www.anz-combustioninstitute.org/local/papers/ACS2013-Conference-Proceedings.pdf, p. 271-274, 2013.
40. Kitoh, O., *Experimental study of turbulent swirling flow in a straight pipe*, Journal of Fluid Mechanics, 225(0), p. 445-479, 1991.
41. Lečić, M. R., Ćoćić, A. S. and Čantrak, S. M., *Original measuring and calibration equipment for investigation of turbulent swirling flow in circular pipe*, Experimental Techniques, 38(3), p. 54-62, 2014.
42. Algifri, A. H., Bhardwaj, R. K. and Rao, Y. V. N., *Turbulence measurements in decaying swirl flow in a pipe*, Applied Scientific Research, 45(3), p. 233-250, 1988.
43. Gupta, A. K., Lilley, D. G. and Syred, N., *Swirl flows*, Tunbridge Wells, Kent, England, Abacus Press, 1984, 488 p., 1, p., 1984.
44. Toh, I., Honnery, D. and Soria, J., *Axial plus tangential entry swirling jet*, Experiments in Fluids, 48(2), p. 309-325, 2010.
45. Oberleithner, K., Sieber, M., Nayeri, C. N., Paschereit, C. O., et al., *Three-dimensional coherent structures in a swirling jet undergoing vortex breakdown: stability analysis and empirical mode construction*, Journal of Fluid Mechanics, 679, p. 383-414, 2011.
46. Farokhi, S., Taghavi, R. and Rice, E. J., *Effect of initial swirl distribution on the evolution of a turbulent jet*, AIAA Journal, 27(6), p. 700-706, 1989.

47. Davoust, S., Jacquin, L. and Leclaire, B., *New results on the structure of turbulence in a mixing layer with and without swirl*, International Journal of Heat and Fluid Flow, 49, p. 11-17, 2014.
48. Örlü, R. and Alfredsson, P. H., *An experimental study of the near-field mixing characteristics of a swirling jet*, Flow, Turbulence and Combustion, 80(3), p. 323-350, 2008.
49. Billant, P., Chomaz, J. and Huerre, P., *Experimental study of vortex breakdown in swirling jets*, Journal of Fluid Mechanics, 376, p. 183-219, 1998.
50. Al-Abdeli, Y. M. and Masri, A. R., *Stability characteristics and flowfields of turbulent non-premixed swirling flames*, Combustion Theory and Modelling, 7(4), p. 731-766, 2003.
51. Chigier, N. A. and Chervinsky, A., *Experimental investigation of swirling vortex motion in jets*, Journal of Applied Mechanics, 34(2), p. 443-451, 1967.
52. Sheen, H. J., Chen, W. J., Jeng, S. Y. and Huang, T. L., *Correlation of swirl number for a radial-type swirl generator*, Experimental Thermal and Fluid Science, 12(4), p. 444-451, 1996.
53. Li, H. and Tomita, Y., *An experimental study of swirling flow pneumatic conveying system in a horizontal pipeline*, Journal of Fluids Engineering, 118(3), p. 526-530, 1996.
54. Yajnik, K. S. and Subbaiah, M. V., *Experiments on swirling turbulent flows. Part 1. Similarity in swirling flows*, Journal of Fluid Mechanics, 60(4), p. 665-687, 1973.
55. Semaan, R. and Naughton, J. W., *Three-component Laser-Doppler-Anemometry measurements in turbulent swirling jets*, AIAA journal, 51(9), p. 2098-2113, 2013.
56. Pratte, B. D. and Keffer, J. F., *The Swirling Turbulent Jet*, Journal of Fluids Engineering, 94(4), p. 739-747, 1972.
57. Al-Abdeli, Y. M. and Masri, A. R., *Precession and recirculation in turbulent swirling isothermal jets*, Combustion Science and Technology, 176(5-6), p. 645-665, 2004.

4.6 Chapter appendices

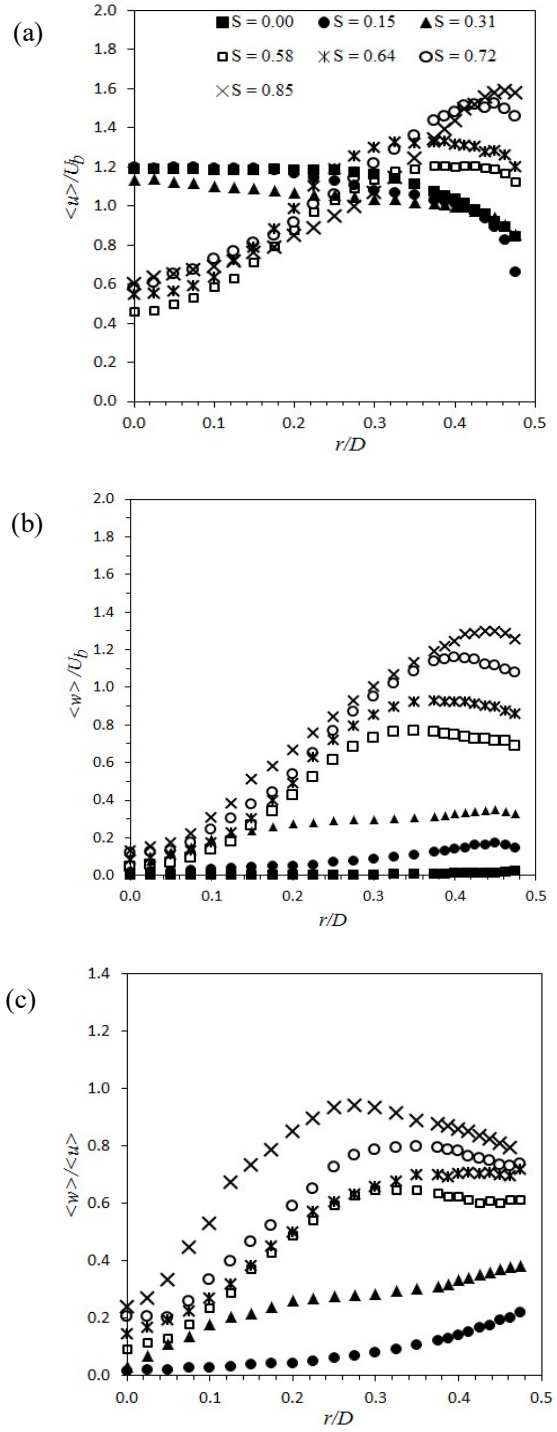

Figure 4.S-1 Inlet velocity profiles measured at the nozzle exit (x/D = 0.025) for both non-swirling (S = 0.00) and swirling jets (S = 0.15 – 0.85) at Re = 24,600: (a) axial velocity, (b) tangential velocity and (c) local swirl profiles. Velocity components are normalised by the non-swirling test case (I24S000).

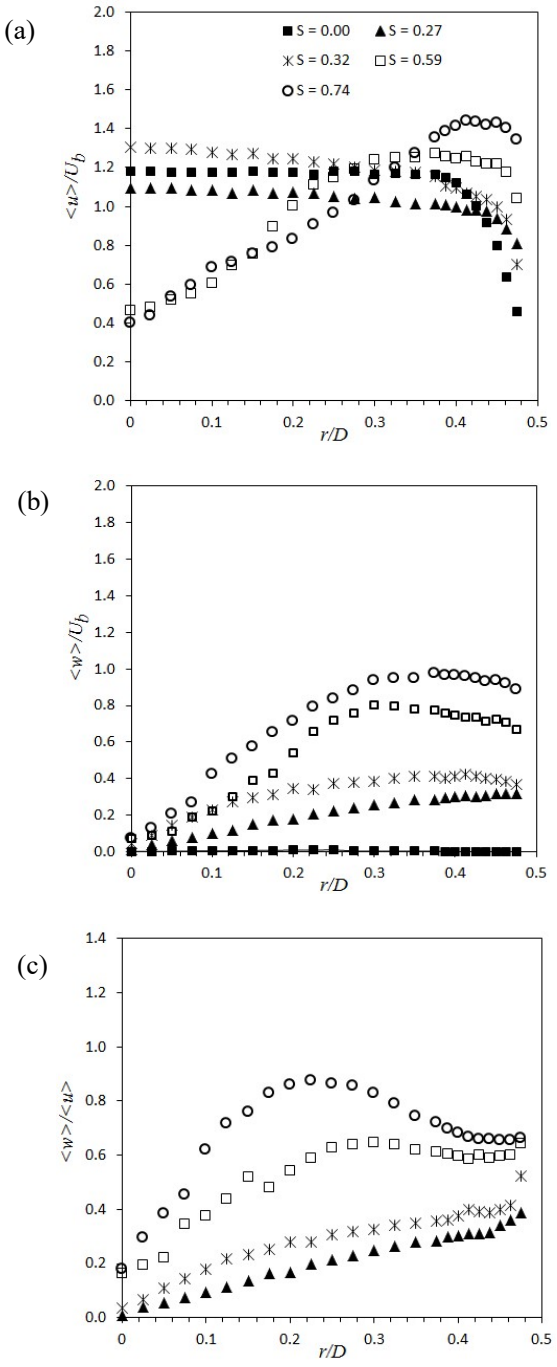

Figure 4.S-2 Inlet velocity profiles measured at the nozzle exit (x/D = 0.025) for both non-swirling (S = 0.00) and swirling jets (S = 0.27 – 0.74) at Re = 11,600: (a) axial velocity, (b) tangential velocity and (c) local swirl profiles. Velocity components are normalised by the non-swirling test case (I11S000).

Chapter 5

5 Heat Transfer Characteristics of Swirling and Non-swirling Impinging Turbulent Jets[11]

This chapter presents experimental measurements of heat transfer using infrared thermography for both swirling and non-swirling impinging jets for the effect of various controlling parameters.

5.1 Introduction

Impinging jets have been widely researched in relation to whether they provide an effective means of achieving higher energy transfer between a fluid and an impingement surface in convective heating and cooling. In this context, jets have been used in quenching of heated surfaces at nuclear reactors and the machining zone in grinding so as to avoid thermal damage [1-5]. Hot jets or direct flame impingement is also used as a means of rapid and efficient heating in furnaces, the melting of scrap metals, shaping glassware and to heat metal billets prior to forging [6-9]. Alternatively, applications involving non-swirling jet impingement can be susceptible to non-uniform heat flux distribution, which leads to localised heating and high temperature gradients [10-15]. Additionally, there have also been numerous treatises into the effectiveness of using swirl impingement in the belief that such jets promote surface heat and mass transfer rates. However, the diverse range of swirl generation mechanisms used in these works and variation in the observed flow behaviours sometimes yield contradicting outcomes. As such, there exists a lack of fundamental understanding for the exact effects and merits of using swirl with turbulent impinging jets.

The flow domain of a single, axisymmetric non-swirling turbulent impinging jet typically consist of three regions [16-19]: the free jet region, starts at the nozzle exit plane and

[11] This chapter has been submitted for publication as a full research paper in:
Ahmed Z. U., Al-Abdeli, Y. M., Guzzomi, F. G., International Journal of Heat and Mass Transfer (In review).
Whilst efforts were made to retain original content of the article, minor changes such as number formats, font size style were implemented in order to maintain consistency in the formatting style of the thesis.

represented by an inner potential core with its peripheral shear layer, a central impingement region, and finally a ring-shaped outer wall jet region on the surface. The potential core length is affected by the nozzle-to-plate distance (H) and typically extends (with impingent) up to six nozzle diameters downstream of the nozzle exit. In the wall jet region of non-swirling impinging jets, the radial velocity is dominant and its maximum is located near the impingement surface at a radial position (r) of approximately $r/D = 1.1$, with D the nozzle diameter. Increased turbulence within the wall jet region as well as large-scale turbulent flow structures in the free jet are believed to influence fluxes on the surface. Vortices formed in the free jet shear layer may also penetrate into, and affect the wall boundary layer generating counter rotating secondary vortices as they sweep the impingement surface [20]. In this case, the beneficial effects of upstream turbulence intensity on the local heat transfer of non-swirling impinging jets is well established [21, 22], whereby it is believed that increase in turbulent kinetic energy leads to enhanced mixing and higher wall heat flux. For non-swirling impinging jets with $H < 6D$, previous research also suggests the radial variation of heat transfer may not monotonically decrease from the centreline but have several peaks (maxima and minima) over different radial distances. The location of these peaks is not agreed upon [23, 24]. One explanation for this variability is that it may be due to the differing nozzle exit conditions. Research, however, indicates that with larger nozzle-to-plate distance ($H > 6D$), magnitudes of local impingement surface heat transfer decreases and the radial distribution of Nusselt number shows a monotonic decrease with a peak at the stagnation point (jet axis) [11, 24, 25]. The decreased heat transfer is attributed to downstream reductions in both jet velocity and turbulent kinetic energy. As such, the literature supports that impingement surface heat transfer characteristics, even in the context of non-swirling jets, are complex and depend on a range of flow and geometrical parameters, such as Reynolds number, nozzle-to-plate distance, nozzle geometry and turbulence. The dependency of such flow and geometrical parameters on impingement (non-swirling) heat transfer is typically described by correlations (Nusselt number with Reynolds number, nozzle-to-plate distance and Prandtl number). The coefficients or constants of such correlations largely rely on experimental setup and flow conditions. A recent study [26], limited to laminar, non-swirling jets, provided some fundamental insights into both the hydrodynamics and heat transfer behaviour of liquid jets and found that velocity profiles (near the impingement surface) dictated the heat transfer distribution at the stagnation zone. The use of turbulent flows and swirl will, however, affect flow mixing and is expected to alter the fundamental behaviour at impingement. These issues will be addressed in the present paper.

With the above in mind, inducing swirl into impinging jets involves a higher degree of flow field complexity which is further exacerbated through the variability of swirl generation methods used. As such, different studies have reported varied outcomes in relation to the effects of swirl on impingement heat transfer. In some experimental and numerical studies, swirl has been found to negatively affect heat transfer [27-31], with this attributed to thicker boundary layer generated at impingement surface and significant aerodynamic blockages (vortex breakdown) at strong swirl intensity. In contrast, other studies [32-34] report much higher surface heat transfer with swirl in the stagnation region compared to a non-swirling jet due to higher flow mixing (improved entrainment) and formation of vortices near the impingement surface. The effects of nozzle-to-plate distance and the resulting radial uniformity of heat transfer in relation to swirling jets has also received attention [28, 31, 35, 36]. However, the exact effects of H on the radial uniformity of Nu and level of heat transfer improvement are equally unresolved. Potentially contributing to this variability in outcomes and boundary conditions is that in almost all these studies, swirl has been generated geometrically (solid inserts or vanes) with very limited works using aerodynamically imparted swirl [37]. The use of aerodynamically generated swirl may help better understanding of the relationship between the swirl intensity and heat transfer over geometrically generated swirl due to undesirable flow perturbation and trailing vortices from inserts or vanes.

In this paper, an incompressible, turbulent impinging (ambient) air jet is used to fundamentally study the effect of swirl on impingement heat transfer characteristics. Swirl is generated aerodynamically for varying intensity from a non-swirling (S = 0) to a highly swirling jet (S = 1.05). The effect of different nozzle-to-plate distances (H = 1D – 6D) and Reynolds number (11,600 – 35,000) are also examined for their effect on heat transfer characteristics at the impingement surface. This analysis extends to the surface integrated average heat transfer as well as its uniformity across the impingement plane. Methodologies used in this study include Constant Temperature Anemometry (CTA) to characterize jet boundary conditions and infrared (IR) thermography to resolve temperatures (and Nusselt number) at the impingement surface.

5.2 Experimental techniques

5.2.1 Swirling jets

Figure 5.1a shows a partial sectional CAD view of the swirl nozzle used in this study. Also shown in Figure 5.1b is a closer view on the nozzle exit plane (x = 0 mm and y-z plane) and the coordinate system used in acquiring data as well as the CTA probe orientation. The turbulent flows obtained from this swirl nozzle can be seamlessly transitioned (aerodynamically) from non-swirling to swirling jets, without any geometric means. Pressure

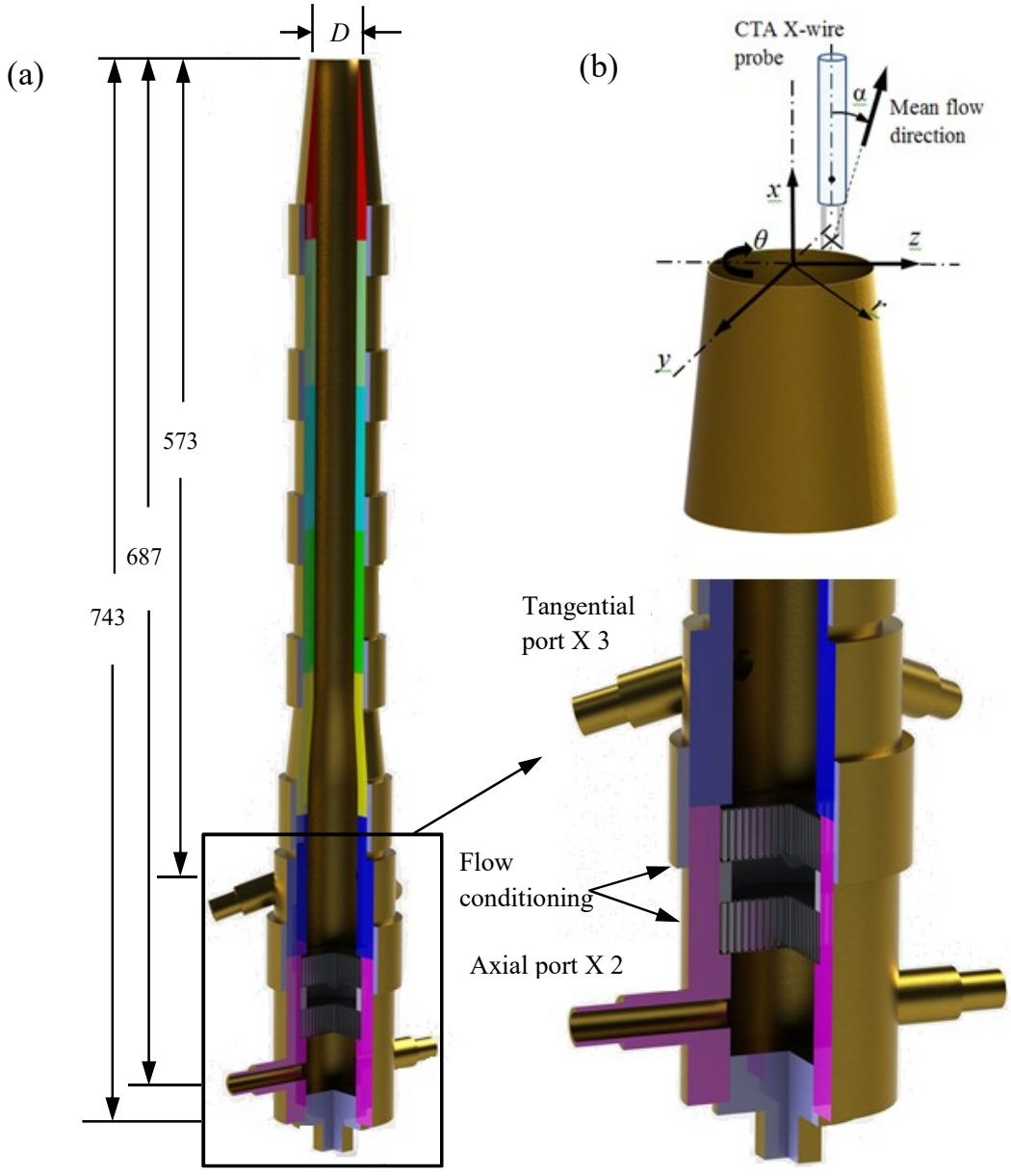

Figure 5.1 (a) Full length (partial) sectional CAD view of the swirl nozzle (dimensions are in mm), (b) setup for CTA measurements and the coordinate system used.

and flow meter regulated compressed air is fed into the base of the nozzle through two axial and three tangential ports. The axial ports are horizontal and 180^o apart whereas the tangential ports are positioned 120^o apart and inclined 20^o off the horizontal plane. By varying the proportions of tangential and axial streams this method thus allows swirl number changes, independent of Reynolds number and vice versa. The literature includes more detail on the design of the nozzle [38, 39], including the main features of its internal cavities and (inlet) port orientations so as to assist in numerical modelling if required. A dual-wire (X-wire) CTA probe (DANTEC, model: 55P61) was used to measure the axial and azimuthal components of the velocity at x = 1 mm above the nozzle exit plane in order to characterise exit conditions. The specific experimental CTA methodologies used to acquire the velocity data and corrections (velocity gradient, probe alignment and directional response) are also available in the literature [40]. The accuracy of mean velocity components from CTA measurements is also verified by comparing to pitot-static tube data, and estimated to be 2 % and 4% of the centreline velocity in non-swirling and swirling flows, respectively.

Flow through the swirl nozzle and the global swirl intensity are characterised at the exit plane by Reynolds number, $Re = 4Q/(\pi D\nu)$ and the swirl number, $S = W_b/U_b$, respectively. This swirl number formulation has been widely used in (free) swirling turbulent jet studies [41]. For the present nozzle geometry, it has also been correlated to flows at the axial and tangential ports [40] as well as other commonly cited swirl numbers (S*) representing the ratio of axial flux of tangential momentum to the axial flux of axial momentum [38]. However, the intricacies and multitude of vane (and helical insert) swirl generators used in the literature [31, 33], preclude establishing a direct comparison between S (or S*) to a swirl number based on a (geometric) vane or insert angle. In geometrically induced swirling jets, flow obstructions (from the solid inserts and vanes) form on the centerline perturb the velocity profiles and complicate a direct comparison to S. The total volume flow rate (Q) is calculated from the flows through all the axial and tangential ports. U_b and W_b are the bulk axial and tangential velocities respectively. Bulk velocities are determined by averaging CTA resolved velocity components across the nozzle exit plane:

$$U_b = \frac{2}{R^2}\int_0^R r < u > dr, \tag{5.1}$$

$$W_b = \frac{2}{R^2}\int_0^R r < w > dr. \tag{5.2}$$

To help better interpret the factors affecting heat transfer on the impingement surface, Figure 5.2 shows the (upstream) mean velocity components and their fluctuations at x/D = 0.025 for different swirl numbers (Re = 35,000). Values given have been plotted in each trend relative to (normalised) the bulk axial velocity (U_b) for the non-swirling test case at Re = 35,000. In non-swirling-to-weakly swirling jets ($S \leq 0.27$), the axial and tangential velocities at the nozzle exit are largely uniform, with some variation near the wall and centreline. Starting with the swirl number S = 0.45, a distinct change in both the axial and tangential velocities is observed. At S = 0.77 - 1.05, the peak tangential velocity distribution departs from the forced vortex (solid-body rotation) [42] like at S = 0.45 and more closely resembles a combined vortex. The peaks of $<w>$ shift radially outward as S increases. Both the fluctuating components (u'/U_b and w'/U_b) generally show similar characteristics and magnitude lies within 40% of the bulk velocity up to S = 0.77.

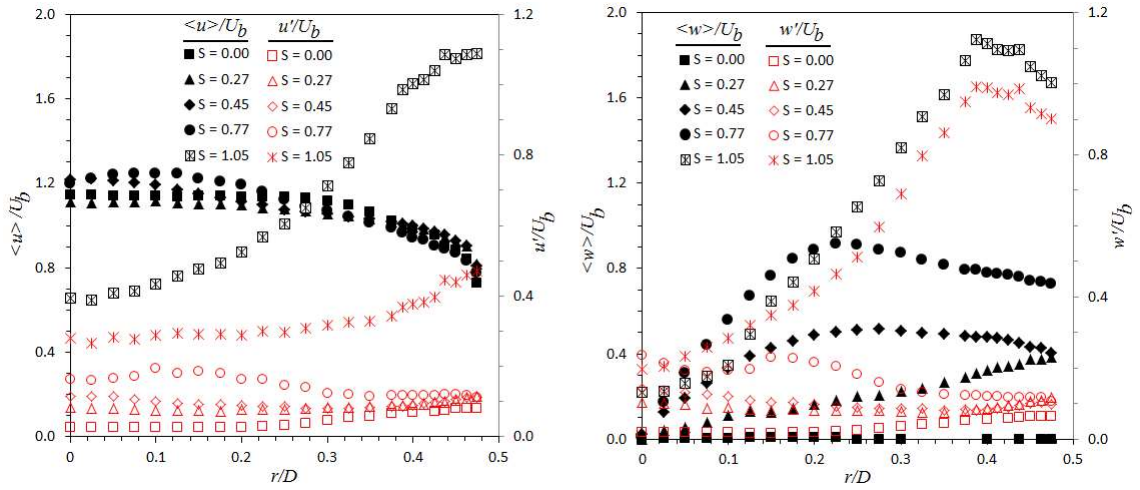

Figure 5.2 Normalised axial and tangential mean velocities ($<u>/U_b$ and $<w>/U_b$) and their respective fluctuations (u'/U_b and w'/U_b) resolved by CTA at x/D = 0.025 for Re = 35,000 over the swirl number range S = 0 – 1.05.

5.2.2 Impingement heat transfer

An infrared camera (FLIR systems, model: A325), operating at the 7.5-13 μm spectral range, is used to measure temperature on the impingement surface at a resolution of 320 x 240 pixels. The FPA (Focal Plane Array) microbolometer detector has a pitch and typical response time of 25 μm and 7 ms, respectively. By resolving surface temperatures, the

convective heat transfer can also be post-processed using the imaged data. Infrared cameras are advantageous in convective heat transfer analyses compared to standard techniques such as thermocouples and resistive sensors due to their non-intrusive measurements, high sensitivity (mK) and low response times [43].

Measurements of the local convective heat transfer coefficient are performed by using a steady-state heated thin foil technique [43, 44], which entails uniformly heating (by the Joule effect) a thin metallic foil and resolving its two-dimensional temperature distribution. In this regard, a constant heat flux was established at the impingement surface for all flow conditions over a steady period (60 min) before the acquisition of data. Typically, the variability in the heat flux distribution over the measurement domain (r/D = 2) is of the order ±2% (foil heated with no jet impingement). A horizontally positioned (tensioned) stainless steel foil (200 mm wide, 320 mm long and 0.025 mm thick) is used in this study. This foil is painted matt black (VHT, model: Flame proof) on the surface facing the infrared camera and is heated by a DC power source (Powertech, model: MP3094). The current (I) and voltage (E) across the impingement surface are measured in real-time using a clamp meter (MICRON, model: Q0966) and a digital multimeter (METREL, model: MD9020), respectively. In this manner, a constant heat flux was established at the impingement surface for all flow conditions. The maximum limit of the DC power source (40 Amperes at 3 Volts) produces a foil temperature of 97^{o}C (at no jet impingement). Preliminary tests revealed that 60 minutes are sufficient to reach steady state operating conditions at the heated foil, with temperature variation less than 0.3^{o}C. Figure 5.3 shows the assembly for the heated impingement surface. Prior to imaging, the emissivity coefficients for both the unpainted and painted face of the impingement surface are derived by the IR thermography in a separate experiment, following the method outlined in [45]. In this regard, a thermostatic-controlled constant temperature water bath (MATEST, model: B051-01) was used for a temperature range of ambient to 60^{o}C (intervals of 10^{o}C), and further detail of the method is available in [46]. These test revealed an emissivity of the unpainted and painted foil surface to be ε = 0.06 and ε = 0.97, respectively. After steady state condition is established for each test condition, 150 thermal images at 5 frames per second are acquired (after the elapsed 60 minutes needed to establish steady state) using the camera software interface (Thermacam Research, version 2.10). All imaged temperature data are post-processed by Matlab (version 2012b). In this manner, impingement surface temperatures are obtained by averaging

instantaneous temperature data over 150 thermal images to derive both mean and fluctuating components.

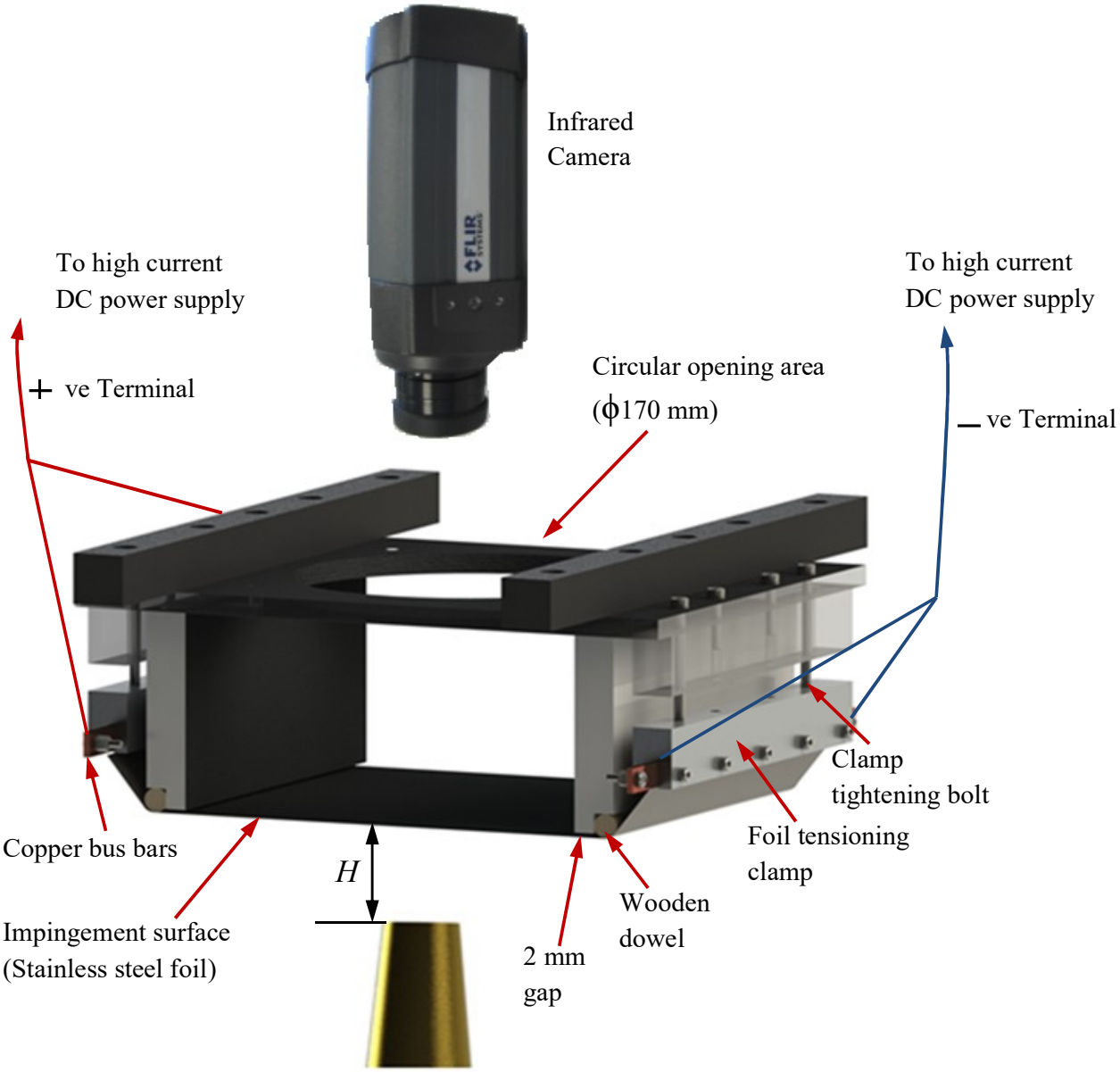

Figure 5.3 CAD view of the heated impingement foil and its tensioning as well as mounting assembly.

The time-averaged local convective heat transfer coefficient (h) for any impinging jet condition is determined by applying an energy balance to each imaged pixel:

$$h(i,j) = \frac{q - q_l(i,j)}{T_W(i,j) - T_{ref}(i,j)}, \tag{5.3}$$

where, (i, j) is the pixel location on an image, q is the applied heating flux (W/m^2), q_l represents the thermal losses due to tangential conduction along the foil (q_c) and radiation (q_r) from the surface and T_W is the heated wall (surface) temperature. The reference temperature (T_{ref}) for incompressible impinging jets is the adiabatic wall temperature, T_{aw} [47] and is determined from running the same jet condition and imaging experiment without heating the surface. Determining the reference temperature via T_{aw} for a given flow is needed so as to compensate for the limited thermal accuracy of the IR camera and varied (background) thermal conditions [47]. The heat flux q is obtained from the product of current (I) and voltage (E) applied to the impingement surface, divided by the foil area, $q = EI/A$. The foil is considered isothermal across its thickness because the Biot Number ($Bi = hb/k_w$, where k_w and b are the foil thermal conductivity and thickness, respectively) is relatively small, i.e. less than 0.1 [48]. Tangential conduction can be calculated by the second derivative of the wall temperature:

$$q_c = -k_w \nabla T_w, \tag{5.4}$$

where, ∇ is the Laplacian operator. The tangential conduction shown in Equation (5.4) is typically small and accounts for approximately 1% of the total heat transferred to the foil [49]. As a result, it is not included in the calculation of q. The loss due to radiation is evaluated according to the Stefan-Boltzmann law:

$$q_r = \left(\varepsilon_p + \varepsilon_{up}\right)\sigma\left(T_w^4 - T_{amb}^4\right). \tag{5.5}$$

In this context, ε_p and ε_{up} are the emissivity coefficients of painted and unpainted impingement surface, σ is the Stefan-Boltzman constant and T_{amb} is the ambient temperature. Typical radiation loss is found to be 4% of the applied heat flux.

The local convective heat transfer is usually determined by the Nusselt number Nu and is defined in Cartesian coordinate:

$$Nu(y,z) = \frac{h(y,z)D}{\lambda} \tag{5.6}$$

where λ is the thermal conductivity of air. The conversion from pixel coordinate to Cartesian coordinate is obtained via experimentally derived pixel resolution (0.67 mm/pixel) for a particular camera-to-surface distance (500 mm). The rms (root mean square) value of the local *Nu* for each condition (over 150 images) is given by:

$$Nu_{rms}(y,z) = \left[\frac{\sum_{i=1}^{N} \left(Nu_i(y,z) - Nu \right)^2}{N-1} \right]^{1/2} \tag{5.7}$$

where, Nu_i is the instantaneous Nusselt number for the ith thermal image. It is worth noting Nu_{rms} is associated with mainly fluctuating impingement surface temperatures (T'_w) from jet turbulence since both the applied heat flux (q) and the adiabatic wall temperature (T_{aw}) are relatively constant. Often local *Nu* is conveniently represented in cylindrical coordinate, which also allows comparing results with the literature. This is done by averaging *Nu* values around a concentric circle of a given radius *r* (an average of 120 pixel values at 3^{o} intervals). The Equations (5.6) and (5.7) are represented in cylindrical coordinate as follows:

$$Nu(r) = \frac{h(r)D}{\lambda}, \tag{5.8}$$

$$Nu_{rms}(r) = \left[\frac{\sum_{i=1}^{N} \left(Nu_i(r) - Nu \right)^2}{N-1} \right]^{1/2} \tag{5.9}$$

The spatially averaged Nusselt number $\overline{Nu}$ is evaluated as a function of the radial distance from the stagnation point:

$$\overline{Nu}(r) = \frac{1}{A} \int_A Nu(r)\, dA \tag{5.10}$$

The uncertainty in *Nu* is estimated as a function of systematic (ε_s) and random (ε_r) errors [50, 51]:

$$\varepsilon = \pm\sqrt{\varepsilon_s^2 + \varepsilon_r^2}\ , \tag{5.11}$$

where, systematic errors are determined from manufacturer specified accuracy for the IR camera and derived emissivity coefficients, and the total systematic error is equal to ±2%. Table 1 shows random errors for the main variables which have been obtained from repeated observations undertaken for different swirl numbers at *Re* = 35,000. Maximum uncertainty (ε) for *Re* and *Nu* derived by Equation (5.11) is found ±4% and ±5%, respectively.

Before presenting the heat transfer results, the methodology used in the current paper is compared against similar techniques used in the literature [23, 52-54]. This validation is done for a similar test condition ($S = 0$, $H = 6D$, $Re \approx 24{,}000$) and is shown in Figure 5.4. Table 5.2 shows the details of the experimental conditions used in Figure 5.4. The figure illustrates *Nu* distributions and the results show good agreement within 4% with other studies over the range $r/D = 0 - 2$, with the exception of a slight deviation around the stagnation point. This discrepancy is attributed to the associated variations in the nozzle size and boundary conditions at the exit plane (velocity profile and turbulence). Such factors potentially affect the downstream flow development and heat transfer characteristics. The results also show the deviation of local *Nu* around a concentric circle about the mean (an average of 120 pixel values at 3^o intervals).

Table 5.1 Random uncertainty of main variables with their typical values.

Variables	Typical value	Random uncertainty (%)
$\langle u \rangle$, $\langle w \rangle$	5-25 m/s	2-4
T_w	20-23 ^{O}C	3
T_∞	30-50 ^{O}C	2
E	3 V	2
I	40 A	0.5
ε_p	0.95	1

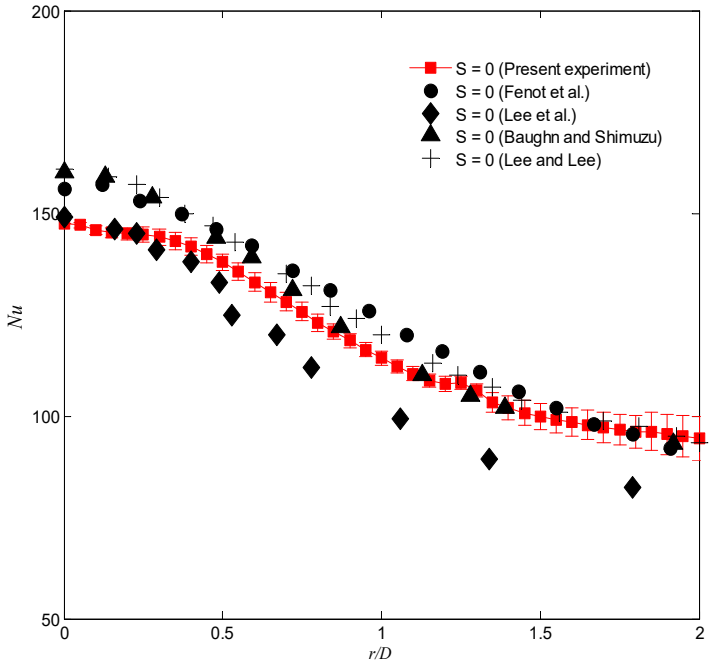

Figure 5.4 *Nu* comparison with other investigations for the similar Reynolds numbers at $H = 6D$ (Re = 23,000 to 25,000; D = 25 to 56 mm). Fenot et al. [52], Lee et al. [53], Baughn and Shimuzu [23], as well as Lee and Lee [54].

Table 5.2 Different experimental conditions used in Figure 5.4 and average Nusselt number ($\overline{Nu}$) over the circular area $r/D = 2.0$ at $H = 6D$. Turbulence intensity values are on the jet axis at the nozzle exit plane.

STUDY	D (mm)	Re $(U_f D/\nu)$	u'/U_b (%)	$\overline{Nu}$
Present study	40	24,600	2	107.78
Fenot et al. [52]	56	23,000	11.0	111.70
Lee et al. [53]	34	23,000	4.0	96.3
Baughn and Shimizu [23]	25	23,750	4.1	110.15
Lee and Lee [54]	25	25,000	-	111

5.3 Results and discussion

5.3.1 Effect of nozzle-to-plate distance

The effects of nozzle-to-plate distance on *Nu* are presented in Figure 5.5[12] for turbulent jets (*Re* = 35,000) covering a wide range of swirl (*S* = 0 – 1.05) over *H* = 1*D* – 6*D*. For the non-swirling jet (*S* = 0), the results show a radially non-uniform *Nu* profile on the impingement surface at all *H*. The highest *Nu* appears outside a small zone of relatively low *Nu* around the stagnation point and focused within 1*D*. Earlier research [55] has attributed relatively low *Nu* occurring in the vicinity of the stagnation point to weaker penetration of (mixing induced) turbulence to the jet centre, and is typical for smaller nozzle-to-plate distances and lower turbulence jets. Higher *Nu* region (outside the inner low *Nu* core), however, is attributed to the rapid change of radial velocity near the impingement surface for the near-field impingement [56]. The size of this relatively high *Nu* area does not appear to spatially grow with impingement distance over *H* = 1*D* – 6*D*. However, its non-uniformity increases as *H* = 6*D* is approached, with a low *Nu* ring on the periphery of this 1*D* zone. The radial extent of the low *Nu* ring (visible at *H* = 1*D* and 2*D*) shifts radially outward as *H* increases, but the trough like zone around the stagnation point remains fairly apparent over *H* = 1*D* – 4*D*. In such non-swirling jets, earlier mapping of the coefficient of pressure (*Cp*) at the impingement plane has also shown it to be fairly independent of *H* upto *H* = 4*D* [38]. The inner low *Nu* ring eventually disappears at *H* = 6*D* and the radial profile of *Nu* takes a monotonic decrease, from a peak at the stagnation point. At *H* = 6*D* (when the impingement plane is positioned beyond the jet potential core length [38]), the peak *Nu* zone appears concentrated at the stagnation point. Such a *Nu* characteristic for far-field impingement is in agreement with similar observations from the literature [10, 24], and is attributed to strong turbulence near the jet centre and immediately downstream of the potential core. The likely effects of increased turbulence on *Nu* near the centreline appear to outweigh the effects of velocity decay due to jet spread, even for an impingement plane in the downstream. The larger downstream distances (e.g. *H* = 6*D*) may also lead to variations in velocity profiles as the jet approaches the surface and contribute to higher stagnation zone heat transfer [26]. These results show that in the case of non-swirling jets, the *Nu* profiles over *H* = 1*D* – 6*D* are both non-uniform and relatively subdued compared to some of the ensuing results, with peak *Nu* occurring over a very narrow area (whose diameter is 1*D*) at *H* = 6*D*.

[12]Two-dimensional line plots of the data in Figures 5, 6, 8 and 9 are available in the Supplementary Material which accompanies this paper (so as to facilitate CFD validation if needed).

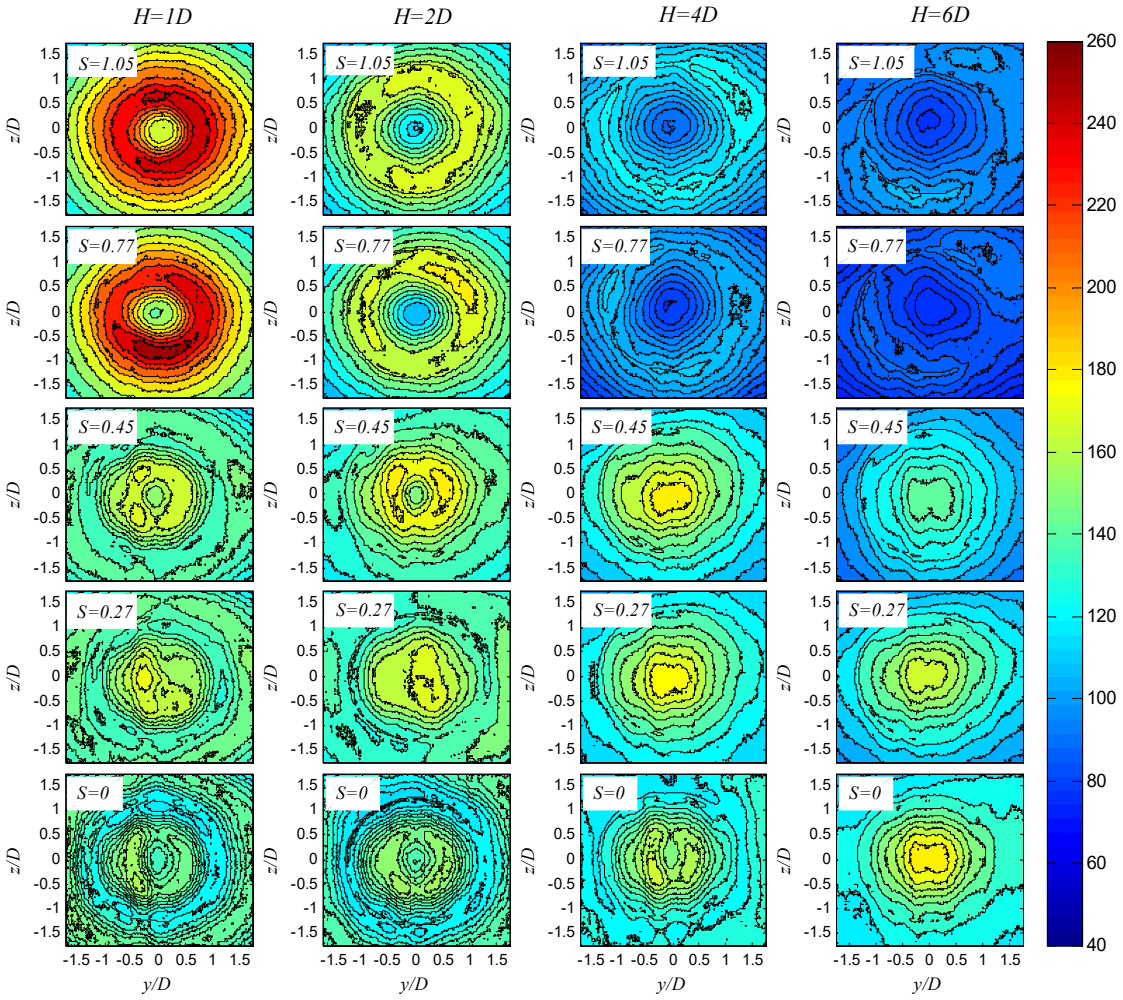

Figure 5.5 Contour maps of *Nu* at $H = 1D - 6D$ for $Re = 35{,}000$. Line plots of these data are provided in the Chapter Appendix (Figure 5.S-1).

For low-to-medium swirl numbers ($S = 0.27 - 0.45$), the first observation is that imparting low swirl appreciably dissipates the ring like (trough) zone of *Nu*. Additionally, the previously observed peak *Nu* zone confined to $1D$ (at $S = 0$, $H = 6D$) now occurs earlier at $H = 4D$ for these low-to-medium swirl numbers. This behaviour of *Nu* may be due to the higher turbulence intensity in swirling jets and increased entrainment [38]. Further increases in plate distance to $H = 6D$ are detrimental to *Nu* at all radial locations. However, increasing impingement plate distance from $H = 4D$ to $H = 6D$ has no qualitative effect on the uniformity of *Nu* and still exhibits a peak zone centred at the stagnation point (within $1D$) followed by a monotonic decrease with radius. Additionally, the *Nu* distributions at $H = 4D$ ($S = 0.27$ and 0.45) appear qualitatively indistinguishable from those in non-swriling jets at *H*

= 6*D*. These results at *S* = 0.27 – 0.45 therefore show that even relatively low levels of swirl can lead to peak *Nu* being realized at smaller plate impingement distances (*H*).

At even higher swirl numbers (*S* = 0.77 and 1.05), drastically different heat transfer characteristics are observed, with significant *Nu* variations compared to both non-swirling and low-to-medium swirl jets as *H* decreases. In near-field impingement ($H \leq 2D$), peak *Nu* appears to occupy a doughnut shaped zone with a relatively low *Nu* core covering a circle of around 1*D* diameter at the centreline (*r/D* = 0). This correlates to the earlier observation of peak *Cp* being displaced from the centerline and occurring at *r/D* = 0.5 – 0.8 at relatively high swirl (*S* = 0.83 and 1.05) [38]. Additionally, the reduced heat transfer over a circle of 1*D* diameter at the centerline may be due to the occurrence of flow separation at this point. Such a behavior on the impingement plane would hinder heat transfer due to the flow reversals occurring at the surface [38]. The overall *Nu* characteristics presented in Figure 5.5 for near-field impingement ($H \leq 2D$) in strongly swirling jets agree with other impingement heat transfer studies featuring aerodynamic swirling jets [37], but disagree with geometric swirl flow studies [31, 32]. The disagreement against geometrically generated swirling jet studies at $H \leq 2D$ may be attributed to the geometry induced flow perturbations and flow blockages around the centerline which alter the flow fields at the nozzle exit plane and downstream locations. The difference in flow developments between geometrically and aerodynamically generated swirling jets in near-field impingement is expected to significantly affect the heat transfer characteristics. However, in far-field impingements ($H \geq 4D$), the variability in *Nu* at the impingement plane (between aerodynamically and geometrically generated swirl) lessens due to diminishing differed jet developments that arise from varied swirl generations. As *H* increases from 1*D* to 6*D*, the radial position of peak *Nu* also appears to gradually shift further radially outward (Figure 5.S-1). The near-field heat transfer at *S* = 0.77 and 1.05 (*H* = 1*D*) exceeds that for any non-swirling or weakly swirling jet over *H* = 1*D* – 6*D*. However, the imposition of high levels of swirl appears detrimental to *Nu* in the case of far-field impingement ($H \geq 4D$), albeit with more uniformity. This reduction in *Nu* may be attributed to the greater jet spread for high swirl at *H* = 4*D* and 6*D*. The *Cp* values at *H* = 4*D* and 6*D* also appear similarly flat at these conditions [38], which again explains the fairly flat *Nu* profiles observed in Figure 5.5 for *S* = 0.77 and 1.05 at *H* = 4*D* and 6*D*. These results highlight that although significant improvements in *Nu* can be achieved at high swirl conditions, this is only realized at low impingement distance. The use of high swirl can lead to detrimental effects on *Nu* if impingement occurs in the far downstream. Both these

behaviours appear dependent on a transitional swirl number ($S \approx 0.45$) and impingement distance ($H \approx 2D$).

Figure 5.6 shows the contour maps of *Nu* fluctuations expressed as Nu_{rms} (Equation 5.7) on the impingement surface for $Re = 35{,}000$ over $H = 1D - 6D$. Similar to Figure 5.5, these data cover non-swirling ($S = 0$), low-to-medium swirl ($S = 0.27 - 0.45$) and higher swirl ranges ($S = 0.77$ and 1.05). Results show that regions of localised high Nu_{rms} correlate very well with regions of high *Nu* (Figure 5.5). Additionally, it is only with the highest swirl conditions ($S = 0.77$ and 1.05) in near-field impingement ($H = 1D$) that the highest localised Nu_{rms} distributions are observed. With Nusselt number strongly dependent on variations of convective heat transfer coefficient (*h*), it is believed that regions of high Nu_{rms} at $S = 0.77$ and 1.05 ($H = 1D$) are caused by increased flow turbulence from swirl at the impingement surface.

Whilst the data presented in Figures 5.5 and 5.6 helps shed light on the variation of localised (pixel resolved) *Nu* with *H* and *S*, the same data are now post-processed to help identify the effects of these parameters on the spatially averaged uniformity of *Nu*. In this regard, Figure 5.7 illustrates *Nu* averaged covering five equally sized circular areas over $r/D = 0 - 2$ using Equation (5.10), which are $r/D = 0$ - 0.89 (A1), 0.89 - 1.27 (A2), 1.27 - 1.55 (A3), 1.55 - 1.79 (A4) and 1.79 – 2 (A5). Five divisions (A1-A5) have been chosen so as to adequately resolve the radial distribution of (area averaged) *Nu*, thereby yielding (within $r/D \leq 2$) areas of approximately 4000 mm^2/each. This allows comparison of spatially averaged *Nu* ($\overline{Nu}$) data to show the relative uniformity of *Nu* for each jet condition. As such, $\overline{Nu}$ in each area is normalised by $\overline{Nu}_{A1}$ which is the Nusselt number in each jet over the first area (A1). In non-swirling and low-to-medium swirl number jets ($S = 0 - 0.45$) at $Re = 35{,}000$, the highest relative heat transfer ($\overline{Nu} / \overline{Nu}_{A1}$) always occurs in areas closer to the stagnation zone

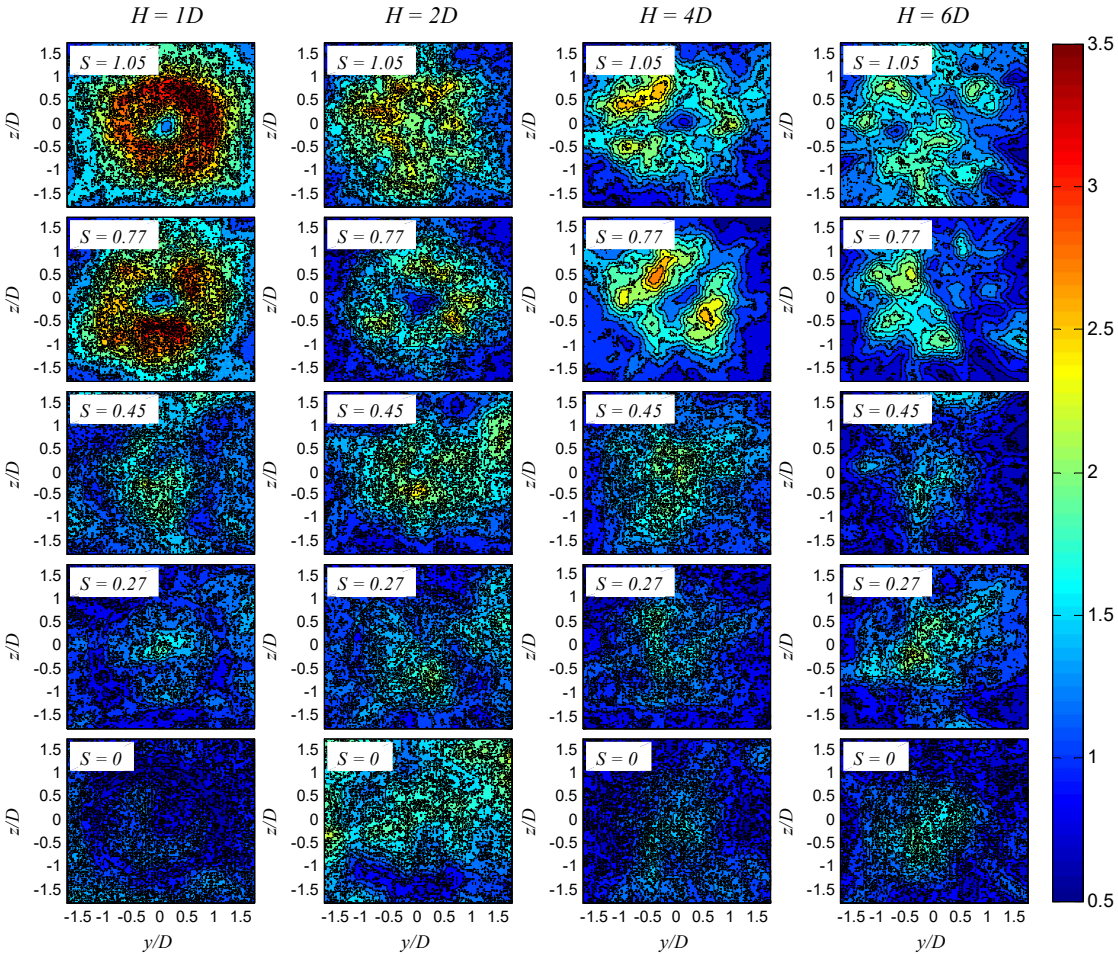

Figure 5.6 Contour maps of Nu_{rms} at H = 1D - 6D for Re = 35,000. Line plots of these data are provided in the Chapter Appendix (Figure 5.S-2).

regardless of the impingement distance (H = 1D – 6D). This relative intensity of heat transfer generally reduces as the radial distance increases for $H \geq 2D$, except for the S = 0 case where an increase of $\overline{Nu} / \overline{Nu}_{A1}$ is observed for H = 2D and 4D from $r/D \approx 1.6$. At H = 1D, the location of relative increase of heat transfer occurs even earlier from $r/D \approx 1.2$. These behaviours can be correlated to the likely secondary vortex ring generation near the impingement surface [20, 31, 56]. For $H \leq 2D$, low swirling jets interestingly exhibit an increase of $\overline{Nu} / \overline{Nu}_{A1}$ after some radial distance away, an opposite tendency to the results for $H \geq 4D$. This relative enhancement effect in lower swirling jets, generally, does not exceed that of a non-swirling jet and becomes weaker when S increases from 0.27 to 0.45. More flow

field testing is required to ascertain causes for the reduction of $\overline{Nu} / \overline{Nu}_{A1}$ in low swirling jets (S = 0.27 and 0.45) at H = 1D. The observations also reinforce the view that "weakly" swirling impinging jets (S = 0.27 and 0.45) exhibit no marked improvement in the overall uniformity of heat transfer over their non-swirling counterparts (S = 0). At higher swirl (S = 0.77 and 1.05), the behaviour is markedly different with the highest relative heat transfer occurring over an intermediate range of r/D which is further out from the inner area (A1). These strongly swirling jets also correlate with a flatter (more uniform) $\overline{Nu}$, particularly at $H \geq 4D$. Similar to the results of Figure 5.5, a transition between two behaviours occurs between S = 0.45 and 0.77, which is largely due to the variation of flow fields at the nozzle exit plane (Figure 5.2). Such transitions appear to occur rather sharply even with an increase of tangential flow by 3% of the total volumetric flow (axial plus tangential) through the nozzle. It is worth noting this transitional swirl number is independent of H, but depends on Re, as discussed in the ensuing results.

Whilst Figure 5.7 helps analyse the effects of impingement plate proximity (H) on the relative uniformity of heat transfer over discretised areas (A1 – A5), the data does not identify how H affects the average (surface integrated) Nu for each jet condition. To achieve that, Table 5.3 shows the area-averaged heat transfer at Re = 35,000 over the range H = 1D – 6D. These data are derived by finding the average Nusselt number ($\overline{Nu}$) over three footprints (r/D = 0 – 0.5, 0 – 1 and 0 – 2). This type of analysis bears practical relevance when an overall (surface integrated) Nu needs to be maximized in different applications. These results clearly show that regardless of the area of impingement (integration over: 1,257 mm^2, 5,027 mm^2 and 20,106 mm^2) and for near-field impingement (H = 1D), the most effective heat transfer is achieved with highly swirling jets (S = 0.77 and 1.05). Alternatively, in the case of far-field impingement (H = 4D and 6D), non-swirling and low-to-medium swirling jets (S = 0 – 0.45) yield the best heat transfer. At H = 2D, both the low-to-medium and highly swirling jets have comparable $\overline{Nu}$ at any surface area.

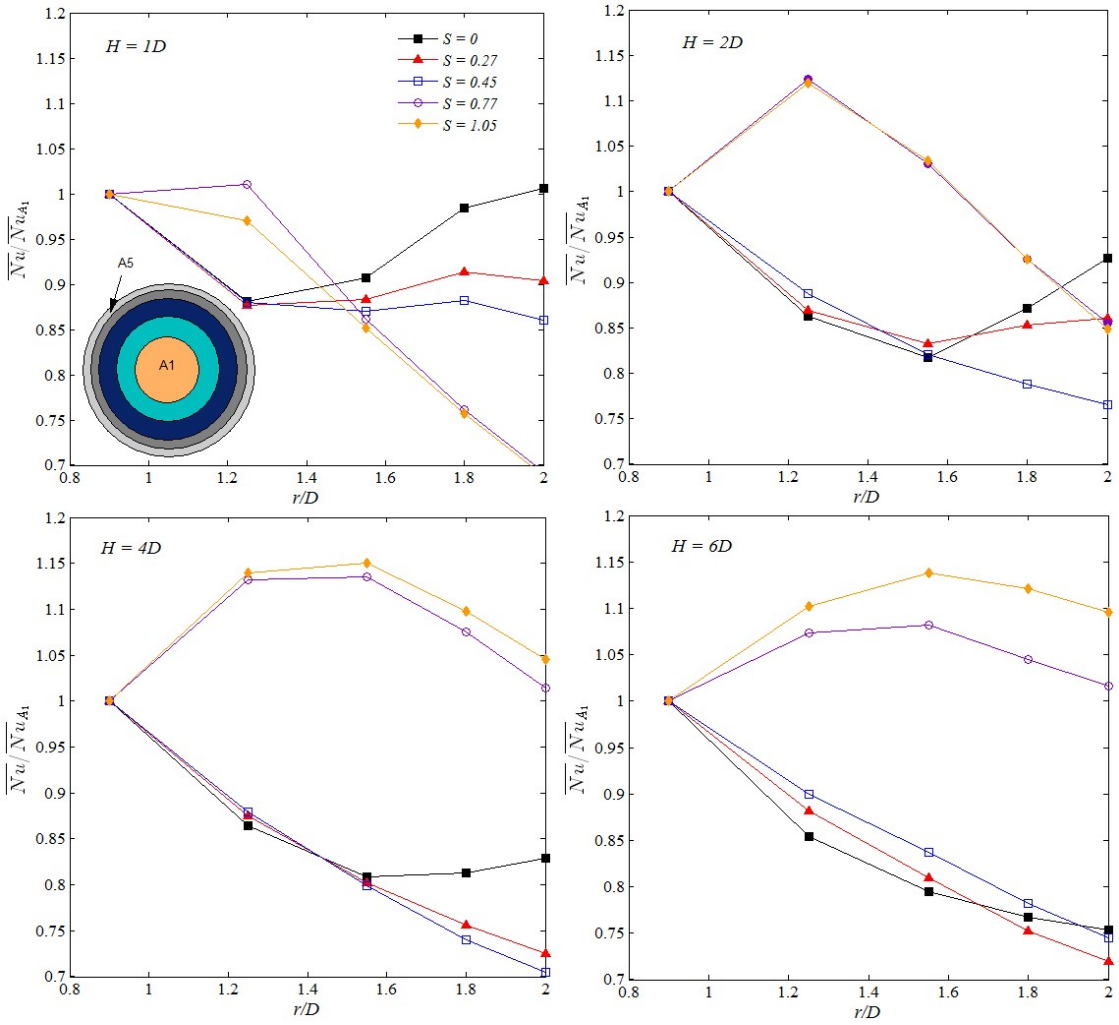

Figure 5.7 The effect of impingement distance (H) and swirl number (S) (at Re = 35,000) on the (normalised spatially averaged) Nusselt number $\overline{Nu}$. Nu is averaged over five equal circular areas (A1: r/D = 0 - 0.89; A2: r/D = 0.89 - 1.27; A3: r/D = 1.27 - 1.55; A4: r/D = 1.55 - 1.79; A5: r/D = 1.79 – 2).

5.3.2 Effect of Reynolds number

Figure 5.8 depicts the heat transfer characteristics for two lower Reynolds numbers (Re = 24,600 and 11,600) and swirl numbers in the range S = 0 – 0.74 at H = 2D. These results show a qualitatively similar behaviour of Nu distributions compared to Re = 35,000 (Figure 5.5). However, these results also indicate that for both non-swirling and swirling jets, the magnitude of Nu significantly reduces across the imaged radial domain as Re decreases. Further analysis of the data in Figures 5.5 and 5.8 also shows that whilst imparting swirl can

lead to increased (localised) *Nu*, this is only sustained upto a threshold swirl number. Beyond these, transitional swirl numbers (which depend on *Re*), lower heat transfer occurs on the impingement surface. These transitional swirl numbers are roughly S ≈ 0.77 (*Re* = 35,000), *S* ≈ 0.58 (*Re* = 24,600) and *S* = 0.32 (*Re* = 11,600). Whilst one possible cause for this variation

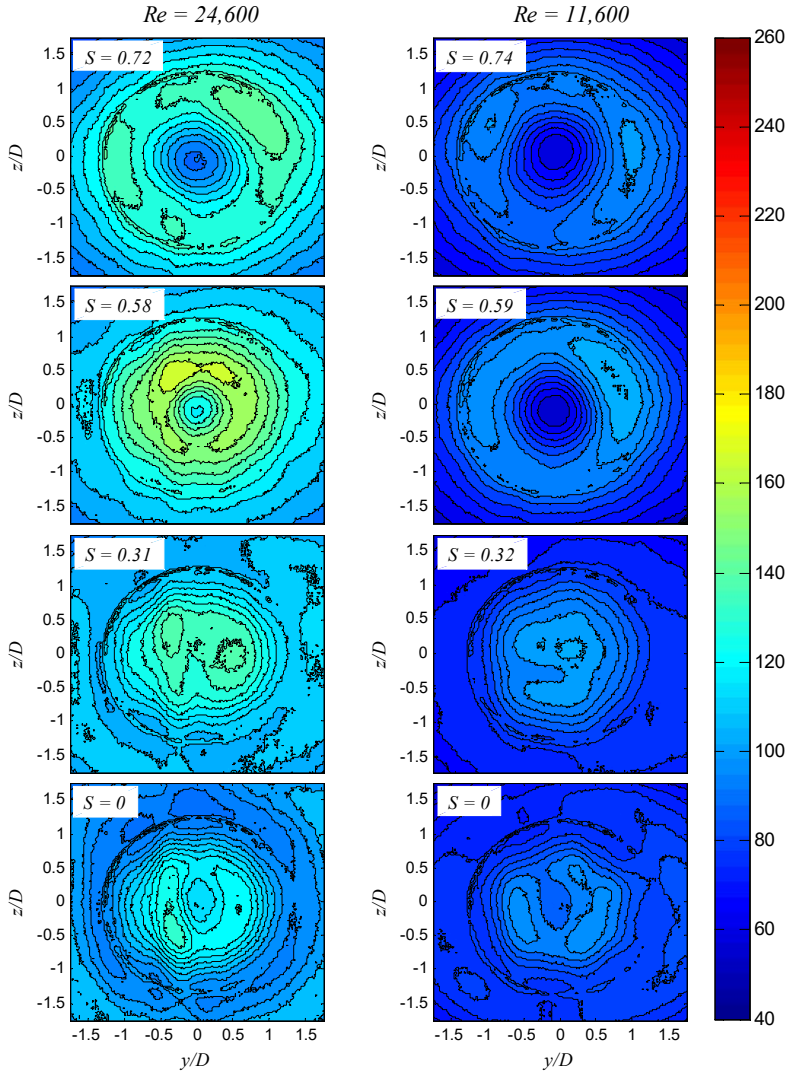

Figure 5.8 Contour maps of *Nu* for two Reynolds number *Re* = 24,600 (left) and *Re* = 11,600 (right) at *H* = 2*D*. Line plots of these data are provided in the Chapter Appendix (Figure 5.S-3).

of transitional swirl number with Reynolds number may be changes to the (upstream) velocity profiles at the nozzle exit plane (already resolved via CTA [38]), additional flow field measurements are required to resolve the characteristics of the entire flow domains (i.e.

the occurrence of flow reversals, stagnation zones etc.). Such measurements would also help explain the trends in impingement pressure and their variation over some ranges of transitional swirl numbers [38]. It is worth noting the *Nu* map for the highest swirl number tested (S = 0.85) at Re = 24,600 is not shown here for brevity since its heat transfer distributions are quantitatively similar to those for S = 0.74.

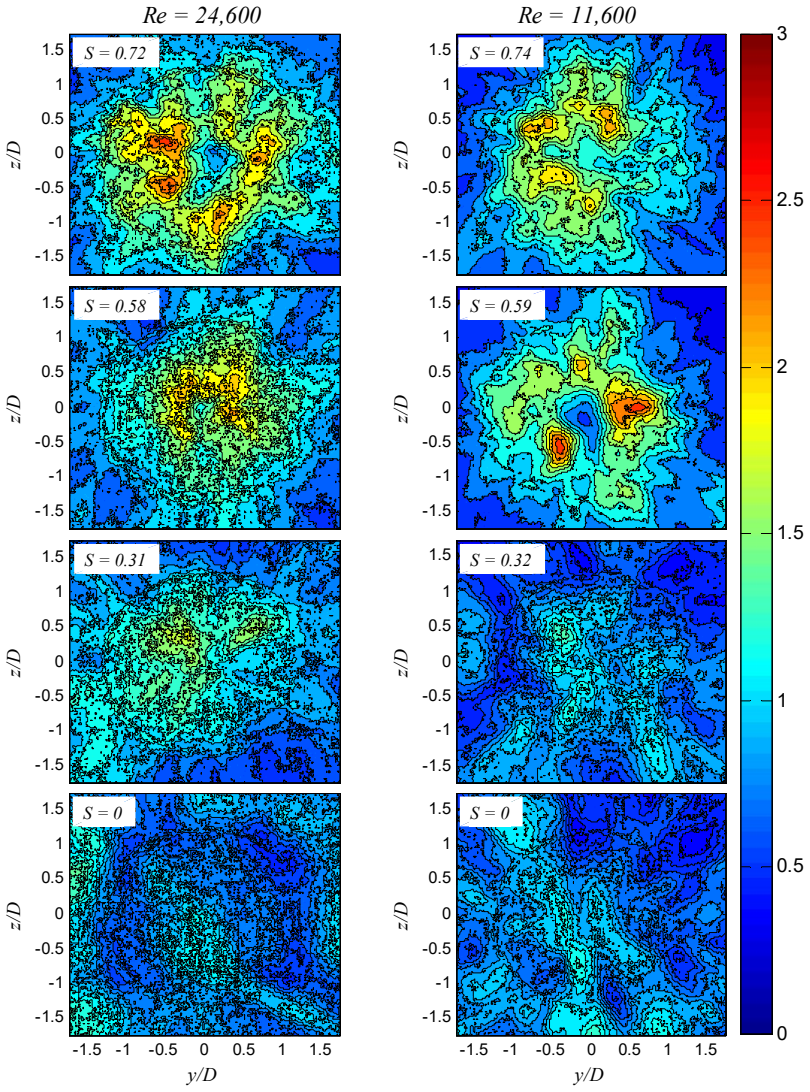

Figure 5.9 Contour maps of Nu_{rms} for two Reynolds number Re = 24,600 (left) and Re = 11,600 (right) at $H = 2D$. Line plots of these data are provided in the Chapter Appendix (Figure 5.S-4).

Figure 5.9 demonstrates the contour maps of Nu_{rms} for the two lower Reynolds numbers (24,600 and 11,600). The results show that rms values are comparable for all Reynolds numbers considered in the study (Re = 11,600 – 35,000). For higher swirl numbers, relatively

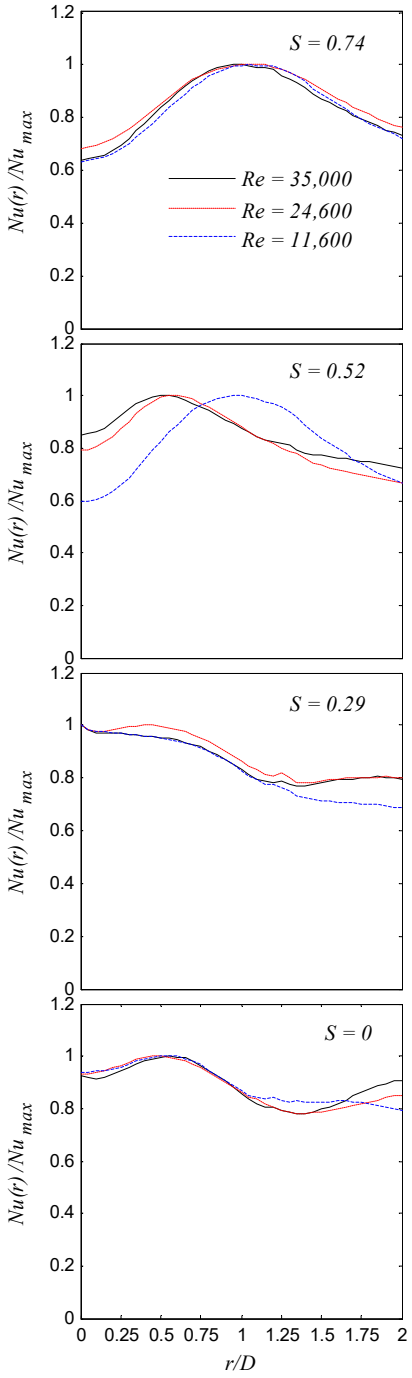

Figure 5.10 The effect of Reynolds number and swirl number at $H = 2D$ on heat transfer distribution: $S = 0$, $S = 0.29 \pm 0.03$, $S = 0.52 \pm 0.07$ and $S = 0.74 \pm 0.02$. The numbers after (±) indicates swirl number variations over the range $Re = 11{,}600 – 35{,}000$.

larger Nu_{rms} are observed around the stagnation points, consistent with the highest *Nu* regions. This result also corroborates the belief that increased flow turbulence at the surface (as witnessed by more fluctuations in convective heat transfer coefficient) correlates well with regions of peak *Nu* (Figure 5.8).

Finally, to analyse the effects of *Re* on the radial uniformity of *Nu* distributions, and the location of peak *Nu*, Figure 5.10 presents the data for swirl numbers in the range $S = 0 – 0.74$ at $H = 2D$ (Re = 11,600 – 35,000). In this regard, the radially resolved *Nu* (Equation 5.8) is normalised by the maximum *Nu* ($Nu_{\max}$) anywhere along the radial profile. For non-swirling ($S = 0$) and higher swirl jets ($S = 0.74$), the heat transfer characteristics do not vary significantly with *Re* over the radial distances considered in this study ($r/D \leq 2.0$). A slight variation in the normalised *Nu*, however, exists for $S = 0$ at $r/D \geq 1$, between the results for Re = 11,600 and Re = 35,000 in this study. This may be attributed to differing characteristics of any large-scale secondary vortex rings (if formed) and their influence on surface heat transfer [20]. However, more flow field testing is required to ascertain this. At relatively lower swirl numbers ($S = 0.29$), slight deviations among the Reynolds number profiles start to occur, particularly at $r/D > 1.25$ for Re = 11,600. The deviation of heat transfer characteristics with Reynolds number is, however, more evident at $S = 0.52$ for the lowest Reynolds number. The overall distributions of $Nu / Nu_{\max}$ for the same swirl numbers (low-to-high) at different Reynolds numbers are found to be similar to the impingement pressure characteristics in our earlier study of swirling jets [38], and were attributed to the varied axial and tangential velocity profiles at different *Re* for a given *S*. The similarity of heat transfer profiles at higher swirl number ($S = 0.74$) is ascribed to the similar upstream flow development and heat transfer characteristics (Figures 5.5 and 5.8). In this regard, earlier testing has also revealed that dimensionless pressure distributions over low-to-high swirl numbers ($S = 0$, 0.29 and 0.74) were found analogous for different *Re* [38]. Upstream flow variation for different *Re* depends on the combined flow through the three tangential ports relative to the total flows via the tangential plus axial ports.

It is worth noting the results in Figure 5.10 display the similarity of local *Nu* distributions for different *Re* at a given *S*, but they do not show the scale of *Re* variations on the magnitude of local *Nu* (Figures 5.5 and 5.8). For non-swirling jets, such scaling with *Re* is commonly represented as $Nu(r) \alpha Re^n$, with *n* having the range 0.5 – 0.85 [54, 57]. The data presented in Figure 5.10 for $S = 0$ also tends to collapse to a single curve when plotted

$Nu(r)/1.2\,Re^{0.47}$ against *r/D*. The relatively smaller value of the index *n* (0.47) in the data presented herein, compared to the literature, may be attributed to upstream variations of the nozzle exit profiles. Interestingly, this scaling of local *Nu* data with *Re* also holds well for different swirl numbers (S = 0.29, 0.52 and 0.74) within deviations of 7%. The only exception to this similarity occurs for S = 0.52 at *Re* = 11,600 where 25% deviation is observed. This high deviation is, again, attributed to the significant variations of the upstream velocity profiles at *Re* = 11,600 compared to higher Reynolds numbers.

5.4 Conclusions

The heat transfer characteristics on an impingement surface have been investigated experimentally in both non-swirling and swirling (incompressible) turbulent jets. Measurements have been performed using a steady-state heated-thin-foil, with surface temperatures acquired using infrared thermography. Results show the effect of swirl on the heat transfer characteristics is a complex relationship, which depends on the Reynolds number and nozzle-to-plate distance. Whilst high swirl can lead to significant improvements in heat transfer, this is not necessarily always the case. It appears that there exists a threshold impingement distance and a transitional swirl number (dependent on *Re*) over which the effect of swirl varies. The results of the investigation can be summarised under three main points:

- **Intensity of heat transfer**: The (spatially resolved) values of *Nu* in non-swirling jets (S = 0) can be significantly improved with the use of high swirl numbers (S = 0.77 and 1.05), particularly at near-field impingement ($H \leq 2D$). Compared to non-swirling jets, even the use of relatively low values of swirl (S = 0.27 and 0.45) can cause the peak values of *Nu* to occur at a lower impingement distance (*H*). Irrespective of the size of impingement area analysed, and for very near-field impingement ($H = 1D$), the use of highly swirling jets (S = 0.77 and 1.05) leads to effectively better heat transfer. For impingement occurring further downstream ($H = 4D$ and $6D$), non-swirling and low-to-medium swirl jet flows (S = 0 – 0.45) appear more effective. The intensity of *Nu* significantly reduces as *Re* decreases for all *Re* considered.
- **Uniformity of heat transfer**: Virtually all the non-swirling and swirling jets studied had non-flat *Nu* profiles at the impingement plane. The imposition of relatively low values of swirl intensity (S = 0.27 – 0.45) does not markedly improve the uniformity of $\overline{Nu}$ compared to their non-swirling counterparts (S = 0). However, higher values of

swirl (S = 0.77 and 1.05) can lead to a flatter (more uniform) profile of $\overline{Nu}/\overline{Nu}_{A1}$, especially in the case of far downstream impingement (H = 4D and 6D). A flatter heat transfer profile can however be accompanied with an overall lower $\overline{Nu}$. The desire for a more uniform heat transfer footprint at the impingement plane needs to be weighed up against the merits of a greater average convective heat transfer rate.

- **Mechanism of heat transfer**: The (spatially resolved) highest heat transfer expressed through *Nu* appears well correlated with Nu_{rms}. This along with the general decline of *Nu* with *Re* indicates that jet generated turbulence is a strong factor to be considered when analyzing the effects of swirl number on the convective heat transfer in impinging jets.

5.5 Chapter references

1. Agrawal, C., Kumar, R., Gupta, A. and Chatterjee, B., *Effect of jet diameter on the maximum surface heat flux during quenching of hot surface*, Nuclear Engineering and Design, 265, p. 727-736, 2013.
2. Agrawal, C., Kumar, R., Gupta, A. and Chatterjee, B., *Rewetting and maximum surface heat flux during quenching of hot surface by round water jet impingement*, International Journal of Heat and Mass Transfer, 55(17), p. 4772-4782, 2012.
3. Agrawal, C., Kumar, R., Gupta, A. and Chatterjee, B., *Determination of rewetting velocity during jet impingement cooling of a hot surface*, Journal of Thermal Science and Engineering Applications, 5(1), p. 011007, 2013.
4. Zhang, J.-Z., Tan, X.-M., Liu, B. and Zhu, X.-D., *Investigation for convective heat transfer on grinding work-piece surface subjected to an impinging jet*, Applied Thermal Engineering, 51(1), p. 653-661, 2013.
5. Nguyen, T., Liu, M. and Zhang, L. C., *Cooling by sub-zero cold air jet in the grinding of a cylindrical component*, The International Journal of Advanced Manufacturing Technology, 73(1-4), p. 341-352, 2014.
6. Singh, S. and Chander, S., *Heat transfer characteristics of dual swirling flame impinging on a flat surface*, International Journal of Thermal Sciences, 89, p. 1-12, 2015.
7. Singh, S. and Chander, S., *Heat transfer characteristics of dual flame with outer swirling and inner non-swirling flame impinging on a flat surface*, International Journal of Heat and Mass Transfer, 77, p. 995-1007, 2014.
8. Luo, D. D., Zhen, H. S., Leung, C. W. and Cheung, C. S., *Premixed flame impingement heat transfer with induced swirl*, International Journal of Heat and Mass Transfer, 53(19), p. 4333-4336, 2010.
9. Fenot, M., Dorignac, E. and Vullierme, J. J., *An experimental study on hot round jets impinging a concave surface*, International Journal of Heat and Fluid Flow, 29(4), p. 945-956, 2008.

10. Greco, C. S., Ianiro, A. and Cardone, G., *Time and phase average heat transfer in single and twin circular synthetic impinging air jets*, International Journal of Heat and Mass Transfer, 73, p. 776-788, 2014.
11. Violato, D., Ianiro, A., Cardone, G. and Scarano, F., *Three-dimensional vortex dynamics and convective heat transfer in circular and chevron impinging jets*, International Journal of Heat and Fluid Flow, 37(0), p. 22-36, 2012.
12. Ozmen, Y. and Baydar, E., *Flow structure and heat transfer characteristics of an unconfined impinging air jet at high jet Reynolds numbers*, Heat and Mass Transfer, 44(11), p. 1315-1322, 2008.
13. Wannassi, M. and Monnoyer, F., *Fluid flow and convective heat transfer of combined swirling and straight impinging jet arrays*, Applied Thermal Engineering, 78, p. 62-73, 2015.
14. Lee, K. H. and Viskanta, R., *Quenching of flat glass by impinging air jets*, Numerical Heat Transfer, Part A: Applications, 33(1), p. 5-22, 1998.
15. King, A. J. C. and Chandratilleke, T. T., *Heat transfer characteristics in impinging jet arrays*, Australian Journal of Mechanical Engineering, 4(1), p. 59-64, 2007.
16. Jambunathan, K., Lai, E., Moss, M. A. and Button, B. L., *A review of heat transfer data for single circular jet impingement*, International Journal of Heat and Fluid Flow, 13(2), p. 106-115, 1992.
17. Viskanta, R., *Heat transfer to impinging isothermal gas and flame jets*, Experimental Thermal and Fluid Science, 6(2), p. 111-134, 1993.
18. Carlomagno, G. M. and Ianiro, A., *Thermo-fluid-dynamics of submerged jets impinging at short nozzle-to-plate distance: A review*, Experimental Thermal and Fluid Science, 58, p. 15-35, 2014.
19. Ahmed, Z. U., Al-Abdeli, Y. M. and Matthews, M. T., *The effect of inflow conditions on the development of non-swirling versus swirling impinging turbulent jets*, Computers & Fluids, 118, p. 255-273, 2015.
20. Greco, C. S., Castrillo, G., Crispo, C. M., Astarita, T., et al., *Investigation of impinging single and twin circular synthetic jets flow field*, Experimental Thermal and Fluid Science, 74, p. 354-367, 2016.
21. Gardon, R. and Akfirat, J. C., *The role of turbulence in determining the heat-transfer characteristics of impinging jets*, International Journal of Heat and Mass Transfer, 8(10), p. 1261-1272, 1965.
22. Hoogendoorn, C. J., *The effect of turbulence on heat transfer at a stagnation point*, International Journal of Heat and Mass Transfer, 20(12), p. 1333-1338, 1977.
23. Baughn, J. W. and Shimizu, S., *Heat transfer measurements from a surface with uniform heat flux and an impinging jet*, Journal of Heat Transfer, 111(4), p. 1096-1098, 1989.
24. Katti, V. and Prabhu, S. V., *Experimental study and theoretical analysis of local heat transfer distribution between smooth flat surface and impinging air jet from a circular straight pipe nozzle*, International Journal of Heat and Mass Transfer, 51(17–18), p. 4480-4495, 2008.
25. O'Donovan, T. S. and Murray, D. B., *Jet impingement heat transfer – Part I: Mean and root-mean-square heat transfer and velocity distributions*, International Journal of Heat and Mass Transfer, 50(17–18), p. 3291-3301, 2007.
26. Rohlfs, W., Ehrenpreis, C., Haustein, H. D. and Kneer, R., *Influence of viscous flow relaxation time on self-similarity in free-surface jet impingement*, International Journal of Heat and Mass Transfer, 78, p. 435-446, 2014.

27. Ward, J. and Mahmood, M., *Heat transfer from a turbulent, swirling, impinging jet*, in Heat transfer 1982: Proceedings of the Seventh International Conference, September 6-10, Munich, West Germany, p. 401-407, 1982.
28. Lee, D. H., Won, S. Y., Kim, Y. T. and Chung, Y. S., *Turbulent heat transfer from a flat surface to a swirling round impinging jet*, International Journal of Heat and Mass Transfer, 45(1), p. 223-227, 2002.
29. Owsenek, B. L., Cziesla, T., Mitra, N. K. and Biswas, G., *Numerical investigation of heat transfer in impinging axial and radial jets with superimposed swirl*, International Journal of Heat and Mass Transfer, 40(1), p. 141-147, 1997.
30. Huang, B., Douglas, W. J. M. and Mujumdar, A. S., *Heat transfer under a laminar swirling impinging jet - A numerical study*, in 6th International Heat Transfer Conference, Toronto: Hemisphere Publishing Corp., p. 311-316, 1978.
31. Ianiro, A. and Cardone, G., *Heat transfer rate and uniformity in multichannel swirling impinging jets*, Applied Thermal Engineering, 49(0), p. 89-98, 2011.
32. Huang, L. and El-Genk, M. S., *Heat transfer and flow visualization experiments of swirling, multi-channel, and conventional impinging jets*, International Journal of Heat and Mass Transfer, 41(3), p. 583-600, 1998.
33. Wen, M. and Jang, K., *An impingement cooling on a flat surface by using circular jet with longitudinal swirling strips*, International Journal of Heat and Mass Transfer, 46(24), p. 4657-4667, 2003.
34. Ichimiya, K. and Tsukamoto, K., *Heat transfer from an inflow-type swirling turbulent impinging jet*, JSME International Journal Series B Fluids and Thermal Engineering, 49(4), p. 995-999, 2006.
35. Nozaki, A., Igarashi, Y. and Hishida, K., *Heat transfer mechanism of a swirling impinging jet in a stagnation region*, Heat Transfer—Asian Research, 32(8), p. 663-673, 2003.
36. Volchkov, E. P., Lukashov, V. V. and Semenov, S. V., *Heat transfer in an impact swirling jet*, Heat Transfer Research, 27(1), p. 14-24, 1996.
37. Abrantes, J. K. and Azevedo, L. F. A., *Fluid flow characteristics of a swirl jet Impinging on a flat plate*, in 13th Int Symp on Applications of Laser Techniques to Fluid Mechanics, 26-29 June, Lisbon, Portugal, http://ltces.dem.ist.utl.pt/lxlaser/lxlaser2006/downloads/papers/28_3.pdf, p. 1-12, 2006.
38. Ahmed, Z. U., Al-Abdeli, Y. M. and Guzzomi, F. G., *Impingement pressure characteristics of swirling and non-swirling turbulent jets*, Experimental Thermal and Fluid Science, 68, p. 722-732, 2015.
39. Thomas, B., Ahmed, Z. U., Al-Abdeli, Y. M. and Matthews, M. T., *The optimisation of a turbulent swirl nozzle using CFD*, in Proceedings of the Australian Combustion Symposium, 6-8 November Perth, Australia, http://www.anz-combustioninstitute.org/local/papers/ACS2013-Conference-Proceedings.pdf, p. 271-274, 2013.
40. Ahmed, Z. U., Al-Abdeli, Y. M. and Guzzomi, F. G., *Corrections of dual-wire CTA data in turbulent swirling and non-swirling jets*, Experimental Thermal and Fluid Science, 70, p. 166-175, 2016.
41. Al-Abdeli, Y. M. and Masri, A. R., *Review of laboratory swirl burners and experiments for model validation*, Experimental Thermal and Fluid Science, 69, p. 178-196, 2015.
42. Sloan, D. G., Smith, P. J. and Smoot, L. D., *Modeling of swirl in turbulent flow systems*, Progress in Energy and Combustion Science, 12(3), p. 163-250, 1986.

43. Carlomagno, G. M. and Cardone, G., *Infrared thermography for convective heat transfer measurements*, Experiments in Fluids, 49(6), p. 1187-1218, 2010.
44. Carlomagno, G. M., *Heat flux sensors and infrared thermography*, Journal of Visualization, 10(1), p. 11-16, 2007.
45. Vollmer, M. and Mollmann, K., Infrared thermal imaging: fundamentals, research and applications, Wiley-VCH Verlag GmbH, Weinheim, Germany, 2010.
46. Ahmed, Z. U., *An experimental and numerical study of surface interactions in turbulent swirling jets*, PhD Thesis, in School of Engineering, Edith Cowan University: Joondalup, Australia, p., 2016.
47. Astarita, T. and Carlomagno, G. M., Infrared Thermography for Thermo-fluid-dynamics, Springer-Verlag, Heidelberg, Berlin, 2013.
48. Cengel, Y. A. and Turner, R. H., Fundamentals of Thermal-Fluid Sciences, McGraw-Hill, Singapore, 2004.
49. Geers, L. F. G., Tummers, M. J., Bueninck, T. J. and Hanjalić, K., *Heat transfer correlation for hexagonal and in-line arrays of impinging jets*, International Journal of Heat and Mass Transfer, 51(21), p. 5389-5399, 2008.
50. Moffat, R. J., *Describing the uncertainties in experimental results*, Experimental Thermal and Fluid Science, 1(1), p. 3-17, 1988.
51. Montgomery, D. C. and Runger, G. C., Applied statistics and probability for engineers, 5th, John Wiley & Sons, Hoboken, NJ, 2011.
52. Fenot, M., Dorignac, E. and Lalizel, G., *Heat transfer and flow structure of a multichannel impinging jet*, International Journal of Thermal Sciences, 90, p. 323-338, 2015.
53. Lee, D. H., S., J. and Jo, M. C., *The effects of nozzle diameter on impinging jet heat transfer and fluid flow*, Journal of Heat Transfer, 126(4), p. 554-557, 2004.
54. Lee, J. and Lee, S., *Stagnation region heat transfer of a turbulent axisymmetric jet impingement*, Experimental Heat Transfer, 12(2), p. 137-156, 1999.
55. Goldstein, R. J. and Behbahani, A. I., *Impingement of a circular jet with and without cross flow*, International Journal of Heat and Mass Transfer, 25(9), p. 1377-1382, 1982.
56. Rohlfs, W., Haustein, H. D., Garbrecht, O. and Kneer, R., *Insights into the local heat transfer of a submerged impinging jet: Influence of local flow acceleration and vortex-wall interaction*, International Journal of Heat and Mass Transfer, 55(25), p. 7728-7736, 2012.
57. Zuckerman, N. and Lior, N., *Jet impingement heat transfer: Physics, Correlations, and Numerical modeling*, in Advances in Heat Transfer, editor: G. A. Greene, J. P. Hartnett, A. B. C. Young, et al., Elsevier. p. 565-631, 2006.

5.7 Chapter Appendix

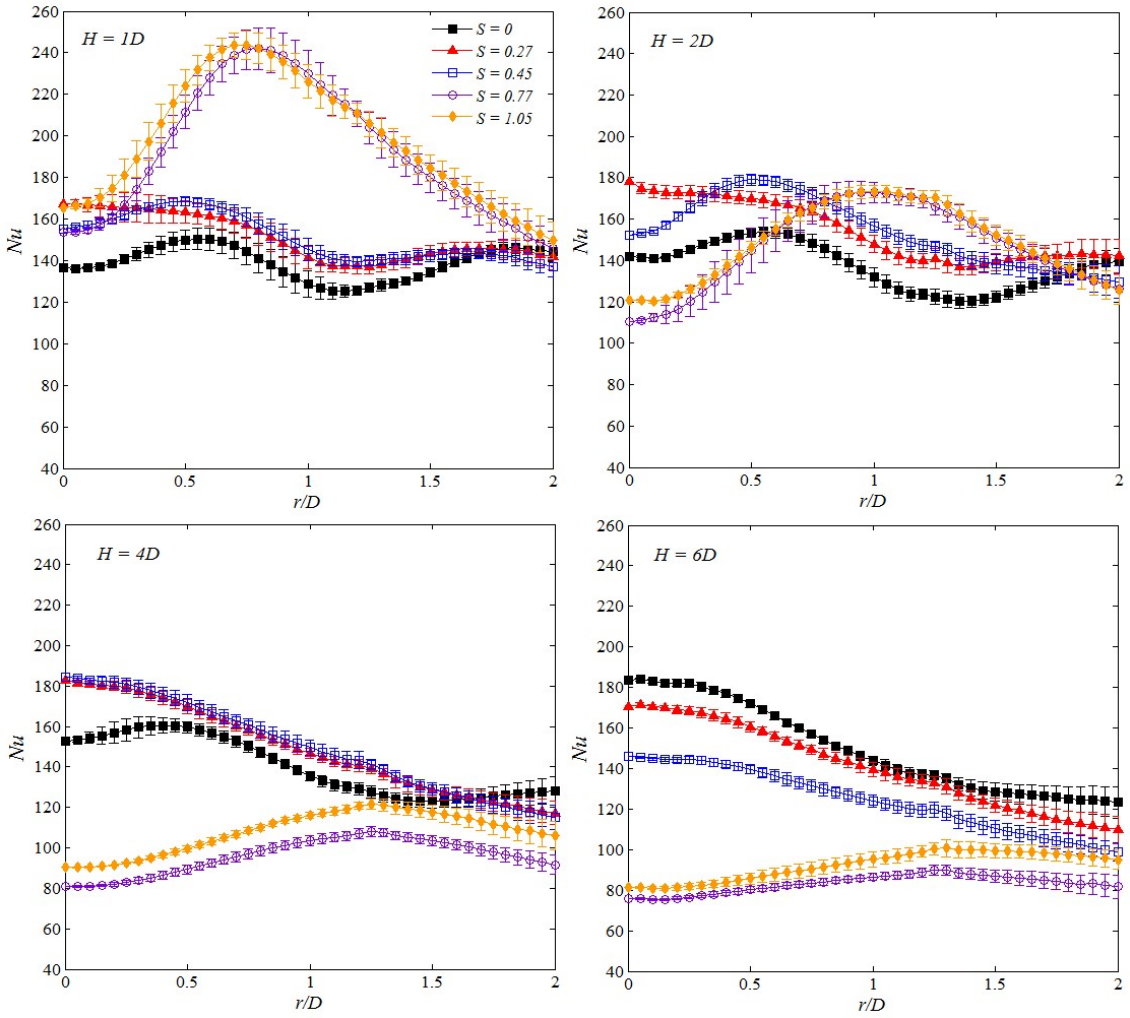

Figure 5.S-1. Radial distributions of *Nu* with *S* and *H* at *Re* = 35,000. Error bars in the plot show the standard deviation of mean data along a concentric circle.

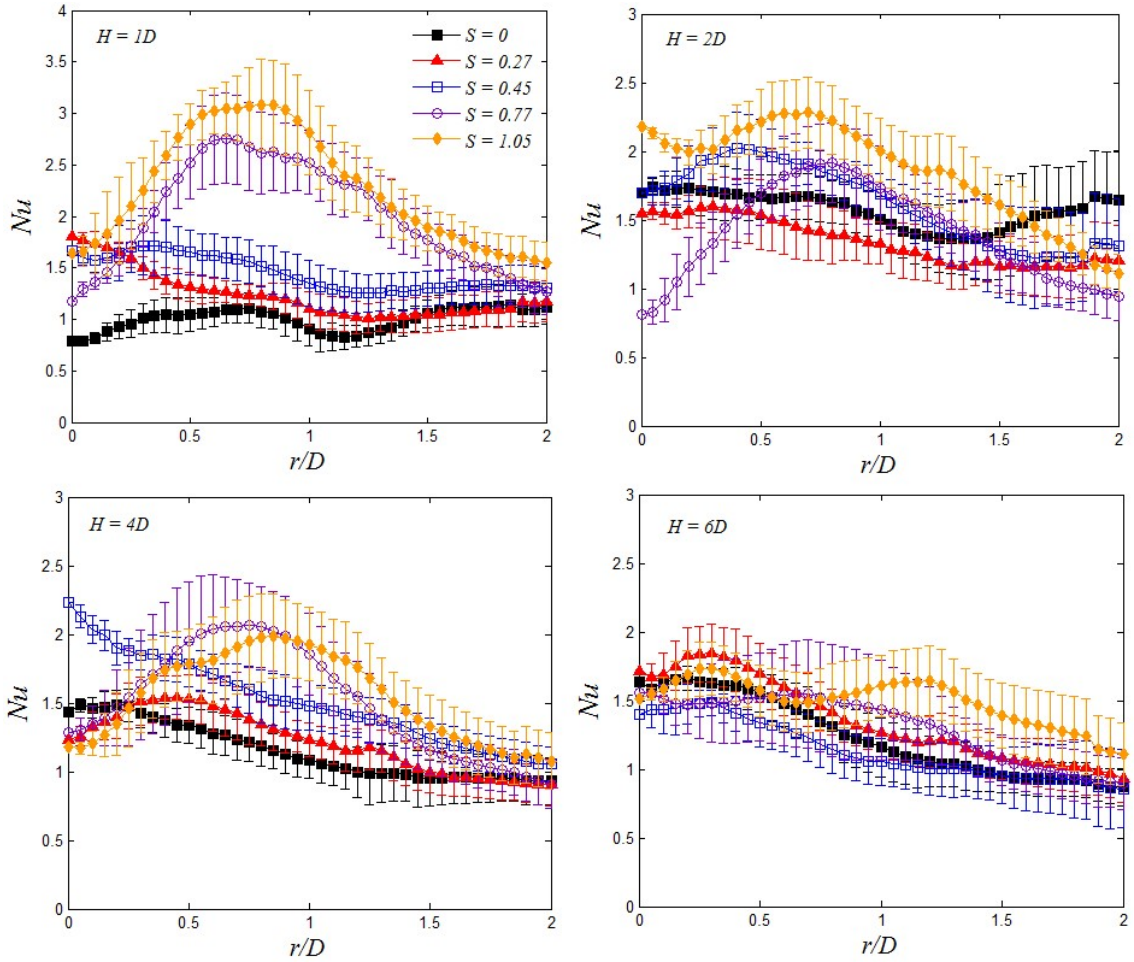

Figure 5.S-2. Radial distributions of Nu_{rms} with S and H at Re = 35,000. Error bars in the plot show the standard deviation of mean data along a concentric circle.

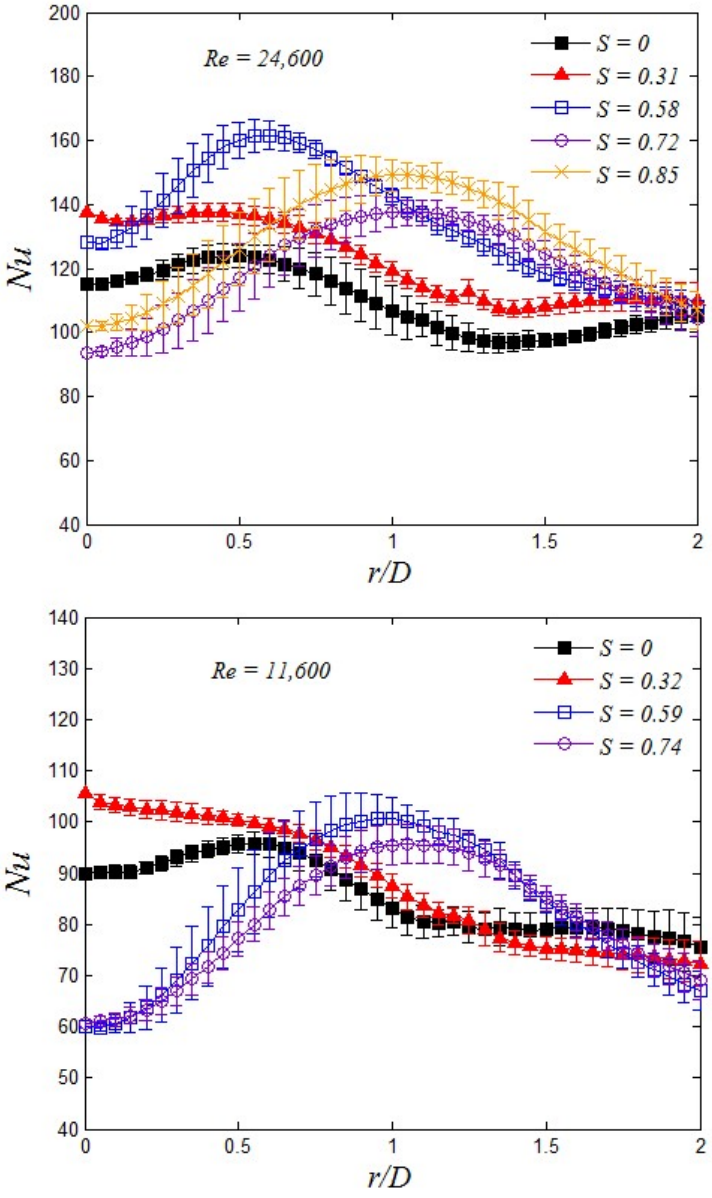

Figure 5.S-3. Radial distributions of *Nu* with *S* at $H = 2D$. Error bars in the plot show the standard deviation of mean data along a concentric circle.

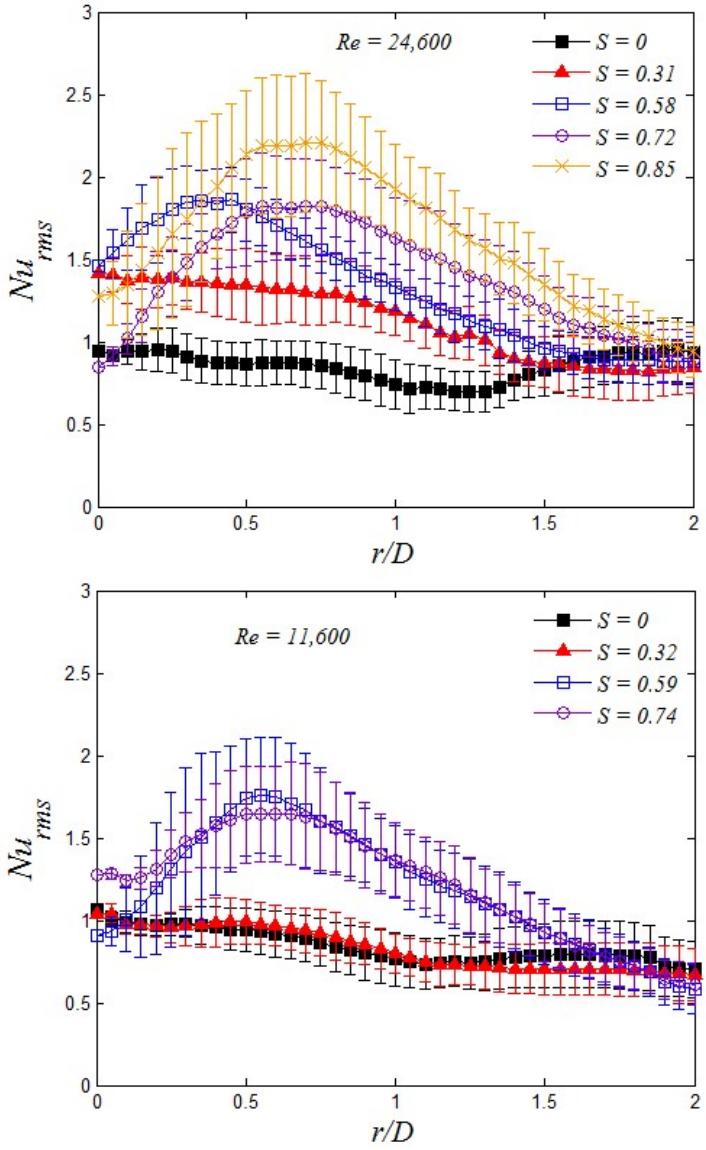

Figure 5.S-4. Radial distributions of Nu_{rms} with S at $H = 2D$. Error bars in the plot show the standard deviation of mean data along a concentric circle.

Chapter 6

6 An Experimental and Numerical Study of Impingement Characteristics in Turbulent Swirling and Non-swirling Jets[13]

This chapter discusses results from numerical data to better understand the effect of swirl on fluid flow characteristics. Factors affecting impingement heat transfer for both non-swirling and swirling jets are also discussed.

6.1 Introduction

Turbulent impinging jets are used in numerous industrial applications due to their higher effectiveness in heat and mass transfer rates. The existence of three independent flow regions, surface interacting flow curvatures and near-wall turbulence makes impinging jet problems challenging, and are attracted to the numerical research for a test case of modelling methodologies. Swirling jets are also investigated in many studies for their strong mixing characteristics. They are often compared to their non-swirling counterparts with an aim of understanding how swirl affects heat transfer on the impingement surface. However, the use of various swirl generating mechanisms (even for the comparable upstream flow conditions) has led to inadequate deductions between swirl and heat transfer improvement (both magnitude and uniformity) on the impingement surface [1-4].

Numerous studies, including recent treatises [2, 5-11], investigate fluid flow behaviour and heat transfer characteristics between a nozzle and an impingement surface for axisymmetric non-swirling impinging jets. The literature reveals the potential core length and the impingement region varies with nozzle-to-plate distance (H) when a turbulent jet impinges at distance less than six nozzle diameters (D) i.e. $H < 6D$. Flow entrainment outside the conical potential core and vortical structures (due to shear layer instability) then affect the impingement and wall jet regions. For $H < 6D$, the heat transfer distribution on the surface

[13] This chapter has been submitted for publication as a full research paper in:
Ahmed Z. U., Al-Abdeli, Y. M., Guzzomi, F. G., International Journal of Thermal Sciences (In review).
Whilst efforts were made to retain original content of the article, minor changes such as number formats, font size style were implemented in order to maintain consistency in the formatting style of the thesis.

does not show a monotonic decrease, with two Nusselt number maxima at a radial distance of $r/D < 2.5$. The outer peak is located in the radial range $r/D = 1.7$ - 2.5 [5, 8, 10], whereas the inner peak is found to occur either on the jet axis ($r/D = 0$) [6, 7] or at $r/D \approx 0.5$ with a local minimum on the jet axis [2, 12]. The exact reasons for these heat transfer peaks are still not adequately understood and several plausible physical explanations have been proposed in the literature [9, 12-14]. Velocity profiles at the nozzle exit are also found to have a strong influence on the impingement heat transfer characteristics [9]. Contradictions in the results for non-swirling jets may primarily be caused by the varied nozzle exit conditions in these studies.

Existing research on swirling impinging jets predominantly used geometrically generated swirl (using helical inserts or guide vanes within the nozzle), and reported both a reduction [3, 15-17] or an enhancement [18-20] of average (area integrated) heat transfer compared to non-swirling counterparts. Heat transfer reduction is largely ascribed to the geometry induced dead-zone, typically around the jet centre. In contrast, intense flow mixing and formation of vortices on the impingement surface are found to contribute to the heat transfer enhancements. For the radial uniformity of impingement heat transfer, the literature disagrees of the relationship between radial uniformity (flatness) of heat transfer and swirl [2, 3, 21]. Although geometry induced intricacies, such as flow blockages and perturbations can be avoided by aerodynamically generated swirl jets, but the limited number of these studies lead to poor understanding of the fundamental relationship between swirl and heat transfer. Moreover, contradictory results in relation to heat transfer improvement and radial uniformity for increasing swirl intensity also exists [20-22]. Substantially different Reynolds numbers, investigation of limited swirl intensities and lack of precise upstream conditions among these studies may contribute to such discrepancies in the results. Similar to the non-swirling jets, disagreement of the radial location of heat transfer peaks with swirl intensity also varies, regardless of the swirl generation. However, explanations for such occurrences of heat transfer peaks at different swirl intensities are not adequately addressed in the literature. This reinforces the need to investigate a swirling impinging jet for a wider range of swirl intensities with well-defined boundary conditions to improve the understanding between flow field characteristics and heat transfer.

Although extensive numerical research on non-swirling, turbulent impinging jets is available in the literature [11, 23-27], the computations for swirling impinging jets are still scarce. Even for the non-swirling impinging jets, the simulations are found to be challenging

to resolve complex flow behaviours near the impingement surface, such as steep pressure gradients and anisotropic flow nature due to the jet-wall interaction [26]. Moreover, choosing a turbulence model is also an issue since no turbulence model was found to predict accurately all the flow features of an impinging jet [28-30]. The inclusion of swirl into the jet exacerbates the modelling complexity of turbulent flow fields and heat transfer characteristics. The absence of highly resolved flow field data (for benchmarking) as well as clearly defined nozzle exit boundary conditions is another drawback of swirling impinging jets computations. Despite these difficulty, the limited works conducted recently on turbulent swirling impinging jets (geometrically generated swirl), are the studies by Ortega-Casanova [31], Amini et al. [32], and Wannassi and Monnoyer [33]. Likewise, similar to experimental investigations, numerical studies show disparity in outcomes in relation to heat transfer improvement.

Previous research shows contradicting heat transfer results regardless of the swirl generating mechanisms and/or investigation methods, i.e. experimental or numerical. A fundamental understanding for the relationship between swirl intensity and flow fields, and the underlying mechanism of heat transfer peaks appears inadequately reported. As such, this research experimentally and numerically investigates swirling jets (aerodynamically generated), which impinge on a surface located at $H = 2D$ and $H = 6D$ for a Reynolds number of 35,000. This paper uses well-defined nozzle exit conditions derived via Constant Temperature Anemometry (CTA) and provides the inlet boundary conditions for CFD simulations. Section 2 briefly details both the experimental and numerical methodologies. Section 3 discusses the results followed by the conclusions in Section 4.

6.2 Methodology

6.2.1 Experimental techniques

The air jets are obtained from a swirl nozzle [34, 35] which can deliver non-swirling and (aerodynamic) swirling jets. The nozzle has two axial and three tangential ports to provide the total axial and tangential flows with the capacity to vary swirl numbers for a constant Reynolds number and vice versa. The nozzle exits with a straight section of diameter $D = 40$ mm and a sharp-edged termination with a wall thickness of 0.2 mm. An X-wire probe (DANTEC, model: 55P61) was used to characterise the nozzle exit conditions via measurements of axial and azimuthal velocity components 1 mm above the nozzle exit plane. The detail of the hotwire measurement methodologies for low-to-high swirl intensity is

demonstrated in our another paper [36]. For non-swirling and swirling flows, the estimated accuracy of CTA measurements was 2% and 4% of centreline velocity, respectively.

Convective heat transfer measurements between the jets and the impingement surface are performed using infrared thermography via an infrared camera (FLIR systems, model: A325). The jet flows vertically upward and impinges on a heated horizontal surface and the infrared camera is positioned above the surface to measure temperature, as shown in Figure 6.1. A

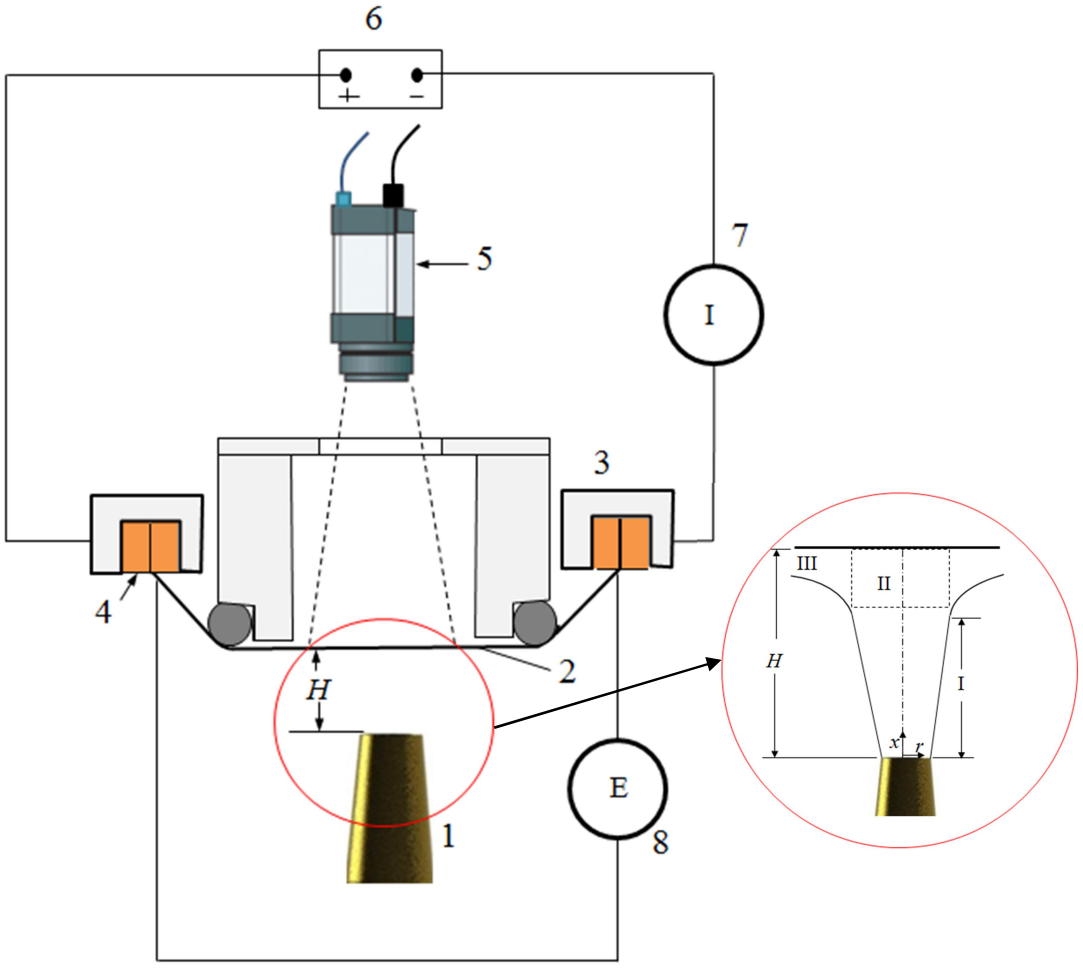

Figure 6.1 Experimental setup for heat transfer measurements. Key: 1. Swirl nozzle, 2. Stainless steel foil (impingement surface), 3. Aluminum assembly to hold copper busbars, 4. Copper busbars, 5. Infrared camera, 6. DC power supply, 7. Clamp meter to measure current at the steel foil, 8. Digital multimeter to measure voltage across the steel foil. I. Free jet region, II. Impingement region and III. Wall jet region. The figure drawn is not to scale.

stainless steel foil (painted matt black on one side) is used for the impingement surface and heated by a DC power source (Powertech, model: MP3094). The foil is considered isothermal across its thickness since the Biot Number is less than 0.1 [37]. The emissivity coefficients for both unpainted and painted impingement surface are measured by IR thermography and equal to 0.97 and 0.06, respectively [38]. Further detail of heat transfer measurement methods is discussed in [39] and is not repeated here.

The time-averaged local convective heat transfer coefficient (h) between the surface and the jet flow is determined from an energy balance defined by the relationship:

$$h = \frac{q - q_l}{T_W - T_{ref}}, \tag{6.1}$$

where q is the known applied heating flux (1120 W/m^2) obtained from the relation EI/A with E, I, and A (0.06 m^2) being the applied voltage, current and foil area, respectively. The total thermal loss q_l consists of losses due to tangential conduction (q_c) along the foil and radiation (q_r) from the surface, which are typically about 1% [40] and 4% of the applied heat flux [39]. T_W is the wall (surface) temperature measured by the infrared camera when the foil is heated and T_{ref} is the reference temperature, typically equal to the adiabatic wall temperature T_{aw} for incompressible impinging jets [41].

The local convective heat transfer is represented by a non-dimensional parameter, Nusselt number Nu which is defined by:

$$Nu(r) = \frac{h(r)D}{k} \tag{6.2}$$

In this regard, local convective heat transfer coefficient h (or Nusselt number) at a given r is derived by averaging values at an interval of 3^o along the concentric circle. Two other non-dimensional parameters, namely, Reynolds number ($Re = 4Q/\pi D\nu$) and swirl number ($S = W_b/U_b$) are used to characterise the flow and the level of swirl intensity, respectively. The total volume flow rate through the nozzle is Q. The bulk axial and tangential velocities (U_b and W_b) are determined by averaging CTA resolved velocity data across the nozzle exit plane. A correlation between the flowrates and swirl number is presented elsewhere [36].

Knowing the nozzle exit condition is important not only to characterise the upstream jets, but also a prerequisite for CFD model simulations for complex flows, such as swirl flow.

Although detailed nozzle exit conditions for the swirl nozzle at different *Re* and *S* are available in [34], Figure 6.2 presents (in different form) the CTA derived mean velocity and turbulence components investigated in this study for completeness. Data shown is the normalised axial ($< u > /U_b$), tangential ($< w > /U_b$) velocity and turbulence (u'/U_b and w'/U_b) profiles at 1 mm above the nozzle exit plane over the range $S = 0 – 1.05$.

Thermal axisymmetry on the impingement surface is tested by measuring surface temperature maps at $H = 2D$. Figure 6.3a depicts an impingement surface temperature contour plot for the highest swirl considered ($S = 1.05$). The temperature data variation displayed in Figure 6.3b for a given concentric circle (up to $r/D = 1.5$) is found to be less than ±2% of the circumferentially mean temperature value.

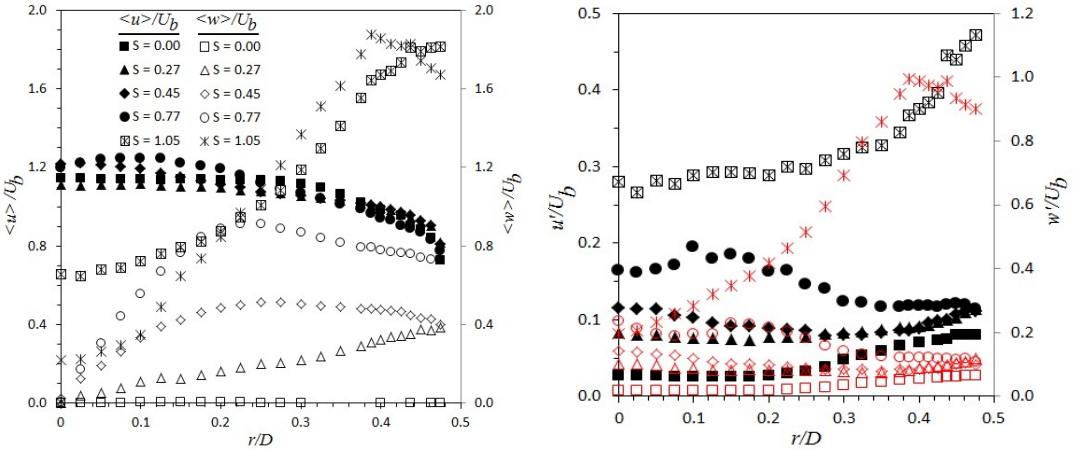

Figure 6.2 Nozzle exit conditions (mean velocity and turbulence profiles) measured by CTA at $x/D = 0.025$ for $Re = 35{,}000$ over the swirl number range $S = 0 – 1.05$.

6.2.2 Numerical methods

The governing equations used for the incompressible steady state turbulent non-swirling and swirling impinging jets are the Reynolds-averaged Navier-Stokes (RANS) equations for mass, momentum and energy conservations. Due to the fairly axisymmetric nature of the experimental data both at the nozzle exit plane and impingement surface, an axisymmetric simulation for the mean flow and turbulent quantities is used in this study. The RANS equations governing the flow field and heat transfer can be expressed by the generalised form [42, 43]:

$$\frac{\partial(\rho u\phi)}{\partial x}+\frac{\partial(r\rho v\phi)}{r\partial r}=\frac{\partial}{\partial x}\left(\Gamma_\phi\frac{\partial\phi}{\partial x}\right)+\frac{\partial}{r\partial r}\left(r\Gamma_\phi\frac{\partial\phi}{\partial r}\right)+S_\phi \tag{6.3}$$

where ϕ, Γ_ϕ and S_ϕ represent the generalised variables, effective transport coefficients and source terms, respectively. Their detailed expressions for each of the governing equations are presented in Table 6.1. A finite-volume based commercial software package ANSYS FLUENT (version 14.5) is used to solve the mean and turbulent flow quantities. The pressure-based coupled algorithm is used to simultaneously solve the governing equations. Pressure is discretised using PRESTO and the second-order upwind scheme is applied for momentum, energy and turbulence closures. The turbulence closure term $\overline{u_i'u_j'}$ in Equation (6.3) is computed via transport equations for individual stress components (Reynolds stress

Table 6.1 Different variables effective transport coefficients and source terms used in the governing equations.

EQUATIONS	ϕ	Γ_ϕ	S_ϕ
Mass	1	0	0
x Momentum	u	μ_{eff}	$-\frac{\partial p}{\partial x}-\frac{\partial}{\partial x}\left(\rho\overline{u'u'}\right)-\frac{\partial}{r\partial r}\left(\rho r\overline{u'v'}\right)$
r Momentum	v	μ_{eff}	$-\frac{\partial p}{\partial r}-\Gamma_\phi\frac{v}{r^2}+\frac{\rho w^2}{r}-\frac{\partial\left(\rho\overline{u'v'}\right)}{\partial x}-\frac{\partial}{r\partial r}\left(\rho r\overline{v'v'}\right)+\frac{\rho\overline{w'w'}}{r}$
θ Momentum	w	μ_{eff}	$-\frac{\rho vw}{r}-\frac{w}{r^2}\frac{\partial}{\partial r}\left(r\Gamma_\phi w\right)-\frac{\partial}{\partial x}\left(\rho\overline{u'w'}\right)-\frac{1}{r^2}\frac{\partial}{\partial r}\left(\rho r^2\overline{v'w'}\right)$
Energy	e	$\frac{\lambda_{eff}}{C}$	$-\frac{\partial}{\partial x}\left(\overline{u'T'}\right)-\frac{\partial}{r\partial r}\left(r\overline{w'T'}\right)$
Turbulent kinetic energy (TKE)	k	$\frac{\mu_{eff}}{\sigma_k}$	$G_k-\rho\varepsilon$
Dissipation rate of TKE	ε	$\frac{\mu_{eff}}{\sigma_\varepsilon}$	$\frac{\varepsilon}{k}\left(C_{\varepsilon1}G_k-C_{\varepsilon2}\rho\varepsilon\right)$
Specific dissipation energy	ω	$\frac{\mu_{eff}}{\sigma_\omega}$	G_ω

PARAMETER KEYS:

μ : Kinematic viscosity, μ_t : Turbulent (eddy) viscosity, G_k : Production rate of turbulent kinetic energy, p: Static pressure; λ_{eff} : Effective thermal conductivity, C : Specific heat at constant pressure, σ_k , σ_ε , σ_ω, $C_{\varepsilon1}$ and $C_{\varepsilon2}$ are model constants.

$\mu_{eff}=\mu+\mu_t$

$G_k=-\rho\left(\frac{\partial u}{\partial r}+\frac{\partial v}{\partial x}\right)\overline{u'v'}-\rho r\frac{\partial}{\partial r}\left(\frac{w}{r}\right)\overline{v'w'}-\rho\frac{\partial w}{\partial x}\overline{u'w'}-\rho\frac{\partial u}{\partial x}\overline{u'^2}-\rho\frac{\partial v}{\partial r}\overline{v'^2}-\rho\frac{v}{r}\overline{w'^2}$;

$G_\omega=\alpha\frac{\omega}{k}G_k$

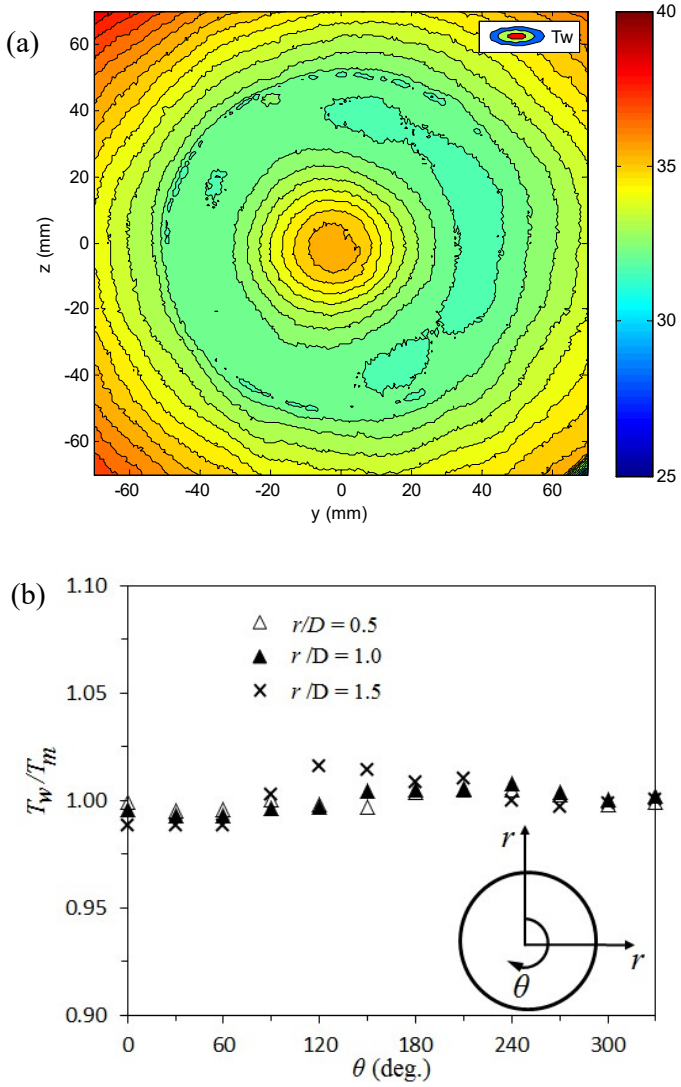

Figure 6.3 (a) Filled isotherm plot for surface (wall) temperature (°C) distribution on the impingement surface for the highest flow (Re = 35,000) at S = 1.05 and H = 2D. (b) Circumferential distribution of wall temperature data at three radial locations (r/D = 0.5, 1.0 and 1.5).

model) or via mean velocity gradients by the Boussinesq hypothesis using turbulent (eddy) viscosity μ_t (k-ε and k-ω variants). The Boussinesq approximation for calculating Reynolds stress components is expressed in indicial notations as:

$$\overline{u_i' u_j'} = 2/3 k\delta_{ij} - \mu_t \left(\frac{\partial u_i}{\partial x_j} + \frac{\partial u_j}{\partial x_i} \right), \tag{6.4}$$

$$\overline{u_i'T'} = -\Gamma_T \frac{\partial T}{\partial x_j}, \tag{6.5}$$

where, μ_t is a function of k and ε or ω, which are determined via two other transport equations (shown in Table 6.1).

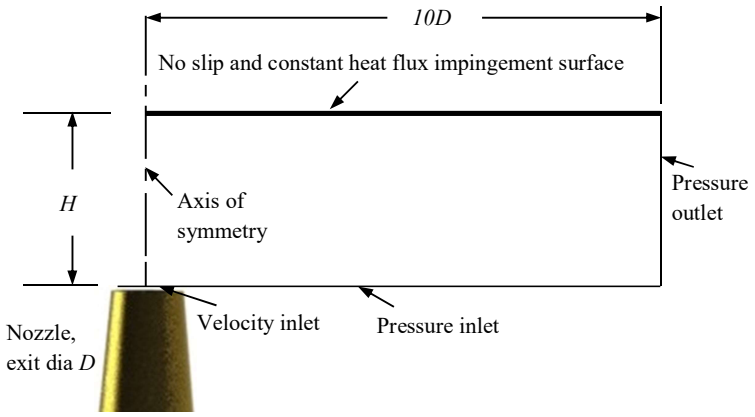

Figure 6.4 The computational domain and boundary conditions applied.

Figure 6.4 shows the computational domain with the corresponding boundary conditions applied. Grid independence and spatial domain tests indicate a mesh density of 23,600 cells and a radial extent of 10D are adequate to resolve the flow field and heat transfer characteristics. For the velocity inlet, mean velocity and turbulence profiles are imposed from the experimental data (Figure 6.2). Turbulence at the inlet plane is implemented via turbulent kinetic energy (k) and energy dissipation rate (ε) or specific energy dissipation rate (ω) and defined by [31, 44]:

$$k = \frac{3}{2}\sqrt{u'^2 + w'^2} \tag{6.6}$$

$$\varepsilon = \frac{C_\mu^{3/4} k^{3/2}}{l} \tag{6.7}$$

$$\omega = \frac{k^{1/2}}{C_\mu^{1/4} l} \tag{6.8}$$

where C_μ is model constant (0.085 for k-ω model and 0.09 for k-ε model) and the turbulent length scale l = 0.07D. Atmospheric pressure is used for both the pressure inlet and pressure

outlet boundaries. Finally, an axial symmetry condition at the geometric axis and, a no-slip with constant wall heat flux wall condition is imposed at the (impingement) surface. In this regard, experimentally measured constant heat flux equal to 1120 W/m^2 is applied at the wall boundary. The computation is assumed to converge upon a solution when the residuals of the flow parameters are less than 10^{-6}. Checks of different near-wall models, discussed in another study [11], suggest an Enhanced Wall Treatment (EWT) [45, 46] performs best near the wall compared to other near-wall boundary layer treatments. As such, Enhanced Wall Treatment (EWT) is used in the study to sufficiently resolve the boundary layer and best predict the surface flux characteristics of the impinging jet.

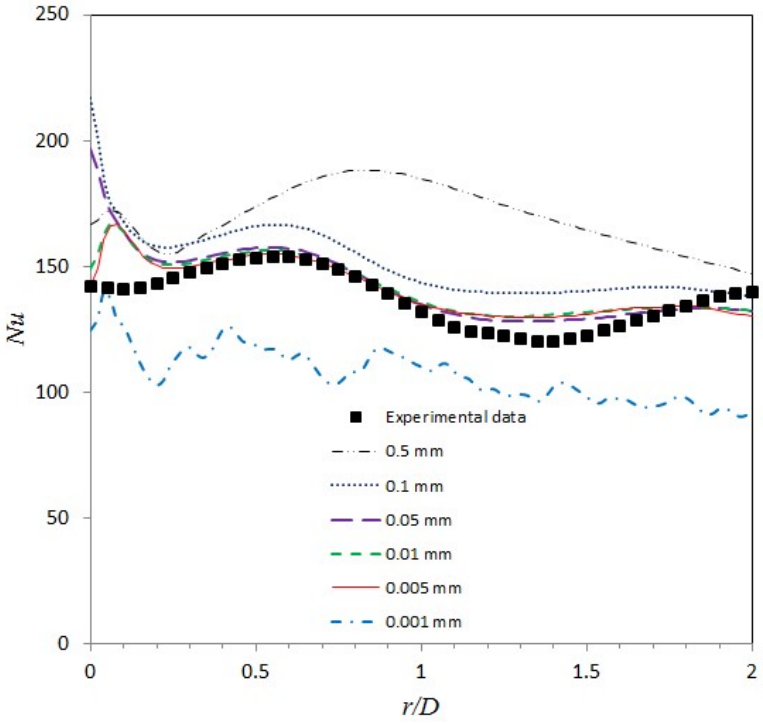

Figure 6.5 Checks of first layer height against experimental data for Re = 35,000 and S = 0 at H = 2D.

Once the numerical model setup and boundary conditions have been established, the next step is to assess the optimum turbulence model. In this regard, three turbulence models (RNG k-ε, SST k-ω and RSM with a linear pressure-strain model) found to outperform other models for an impinging jet [11], were then tested against experimentally derived impingement surface data (static pressure [34] and heat transfer coefficient discussed in Section 6.2.1).

Comparisons of numerically obtained radial distribution of pressure coefficient *Cp* (defined as the gauge static pressure divided by the dynamic pressure) and *h* against experimental data shows SST *k-ω* model performs best when considered both non-swirling and swirling flows. Therefore, SST *k-ω* model is used in all subsequent simulations and results. A typical comparison among three models for non-swirling flow is shown in the Appendix (Figure 6.A-1).

Another important parameter to help resolve the wall characteristics is the first mesh layer height that describes the wall y^+ values. Figure 6.5 shows a check for different first mesh layer heights over the range 0.001 - 0.5 mm and the result is compared against the experimental data set for $S = 0$. It appears the first cell height plays an important role in predicting surface heat transfer characteristics and a cell height of more than 0.1 mm or less than 0.001 mm poorly predicts the overall *Nu* distribution. This analysis shows that a height of 0.005 mm gives the best experimental data prediction at both the stagnation point and the wall jet region, and is used in all subsequent simulations. Such parameter settings for the numerical modelling ensure y^+ value less than unity.

6.3 Results and discussion

Figure 6.6 shows contour maps of convective heat transfer coefficient (*h*) over the range $S = 0 – 1.05$ both in near-field ($H = 2D$) and far-field ($H = 6D$) impingement. For non-swirling jets ($S = 0$) at $H = 2D$, a higher convective heat transfer coefficient (*h*) band appears outside the jet centre ($0.25 < r/D < 0.75$), with a lower *h* zone occurring immediately at the jet centre ($r/D = 0$). Outside the periphery of this higher *h* zone, another (outer) low *h* zone sits covering $0.75 < r/D < 1.5$, before heat transfer peaks up again at even further radial distances. The occurrence of these relatively two maxima in convective heat transfer coefficient (inner and outer) have been attributed to the rapid change of radial velocity in the streamline deflection region and to destruction of the thermal boundary layer by the large-scale eddies which strikes the surface [6, 9, 10, 47]. The minima in *h* around the jet centre may also be attributed to the weak penetration of shear layer induced turbulence, which is particularly true at $H = 2D$ due to this relatively small impingement distance. When low-to-medium swirl numbers are used ($S = 0.27 – 0.45$), the results show a higher (localised) *h* over the imaged region compared to $S = 0$. Such increased heat transfer coefficients are due to swirl enhanced turbulence and mixing. At even higher swirl numbers ($S = 0.77$ and 1.05), the ring shaped band of high *h* over $0.25 < r/D < 0.75$ and seen at $S = 0.45$, grows radially outwards and also

increases in strength. However, even for the highest swirl numbers tested at $H = 2D$ ($S = 0.77$ and 1.05), a zone of low h spanning $r/D = 0.5$ remains centred at the jet axis.

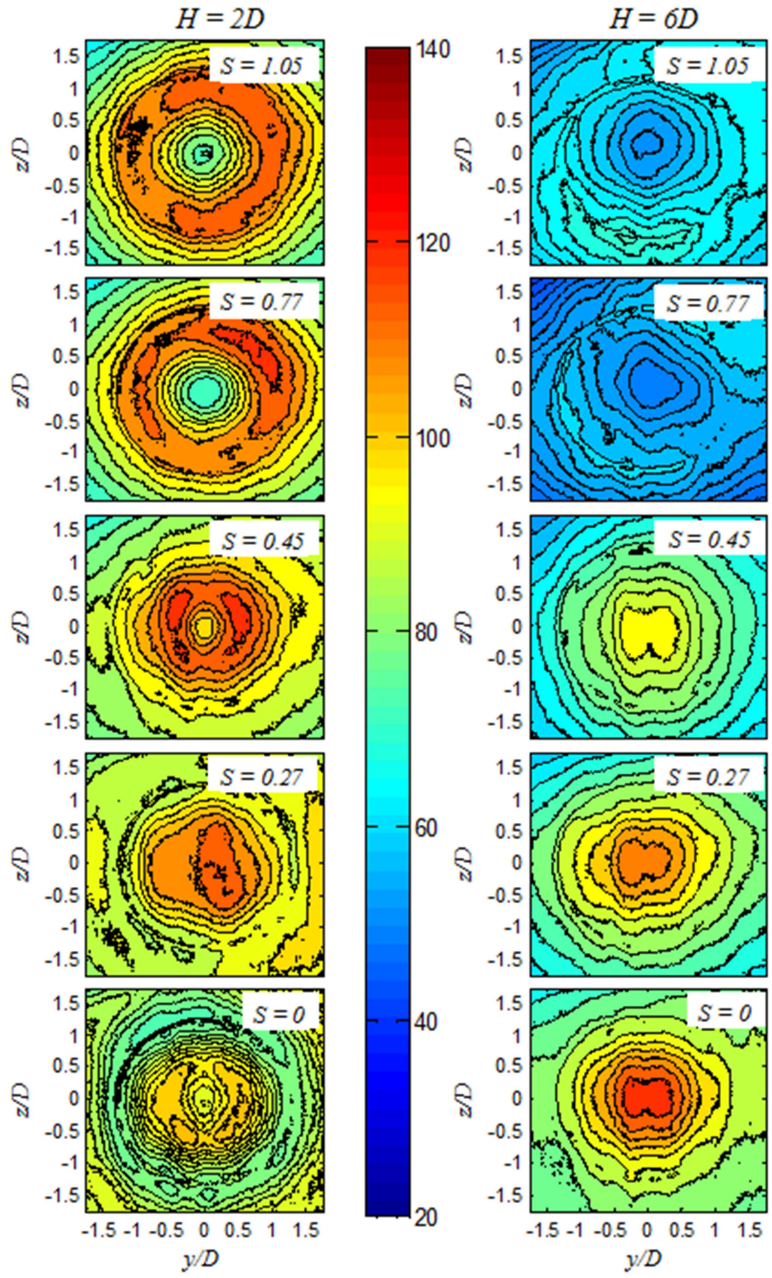

Figure 6.6 Contour maps of convective heat transfer coefficient h ($W/m^2.^oC$) on the impingement surface for various swirl numbers over $H = 2D$ and $6D$.

In comparison, the results at $H = 6D$ show that in the case of far-field impingement, the highest localised h occurs on the centreline, both in non-swirling ($S = 0$) and weakly swirling jets ($S = 0.27$ and 0.45). The results also show two other interesting observations at $H = 6D$: the highest convective heat transfer does not occur with swirl, but in non-swirling jets, and the presence of a transitional behaviour in the magnitude of h at around $S = 0.45$. Beyond this transitional swirl number, further increases in swirl number ($S = 0.77$ and 1.05) lead to an overall reduction in h intensity, which is attributed to the greater relative opportunity for gradual jet widening when using far-field impingement as swirl increases (from $S = 0$ to 0.45 and then from 0.77 to 1.05). The experimental results presented in Figure 6.6 thus identify important trends for the effect of two operating parameters (H, S) on impinging jet heat transfer. The remainder of this paper will now use CFD to further investigate the fundamental linkage between the velocity and turbulence field over these different jet conditions, and the heat transfer characteristics just reported. Furthermore, because there appears to be very little qualitative and quantitative difference in heat transfer characteristics between $S = 0.77$ and $S = 1.05$ at both $H = 2D$ and $6D$, the ensuing numerical results will focus on two swirl numbers ($S = 0.45$ and 0.77) as well as their comparison to a (baseline) non-swirling jet, both in near-field ($H = 2D$) and far-field ($H = 6D$) impingement.

Figure 6.7a[14] demonstrates numerically computed convective heat transfer coefficient for both impingement distances ($H = 2D$ and $6D$). The results show a fairly good agreement with the experimental data (Figure 6.6) in relation to both the magnitude and radial location of h peaks over all S considered. The local minimum around the jet centre for the strongly swirling jet ($S = 0.77$) is well predicted for both H. However, relatively poor agreement exists around the jet centre ($r/D \leq 0.25$) for $S = 0.77$. This may attributed to the insufficient accuracy of RANS based computations at higher swirl and the flow field complexity as well as turbulence near the impingement zone, even though it has been applied to non-impinging swirl stabilised jets [43, 48, 49]. Typical deviations of h (from experimental data) around the jet centre are within 10% for $S = 0$ and 0.45, and roughly around 50% for $S = 0.77$. Figure 6.7b also presents computations validated against experimentally derived impingement pressure data [34]. These results show that a more qualitative and quantitative agreement with the experimental data exists, with the only exception occurring at transitional swirl number S

[14] Corresponding impingement surface temperature data (T_W) and their comparison with the computed data are available in the Appendix D-4-1.

= 0.45 at $H = 6D$. The above comparisons for pressure and heat transfer validate the numerical methodology adopted reasonably well.

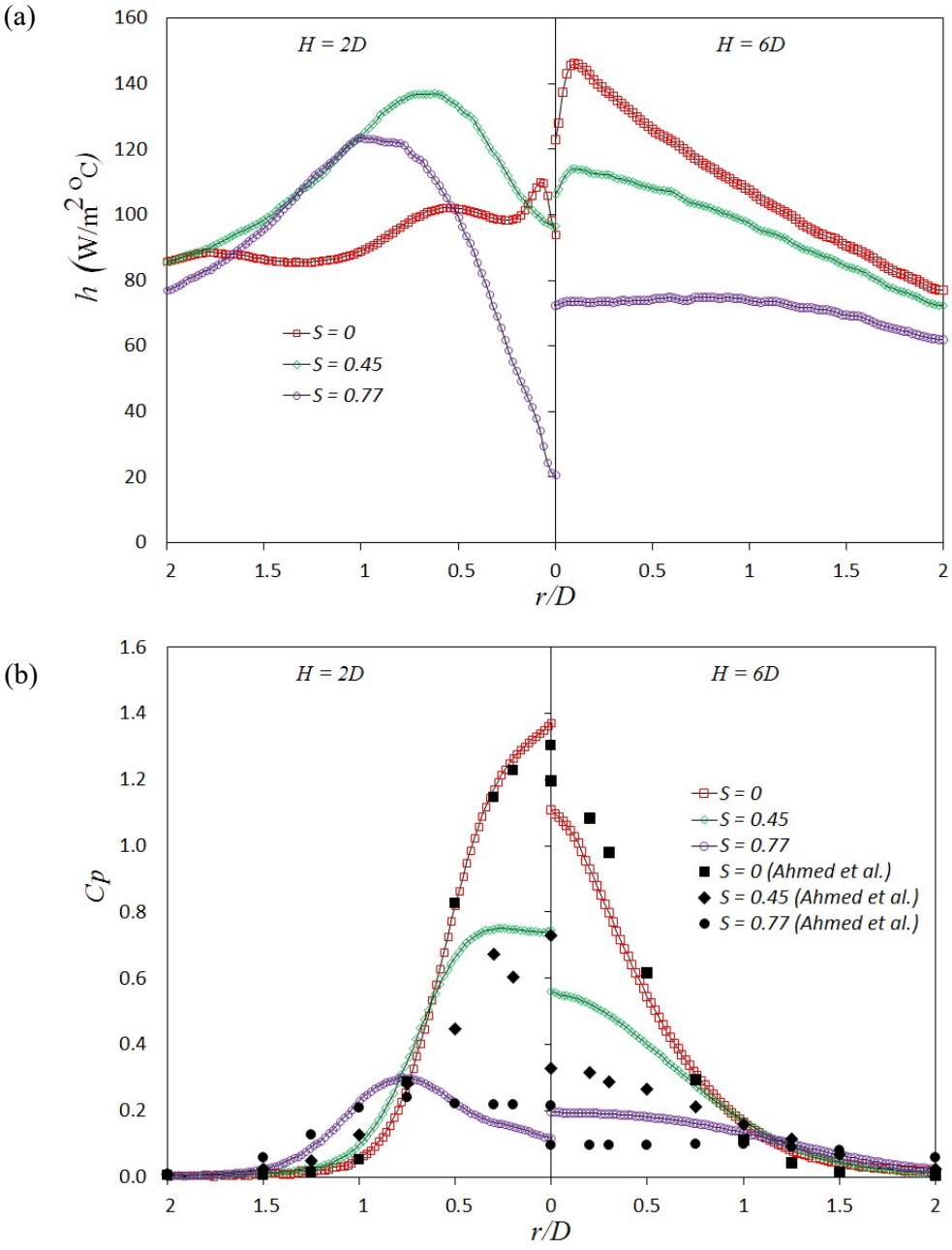

Figure 6.7 Computed results over $r/D = 0 – 2$ at $H = 2D$ for: (a) heat transfer coefficient (h) and (b) the coefficient of pressure ($Cp = P - P_\infty \Big/ 0.5\rho U_b^2$) compared against experimental data (Ahmed et al. [34]).

Figure 6.8 illustrates a CFD analysis of the contour maps for the mean velocity field over S = 0 - 0.77 at $H = 2D$. For S = 0 and 0.45, the contour profiles of $\langle u \rangle$ show fairly similar shape, but for the latter, $\langle u \rangle$ around the jet centre (r/D = 0) exhibits a stronger velocity gradient and a relatively faster jet spread. This behaviour is attributed to the effect of swirl. For even more strongly swirling jets (S = 0.77), the most striking difference is the appearance of a recirculation zone, which extends axially from x/D = 1.5 – 2 and stagnates on the surface at $r/D \approx 0.5$. The larger spreading rate of the jet and swirl induced streamwise pressure gradient also cause the axial velocity to undergo a stronger deceleration compared to S = 0 and 0.45. This behaviour also gives rise to a second shear layer between the emerging central jet and the recirculation zone. The contour plots of $\langle v \rangle$ for S = 0 and 0.45 show a similar behaviour, compared to S = 0.77. The contour of $\langle w \rangle$ for S = 0.77 shows a stronger rotational velocity near the exit plane, as well as a greater widening of the jet compared to others. This is contrast to the $\langle w \rangle$ contour for S = 0.45 which generally exhibits only a modest widening of the jet until it reaches near the impingement surface. The location of this swirl induced recirculation zone at S = 0.77 coincides (spatially) with the trough of convective heat transfer located on the centreline in this jet (Figure 6.6). When the impingement distance increases to $H = 6D$, interestingly the recirculation zone which had occurred at S = 0.77 entirely disappears. For brevity, Figure A-2 (Appendix) presents the mean velocity field at $H = 6D$.

Figure 6.9 presents the effect of swirl on the computed wall shear stress distributions for moderately swirling (S = 0.45) and strongly swirling jets (S = 0.77) at $H = 2D$ and $6D$ when compared to another baseline non-swirling (S = 0) jet case [50]. At $H = 2D$, wall shear stress distribution for the computed S = 0 jet agrees well with the experimental data [50], except for the location of the (weak) peak at $r/D \approx 2$ which is observed in the experiment. This discrepancy may be attributed to slight variations in the specified nozzle boundary condition profiles ($\langle u \rangle$), as upstream variations can affect downstream flow development [11]. For both impingement distances studied, swirl causes a reduction of τ_w, and the τ_w peaks shift radially outward with the increase of S. The reduction of wall shear stress in the swirl jets can be attributed to the weak velocity gradients prevailing at or near the impingement region due to jet spread (Figure 6.8). The computed profiles at $H = 2D$ and the outward radial shifting of the peaks with swirl number also correlates with the widening (outwards) of the intense band of h (Figure 6.6). The broadening of these distributions with swirl at $H = 6D$ also indicates

that flatter wall shear stress distributions appear to correlate with relatively subdued convective heat transfer distributions (Figure 6.6).

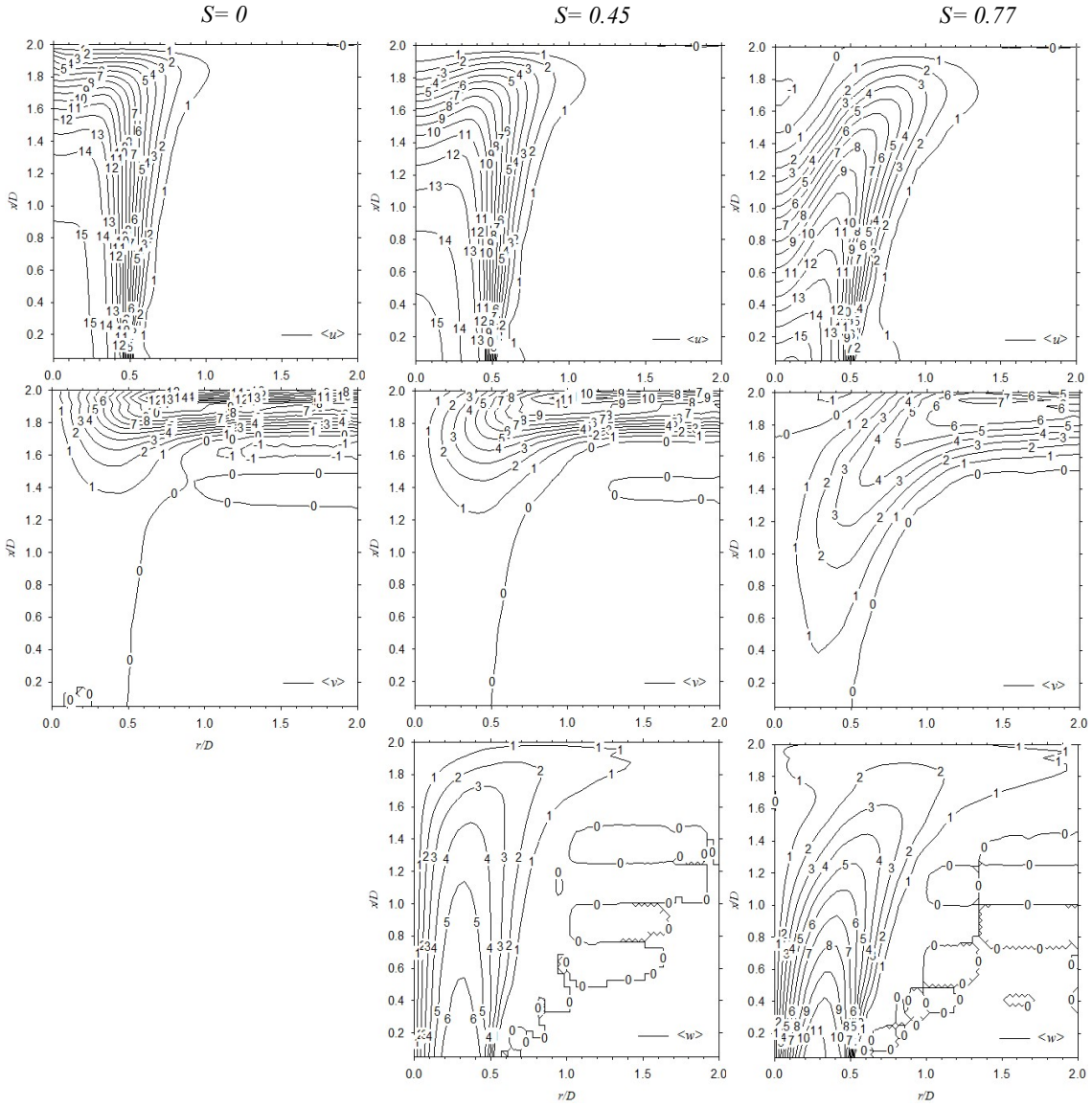

Figure 6.8 Numerically derived contour plots of mean velocity components over the range $S = 0 – 0.77$ at $H = 2D$.

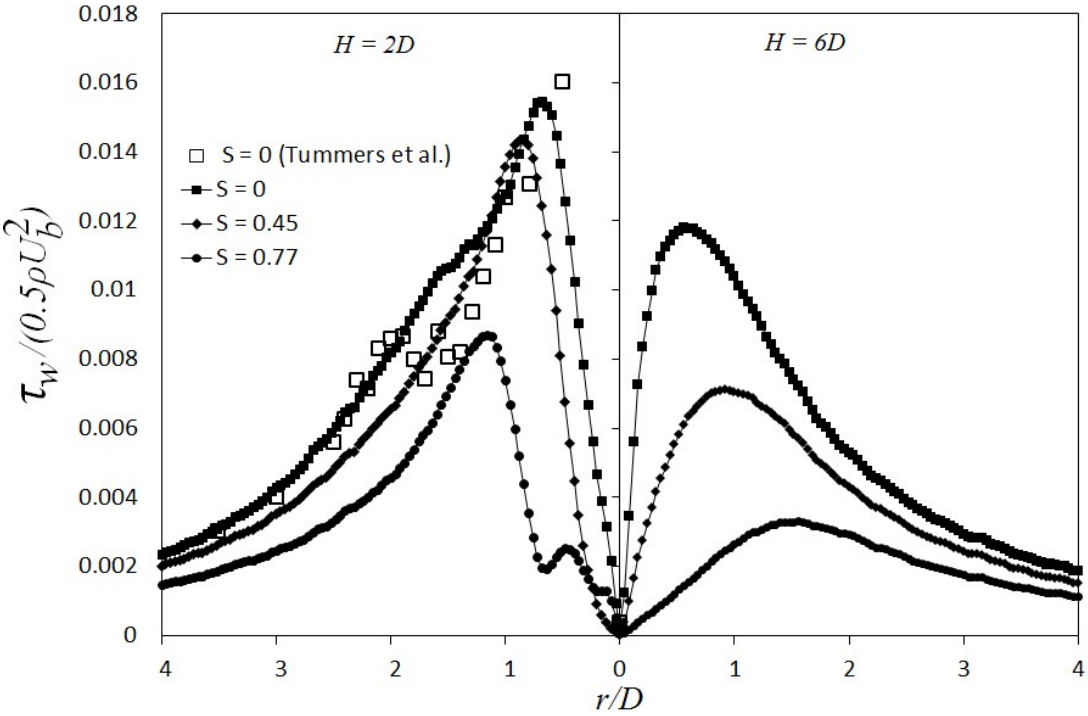

Figure 6.9 Wall shear stress distribution for different swirl numbers at $H = 2D$ and $6D$. A benchmark data for $S = 0$ (Tummers et al. [50]) is also superimposed in the figure.

Figure 6.10 shows the contour plots of normalised turbulent kinetic energy k (normalised by U_b^2) from CFD data. These results show that in the free jet region of non-swirling jets, stronger turbulence is largely associated with the shear layer (mixing region), and located at around $r/D = 0.5$. As the jet approaches the surface (in both $H = 2D$ and $6D$), the highest k then occurs in the wall jet region. These results also correlate well with the locations of peak convective heat transfer which are off the centreline in non-swirling jets ($S = 0$). Earlier results had also shown (Figure 6.6) that at $H = 2D$, a recovery of h occurred at $r/D \approx 0.5$. This is shown to coincide with a relatively high k/U_b^2 (Figure 6.10). Similarly in the case of non-swirling jets at $H = 6D$, the highest h was concentrated at the centreline (Figure 6.6) and extended to $r/D \approx 1$. The computations (Figure 6.10) show the location of peak h correlates fairly well with increased k/U_b^2. The overall behaviour of turbulent kinetic energy and its magnitude agree well with the literature [51, 52]. When swirl is imparted at $S = 0.45$ for $H = 2D$, a more extensive presence of high intensity k/U_b^2 is observed in the stagnation (central) region of the jet. For near-field impingement at $H = 2D$, computations also indicate there also

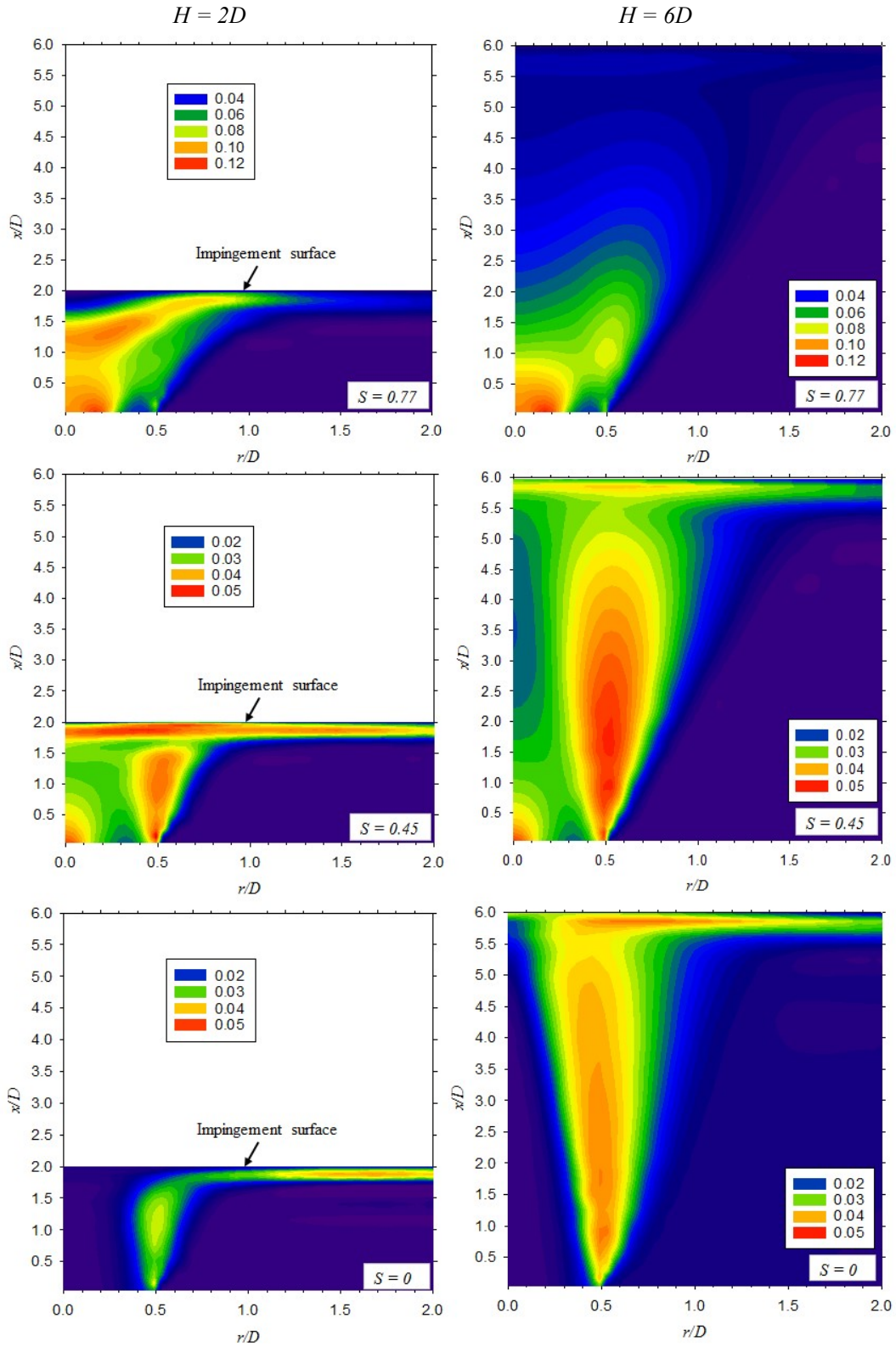

Figure 6.10 Contour plots of non-dimensional turbulent kinetic energy k / U_b^2 (from CFD) for three swirl numbers (S = 0, 0.45 and 0.77) at $H = 2D$ and $H = 6D$.

appears a pocket of relatively low k/U_b^2 in the neighbourhood of jet centreline at the impingement surface and confined to $r/D < 0.5$. This also correlates fairly well with the relatively low intensity h observed at the stagnation point in the experimental data (Figure 6.6). The computed pocket of low k/U_b^2 adjacent to the surface at $H = 2D$ appears to diminish at $H = 6D$. This may also explain why there is no zone of low h at the stagnation point at $H = 6D$ and $S = 0.45$ (Figure 6.6). When swirl number increases further to $S = 0.77$ at $H = 2D$, a significantly different behaviour of k/U_b^2 is observed in all regions of impinging jets. A relatively higher turbulence is also seen in the central part of the nozzle exit plane which almost maintains its magnitude as the flow moves downstream up to $x/D = 1.0$ for $S = 0.77$ in both $H = 2D$ and $6D$. This high k/U_b^2 then diminishes abruptly and shifted radially away due to the appearance of recirculation zone when impingement occurs at near-field ($H = 2D$) and to the larger jet spread at far-field impingement ($H = 6D$). The normalised turbulent kinetic energy takes lower values near the impingement surface in both $H = 2D$ and $6D$ ($r/D \leq 0.5$). The numerically predicted behaviour of k/U_b^2 at $H = 6D$ and S = 0.77, also explains the subdued intensity of h as it correlates to the relative reduction in the normalised turbulent kinetic energy at those conditions. The swirl induced impingement zone at $H = 6D$ and $S = 0.77$ is therefore seen to lead to lower k/U_b^2 as the jet appears to diverge away from the surface at an earlier stage, compared to $S = 0.45$.

Before presenting the final correlations between the Nusselt number and wall shear stress with the flow field turbulence components ($u'u', v'v', w'w'$) close to the wall, Figure 6.11 shows how these turbulence components develop further upstream for $H = 2D$. The numerical results are presented for $S = 0.45$ and 0.77, and compared with non-swirling jets ($S = 0$). As anticipated, jets with a larger swirl number generally have greater turbulence compared to those at lower S or non-swirling ($S = 0$). The results show that $v'v'/U_b^2$ appears to have a negligible impact on the velocity field close to the impingement surface since it diminishes beyond $x/D = 1.5$. The more interesting observation is that a swirl induced recirculation zone which stabilises at the impingement surface for $S = 0.77$ and reaches to $x/D \approx 1.5$, appears to cause the $u'u'/U_b^2$ and $w'w'/U_b^2$ peaks to similarly depart off the geometric centreline. This is believed to be due to the spreading of the free jet as it approaches the recirculation zone and impingement plane. This behaviour thus causes the peak normal stresses to be distributed in a band like formation as the jet gets close to impingement.

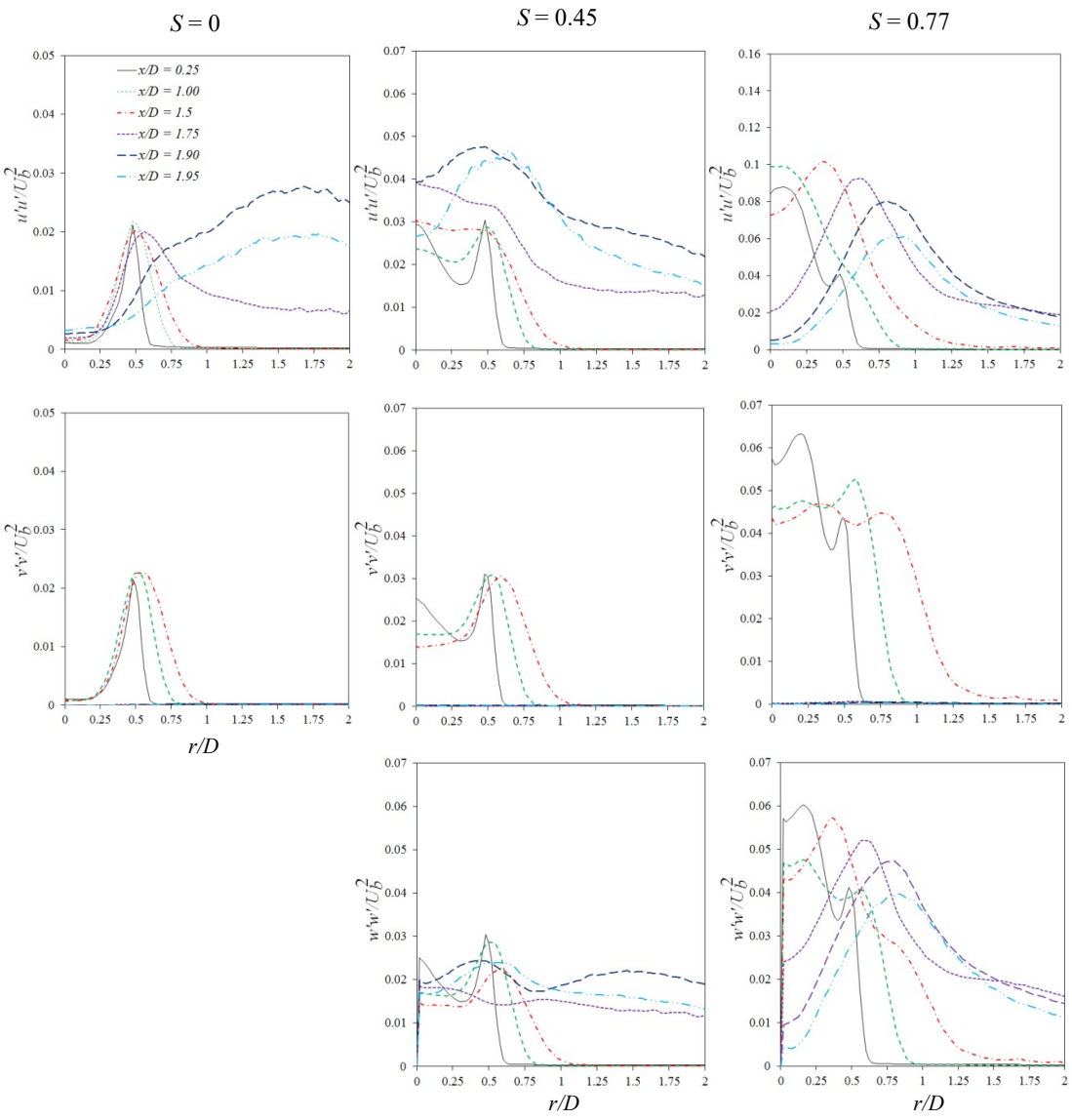

Figure 6.11 Reynolds normal stress at various downstream positions (x/D = 0.25 – 1.95) ahead of the impingement surface at $H = 2D$ for three jet conditions over the range S = 0 – 0.77.

Finally, Figure 6.12 shows the radial distributions of *Nu* in both non-swirling (S = 0) and swirling jets (S = 0.45 and 0.77) at $H = 2D$ and $6D$. In this regard, *Nu* is derived with Equation (6.2) using the data shown in Figure 6.6. Figure 6.12 also includes the numerically resolved normalised mean velocity field and turbulence quantities ($u'u'/U_b^2$, $w'w'/U_b^2$,

$< v > /U_b$, $< w > /U_b$ and $\tau_w / 0.5\rho U_b^2$) at the impingement surface. The data for $v'v'/U_b^2$ has not been included because earlier results (Figure 11) showed it diminished for $x/D > 1.5$,

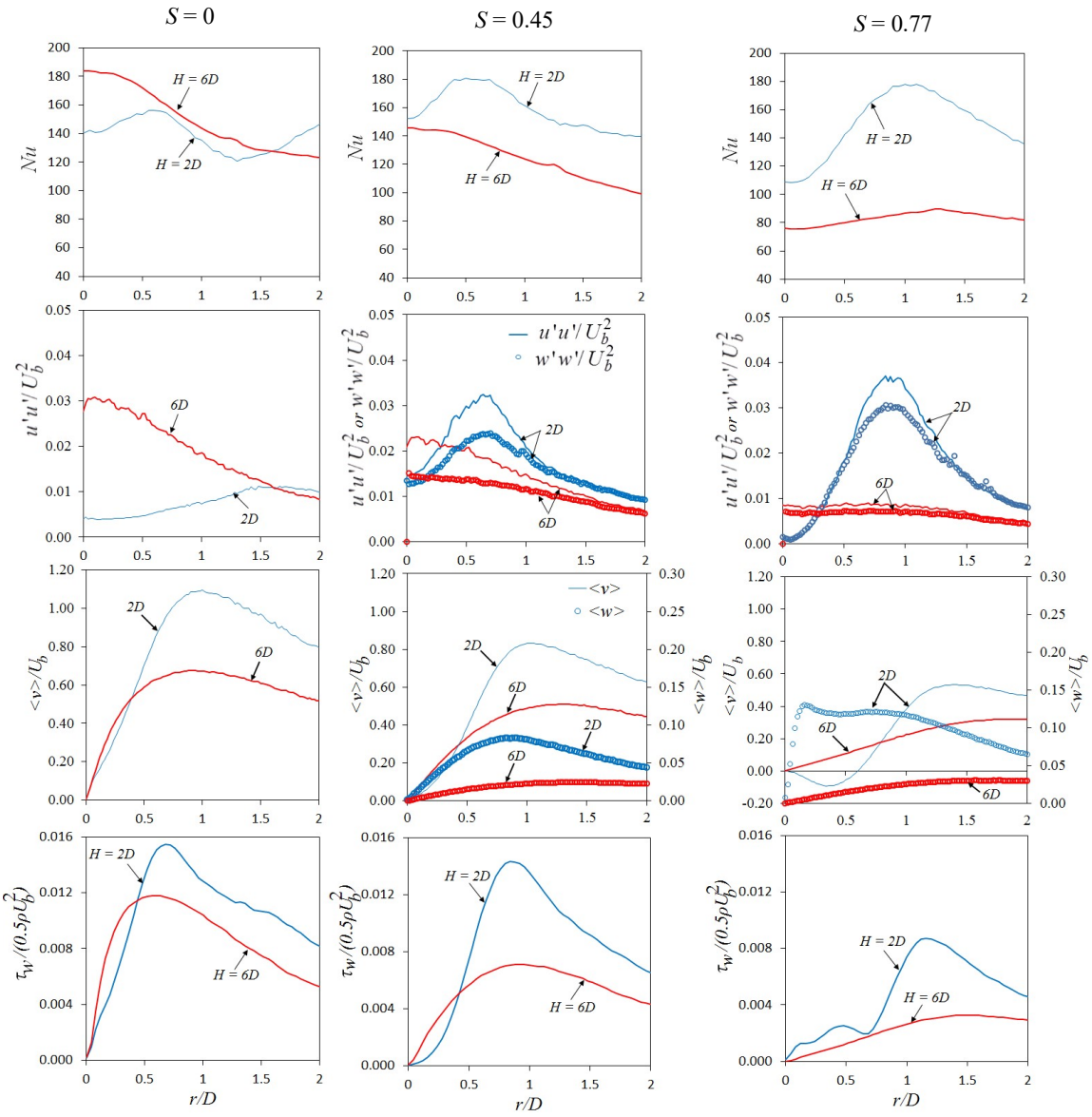

Figure 6.12 Experimentally derived *Nu* data (top) at the impingement surface ($H = 2D$ and $6D$) and numerically resolved mean flow and turbulence field parameters at 0. $02D$ (0.8 mm) above the impingement surface over the range $S = 0 – 0.77$.

i.e. close to impingement. The aim here is to resolve any spatial correlations between the (mean) velocity and turbulence fields with the *Nu* distribution. Such correlations would be very valuable to help ascertain not only the factors leading to high *Nu*, but also gaining a

fundamental insight into how swirl affects the value at distributions of *Nu* at impingement. The results show that in most cases the *Nu* peaks at the surface appear more clearly correlated to the $u'u'/U_b^2$ and $w'w'/U_b^2$ behaviour resolved at 0.02*D* upstream of the impingement surface. The occurrence of peaks and troughs in the convective heat transfer profiles (*h*, *Nu*) in both non-swirling and swirling jets is thus strongly affected by the flow field turbulence. The mean flow characteristics (radial and tangential velocity components or the wall shear stress) near the impingement surface have relatively little effect for the occurrence of *Nu* peaks compared to turbulence, except the inner peak in non-swirling jets.

6.4 Conclusion

Experimental measurements (CTA, infrared thermography) and numerical predictions (RANS with SST *k*-ω model) have been used to investigate the effects of swirl number (S = 0 – 0.77) and impingement distance (H = 2*D* and 6*D*) on convective heat transfer under turbulent (Re = 35,000) jet impingement. By studying the interplay between both the mean velocity (<*u*>, <*v*>. <*w*>) and turbulence field ($u'u', v'v', w'w'$) on the impingement surface (τ_w, *h*, *Nu*), a better insight can be gained to understand the fundamental effects of turbulent swirl on impingement heat transfer. The results of the study are summarised below:

- The imposition of varied levels of swirl (S = 0.27 – 1.05) is found to increase the overall convective heat transfer coefficient (*h*) for only near-field impingement (H = 2*D*) compared to non-swirling (S = 0) jets. In the case of far-field impingement (H = 6*D*), the enhancement in *h* with swirl is more limited and confined to S = 0.27 – 0.45 (Figure 6). In far-field impingement conditions, the highest heat transfer is not achieved with swirl, but in non-swirling jets.
- Swirl induced recirculation zones appear stabilised on the impingement surface (and around the jet centre) occur only with strongly swirling jets (S = 0.77) in the case of near-field impingement (Figure 8). These recirculation zones are believed to affect the heat transfer coefficient at near-field impingement.
- Imparting swirl in jets reduces wall shear stress (τ_w) with a gradual decrease in peak values, coupled with outward radial widening as swirl number increases, regardless of impingement distance (Figure 9).

- For near-field impingement, an occurrence of a pocket of relatively low turbulent kinetic energy near the impingement surface (over $r/D < 0.5$) at all swirl numbers leads to relatively poor heat transfer in this zone (Figure 6 and Figure 10).
- The investigations very close to the impingement surface reveal the occurrence of peaks and troughs in *Nu* distributions in both non-swirling and swirling jets. These appear to correlate with localised jet turbulence ($u'u'$ and $w'w'$), both in near-field ($H = 2D$) and far-field ($H = 6D$) impingement (Figure 12).

6.5 Chapter references

1. Davoust, S., Jacquin, L. and Leclaire, B., *New results on the structure of turbulence in a mixing layer with and without swirl*, International Journal of Heat and Fluid Flow, 49, p. 11-17, 2014.
2. Fenot, M., Dorignac, E. and Lalizel, G., *Heat transfer and flow structure of a multichannel impinging jet*, International Journal of Thermal Sciences, 90, p. 323-338, 2015.
3. Ianiro, A. and Cardone, G., *Heat transfer rate and uniformity in multichannel swirling impinging jets*, Applied Thermal Engineering, 49(0), p. 89-98, 2011.
4. Singh, S. and Chander, S., *Heat transfer characteristics of dual swirling flame impinging on a flat surface*, International Journal of Thermal Sciences, 89, p. 1-12, 2015.
5. Guerra, D. R., Su, J. and Silva Freire, A. P., *The near wall behavior of an impinging jet*, International journal of heat and mass transfer, 48(14), p. 2829-2840, 2005.
6. O'Donovan, T. S. and Murray, D. B., *Jet impingement heat transfer – Part I: Mean and root-mean-square heat transfer and velocity distributions*, International Journal of Heat and Mass Transfer, 50(17–18), p. 3291-3301, 2007.
7. Ozmen, Y. and Baydar, E., *Flow structure and heat transfer characteristics of an unconfined impinging air jet at high jet Reynolds numbers*, Heat and Mass Transfer, 44(11), p. 1315-1322, 2008.
8. Katti, V. and Prabhu, S. V., *Experimental study and theoretical analysis of local heat transfer distribution between smooth flat surface and impinging air jet from a circular straight pipe nozzle*, International Journal of Heat and Mass Transfer, 51(17–18), p. 4480-4495, 2008.
9. Rohlfs, W., Haustein, H. D., Garbrecht, O. and Kneer, R., *Insights into the local heat transfer of a submerged impinging jet: Influence of local flow acceleration and vortex-wall interaction*, International Journal of Heat and Mass Transfer, 55(25), p. 7728-7736, 2012.
10. Greco, C. S., Ianiro, A. and Cardone, G., *Time and phase average heat transfer in single and twin circular synthetic impinging air jets*, International Journal of Heat and Mass Transfer, 73, p. 776-788, 2014.
11. Ahmed, Z. U., Al-Abdeli, Y. M. and Matthews, M. T., *The effect of inflow conditions on the development of non-swirling versus swirling impinging turbulent jets*, Computers & Fluids, 118, p. 255-273, 2015.

12. Gardon, R. and Akfirat, J. C., *The role of turbulence in determining the heat-transfer characteristics of impinging jets*, International Journal of Heat and Mass Transfer, 8(10), p. 1261-1272, 1965.
13. Lytle, D. and Webb, B. W., *Air jet impingement heat transfer at low nozzle-plate spacings*, International Journal of Heat and Mass Transfer, 37(12), p. 1687-1697, 1994.
14. Kataoka, K., Suguro, M., Degawa, H., Maruo, K., et al., *The effect of surface renewal due to large-scale eddies on jet impingement heat transfer*, International Journal of Heat and Mass Transfer, 30(3), p. 559-567, 1987.
15. Lee, D. H., Won, S. Y., Kim, Y. T. and Chung, Y. S., *Turbulent heat transfer from a flat surface to a swirling round impinging jet*, International Journal of Heat and Mass Transfer, 45(1), p. 223-227, 2002.
16. Owsenek, B. L., Cziesla, T., Mitra, N. K. and Biswas, G., *Numerical investigation of heat transfer in impinging axial and radial jets with superimposed swirl*, International Journal of Heat and Mass Transfer, 40(1), p. 141-147, 1997.
17. Volchkov, E. P., Lukashov, V. V. and Semenov, S. V., *Heat transfer in an impact swirling jet*, Heat Transfer Research, 27(1), p. 14-24, 1996.
18. Huang, L. and El-Genk, M. S., *Heat transfer and flow visualization experiments of swirling, multi-channel, and conventional impinging jets*, International Journal of Heat and Mass Transfer, 41(3), p. 583-600, 1998.
19. Wen, M. and Jang, K., *An impingement cooling on a flat surface by using circular jet with longitudinal swirling strips*, International Journal of Heat and Mass Transfer, 46(24), p. 4657-4667, 2003.
20. Ichimiya, K. and Tsukamoto, K., *Heat transfer from an inflow-type swirling turbulent impinging jet*, JSME International Journal Series B Fluids and Thermal Engineering, 49(4), p. 995-999, 2006.
21. Ward, J. and Mahmood, M., *Heat transfer from a turbulent, swirling, impinging jet*, in Heat transfer 1982: Proceedings of the Seventh International Conference, September 6-10, Munich, West Germany, p. 401-407, 1982.
22. Abrantes, J. K. and Azevedo, L. F. A., *Fluid flow characteristics of a swirl jet Impinging on a flat plate*, in 13th Int Symp on Applications of Laser Techniques to Fluid Mechanics, 26-29 June, Lisbon, Portugal, http://ltces.dem.ist.utl.pt/lxlaser/lxlaser2006/downloads/papers/28_3.pdf, p. 1-12, 2006.
23. Angioletti, M., Nino, E. and Ruocco, G., *CFD turbulent modelling of jet impingement and its validation by particle image velocimetry and mass transfer measurements*, International Journal of Thermal Sciences, 44(4), p. 349-356, 2005.
24. Bovo, M. and Davidson, L., *On the numerical modeling of impinging jets heat transfer-A practical approach*, Numerical Heat Transfer Part A: Applications, 64(4), p. 290-316, 2013.
25. Isman, M. K., Pulat, E., Etemoglu, A. B. and Can, M., *Numerical investigation of turbulent impinging jet cooling of a constant heat flux surface*, Numerical Heat Transfer, Part A: Applications, 53(10), p. 1109-1132, 2008.
26. Zuckerman, N. and Lior, N., *Jet impingement heat transfer: Physics, Correlations, and Numerical modeling*, in Advances in Heat Transfer, editor: G. A. Greene, J. P. Hartnett, A. B. C. Young, et al., Elsevier. p. 565-631, 2006.
27. King, A. J. C. and Chandratilleke, T. T., *Heat transfer characteristics in impinging jet arrays*, Australian Journal of Mechanical Engineering, 4(1), p. 59-64, 2007.

28. Jaramillo, J. E., Pérez-Segarra, C. D., Rodriguez, I. and Oliva, A., *Numerical study of plane and round impinging jets using RANS models*, Numerical Heat Transfer, Part B: Fundamentals, 54(3), p. 213-237, 2008.
29. Pulat, E., Isman, M. K., Etemoglu, A. B. and Can, M., *Effect of turbulence models and near-wall modeling approaches on numerical results in impingement heat transfer*, Numerical Heat Transfer, Part B: Fundamentals, 60(6), p. 486-519, 2011.
30. Balabel, A. and El-Askary, W. A., *On the performance of linear and nonlinear turbulence models in various jet flow applications*, European Journal of Mechanics - B/Fluids, 30(3), p. 325-340, 2011.
31. Ortega-Casanova, J., *CFD and correlations of the heat transfer from a wall at constant temperature to an impinging swirling jet*, International Journal of Heat and Mass Transfer, 55(21–22), p. 5836-5845, 2012.
32. Amini, Y., Mokhtari, M., Haghshenasfard, M. and Gerdroodbary, M. B., *Heat transfer of swirling impinging jets ejected from Nozzles with twisted tapes utilizing CFD technique*, Case Studies in Thermal Engineering, 6, p. 104-115, 2015.
33. Wannassi, M. and Monnoyer, F., *Fluid flow and convective heat transfer of combined swirling and straight impinging jet arrays*, Applied Thermal Engineering, 78, p. 62-73, 2015.
34. Ahmed, Z. U., Al-Abdeli, Y. M. and Guzzomi, F. G., *Impingement pressure characteristics of swirling and non-swirling turbulent jets*, Experimental Thermal and Fluid Science, 68, p. 722-732, 2015.
35. Thomas, B., Ahmed, Z. U., Al-Abdeli, Y. M. and Matthews, M. T., *The optimisation of a turbulent swirl nozzle using CFD*, in Proceedings of the Australian Combustion Symposium, 6-8 November Perth, Australia, http://www.anz-combustioninstitute.org/local/papers/ACS2013-Conference-Proceedings.pdf, p. 271-274, 2013.
36. Ahmed, Z. U., Al-Abdeli, Y. M. and Guzzomi, F. G., *Corrections of dual-wire CTA data in turbulent swirling and non-swirling jets*, Experimental Thermal and Fluid Science, 70, p. 166-175, 2016.
37. Cengel, Y. A. and Turner, R. H., Fundamentals of Thermal-Fluid Sciences, McGraw-Hill, Singapore, 2004.
38. Ahmed, Z. U., *An experimental and numerical study of surface interactions in turbulent swirling jets*, PhD Thesis, in School of Engineering, Edith Cowan University: Joondalup, Australia, p., 2016.
39. Ahmed, Z. U., Al-Abdeli, Y. M. and Guzzomi, F. G., *Impingement heat transfer characteristics of swirling and non-swirling turbulent jets*, International Journal of Heat and Mass Transfer, p., 2015 (In review).
40. Geers, L. F. G., Tummers, M. J., Bueninck, T. J. and Hanjalić, K., *Heat transfer correlation for hexagonal and in-line arrays of impinging jets*, International Journal of Heat and Mass Transfer, 51(21), p. 5389-5399, 2008.
41. Astarita, T. and Carlomagno, G. M., Infrared Thermography for Thermo-fluid-dynamics, Springer-Verlag, Heidelberg, Berlin, 2013.
42. Yang, X. and Ma, H., *Computation of strongly swirling confined flows with cubic eddy□viscosity turbulence models*, International Journal for Numerical Methods in Fluids, 43(12), p. 1355-1370, 2003.
43. Vanierschot, M. and Van den Bulck, E., *Numerical study of hysteresis in annular swirling jets with a stepped□conical nozzle*, International Journal for Numerical Methods in Fluids, 54(3), p. 313-324, 2007.

44. *ANSYS, Inc., ANSYS FLUENT (version 14.5)*. http://www.ansys.com/Products/Simulation+Technology/Fluid+Dynamics/Fluid+Dynamics+Products/ANSYS+Fluent, Date Accessed: 13 May, 2013, 2012.
45. Kader, B. A., *Temperature and concentration profiles in fully turbulent boundary layers*, International Journal of Heat and Mass Transfer, 24(9), p. 1541-1544, 1981.
46. Jongen, T., *Simulation and modelling of turbulent incompressible flows*, PhD, in EPF Lausanne: Lausanne, Switzerland, p., 1992.
47. Meola, C., de Luca, L. and Carlomagno, G. M., *Influence of shear layer dynamics on impingement heat transfer*, Experimental Thermal and Fluid Science, 13(1), p. 29-37, 1996.
48. Yang, Y. and Kær, S. K., *Comparison of Reynolds averaged Navier-Stokes based simulation and large-eddy simulation for one isothermal swirling flow*, Journal of Thermal Science, 21(2), p. 154-161, 2012.
49. Guo, B., Fletcher, D. F., Marquez, G., Al-Abdeli, Y. M., et al., *RANS calculation and measurements of instabilities in swirl-stabilized jets and flames*, in 2003 Australian Symposium on Combustion & The 8th Australian Flame Days, Monash University, Australia, p., 2003.
50. Tummers, M. J., Jacobse, J. and Voorbrood, S. G. J., *Turbulent flow in the near field of a round impinging jet*, International Journal of Heat and Mass Transfer, 54(23–24), p. 4939-4948, 2011.
51. Behnia, M., Parneix, S. and Durbin, P. A., *Prediction of heat transfer in an axisymmetric turbulent jet impinging on a flat plate*, International Journal of Heat and Mass Transfer, 41(12), p. 1845-1855, 1998.
52. Behnia, M., Parneix, S., Shabany, Y. and Durbin, P. A., *Numerical study of turbulent heat transfer in confined and unconfined impinging jets*, International Journal of Heat and Fluid Flow, 20(1), p. 1-9, 1999.

6.6 Chapter Appendices

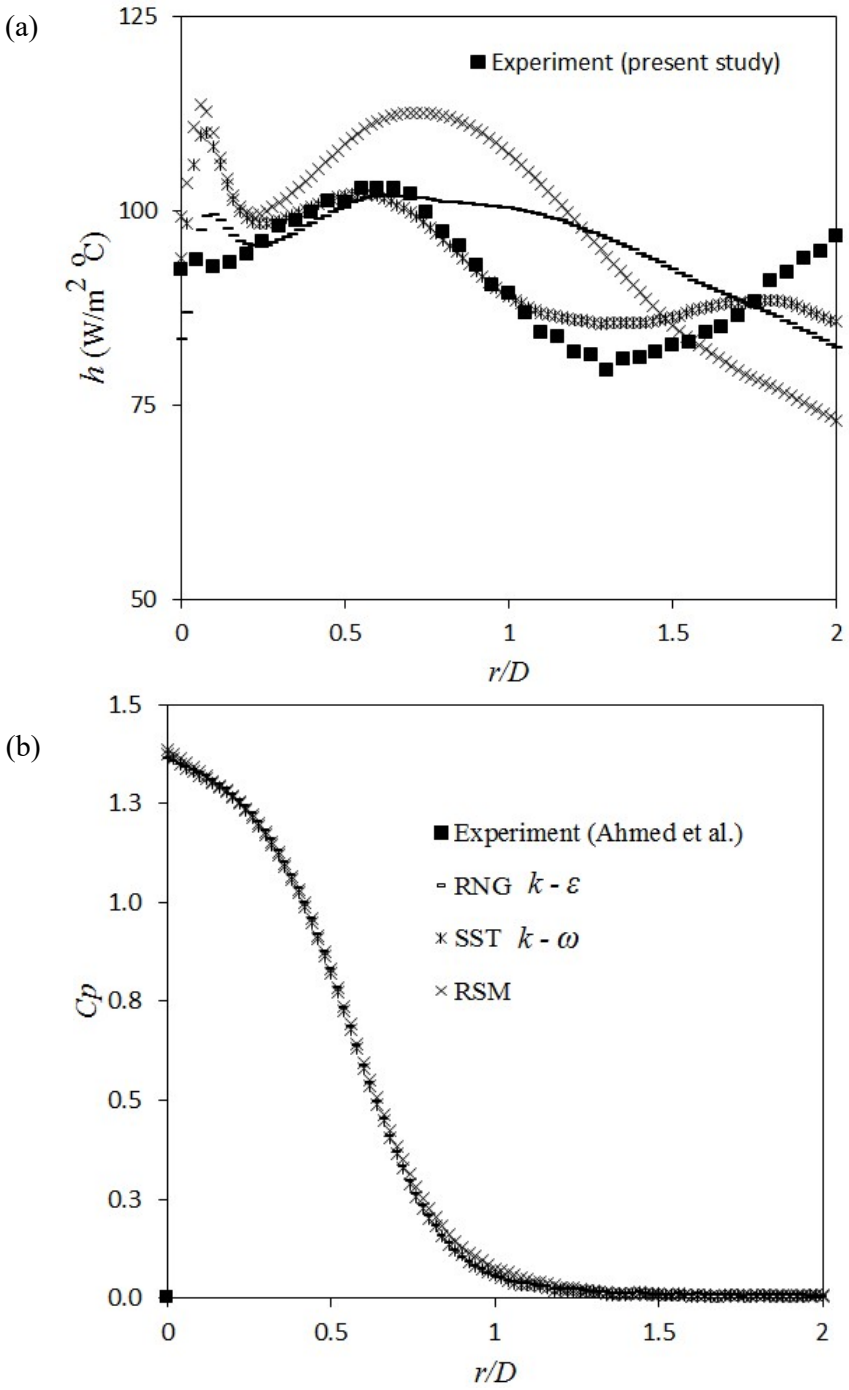

Figure 6.A-1 Comparison of three turbulence models (RNG k-ε, SST k-ω and RSM) against experimental data sets (Ahmed et al. [34] and present study) for $S = 0$ at $H = 2D$: (a) convective heat transfer coefficient (h) and (b) coefficient of pressure (Cp).

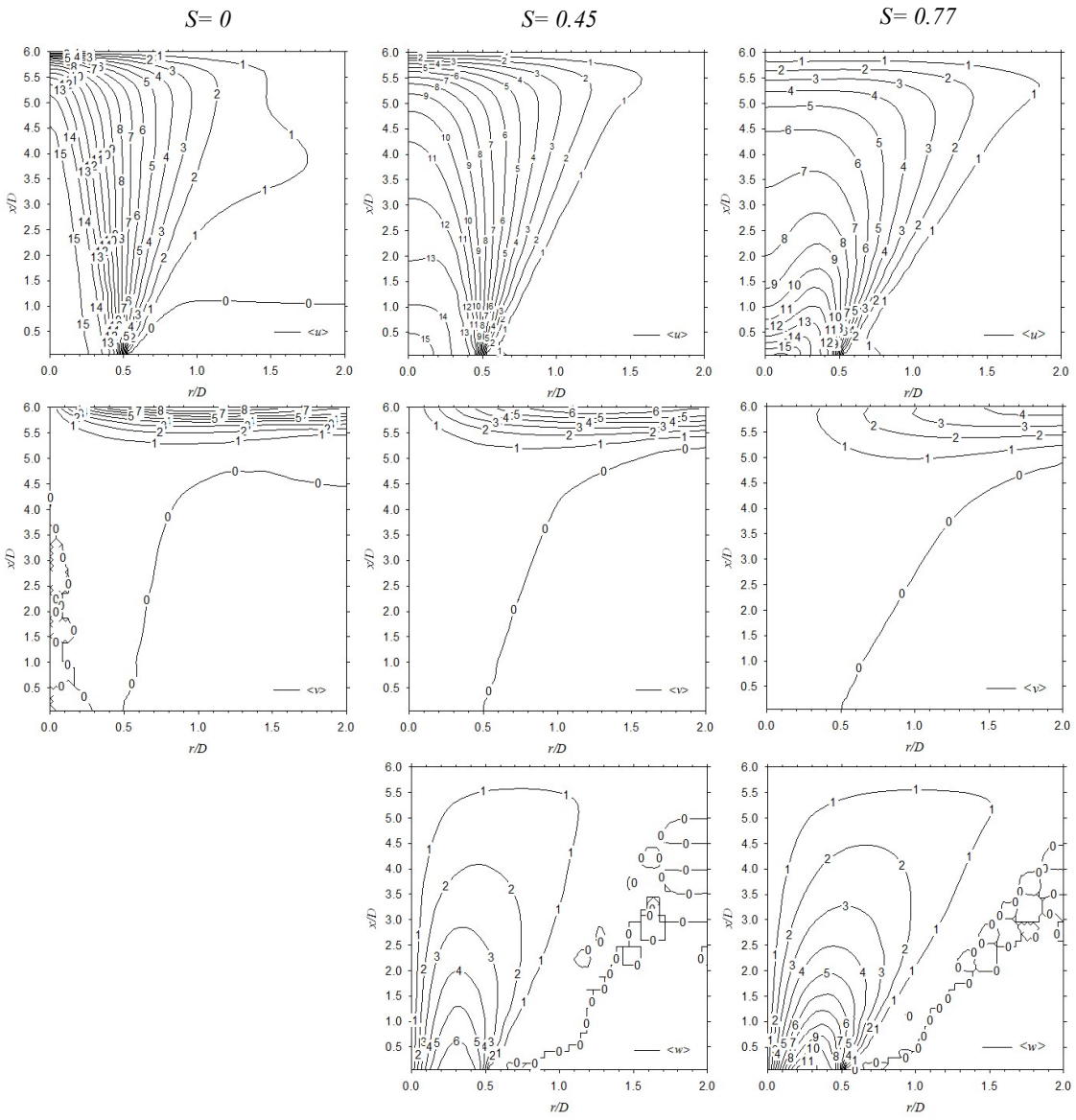

Figure 6.A-2 Numerically computed contour plots of mean velocity components over the range $S = 0 – 0.77$ at $H = 6D$.

Chapter 7

7 General Discussion

Although turbulent impinging jets have practical relevance to industry, achieving further improvements in heat transfer, its magnitude and spatial uniformity, remains one of the outstanding challenges in these jets. The literature published remains undecided in relation to the exact effects of swirl with regard to impingement, with some contrary results. Moreover, the use of geometrically generated swirl in jets influences both the fluid flow and heat transfer characteristics, which further complicates resolving the fundamental understanding of how increased swirl influences the surface heat transfer. This PhD research project has therefore investigated the use of aerodynamically induced swirl on both the fluid flow and heat transfer characteristics. The nozzle used can deliver turbulent jets which seamlessly transit from non-swirling to highly swirling.

This chapter discusses the overall results presented in the thesis. The specific results already discussed in the earlier chapters will not be repeated, but the aim is to integrate those distinct outcomes in order to help build a better overall picture in this area. In this way, this chapter will not only establish connections among the chapters, but will also address the research questions presented in Chapter 1. To facilitate this, the discussion will be grouped and organised under a few sub-topics as follows.

7.1 Fundamental behaviour

7.1.1 Influence of swirl on the impingement pressure characteristics

The effect of swirl number (S = 0 – 1.05) on the impingement pressure distribution was investigated over the Reynolds number range (Re = 11,600 – 35,000) for different nozzle-to-plate distances (H = 1D – 6D) in Chapters 2 and 4 as well as Appendix D-2. The results showed for non-swirling-to-weakly swirling jets ($S \leq 0.3$), the coefficient of pressure (Cp) profiles demonstrated a comparable magnitude and radial distributions, with peaks on the jet axis in near-field impingement ($H \leq 2D$). As S increases, the peak Cp shifted radially away from the jet centre at some critical S (dependent on Re) and the magnitudes of these peaks

reduced when H increases further ($H \geq 4D$). For the closest impingement distance ($H = 1D$), flow separation from the impingement surface occurred around the jet centre at strongly swirl flows, but such separated flow did not appear for larger H. These results suggest the swirl effect is predominantly stronger in the near-field impingement, and the pressure distribution largely depends on the upstream flow characteristics (at the nozzle exit plane). The magnitude of Cp was found to diminish with decreasing Re (Figure 4.8 and Appendix D-2). However, for a given S, the effect of Re had little effect on radial pressure distributions and showed similar profiles, except for the transitional swirl numbers. This variation was explained by the difference in velocity profiles at the transitional S in each Re. Such different pressure behaviours on the impingement surface at varied S, H and Re warranted investigation of their effects on impingement heat transfer characteristics as well as upstream flow field for varied swirl number.

7.1.2 Influence of swirl on the impingement flow field

The flow field (mean velocity components and turbulence) characteristics for the effect of swirl ($S = 0 – 0.77$) and nozzle-to-plate distance (H) were numerically presented in Chapter 2 ($H = 2D$, $Re = 23{,}000$) and Chapter 6 ($H = 2D$ and $6D$, $Re = 35{,}000$). Flow visualizations (Chapter 4) near the impingement and wall jet regions ($Re = 35{,}000$ over $H = 1D – 6D$) were also performed to shed further light into the reasons behind distinctive pressure behaviours in low-to-highly swirling impinging jets. Generally, mean axial ($<u>$) and radial ($<v>$) velocity components resembled the non-swirling jet behaviour upto medium swirling jets within $S \leq 0.45$ (Figures 2.13-2.15, 6.8, 6.A-2). The stronger jet spread with increased swirl caused $<u>$ to reduce faster, and eventually flow stagnation and recirculation occurred in near-field impingement ($H \leq 2D$) at strongly swirling ($S = 0.77$) jets (Figure 6.8). Similar to the mean flow field, turbulence quantities also showed distinctive features between low and high swirl numbers (Figures 2.16, 6.10 and 6.11). When impingement occurred further downstream ($H = 6D$), turbulence was mostly confined within $x/D = 2$ for highly swirling jets, and then strong turbulence dissipation leads to weak turbulent kinetic energy near the impingement surface (Figure 6.10). Flow visualisation results near the impingement surface showed that for both non-swirling and weakly swirling jets, the flow direction near the surface was largely oriented radially, and this observation was consistent with numerical results presented in Chapters 2 and 6 for non-swirling and weakly swirl jets. In contrast, for strongly swirling flows ($S = 1.05$), a rotating reversed flow around the jet centre appeared at $H \leq 2D$. In this regard, complex flow features near the impingement surface were visualised with three

independent flows: radially inward ($r/D \leq 0.5$), radially outward ($r/D \geq 1.0$) and a transitional flow between them (Figure 4.10). As H increases, the occurrence of reverse flow between the nozzle and the surface disappeared, and the flow gradually became weaker. Whilst appreciable effects onto the mean velocity components and turbulence were seen from the coupled effects of swirl and nozzle-to-plate distance, such changes were rather less significant on the wall shear stress. The wall shear stress was largely found to deteriorate monotonically with increased swirl or nozzle-to-plate distance (Figures 2.13 and 6.9). The location of peak wall shear stress shifted radially outward when swirl number were increased.

7.1.3 Influence of swirl on the magnitude of heat transfer

The effect of aerodynamic swirl ($S = 0 – 1.05$) and nozzle-to-plate distance ($H = 1D – 6D$) on the magnitude of impingement heat transfer characteristics over Re = 11,600 - 35,000 was discussed in Chapter 5. For a given Re, when S increased initially from a non-swirling flow, heat transfer (Nu) enhanced in the impingement region due to the increased level of turbulence, but this enhancement was largely confined to within $1D$. The stronger effect of swirl in Nu only realised in the near-field impingement ($H \leq 2D$) and the magnitude of Nu non-linearly diminished as H increases. For strongly swirling flows, local heat transfer improvement occurred only outside the impingement region, with a low Nu core around the jet centre. Since it is difficult to quantify the heat transfer improvement from local Nu for the effect of swirl due to non-uniform Nu distributions, a common practice is to achieve a single average (area integrated) Nusselt number $\overline{Nu}$ for each swirl conditions. As such, Table 7.1 (not reported earlier in this form) shows the percentage improvement or deterioration of heat transfer compared to non-swirling ($S = 0$) jets over the range $S = 0.27 – 1.05$ at Re = 35,000. A significant heat transfer improvement upto 60% is found for the highest swirl number (S = 1.05) at $H = 1D$. In general, heat transfer augments considerably at $H \leq 2D$, deteriorates at $H \geq 4D$. It appears from the results that there is a transitional swirl number (S = 0.45) and impingement distance ($H = 2D$) exists which largely controls the heat transfer improvement. This finding appeared to be common in other Reynolds numbers as well. However, the magnitude of Nu subdued as Re reduced due to the lower mass flow rates that contributes to the convective heat transfer (Appendices 5.A-1 and D-3). For a given S, the effect of Re on the heat transfer distributions was largely dependent on the boundary conditions at the nozzle exit plane, similar to the impingement pressure (Chapter 4).

These observations indicate the effectiveness of impingement heat transfer, in relation to the magnitude and uniformity of Nu is complicated, and a function of swirl intensity,

nozzle-to-plate distance, and the impingement area considered. The desire for a more uniform heat transfer on the impingement surface needs to be weighed up against the merits of a higher average convective heat transfer rate. Heat transfer improvement from swirling jets would bring benefit to various engineering applications, such as grinding processes or drying of woods where rapid cooling or drying may significantly reduce lead time and running cost.

Table 7.1 Percentage improvement/deterioration of $\overline{Nu}$ in swirling jet conditions compared to their non-swirling counterpart for each H and circular area at Re= 35,000. Negative sign (-) before numbers indicate deterioration.

SWIRL NUMBER	$H = 1D$ (%)	$H = 2D$ (%)	$H = 4D$ (%)	$H = 6D$ (%)
Circular area $r/D = 0.50$				
S = 0.27	14.2	15.7	10.6	-6.9
S = 0.45	14.1	15.2	11.7	-19.9
S = 0.77	26.6	-13.1	-46.5	-56.3
S = 1.05	36.1	-10.3	-40.3	-53.4
Circular area $r/D = 1.0$				
S = 0.27	10.2	11.9	7.3	-5.3
S = 0.45	12.4	16.2	8.9	-17.13
S = 0.77	56.3	7.0	-37.2	-49.0
S = 1.05	59.8	7.8	-29.8	-44.8
Circular area $r/D = 2.0$				
S = 0.27	5.6	10.4	3.4	-5.8
S = 0.45	5.6	10.3	3.9	-15.9
S = 0.77	37.0	13.1	-24.9	-38.2
S = 1.05	39.6	14.0	-15.0	-30.3

7.1.4 Influence of swirl on the radial uniformity of heat transfer

The results presented in Chapter 5 also showed that the spatial uniformity of Nu was strongly dependent on S and H. For non-swirling-to-medium swirling jets (S = 0 – 0.45), the results at Re = 35,000 generally showed an improved Nu uniformity on the impingement surface only at H = 2D. As H increased from 2D, the number of peaks and troughs were diminished, but not much improvement in relation to the spatial uniformity of Nu. In contrast, for $S \geq 0.77$, opposite trends was observed for heat transfer uniformity. In this regard, a radially non-uniform Nu distribution was more evident in the near-field impingement ($H \leq$ 2D). At $H \geq 4D$, dramatically improved uniformity of heat transfer across the radial distance

$r \leq 2D$ was found, but at the expense of magnitudes. The overall behaviours of heat transfer uniformity with S at other Reynolds numbers (Re = 24,600 and 11,600) were found qualitatively similar, but swirl number transition occurred earlier as Re reduces.

7.1.5 Turbulence-heat transfer interactions

The results presented in the thesis (Chapters 2 and 6) also showed that the effect of swirl in jets and the nozzle-to-plate distance predominantly affected downstream turbulence development as well as very close to the impingement surface. These results resolved the interactions between varied swirl induced turbulence and heat transfer distributions on the impingement surface. In non-swirling jets, the regions of relatively higher turbulence correlated well with the locations of peak convective heat transfer for both near- and far-field impingements. When low-to-medium swirl was imparted to the jets, a more extensive presence of high turbulent kinetic energy was observed in the impingement (central) region of the jet (Figures 2.16 and 6.10), which also largely matched with the occurrence of peak heat transfer zones. Conversely, for strongly swirling jets, a significantly different turbulence development in the downstream locations was observed due to the appearance of recirculation zones in the near-field impingement and stronger turbulence dissipation in the far-field impingement (Figures 6.10 and 6.11). These behaviours caused lower turbulence near the impingement surface which also explained the subdued convective heat transfer around the jet centre at strongly swirling jets. Finally, any spatial correlations of different peaks and troughs of Nu distribution with the mean velocity and turbulence fields were also investigated in Chapter 6. The results showed the occurrence of different Nu peaks in swirling jets was largely correlated by the peaks of turbulent kinetic energy and the Reynolds normal stress components (axial and tangential) near the impingement surface (Figure 6.12). Flow recirculation and very low turbulence around the jet centre at strongly swirling jets may contribute to the low heat transfer core. Overall, mean flow characteristics were found to have little influence in impingement heat transfer peaks for swirling jets, compared to flow turbulence.

7.2 Methodologies

7.2.1 Effect of inflow (upstream) conditions

The investigations of any complex flows, such as impinging jets and swirling flows, typically requires a well-defined flow conditions to resolve the fundamental characteristics more accurately. Such flow characterisations are equally important in CFD simulations to

mimic experimental data or deeper insights into a problem for unresolved experimental data. As such, this PhD research project performed considerable works to investigate how upstream (inflow) condition varies in downstream development (Chapter 2) and to achieve a well resolved nozzle exit boundary conditions (Chapter 4). The upstream variations involved the transition from free-to-impinging and non-swirling-to-swirling jets for the similar mass flow rates and nozzle conditions. Nozzle exit boundary conditions included mean velocity and turbulence components measurement via CTA, checks of axisymmetry using circumferential velocity scan and checks of flow recirculation associated with vortex breakdown along the centerline (Chapter 4). Despite the differed upstream conditions, results showed mean velocity developments are similar upto $1D$ from the nozzle exit for non-swirling jets when transits from free-to-impinging ($H = 2D$). However, such similar flow developments were not observed when transits from non-swirling-to-swirling. From free jet centerline mean velocity characterisations (Figure 4.7), the test conditions in this research were chosen such that no vortex breakdown occurs due to avoid detrimental heat transfer effects in the impingent region from flow recirculation, which may be stronger with the presence of impingement surface.

7.2.2 Intricacy of applying CTA to swirling jets

Although there exists some literature in relation to CTA measurements in weakly swirling flows, the challenge of using dual-wire CTA probe in turbulent medium-to-strongly swirling jets still remains. A systematic approach to improve possible measurement inaccuracies in relation to the probe misalignment and the velocity gradient effect was presented in Chapter 3. The methodology applied for probe misalignment was mainly to ensure the mean flow direction (with respect to the CTA probe axis) falls within a certain angular range ($< \pm 25^{o}$). Outside this angular range, calibration of the probe suggested relatively large errors in velocity measurements. The results also provided a guideline whether the probe inclination (or rotation) is necessary for a given S, and the probe inclination angles were found to be largely proportional to the ratio of tangential-to-total flow (Q_t/Q_T), as shown in Table 3.3 and Figure 3.4. Conversely, the method applied for the velocity gradient effect was found to improve the measured (uncorrected) data (Figure 3.8). The percentage improvement in the shear layer for different Reynolds numbers was also presented. It appeared that the velocity gradient effect is apparent when the probe approaches the wall and for increasing Re. Without such corrections, the bulk velocity U_b would be underestimated by around 2% at the highest Re. CTA measurements of time-mean and turbulent velocity components at the nozzle exit

plane from this chapter were used in characterising flow conditions and in numerical simulations as inlet boundary (Chapter 6).

Chapter 8

8 Conclusion and Future Work Recommendations

This chapter integrates the findings of all chapters and offers suggestions for possible future works.

8.1 Conclusions

This thesis largely focused on the impact of aerodynamically induced turbulent swirl jets on the fluid flow and impingement heat transfer characteristics. The results have also been compared to (baseline) non-swirling jets. Both experimental and numerical techniques were utilised to address the research questions stated in Chapter 1. Experimental methods included a three channel CTA, pressure tappings, flow visualisations and time-resolved infrared thermography. A specially designed swirl nozzle allowed a seamless transition from non-swirling (S = 0) to highly swirling jets (S = 1.05). A heated foil assembly and impingement pressure plate were also designed and used. To enable CFD modelling and characterise swirl numbers as well as the uniformity of jet conditions studied, CTA measurements were performed at the nozzle exit plane and along the centerline. A commercial CFD software package ANSYS Fluent (version 14.5) was applied to resolve both the non-swirling and swirling jets numerically using RANS and energy equations coupled with different turbulence models. The effect of swirl number (S = 0 - 1.05) on fluid flow and heat transfer characteristics was examined for two controlling parameters, namely the Reynolds number (Re = 11,600 - 35,000) and the nozzle-to-plate distance (H = 1D - 6D). An overall summary of the results discussed in previous chapters is given below.

- For the near-field impingement (H = 2D), the centreline velocity and the jet spread of non-swirling jets develop similarly to their free jets counterpart upto about one diameter downstream from the nozzle exit plane ($x/D \leq 1$). For weakly swirling jets ($S \leq 0.3$), the different shapes of swirl velocity profile at the nozzle exit plane influences mean velocity components near the impingement surface.

- For a weakly swirling flow ($S \leq 0.3$), the overall behaviour of the static pressure distribution on the impingement surface follows the classical trend for non-swirling impinging jets. For relatively larger swirl numbers ($S > 0.3$), the effect of swirl is found more significant. Beyond a transitional swirl number (dependent on both H and Re), the maximum Cp shifts away from the stagnation point. At $H > 2D$, a flatter Cp profile with a weak peak is evident when S further increases.
- For near-field impingement ($H = 1D$), negative wall pressure coefficients occur near the impingement region indicating separated flow at strongly swirl flows ($S \geq 0.83$) for $Re = 35{,}000$. This flow separation appears even earlier when Re reduces ($S = 0.74$ at $Re = 24{,}600$ and $S = 0.72$ at $Re = 11{,}600$). Regardless of Reynolds number (Re), flow separations which occurred at strongly swirl flows, however, disappear for larger nozzle-to-plate distances ($H \geq 2D$).
- Whilst the flow largely directed radially on the impingement surface for weakly swirl ($S \leq 0.3$), three different flow regions from the stagnation point are, however, identified for storngly swirl flows ($S = 1.05$): an inward rotating flow at $r/D \leq 0.5$, a transition region at $0.5 < r/D \leq 0.75$ and an outward directed flow region at $r/D \geq 1.0$.
- Compared to non-swirling jets ($S = 0$), the use of swirl at near-field impingement ($H \leq 2D$) is found to significantly improve heat transfer ($\overline{Nu}$). For impingement occurring further downstream ($H = 4D$ and $6D$), non-swirling and low-to-medium swirl jet flows ($S = 0 – 0.45$) appear more effective.
- The imposition of relatively low values of swirl intensity ($S = 0.27 – 0.45$) does not markedly improve the spatial uniformity of heat transfer ($\overline{Nu}$) compared to their non-swirling counterparts ($S = 0$). However, higher values of swirl ($S = 0.77$ and 1.05) can lead to much flatter (more uniform) heat transfer for far downstream impingement ($H = 4D$ and $6D$), but accompanied with significantly low heat transfers. The desire for a more uniform heat transfer footprint at the impingement plane needs to be weighed up against the merits of a higher average convective heat transfer rate.
- Numerical results predicts a recirculation zone near the impingement surface and around the jet centre at strongly swirling jets ($S = 0.77$) and $H = 2D$. The recirculation zone extends axially from $x/D \approx 1.5$ and stagnates on the surface away from the jet centre at $r/D \approx 0.5$.

- Imparting any level of swirl (weak or strong) reduces the wall shear stress at the impingement surface and the location of the maximum wall shear stress shifts radially outward with increasing swirl.
- Turbulent kinetic energy and Reynolds normal stress components ($u'u'$ and $w'w'$) near the surface is found to largely affect the *Nu* distributions for both non-swirling and swirling jets on the impingement surface, compared to the mean velocity fields.
- The effect of *Re* on the overall radial pressure and heat transfer distributions is found insignificant. However, the intensities of *Cp* and *Nu* reduce as *Re* decreases for all *Re* considered.

8.2 Future works recommendation

i. Experimental measurements using non-intrusive techniques such as LDA, PIV between nozzle and impingement surface may provide a better understanding of the flow field at varied swirl numbers. The exact nature or detailed extent of the reverse flow region may be more accurately identified using such measurements. Data derived from non-intrusive measurements may also serve as a benchmark for future CFD model validation and allow comparisons to other experimental studies.

ii. It is well established in the literature that the effect of different nozzle geometry and upstream turbulence strongly influence the downstream flow developments in free jets. As such, it is similarly worth investigating how swirling jets with different levels of upstream turbulence affect Nusselt number at impingement.

iii. Whereas the present study has used a non-heated jet, largely to facilitate the accuracy of CTA measurements, a future research project using non-intrusive diagnostics may investigate heat transfer between a heated jet and a surface of ambient temperature, which is widely used in industrial heating and drying applications (drying of timbers and food products). In this case, a range of controlling parameters, such as Reynolds number, nozzle-to-plate distance and wider range of swirl number can be examined with a view to resolving the overall performance of heat transfer.

iv. Other possible works include thermo-acoustic instabilities of swirling impinging jets. This could provide further understanding of the investigations into the effect of instability on heat transfer on the impingement surface.

Appendices

Appendix A Permission of copyrighted material

Please refer to the attached CD (CD-1) for the permissions of published article to use in the thesis.

Appendix B Statement of coauthors contribution

Please refer to the attached CD (CD-2) for detailed documents of statement of co-authors contribution for each publication listed.

Appendix C Experimental Methods

C-1 Flowmeter calibrations and settings

C-1-1 Flowmeter calibrations

Three different types of air flow meters LV2S15-AI 27 (Make: Influx), LPL 1"LH40 - AI 58 (Make: Influx) and RSF-025V (Make: Dwyer) were used to achieve desired test conditions. The standard factory calibration is typically performed with free flow from meter outlet at atmospheric pressure and 20^{o}C, and the operating environment involves compressed air flow at 400 kPa (Gauge) upstream of the flowmeters, followed by passing through the swirl nozzle at a range of ambient temperature. As such, these flowmeters were calibrated first using CTA measurements at the operating conditions to account for the variation of the scale values.

For calibrations, different (volumetric) flow rates from flowmeters are fed through the axisymmetric nozzle which delivers non-swirling flows (only) and a single-wire CTA probe (Dantec, model: 55P11) is used to acquire velocity data in a radial scan. Pitot-static probe is also used to validate the CTA data and the variation was less than 2%. Once local velocity data acquired across the nozzle exit plane, the bulk velocity is determined as,

$$U_b = \frac{2}{R^2}\int_0^R < u > r dr\,, \tag{C-1}$$

where, $< u >$ is the CTA derived local mean velocity data and R is the nozzle radius. Flow rate is then calculated by,

$$Q = U_b A\,, \tag{C-2}$$

with A being the nozzle exit area equals to πR^2.

Each flow rate considered for calibration was tested several times (5 – 10 samples) and acquired CTA data. Consistent results of these tests ensured reliable data acquisition and repeatability of the flow settings. The following graphs show the calibration of three different flowmeters and the measurement deviations.

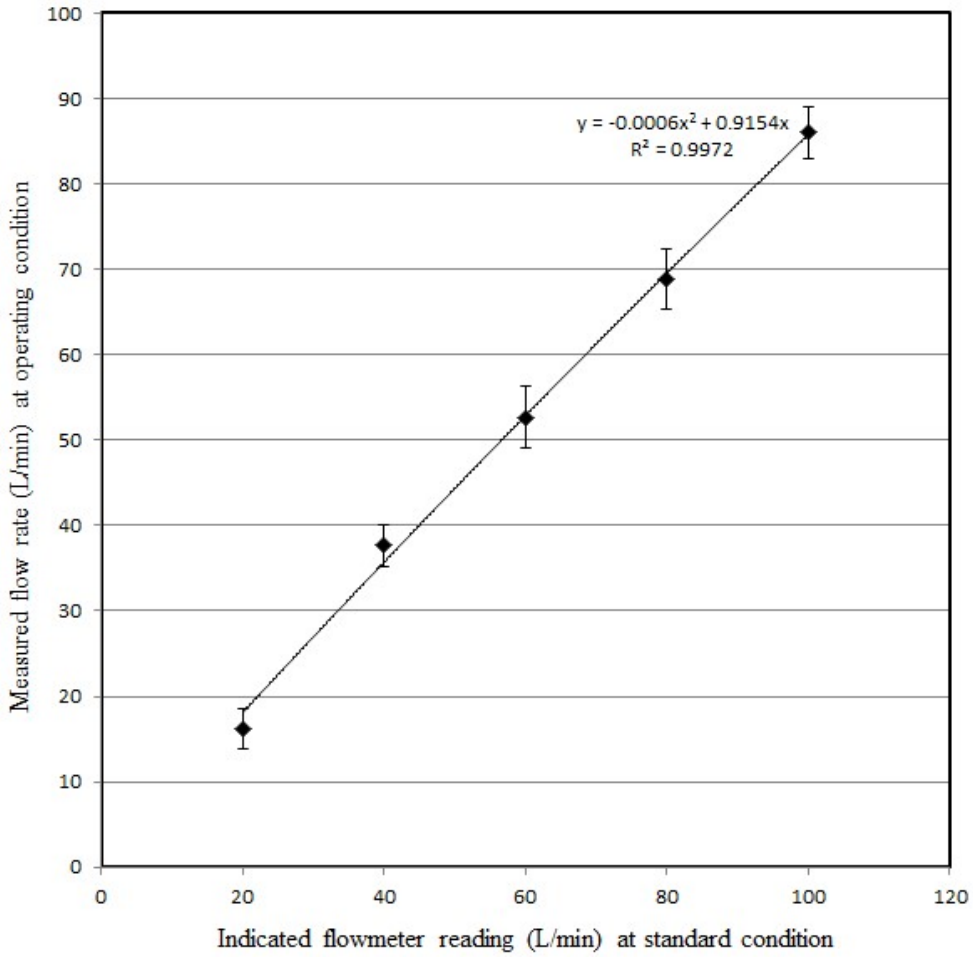

Figure C-1-1. Calibration graph for the flowmeter LV2S15-AI 27 (make: Influx). A straight pipe (13 mm diameter) was used for the calibration.

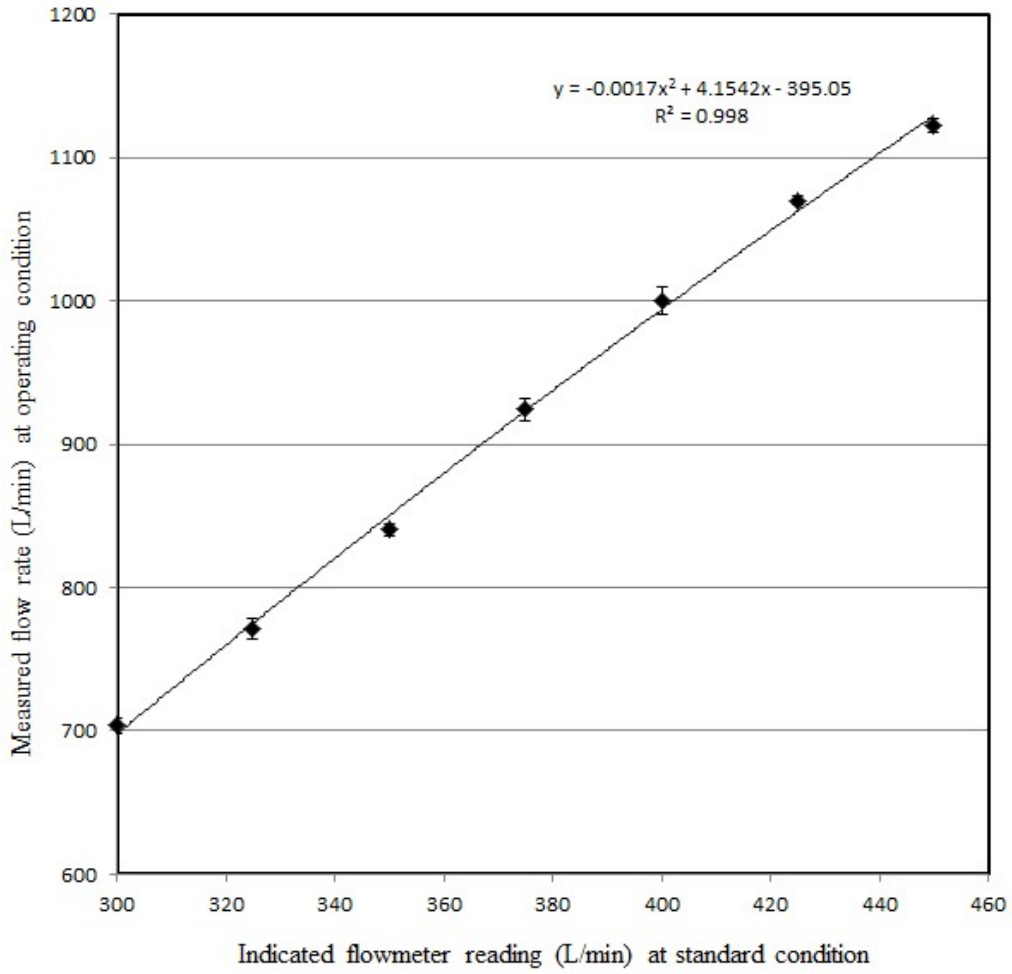

Figure C-1-2. Calibration graph for the flowmeter LPL 1"LH40 - AI 58 (Make: Influx). Swirl nozzle (40 mm diameter) was used for the calibration.

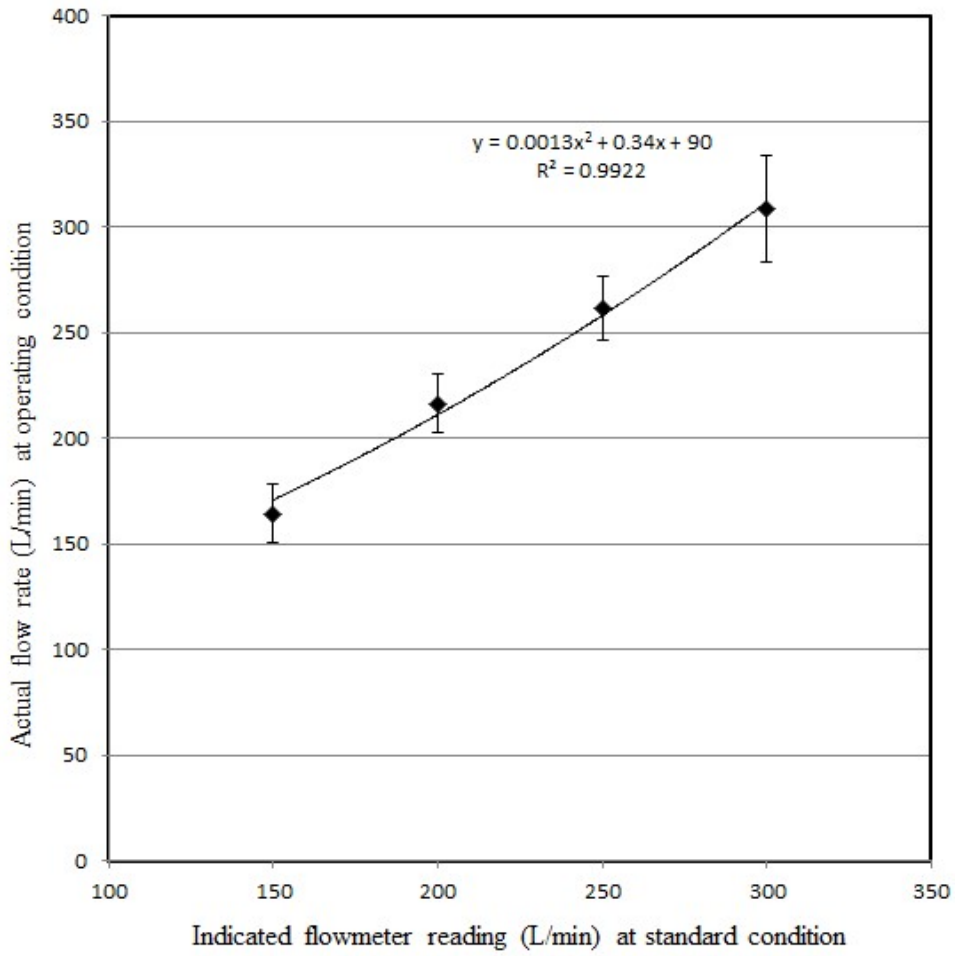

Figure C-1-3. Calibration graph for the flowmeter RSF025V (make: Dwyer). Swirl nozzle (40 mm diameter) was used for the calibration.

C-1-2 Flowmeters settings

A range of axial and tangential flow rates of air were passed through swirl nozzle in order to achieve different test conditions in the experiments.

Experimental conditions									
Actual flow rate								Flowmeter distributions	
Q_a (L/min)	Q_t (L/min)	Q_T (L/min)	*Re*	*Ub* (m/s)	*Wb* (m/s)	*S*	*ψ*	Q_a (1 meter)	Q_t (3 meters)
1000	0	1000	35 000	13.26	0.00	**0.00**	0		
703	291	994		12.99	2.04	**0.16**	0		
565	435	1000		13.14	3.50	**0.27**	0		
440	560	1000		13.74	6.18	**0.45**	5		
360	640	1000		13.71	10.51	**0.77**	10		
225	775	1000		17.39	14.43	**0.83**	15		
0	1011	1011		17.57	18.38	**1.05**	25		
703	0	703	24 600	9.32	**0.00**	**0.00**	0		
530	177	707		9.26	1.15	**0.12**	0		
370	330	700		9.10	2.81	**0.31**	0		
320	380	700		9.91	5.79	**0.58**	5		
250	450	700		11.00	7.01	**0.64**	10		
160	540	700		11.55	8.36	**0.72**	15		
0	712	712		11.00	9.34	**0.85**	25		
331	0	**331**	11 600	4.39	0.00	**0.00**	0		
220	110	330		4.31	0.91	**0.21**	0		
195	135	330		4.28	1.15	**0.27**	0		
150	180	330		5.03	1.63	**0.32**	5		
110	220	330		4.95	2.92	**0.59**	10		
0	330	330		5.08	3.75	**0.74**	25		

Color keys:

LPL1H40-AI58
RSF-025V
LV2S15-AI27

C-2 Infrared thermography

C-2-1 Emissivity measurements

For temperature measurements on the impingement surface using infrared (IR) camera (discussed in Chapter 5), a thin (25 μm thickness) stainless steel foil was used, which was painted Flat black in one side to attain a high emissivity surface for the camera. Since accurate irradiation to IR detectors strongly depends on the correct emissivity of a surface, the emissivity values of both unpainted and painted sides of the foil are determined by the following experiment.

First, a 120 X 310 mm foil strip was chosen and painted Flat black in one end and left unpainted in the other end, as shown in Figure A-3-1. In the middle section, black electrical insulating tape was mounted as a reference for its high emissivity coefficient value (approximately 0.98 [1]. The foil strip divided in such three sections was placed in a thermostatic-controlled constant temperature water bath (MATEST, Model: B051-01) in such a way that the foil just touches the upper surface of the water. The water is heated from ambient to 60^{o}C with 10^{o}C intervals. A thermocouple was also placed to measure the water surface temperature using a digital standard multimeter with a resolution of 0.1^{o}C. When the temperature reaches to a constant value (maximum variations within 0.2^{o}C), the emissivity of unpainted surface, painted surface and electrical tape were separately determined by the method outlined in [1, 2]. A typical image is shown in Figure A-3-2 and results are shown in Table A-3-1. The largest difference in temperature in a box (see Figure A-3-2) for painted surface was 0.5^{o}C for measurements of 60 ^{o}C.

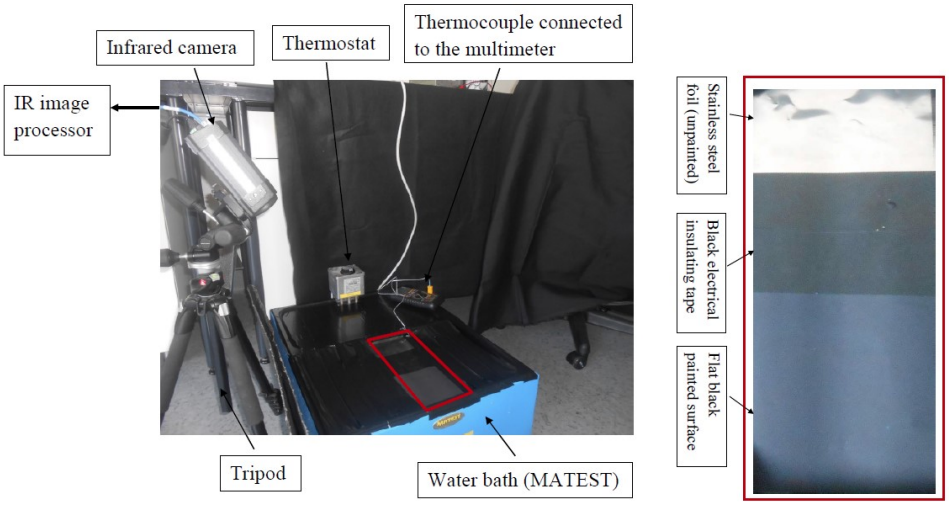

Figure C-2-1: Emissivity measurements setup for unpainted and painted stainless steel foil.

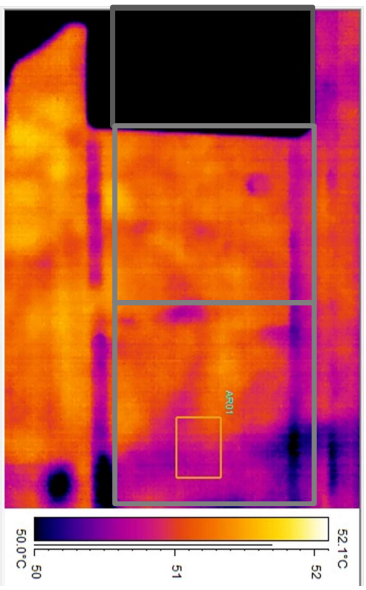

Figure C-2-2. A typical infrared image of three sections outlined in gray box: (left) full temperature scale, (right) refined temperature scale to clearly show the range of the electrical tape and painted surface sections.

Table C-2-1: Emissivity values of unpainted and painted surfaces of stainless steel (AISI316) foil at ambient and higher temperatures.

Temperature (^{o}C)	**Emissivity**		
	Unpainted SS foil	Black painted SS foil	Black electrical tape
Ambient (23^{o})	0.75	0.98	0.98
30^{o} – 60^{o}	0.057 ± 0.003	0.970	0.98

C-3 Uncertainty analysis

Whilst the used experimental flow and temperature measurement devices, such as CTA probe, micromanometer and IR camera are examples of effective and reliable instruments, they are, however, not free of errors, like other measurement methods. This section briefly presents the sources of uncertainty associated with these instruments and the derived uncertainties for different parameters.

C-3-1 General theory

In this research, the experimental uncertainty is estimated as a function of a systematic error ε_S and a random error ε_r. [3, 4]:

$$\varepsilon = \pm\sqrt{\varepsilon_S^2 + \varepsilon_r^2} \ . \tag{C-3}$$

Systematic or fixed errors are those which will remain constant during an experiment and it passes along non-altered from a test condition to another. This type of error typically involves tolerances and accuracy limits of the instruments, errors due to calibration, data acquisition and data reduction processes. The overall systematic limit of a certain measurement is represented by the root-sum-square combination of all the systematic error components:

$$\varepsilon_S = \sqrt{\sum_{i=1}^{n} \varepsilon_{S,i}^2} \ , \tag{C-4}$$

where, n is the number of error sources. Conversely, random errors are related to the measured data only and are often estimated from the statistics in the form of standard deviation or standard error. The overall random error is calculated as:

$$\varepsilon_r = \sqrt{\sum_{i=1}^{n} \varepsilon_{r,i}^2} \ , \tag{C-5}$$

where, individual component of the error is determined from the repeated observations in the form of standard uncertainty [4]:

$$\varepsilon_{r,i} = \sqrt{\frac{\sum_{i=1}^{N} \left(\phi_i - \bar{\phi}\right)^2}{N(N-1)}} = \frac{\sigma_S}{\sqrt{N}} \ , \tag{C-6}$$

with N is the number of samples in the repeated observations, σ_S is the estimated standard deviation of a sample mean and $\bar{\phi}$ is the mean of a variable defined as:

$$\bar{\phi} = \frac{1}{N}\sum_{i=1}^{N}\phi_i \,. \tag{C-7}$$

C-3-2 Sources of uncertainties/errors

Systematic uncertainty:

Uncertainties in CTA measurements typically arise from different sources, such as calibration inaccuracies, probe misalignments, velocity gradients, temperature drift and free convection effect. The maximum calibration error for mean velocity measurements was found to be 2% (Chapter 3). Chapter 3 also presents a detailed methodology to mitigate uncertainties associated with probe misalignments, velocity gradient effects and temperature drift. The error due to the free convection is likely to be negligible quantity for the range of *Re* (11,600 - 35,000) in this research.

Uncertainties in pressure measurements are largely associated with the manufacturer specified measurement accuracy of the micromanometer, which is ±1% of the reading.

Accuracy of IR Camera and determination of emissivity coefficient of the surface (where temperature measurements are performed) are predominantly significant for accurate temperature (heat transfer) measurements using IR thermography technique. Manufacturer specified accuracy for the IR camera used in the research is ±2%, whereas derived emissivity coefficients (Appendix C-2) are estimated to be accurate within ±1%.

Random Uncertainty:

Random uncertainty for each variable in the experiment is usually determined from repeated observations for different swirl numbers at the highest Reynolds number condition using Equation (C-6). The results of these tests are shown in Table C-3 1.

Table C-3 1. Random uncertainty of different variables.

VARIABLES	UNCERTAINTY (±%)
$<u>$, $<w>$	2 – 4
P	2
T_W	3
T_∞	2
E	2
I	0.5

As mentioned earlier in the thesis, the total flow rate to the swirl nozzle is the sum of axial flows and tangential flows, and contributes to the calculation of Reynolds number in this research. The axial and tangential flows came from a range of flowmeters of different types. As such, random uncertainty in relation to the total flow rate is determined by the method described in [5] for a flow consists of several flowmeters. Further detail is available in Chapter 3.

Overall uncertainty:

When systematic and random uncertainty are determined for each instrument and variable used, the overall systematic, overall random and total uncertainty values for various parameters are derived using Equations (C-4), (C-5) and (C-3), respectively. The results are shown in Table C-3 2.

Table C-3 2. Overall systematic, overall random and total uncertainty of different parameters.

PARAMETERS	OVERALL SYSTEMATIC UNCERTAINTY (±%)	OVERALL RANDOM UNCERTAINTY (±%)	TOTAL UNCERTAINTY (±%)
Re	2	3.75	4
S	2	2.8	3.5
Cp	1	2	2.2
Nu	2.2	4.15	4.7

Appendix D Boundary and impingement plane characteristics

D-1 Turbulence profiles for *Re* = 24,600 and 11,600

The turbulence conditions at the nozzle exit plane (*x/D* = 0.025) which were not presented in Chapter 4 (Figure 4-S-1 and Figure 4-S-2) are shown here for completeness of nozzle exit conditions at *Re* = 24,600 and *Re* = 11,600.

Figure D-1-1 depicts the axial (u'/U_b) and tangential (w'/U_b) components of turbulent intensity profiles at *Re* = 24,600. Results show for $S \leq 0.31$, enhancement of u'/U_b with increasing *S* is evident within $r/D \leq 0.35$ and beyond this all profiles tends to merge together with an increase due to the wall effect. The tangential component w'/U_b also show similar distributions except a sudden increase in turbulence at $S = 0.31$ in the central region of the nozzle. A significantly larger turbulence (both u'/U_b and w'/U_b) but comparable in magnitude are found for $S \geq 0.58$ at $r/D \leq 0.25$ and then decreases with *r*. An abrupt increase in w'/U_b near the wall for $S \geq 0.72$ may be due to the stronger interactions of the jet with the wall. The axial turbulent intensity is fairly uniform within 20-30% of bulk velocity compared to tangential component.

Figure D-1-2 shows u'/U_b and w'/U_b profiles at *Re* = 11,600, and the results show qualitatively similar distributions to those of *Re* = 24,600 for both weakly and strongly swirl flows.

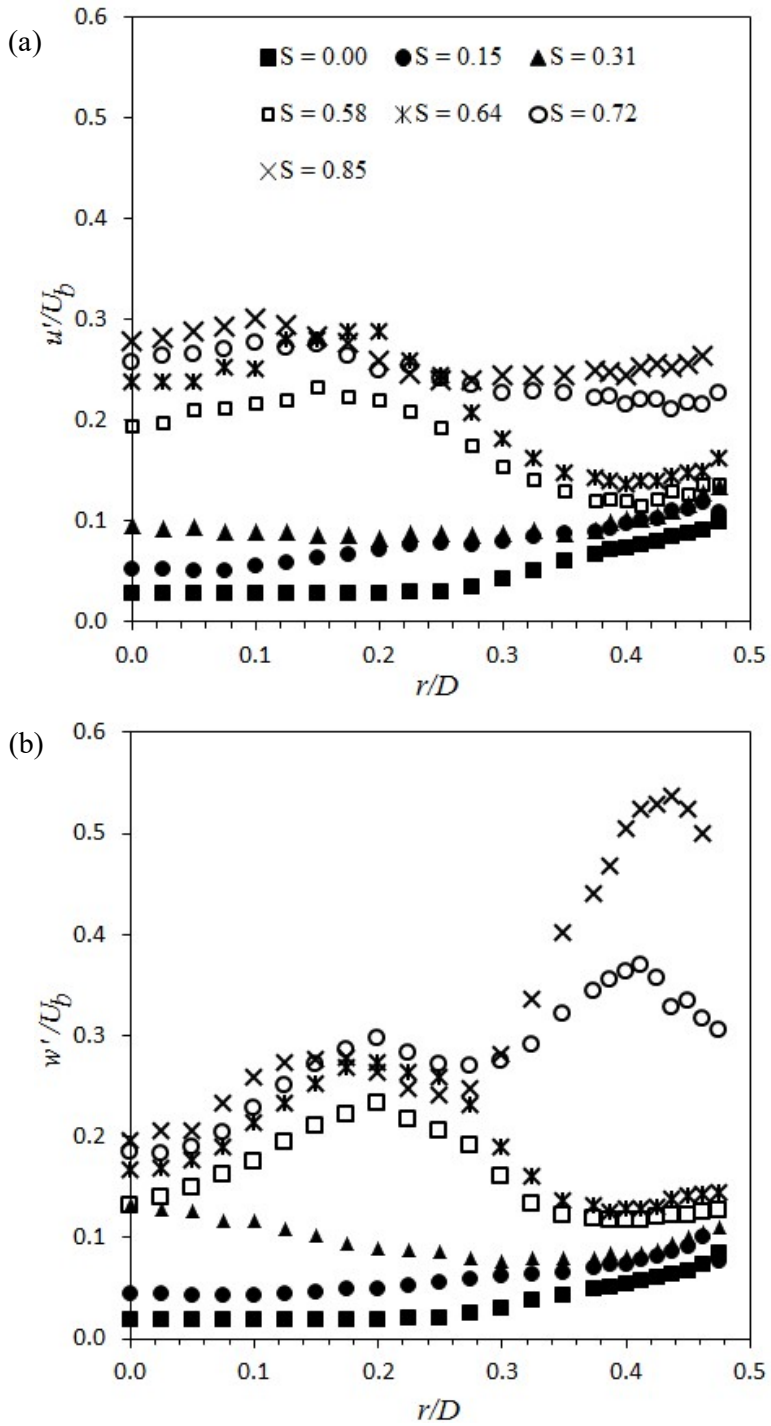

Figure D-1-1: Turbulence intensities measured at the nozzle exit (x/D = 0.025) for both non-swirling (S = 0.00) and swirling jets (S = 0.15 – 0.85) at Re = 24,600: (a) axial (u'/U_b) and (b) tangential (w'/U_b) turbulence intensity profiles.

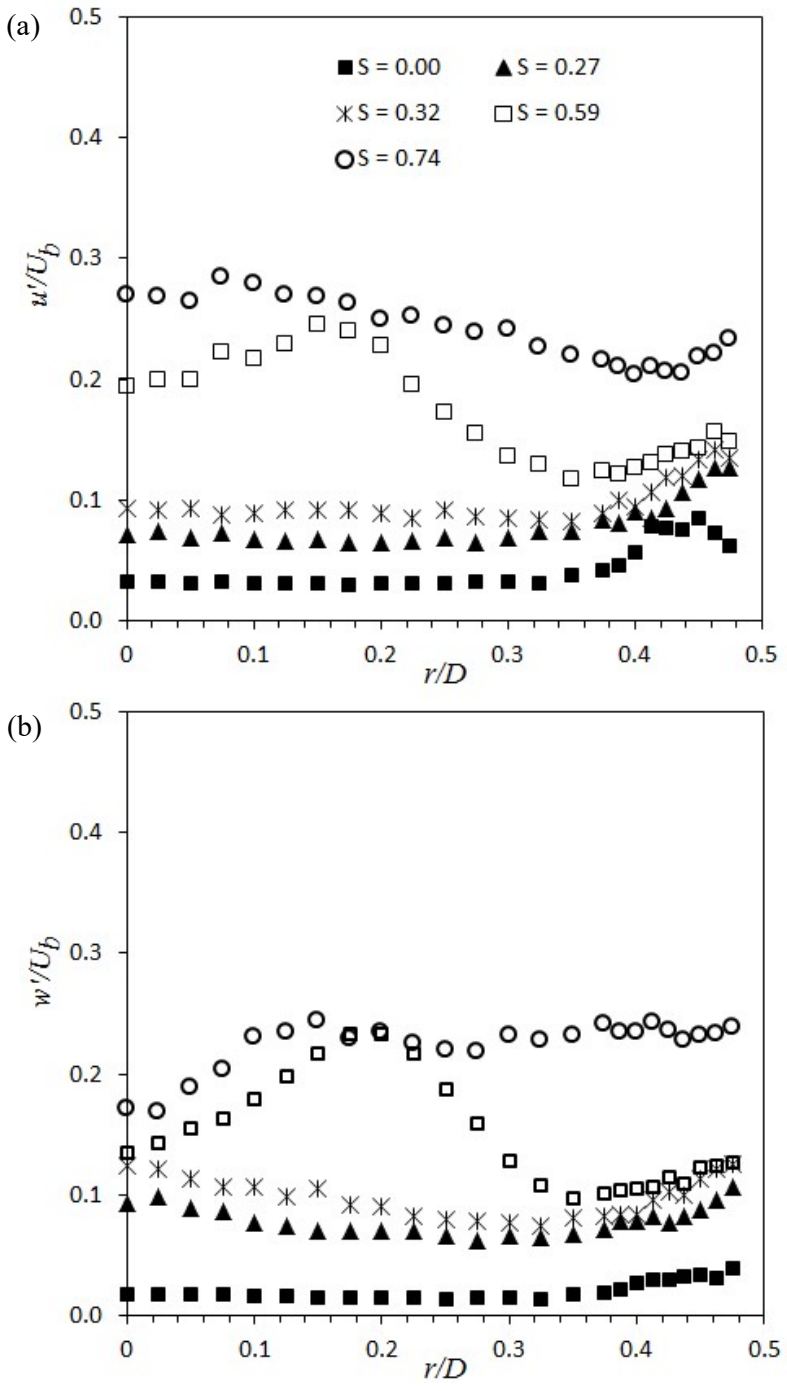

Figure D-1-2: Turbulence intensities measured at the nozzle exit (x/D = 0.025) for both non-swirling (S = 0.00) and swirling jets (S = 0.27 – 0.74) at Re = 11,600: (a) axial (u'/U_b) and (b) tangential (w'/U_b) turbulence intensity profiles.

D-2 Coefficient of pressure distribution for Re = 24,600 and 11,600

The effect of swirl (S) on the coefficient of pressure (Cp) for varied nozzle-to-plate distance (H) was presented in detail in the Chapter 4 (Figure 4.8) at Re = 35,000 only. The interplay between S and H on Cp for other two Reynolds numbers (Re = 24,600 and 11,600) is briefly discussed here.

Figure D-2-1 depicts the local Cp profile on the impingement surface for the range $0 \leq S \leq 0.85$ and $H = 1D$ to $6D$ at Re = 24,600. The overall characteristics of Cp profiles at different S are almost similar to those of Re = 35,000. Gaussian-like distributions with a maximum at the stagnation point is found for weakly-to-medium swirl flows ($S \leq 0.31$) at all H. A transitional swirl number reduces to $S = 0.58$ when the maximum Cp value shifts (radially) from the stagnation point and beyond this value flow separation occurs only at $H = 1D$. At $H \geq 2D$, Cp distribution tends to be spatially uniform with low magnitudes for increasing H at strongly swirl flows ($S \geq 0.72$). It appears the rate of reduction in Cp with S is little stronger for Re = 24,600 than Re = 35,000 as H increases. The effect of S is more evident in the near-field impingement (i.e. $H = 1D$) as S causes more abrupt change in Cp trend. As H increases, the effect of S weakens and the Cp peaks (outside the stagnation point) completely diminishes at $H = 6D$, where the flow revert to non-swirl-flow-like behaviour.

Figure D-2-2 illustrates the distributions of Cp for $0 \leq S \leq 0.74$ at Re = 11,600 over the range $H = 1D - 4D$. Likewise other higher Reynolds numbers (Re = 24,600 and 35,000), similar qualitative flow features and distributions of Cp are found for both weakly and strongly swirling flows with transitional swirl number S = 0.32. Again, flow separation occurs at $H = 1D$ and $S = 0.74$ only.

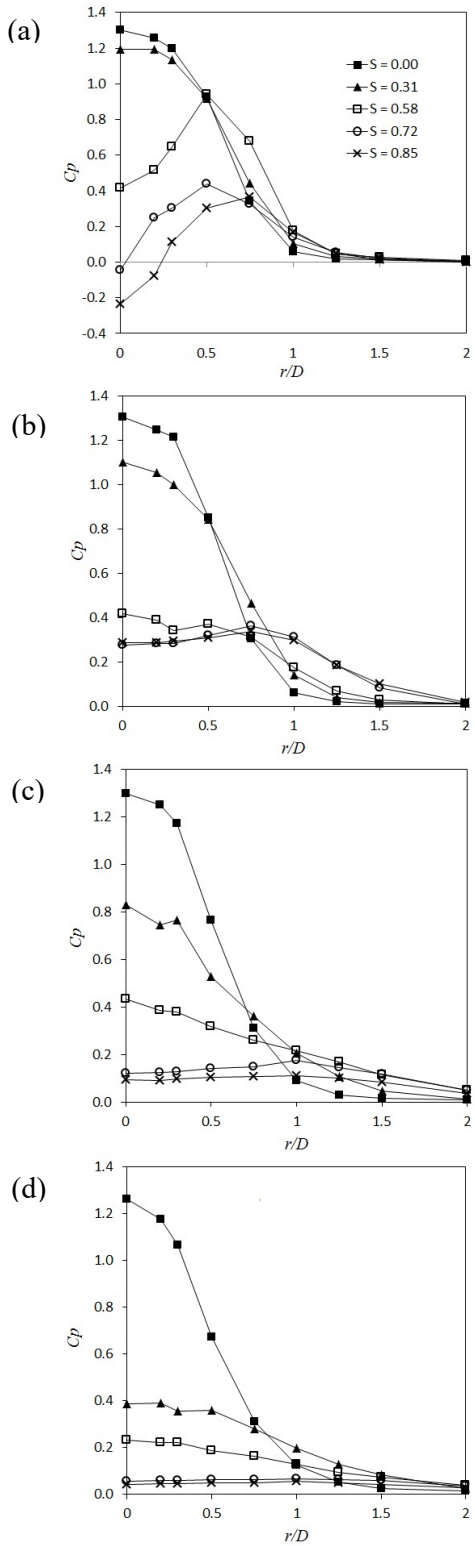

Figure D-2-1: The effect of nozzle-to-plate distance and swirl number at *Re* = 24,600 on the impingement surface pressure distribution: (a) *H* = 1*D*, (b) *H* = 2*D*, (c) *H* = 4*D* and (d) *H* = 6*D*.

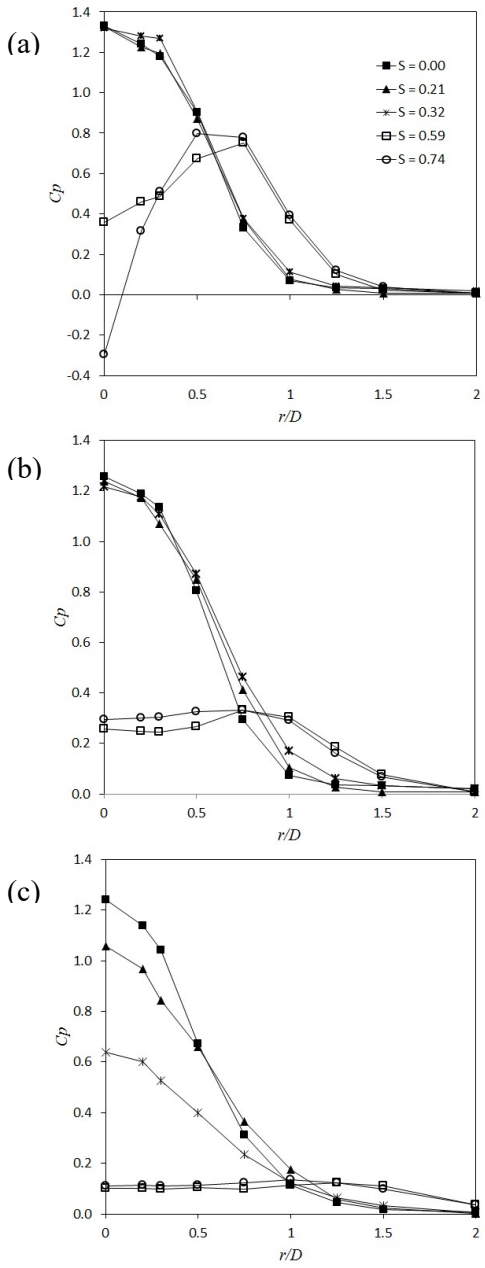

Figure D-2-2: The effect of nozzle-to-plate distance and swirl number at *Re* = 11,600 on the impingement surface pressure distribution: (a) $H = 1D$, (b) $H = 2D$ and (c) $H = 4D$.

D-3 Nusselt number distributions for Re = 24,600 and 11,600

The effect of swirl (S) on the Nusslt number (Nu) for varied nozzle-to-plate distance (H) was presented in detail in the Chapter 5 (Figures 5.5 and 5.A-1) at Re = 35,000 only. The interplay between S and H on Nu for other two Reynolds numbers (Re = 24,600 and 11,600) is briefly discussed here.

Figure D-3-1 shows radial profiles of Nu distributions over the range S = 0 – 0.74 and H = 1D - 6D at Re = 24,600, along with the corresponding standard deviations from the circumferentially averaged value for a given r. Results show that the overall Nu characteristics for non-swirling (S = 0), weakly swirling (S = 0.31) and highly swirling (S ≥ 0.72) flows at all H are qualitatively almost similar to those for Re = 35,000 (Figure 5.A-1), but magnitude of Nu for a given S reduces at Re = 24,600. The transitional Nu behaviours between weakly and strongly swirl flows occur at $S \approx 0.58$. Both local and average Nu improvements compared to that of S = 0 also occurs at $H \leq 4D$ for $S \leq 0.58$. The location of the peak Nu gradually shifts radially outward and tends to be spatially uniform distribution as H increases at high swirl numbers ($S \geq 0.72$).

Figure D-3-2 also illustrates radial profiles of Nu distributions over the range H = 1D - 6D but at further lower Reynolds number (Re = 11,600) and S = 0 - 0.74, along with the corresponding standard deviations. Although general Nu characteristics with S at this low Reynolds number are again almost qualitatively similar to those for Re = 35,000 and Re = 24,600 (Figures 5.A-1 and B-3-1) for all H, some distinctive features are also observed other than the further reduction of magnitude of Nu. For Re = 11,600, two peaks ($r/D \approx 0.5$ and 2) and two trough ($r/D \approx 0$ and 1.3) for S = 0 only occurs at H = 1D, and the disappearance of the second peak and manifestation of inner peak at the stagnation point occurs at H = 4D as opposed to 6D for other Reynolds numbers. Relatively less uniform Nu distributions for Re = 11,600 are seen in the near-field ($H \leq 2D$). In comparison with S = 0, the medium swirl (S = 0.32) improves Nu locally around the jet centre for $H \leq 2D$ and outside these swirl is found to be detrimental. The transitional swirl number in this case is found even smaller ($S \approx 0.32$).

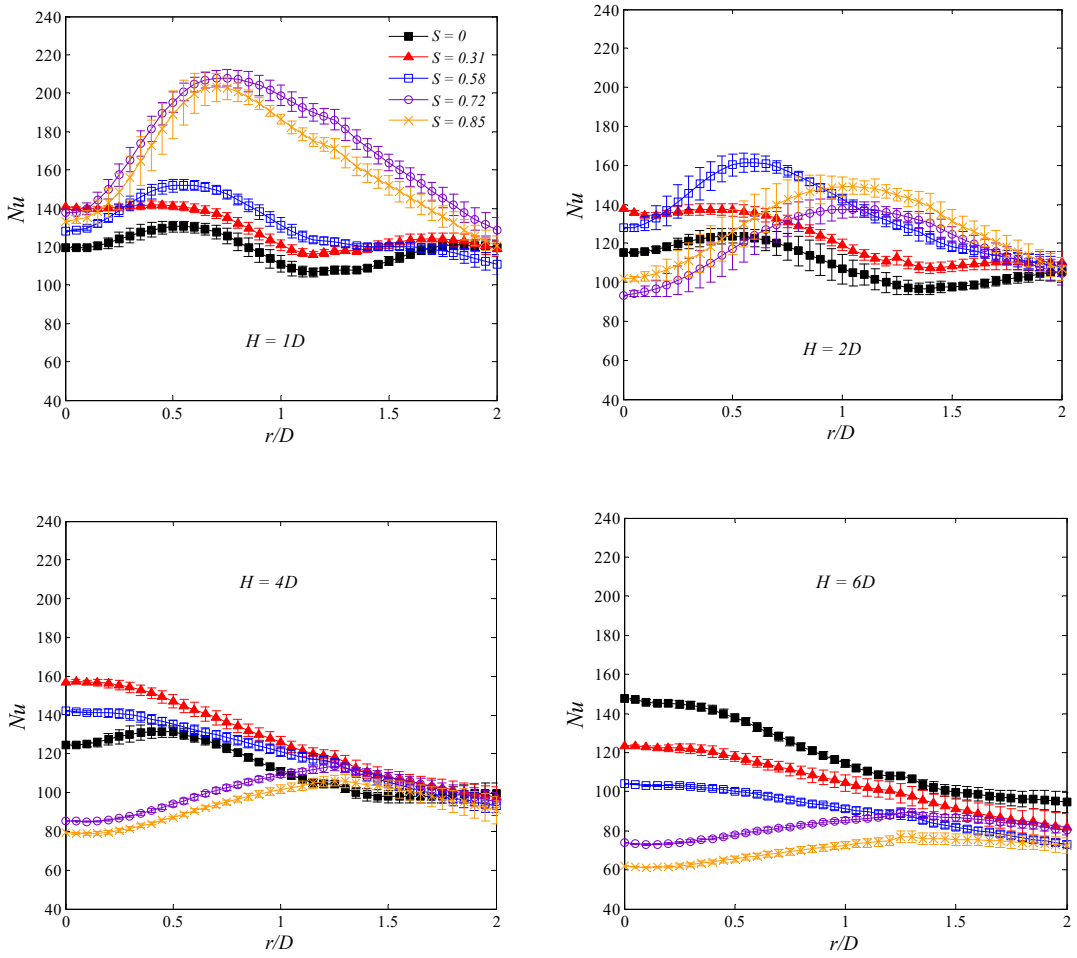

Figure D-3-1: Effect of swirl number and nozzle-to-plate distance on the radial distributions of *Nu* for *Re* = 24,600.

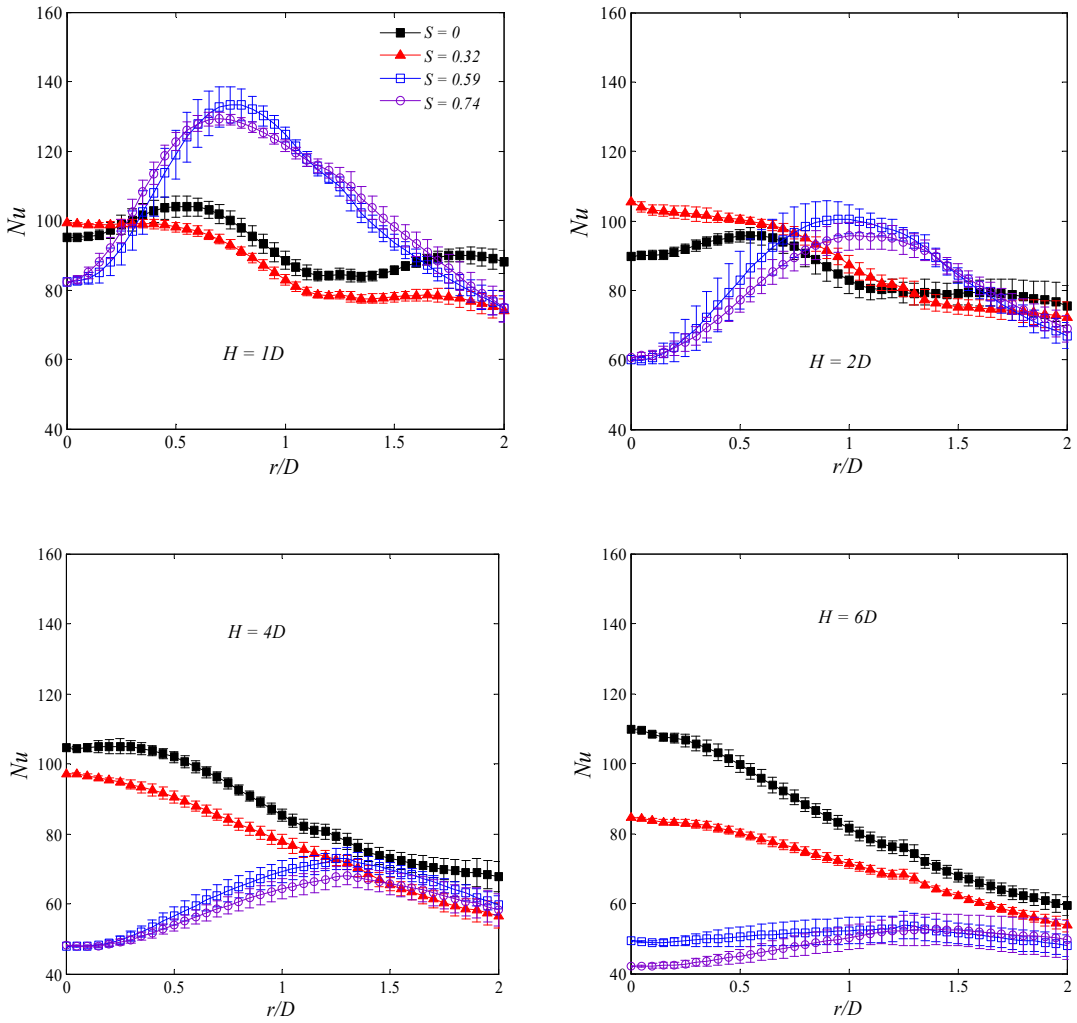

Figure D-3-2: Effect of swirl number and nozzle-to-plate distance on the radial distributions of *Nu* for *Re* = 11,600.

D-4 Impingement surface temperature: comparison of experimental data and numerical simulations

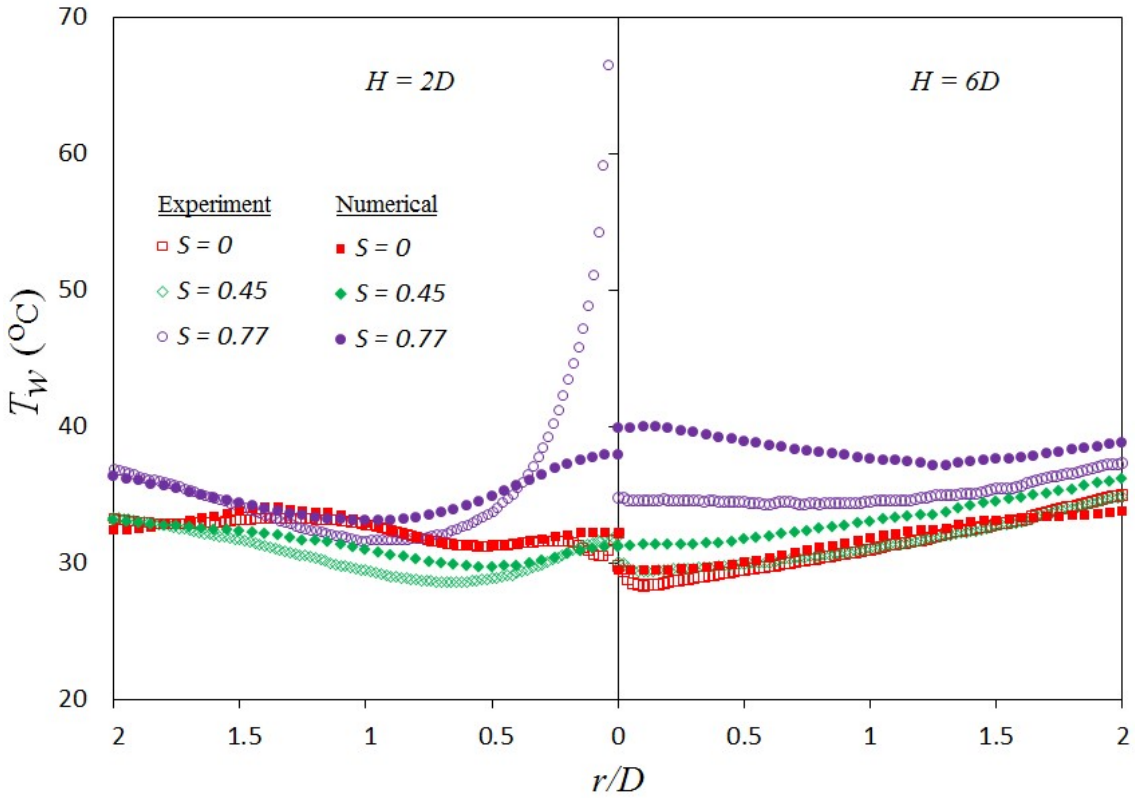

Figure D-4-1: Comparison of measured impingement surface temperature for three swirl numbers (S = 0, 0.45 and 0.77) at Re = 35,000 with numerical simulation.

Appendix E Amplitude and power spectrums of X-wire CTA probe data

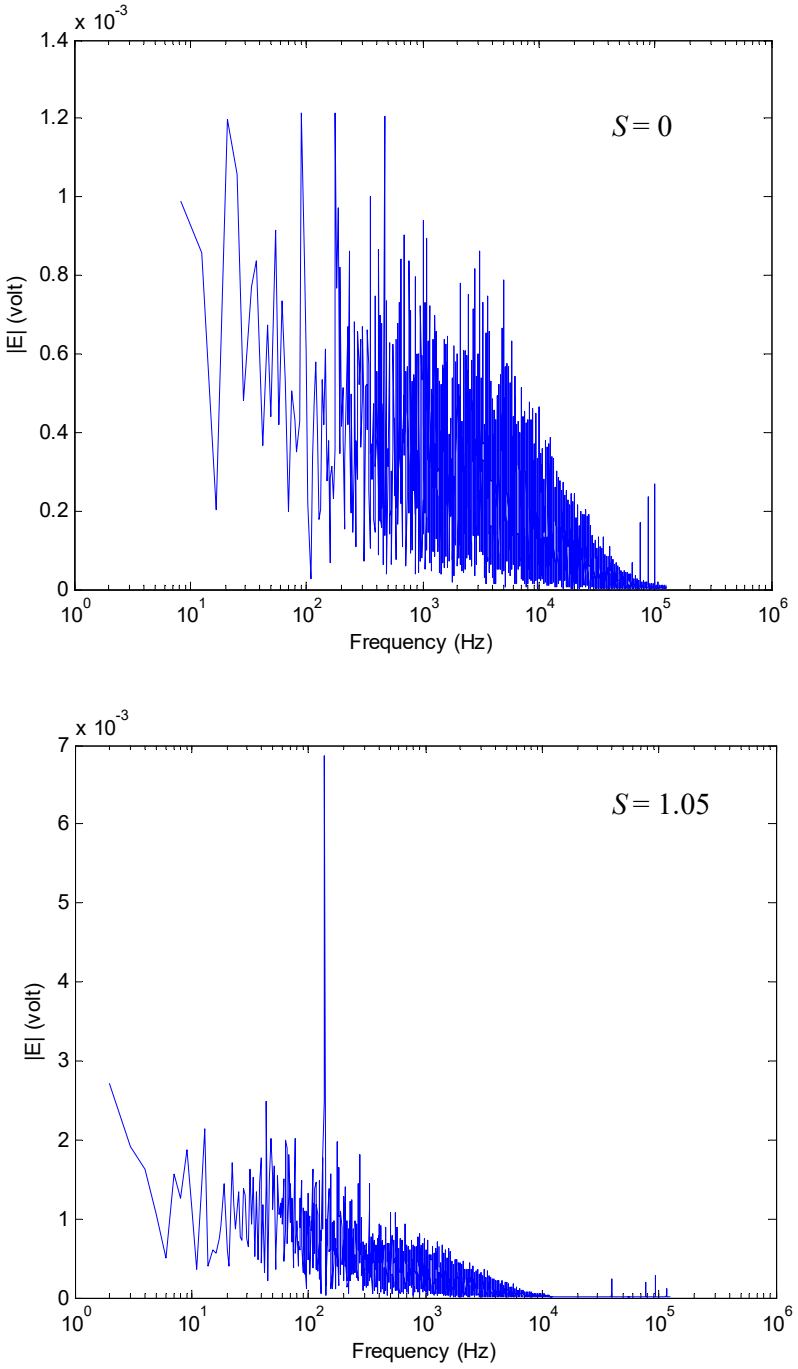

Figure E-1: Amplitude spectrum of CTA signals of the X-wire probe at Re = 35,000 for both non-swirling (S = 0) and highly swirling (S = 1.05) flows. Raw data acquired at r = 15 mm are post-processed by Fast Fourier Transform (fft) in Matlab.

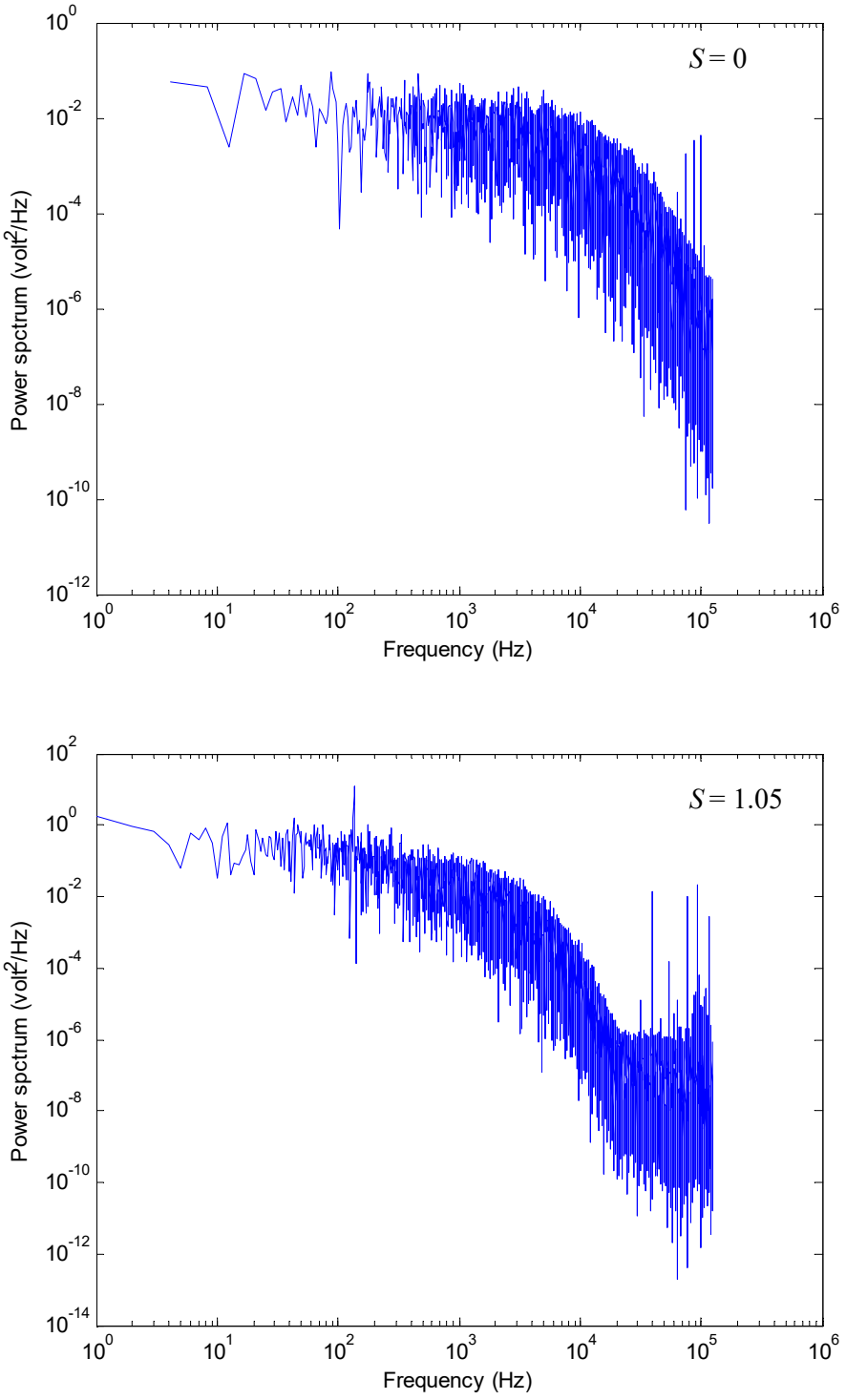

Figure E-2: Power spectrum of CTA signal of X-wire probe at *Re* = 35,000 for both non-swirling ($S = 0$) and highly swirling ($S = 1.05$) flows. Raw data are acquired at $r = 15$ mm and post-processed in Matlab.

Appendix F Supplementary materials

Following datasets and swirl nozzle design are included in the attached CD of the thesis.

i. Boundary conditions at 1 mm (x/D = 0.025) above the nozzle exit plane for all jet conditions in this thesis over Re = 11,600 – 35,000 (CD-3).
ii. Swirl nozzle design files (CD-4).
iii. Video capturing files for flow visualisations (presented in Chapter 4) for H = 1D and 2D, and S = 0, 0.27 and 1.05.
iv. Matlab code for processing of image data (CD-6).

Appendix references

1. *FLIR User Manual*, in FLIR System, p., 2009.
2. Vollmer, M. and Mollmann, K., Infrared thermal imaging: fundamentals, research and applications, Wiley-VCH Verlag GmbH, Weinheim, Germany, 2010.
3. Moffat, R. J., *Describing the uncertainties in experimental results*, Experimental Thermal and Fluid Science, 1(1), p. 3-17, 1988.
4. Montgomery, D. C. and Runger, G. C., Applied statistics and probability for engineers, 5th, John Wiley & Sons, Hoboken, NJ, 2011.
5. Dieck, R. H., Steele, W. G. and Osolsobe, G., *Test uncertainty. ASME PTC 19.1-2005*, in American Society of Mechanical Engineers: New York, NY, p., 2005.